

Vegetation structure and function measurement and modelling using drone based sensing techniques

Submitted by Dominic Fawcett, to the University of Exeter as a thesis for the
degree of Doctor of Philosophy in Geography, November 2020.

Supervisors: Dr Karen Anderson, Dr Jonathan Bennie

This thesis is available for Library use on the understanding that it is copyright
material and that no quotation from the thesis may be published without proper
acknowledgement.

I certify that all material in this thesis which is not my own work has been
identified and that any material that has previously been submitted and
approved for the award of a degree by this or any other University has been
acknowledged.



Abstract

This thesis explores the use of drone-based data acquisitions for deriving structural plant traits and spectral reflectance of vegetation which are variables of interest for carbon stock estimations and for understanding vegetation functioning. Previous work demonstrated that fine-grained spatio-temporal insights gained from drone-acquired data are critical for understanding local processes but also for interpreting dynamics in coarse scale representations of landscapes from Earth observing satellite data. This work builds on this by assessing uncertainties in data acquisition and processing workflows and demonstrating novel applications of drone acquired data. The findings from the individual chapters presented herein allow conclusions on which metrics can be used with confidence to assess the status and track changes in vegetation structure over time. An example of how the finely resolved spatial information on structural plant traits can be used for simulations of radiation propagation, towards functional landscape representations is demonstrated.

The presented work includes experiments conducted in the United Kingdom, Italy and Malaysia arising from international collaborations and addresses three critical questions in the proximal sensing of vegetation:

1. To what extent can drone Structure-from-Motion (SfM) photogrammetry-derived products deliver accurate information about vegetation height parameters? Using SfM photogrammetry for deriving robust vegetation height parameters is of particular interest when seeking to derive growing stock volume and biomass for plantation and forest management purposes and for the assessment of carbon stocks. The associated study focused on an oil palm plantation in Sarawak, Malaysia and examined the quality of SfM-based estimates of palm height and inferred stem height, both metrics which are commonly used for allometric estimates of biomass. Further, the impact of acquisition methodology on point cloud precision was investigated. Results showed that SfM could provide palm height metrics at the individual tree level with mean relative errors between 11.7% and 18.9% dependant on palm age and that for mature palms (>10 years)

flight plans favouring coverage over spatial resolution and overlap did not decrease the accuracy.

2. How accurate and consistent are surface reflectance and vegetation index products acquired from drone-based sensors over vegetation canopies? Quantifying the spatial and temporal consistency of surface reflectance and vegetation index data acquired by lightweight sensors mounted on drone platforms is essential for applications in precision agriculture, for species classification and for studying vegetation functioning. This topic was addressed through two studies. The first study compared drone acquired spectral data over a maize field in Grosseto, Italy against reference datasets from near simultaneous airborne and satellite based image acquisitions. While uncertainties in drone acquired surface reflectance were found to be greater than anticipated (5-28% relative errors over the maize field), VIs were highly correlated and comparable across scales. The second study investigated the use of vegetation index data to track phenology related changes over time for mostly deciduous tree species in Cornwall, UK. VIs proved to be sufficiently consistent for both, acquisitions under overcast and cloud free skies to resolve phenological changes with illumination based uncertainties an order of magnitude smaller than the total increase in index values across Spring green-up.
3. Can drone-based data be used to constrain and drive models of radiative transfer for understanding photon-plant interactions in complex heterogeneous canopies? Combining drone acquired canopy height models and vegetation index information to represent vegetation in a 3D radiative transfer model represents a new opportunity for simulating the interaction of light with vegetation at fine spatial scales. Previously, the information required for modelling heterogeneous vegetation canopies could only be acquired through laborious measurements in-situ or financially costly laser-scanning methods. This topic was explored by creating a representation of a local wildlife conservation site in Cornwall, UK within the Discrete Anisotropic Radiative Transfer (DART) model. The model was used for a case study focused on simulating the photosynthetically active radiation (PAR) reaching the understory as hourly fractions and spatially explicit (1 m spatial resolution) daily light

integrals across Spring green-up. Results showed that while the drone-data parameterised model could represent the variability across discontinuous vegetation cover, PAR reaching the understory was considerably overestimated at start-of-peak greenness due to uncertainties in modelled plant area density and leaf angular distributions.

The primary data acquisitions of all the presented studies were performed exclusively with lightweight multi-rotor drones, trialling relatively low-cost consumer grade and multi-spectral cameras which have since been widely adopted by research groups globally. The presented results therefore represent a timely contribution with relevant insights from appropriate acquisition methodologies to novel applications of drone acquired data for representing vegetation in a radiative transfer modelling context.

Acknowledgements

This PhD was funded by the European Union's Horizon 2020 research and innovation programme under the Marie Skłodowska-Curie Grant Agreement No. 721995.

I want to thank my supervisors Karen Anderson and Jon Bennie for their tireless support, encouragement and guidance throughout my work on this thesis and many aspects beyond. It was a pleasure to work closely with Karen and I also greatly appreciate the opportunities she gave me to develop my interests as an independent researcher.

The presented work was made possible through the invaluable support of many collaborators. I'd like to thank James Duffy for his help and introduction to the workings of the DroneLab along with Leon DeBell and Andy Cunliffe for further drone related support. Tim Hill and Khoon Lip Kho enabled and greatly supported a successful first field campaign in Malaysian Borneo. The DISAT team at UNIMIB provided a stimulating research environment during my secondment in Italy and it was a pleasure to be able to work with all of them and collaborators from IREA CNR on joint field campaigns. I'd also like to thank Robin Curtis for supporting my fieldwork in Cornwall and Ruolin Leng for our fruitful collaboration. Thanks to Javier Blanco for all our helpful discussions and his contribution, together with Pia Benaud, to the writing of our joint manuscript.

I extend my thanks to the entirety of the TRUSTEE network including project coordinators Micol Rossini and Cinzia Panigada as well as my fellow PhD students, which contributed to the training and unforgettable experiences I had as part of this network.

Last but not least I want to thank my family, friends and my partner Chengxiu for supporting me throughout this journey, I couldn't have done it without you.

Table of Contents

1	Introduction and Research Context	38
1.1	Introduction	38
1.2	Drone-based vegetation structure characterisation towards improved carbon stock estimations.....	41
1.2.1	Established methods of remote biomass retrieval	41
1.2.2	Drone based methods for vegetation structure and biomass estimation	43
1.2.2.1	Drone LiDAR	43
1.2.2.2	Drone-based structure from motion photogrammetry.....	45
1.2.2.3	Biomass estimation from drone measurements	48
1.2.3	Upscaling.....	50
1.3	Contribution of drone measurements to understanding and modelling fluxes	51
1.3.1	Core canopy structural measurements from drones	53
1.3.2	Drone-based multispectral imaging	55
1.3.3	Drone acquired indicators of light use efficiency.....	56
1.3.4	Drone-based hyperspectral imaging	59
1.3.5	Modelling radiation interaction with vegetation representations based on drone data	60
1.3.6	Drones as a tool for studying vegetation phenology	61
1.4	Conclusions.....	62
2	Overview of research aims	64
3	Methods	67
3.1	Chapter overview	67
3.2	Study systems.....	67
3.2.1	Oil palm plantation (Chapter 4)	68
3.2.2	Maize field (chapter 5)	69
3.2.3	Heterogeneous conservation area (Chapter 7 & 8)	70

3.3	Drone data acquisition and processing	71
3.3.1	Drone platform	71
3.3.2	Sensors	72
3.3.3	Flight planning	75
3.3.4	Ground control and georeferencing	76
3.3.5	Structure-from-motion photogrammetry and point cloud processing	78
3.3.6	Radiometric calibration	79
3.4	Supporting <i>in situ</i> measurements	82
3.4.1	Vegetation structural measurements	83
3.4.1.1	Height metrics	83
3.4.1.2	Leaf and plant area index.....	83
3.4.2	Spectral measurements	86
3.4.3	Photosynthetically active radiation measurements	87
3.5	Radiative transfer modelling	89
3.5.1	1-D radiative transfer modelling.....	89
3.5.2	3-D radiative transfer modelling.....	90
3.6	Statistical methods	92
3.6.1	Linear and non-linear regression models.....	92
3.6.2	Monte Carlo approach for point cloud uncertainty estimation	93
4	Drone derived structure-from-motion photogrammetry point clouds for oil palm (<i>Elaeis guineensis</i>) canopy segmentation and height estimation	94
4.1	Introduction	96
4.2	Materials and Methods	100
4.2.1	Study site	100
4.2.2	Data acquisition	101
4.2.2.1	Field sampling	101
4.2.2.2	Drone flights and GPS data.....	102
4.2.3	Photogrammetric processing	104

4.2.4	Point cloud processing and parameter retrieval.....	105
4.3	Results	108
4.3.1	Photogrammetric dense clouds	108
4.3.2	Digital terrain models	110
4.3.3	Palm identification.....	111
4.3.4	Height metrics.....	112
4.4	Discussion.....	115
4.4.1	Uncertainties within resulting SfM point clouds.....	115
4.4.2	Quality of derived DTMs	116
4.4.3	CHM-based palm identification.....	116
4.4.4	Assessing maximum point cloud height against TFH	117
4.4.5	Point cloud height metric based stem height estimation	118
4.4.6	Implications for oil palm plantation management and research..	119
4.5	Conclusions.....	121
5	Multi-Scale Evaluation of Drone-Based Multispectral Surface Reflectance and Vegetation Indices in Operational Conditions.....	122
5.1	Introduction	125
5.2	Materials and Methods.....	128
5.2.1	Study Site	128
5.2.2	Image Data	129
5.2.3	Field Measurements	131
5.2.3.1	Field Spectral Measurements for Calibration and Validation	131
5.2.3.2	Leaf Area Index Measurements.....	132
5.2.4	Image Data Processing.....	133
5.2.4.1	Surface Reflectance from Drone Image Data	133
5.2.4.2	Vegetation Index Products.....	135
5.2.4.3	Multi-Scale HCRF and VI Intercomparison	135
5.3	Results	136

5.3.1 HCRF Products.....	136
5.3.1.1. Reference Target Validation of Drone Derived HCRF	137
5.3.1.2. Spatial Comparison between Airborne and Drone Derived Surface Reflectance	140
5.3.2 Vegetation indices.....	144
5.4 Discussion.....	148
5.4.1 HCRF Accuracy	148
5.4.2 Multi-Scale VI Consistency and Sensitivity	150
5.5 Conclusions.....	151
6 Monitoring spring phenology of individual tree crowns using drone-acquired NDVI data.....	153
6.1 Introduction	156
6.2 Materials and Methods	159
6.2.1 Study site.....	159
6.2.2 Drone data acquisition and processing.....	159
6.2.3 Field reference data.....	161
6.2.4 Assessment of crown NDVI values in direct versus diffuse conditions.....	163
6.2.5 Green-up modelling and phenophase estimation	163
6.3 Results	165
6.3.1 Surface reflectance and NDVI orthomosaics	165
6.3.2 NDVI sensitivity to illumination and aggregation metrics	167
6.3.3 NDVI time-series.....	169
6.3.4 Extracted species phenophases	172
6.4 Discussion.....	175
6.4.1 Robustness of drone based NDVI time-series	175
6.4.2 Drone derived phenology metrics	177
6.4.3 The future of drone-based phenological studies	179
6.5 Conclusions.....	180

7	Modelling understory light availability in a heterogeneous system using drone captured structural and spectral data	181
7.1	Introduction	184
7.2	Materials and Methods	186
7.2.1	Study site	186
7.2.2	Field measurements	188
7.2.3	Drone datasets	189
7.2.3.1	Vegetation index orthomosaics	189
7.2.3.2	Photogrammetric point cloud.....	190
7.2.4	Irradiance measurement and modelling.....	191
7.2.5	Scene 3D structure	191
7.2.6	Plant area index.....	193
7.2.7	Understory PAR simulation experiments with DART	193
7.3	Results	197
7.3.1	Photogrammetry products and scene 3D structure.....	197
7.3.2	Vegetation index mosaics and PAI modelling	198
7.3.3	PAR simulation outputs and validation	200
7.4	Discussion.....	207
7.4.1	Capability of drone SfM and multispectral data for representing complex vegetated landscapes.....	207
7.4.2	Accuracy of understory PAR simulations across Spring green-up using DART informed by drone data.....	209
7.4.3	Capability of drone-data parameterised models to improve simulations of small-scale understory PAR variations	210
7.4.4	Opportunities for 3D RT models informed by drone acquired data ...	
	212
7.5	Conclusions.....	212
8	Synthesis	214

8.1	Retrieving vegetation height metrics using drone-based SfM photogrammetry	214
8.2	Accuracy and consistency of surface reflectance and vegetation indices derived from drone acquired measurements.....	217
8.2.1	Drone acquired surface reflectance and vegetation indices	217
8.2.2	Deriving LAI and PAI from drone NDVI measurements	219
8.3	Use of drone-acquired data to constrain and drive 3D radiative transfer models	221
8.4	Drone based observations for global studies of the carbon cycle	224
9	Conclusions	226
10	References	228
11	Appendices.....	285
	A1 Supplementary information for chapter 4.....	285
	A2 Supplementary information for chapter 5.....	287
	A3 Supplementary information for chapter 6.....	289
	A4 Supplementary information for chapter 7.....	298
	A5 Hemispherical flight experiment for tree crown reconstruction	308
	A6 Investigating impacts of calibration methodology and irradiance variations on lightweight drone-based sensor derived surface reflectance products...	310
	A7 TRUSTEE deliverable 1.6: Procedure for the in-flight definition of the flight plan for multi-rotor drones	327
	A8 TRUSTEE training certificates	346

List of Tables

Table 1-1: Drone-mountable hyperspectral sensor technologies and examples	60
Table 3-1: Acquisition parameters set during flight planning for different studies, separated by sensor type: RGB primarily used for generating dense point clouds yielding structural information and multispectral primarily used for generating surface reflectance orthomosaics.	76
Table 3-2: Formulas used to convert DNs as measured by the Sequoia camera and irradiance sensor to hemispherical-conical reflectance factors (HCRF). Left column: reflectance calibration not considering irradiance, Right column: Reflectance calibration with irradiance compensation.	82
Table 4-1: List of drone flights used in this study, indicating the flight parameters, the palm age plot site (including the replicate for the 10 year old plot) and date of acquisition.	104
Table 4-2: Parameters for the two different acquisitions over the 10 year old plot along with mean precision estimates in X, Y and Z directions....	110
Table 4-3: Linear stem height model strength and errors for the 30 th -90 th point cloud height percentiles as well as the maximum and mean values. Reported for the 7 year old plot and the 10 year old plot with high and low quality acquisitions. The highlighted rows show the models with the highest R ² values which are used subsequently for stem height estimation.	114
Table 5-1: Description of image datasets used within this study, including sensor, acquisition time, GSD (spatial resolution) and spectral bandwidths (spectral resolution).....	131
Table 5-2: MAD of Sequoia derived HCRF values per band for the three calibration approaches, estimated from the comparison with field measured reference panels and surfaces.	140
Table 5-3: MAD of Sequoia derived HCRF values per band for the three calibration approaches, estimated from the comparison with HyPlant HCRF values.....	143

Table 5-4: Bias and relative errors of the HyPlant HCRF for the Sequoia band spectral ranges over three differently reflective validation surfaces (tarps).....	143
Table 5-5: MAD of Sequoia derived VI values (NDVI and CHL) for the three calibration approaches, estimated from the comparison with HyPlant derived index values.....	147
Table 6-1: Relationship between crown NDVI values extracted from drone orthomosaics acquired during direct and diffuse illumination conditions for leaf-off and leaf-on stages. The dates included in this analysis for leaf-off are a) 22 March 2019 (diffuse) and 24 March 2019 (direct), b) 31 March 2019 (direct) and 1 April 2019 (diffuse), and c) for leaf-on are 22 July 2019 (diffuse) and 23 July 2019 (direct). This relationship is assessed for different aggregation metrics to derive crown NDVI values: Median, mean, and the mean of the 20% brightest pixel method. (assessed using R ² , MAD, bias and a t-test for significant differences between aggregated values for direct and diffuse acquisitions).....	169
Table 7-1: Input parameters for the DART model to perform simulations of radiative transfer in the PAR wavelength range and the data sources used to derive them in this study.....	196
Table 7-2: A reference list of the DART simulations compared, with different combinations of PAD and crown geometry information. PAD is defined as the mean for all vegetation or varied at crown level informed by drone NDVI data. Crown geometry is informed either by DSM-based segmentation or manually identified crown ellipsoids.	
.....	197
Table 7-3: Correlation of understory simulated DLI values with HOBO logger measurements as well as differences (total and relative) to quantum sensor measured DLI and correlations with true hourly PAR fractions at the “woodland north” location for the cloud-free conditions of 15 July 2019. Simulations are described in Table 7-2.....	206

Table A 1: Simulated Sequoia and Sentinel 2A derived NDVI and CHL values for simulations of varying LAI and Chlorophyll a + b content respectively.....	288
Table A 2: Sampling date and illumination conditions for each drone acquisition of the study site, along with the panel reflected pseudo-radiance (homogenous to actual radiance, (Parrot, 2017) measured by the Parrot Sequoia in the red and NIR band as well as their ratio which indicates wavelength-specific differences in reflected radiance.	289
Table A 3: Per-class mean of the RSE of the logistic model fits to the NDVI time series for each individual deciduous crown.	290
Table A 4: Reported timing (DOY) for budburst and first leaf of individual trees in the South West UK from the Nature's Calendar database for Spring 2019. The number of individuals (n), mean, median and standard deviation (sd) are reported for 7 species. The median of drone NDVI derived SOS per species is compared to the Nature's Calendar budburst and first leaf mean and the difference reported (SOS minus budburst or first leaf). Where the difference is greater than ± 1 sd, the cell is shaded.....	295
Table A 5: Difference between the means of phenological metrics over all deciduous classes extracted from crown time-series using the 20% brightest pixel method and the mean of all crown pixels.	297
Table A 6: Days for which half-hourly understory PAR and DLI were simulated, divided into SOS, MOG and SOP time periods. Includes the corresponding date of the closest drone observation, the location of the PAR loggers and summary of illumination conditions for the simulated day. 'Mixed' indicates variable conditions throughout the day with the predominant illumination condition specified in brackets.	298
Table A 7: Formulas for the calculation of the five assessed VIs from Parrot Sequoia surface reflectance bands as well as references to studies using or developing these indices.	302
Table A 8: Coefficient of determination R ² and RMSE from LOOCV for the OLS and nonlinear (exponential) regression models of PAI against five vegetation indices for sampled trees/plots. For nonlinear models	

only RMSE is reported due to a potentially misleading R2 metric.	
.....	302
Table A 9: Formulas used to convert DNs as measured by the Sequoia camera and irradiance sensor to surface reflectance. Left column: reflectance calibration not considering irradiance, Right column: Reflectance calibration with irradiance compensation.....	316
Table A 10: RMSE per band and calibration method between the measured reflectance and the reference reflectance for the reference panels. In brackets: Standard deviations over the pixels of each panel.	320
Table A 11: Means and standard deviations of per-palm index values for the two acquisitions F1 and F2, with and without irradiance compensation.	
.....	323
Table A 12: Standard deviations of measured illumination values of the Vis and IR photodiodes for the three performed acquisitions.....	341

List of Figures

Figure 1-1: Pan-tropical aboveground carbon estimations based on GLAS and MODIS satellite data and field measurements (Baccini et al., 2012). The colour scheme from brown to green indicates the amount of carbon, see upper panels for numeric values.....	43
Figure 1-2: Overview of typical drone SfM photogrammetry workflows for vegetation studies (Dandois and Ellis, 2013). Letters (a) to (e) indicate the typical order of the steps in a standard workflow.....	46
Figure 1-3: a) Side-view of a transect through a study plot containing eucalypt trees, generated from the point cloud of an ALS system and b) the same produced using RGB images and SfM photogrammetry (Wallace et al., 2016).	48
Figure 1-4: Platforms and spatial scales of data in remote sensing (HiLDEN, https://arcticdrones.org/ , 2018).....	51
Figure 1-5: Example of modelled footprints (50-99%) and landcover classification of heterogenous flux-tower sites in Canada (Chen et al., 2012)....	54
Figure 1-6: Drone Multispectral imagery (false colour) of an olive orchard acquired using an MCA-6 multispectral sensor (a) and derived chlorophyll content (b) and LAI (c) per canopy (Berni et al., 2009)	58
Figure 2-1: Structure of the presented thesis with numbers corresponding to chapters. The case studies or data chapters are presented with abridged titles and arrows indicating which studies are related and inform following studies in terms of data or methodology used.	66
Figure 3-1: Study site locations shown in a global context, with indications of data chapters in which they are featured.....	68
Figure 3-2: Images from the field campaign in the oil palm plantation in Sarawak, Malaysia: a) Drone image taken above the 10 year-old plantation including flux-tower, b) oil palm from the 2 year-old plantation, c) author and co-pilot standing between the 7 and 2 year-old plantation blocks while carrying out a drone flight.....	69
Figure 3-3: Images from the field campaign in Grosseto, Italy: a) drone image showing the heterogeneity of the studied maize field, b) reflectance panels for calibration and validation of multispectral images	

(dimensions: 50 x 50 cm and 40 x 60 cm), c) collaborators performing field spectral measurements, d) maize plant in tasselling stage....	70
Figure 3-4: Images from the Trelusback Farm study site: a) drone image of a study site subset including the mixed woodland (c) and an isolated oak tree (b), b) oblique view of the oak tree shortly after budburst, c) image from within the woodland showing flowering of the understory (<i>Hyacinthoides non-scripta</i>) and quantum sensors mounted on posts (bottom).....	71
Figure 3-5: The 3DR Solo drone (a) used for this project, with 3D printed mounting solutions for a powerbank (b) and Parrot Sequoia irradiance (c) and multispectral imaging sensors (d).....	72
Figure 3-6: Reflectance spectrum of vegetation (grass, measured using an ASD spectrometer) with characteristic spectral features annotated. The spectral response curves of the four Sequoia cameras are overlaid.	
.....	74
Figure 3-7: Central GCP network being deployed in a Malaysian forest clearing by collaborators including (a) 40 x 40 cm painted PVC targets and (b) 80 x 80 cm canvas targets.....	77
Figure 3-8: Results of a dark current experiment conducted with the Sequoia (lenses covered in dark room) depicting DN changes with increasing sensor temperature. a) mean and median DN values for images in the red band, b) DN values for a sequence of nine pixels (vertical downwards transect from image centre) for images in the red band.	
.....	81
Figure 3-9: DHP images of a) woodland pre green-up, b) woodland post green-up, c) single oak tree post green-up.....	84
Figure 3-10: a) Schematic of 90° sectors extracted from four hemispherical images taken below the tree crown. d is the distance of ring i from the image centre. b) Schematic showing the path length $S(\theta_i)$ as approximated for each crown, ring and sector in this study.....	86
Figure 3-11: a) Levelled LightScout quantum sensor (Spectrum Technologies Inc.) for measuring PAR, b) woodland understory sensor arrangement with data logger (centre).....	88

Figure 3-12: Figure representing a 3D scene cell matrix as can be simulated by DART, including parameterised voxels and 3D objects. Modified from (Gastellu-Etchegorry et al., 2012).....	92
Figure 4-1: Top: The state of Sarawak in Malaysian Borneo with a star marking the location of the studied plantation (shapefiles from www.divagis.org, last accessed 01.11.2020). Bottom: Satellite imagery with the location, extent and age in years of the studied plots (Google Earth).	101
Figure 4-2: Processing workflow for deriving per-palm height metrics from drone data	107
Figure 4-3: RGB dense point cloud subsets (33 x 33 m) of the 2, 7 and 10 year old plantation datasets.	108
Figure 4-4: Maps of interpolated point precisions in X, Y and Z direction for the 10 year old palm plot. Top row: Acquisition with 4.43 cm/pixel GSD and 60% nominal overlap. Bottom row: Acquisition with 1.71 cm/pixel GSD and 75% nominal overlap.	110
Figure 4-5: Interpolated DTM heights above mean sea-level versus GPS measured reference ground heights. Left: 2 year old plot, Middle: 7 year old plot, Right: 10 year old plot.	111
Figure 4-6: Left: Resulting palm locations (yellow points) for the 10 year old plot and subset location (white rectangle), right: Subset illustrating omitted palms (red circles).	112
Figure 4-7: Maximum point cloud heights plotted against field measured TFHs for 2 year, 7 year and 10 year old palms.	113
Figure 4-8: Maximum point cloud height compared for the same palms between replicates of the 10 year old plot.....	114
Figure 4-9: Histograms of estimated stem heights for the 7 year old plot (left) and 10 year old plot (right).	115
Figure 5-1: Overview of the multisource datasets, including details on spatial resolution, and comparison experiments performed. Arrows indicate which datasets are compared within this study.	128
Figure 5-2: The studied maize field in the province of Grosseto, Italy is depicted along with its location (inset map). The flight lines and coverage of the drone (Sequoia, red) and airborne (HyPlant, blue) datasets are also shown. Image data licensed by ESRI, © DigitalGlobe.	129

Figure 5-3: Relative spectral responses of the four Parrot Sequoia cameras as well as the most closely corresponding Sentinel 2A bands (bands 3, 4, 6 and 7), overlaid on a measured grass reflectance spectrum.	131
Figure 5-4: Position and values of LAI measurements available for the analysis (a), acquired along a transect on 10 × 10 m plots (b).	133
Figure 5-5: False-colour infrared representations (a) and representative HCRF spectra (b) of the Sequoia (top), HyPlant (middle) and S2 (bottom) surface reflectance products over the maize field study site (no pure soil pixel for S2). The subsets shown are the extents analysed. Aerosol and water vapour bands of S2 were omitted.	137
Figure 5-6: Sequoia multispectral image data-derived HCRF of validation targets compared to ASD measurements.	139
Figure 5-7: Scatterplot comparisons of Sequoia and HyPlant based HCRF values for the four bands analysed over the region of interest with an ordinary least squares regression line (bold), the R ² and the MAD.	142
Figure 5-8: Difference images (Sequoia A2 minus HyPlant) of the HCRF values of the four analysed bands over the studied maize fields.	143
Figure 5-9: Scatterplot comparisons of Sequoia and HyPlant based NDVI (a) and CHL (b) values for the region of interest with an ordinary least squares regression line (bold) and the MAD.	145
Figure 5-10: Top: Scatterplots of NDVI (a) and CHL values (b) derived from S2 and Sequoia imagery (resampled to 20 m spatial resolution). Bottom: Scatterplots of NDVI (c) and CHL values (d) derived from S2 and HyPlant imagery (resampled to 20 m spatial resolution).	146
Figure 5-11: Histograms of Sequoia (a–c) and HyPlant (d–f) NDVI values for three 10 × 10 m ESUs of varying LAI. g) NDVI values averaged over ESU extents and the corresponding LAI value measured in the field. Non-linear model fits are provided for illustrative purposes.	147
Figure 6-1: A: RGB orthomosaic from consumer-grade camera images as overview of the Trelusback Farm study site in Cornwall, UK (50°12'10.0"N 5°12'22.6"W) on 22 July 2019, with crosses indicating GCP locations, dashed lines the locations of DHP transects and the square showing the location of the concrete reference surface. B and C: False-colour orthomosaics from Parrot Sequoia image data (red:	

- NIR band, green: red band, blue: green band) of the study site, B: on 22 July 2019 with overcast conditions resulting in diffuse illumination and C: on 23 July 2019 with cloud free conditions resulting in direct illumination with clearly visible cast shadows. 162
- Figure 6-2: Example of a sigmoid model fitted to NDVI data of a grey willow crown from this study, with vertical lines indicating the timing of SOS, MOG and SOP, determined based on the rate of change of curvature. 164
- Figure 6-3: False-colour infrared representations (red: NIR band, green: red band, blue: green band) of surface reflectance orthomosaics of the study site generated from drone acquired multispectral images during a) leaf-off (22.03.2019) and b) leaf-on (22.07.2019) conditions. (colour range scaled to better match reflectance value range of leaf-off image) c) A map of the digitised tree samples colour coded by species. 166
- Figure 6-4: A fully greened-up single oak tree crown on the study site ($50^{\circ}12'07.6''\text{N}$ $5^{\circ}12'23.6''\text{W}$), imaged a) in true-colour using a consumer grade camera and its NDVI derived from multi-spectral imagery during b) overcast (10:51, 22 July 2019) and c) cloud-free conditions (11:48, 23 July 2019). The colour scale is scaled between 0.8 and 0.92 to reveal small NDVI differences within the crown between acquisitions. 168
- Figure 6-5: Density distributions of crown pixel NDVI values (all pixels of delineated crowns, see Figure 6-3 c), for leaf-off and leaf-on stages during contrasting illumination conditions (direct and diffuse). a) leaf-off NDVI values for 22 March 2019 (diffuse) and 24 March 2019 (direct), b) leaf-off NDVI values for 31 March 2019 (direct) and 1 April 2019 (diffuse) and c) leaf-on NDVI values for 22 July 2019 (diffuse) and 23 July 2019 (direct). 168
- Figure 6-6: Time-series of NDVI per species from 20 drone acquisitions, covering the period of spring green-up. NDVI values are aggregated per crown using the mean of the 20% brightest pixels in the green band. Lines represent the means and ribbons the standard deviation of all individual crown NDVI values per species. The NDVI time series of the concrete reference surface is also included. Species names and number of individuals (n) are reported. 171

Figure 6-7: Time-series of a) NDVI from drone acquisitions ($n = 20$) and b) PAI from DHP ($n = 10$) averaged over the woodland transects (see Figure 6-1). The ribbons represent \pm one standard deviation in NDVI and PAI respectively, c) depicts the NDVI-PAI relationship with NDVI values linearly interpolated where they don't correspond to PAI observation dates.....	172
Figure 6-8: Boxplots of SOS, MOG and SOP of all individual deciduous crowns grouped by species and ordered by mean values. The bold line represents the mean value, the lower and upper bounds of the boxes represent the 25 th and 75 th percentiles, the whiskers extend to the furthest values from the mean within 1.5 times the interquartile range and the circles are identified as outliers beyond this range.	174
Figure 7-1: A) Location of the study site in Cornwall, UK, marked by star, B) RGB orthomosaic of the study site on 22 July 2019, indicating locations of PAR validation measurements and GCPs for georeferencing multispectral drone images. The woodland area subset is indicated by a dashed line. C) quantum sensor configuration for PAR validation measurement in woodland locations, D) woodland with posts indicating HOBO light logger locations. Satellite image source: Satellite imagery source: Esri, Maxar Technologies, DigitalGlobe.	187
Figure 7-2: Isolated trees for which PAR validation measurements were taken (letters corresponding to locations in Figure 7-1). A, B and D are oak trees (<i>Quercus</i> spp.) in order of decreasing crown size, C is a hawthorn tree (<i>Crataegus monogyna</i>).	189
Figure 7-3: a) CHM generated from points classified as vegetation. b) segmented crown extents. c) visualisation of vegetated voxels and DTM as input for the DART model.....	198
Figure 7-4: Exponential regression model between drone-derived NDVI values and estimated PAI from hemispherical photography at crown and subplot level. Dashed lines indicate \pm 1 standard deviation of the residuals.....	200
Figure 7-5: Modelled PAI per segmented crown (top) and DART simulated DLI at 1 x 1 m resolution for three cloud-free days (predominantly direct	

irradiance) representing SOS (20 April 2019), MOG (21 May 2019), and SOP (9 July 2019).	203
Figure 7-6: Boxplots of a) hourly understory PAR fraction and b) error in hourly understory PAR fraction for three stages of spring green-up (SOS, MOG, SOP) at woodland validation locations. The bold line represents the median value, the lower and upper bounds of the boxes represent the 25 th and 75 th percentiles, the whiskers extend to the furthest values from the mean within 1.5 times the interquartile range and the circles are identified as outliers beyond this range.	204
Figure 7-7: Comparisons of measured versus simulated hourly below canopy PAR fractions for the three woodland validation sites (a) South, b) Mid, c) North) as well as the four individual trees (d) oak tree A, e) oak tree B, f) hawthorn tree C, g) oak tree D). For each site, hourly values for a total of 6 days are displayed which represent two days per green-up stage (SOS, MOG, SOP) with contrasting illumination conditions (predominantly direct or diffuse, diffuse fractions ranging from 0.15 to 1). RMSE values show the error in simulated PAR fraction.	205
Figure 7-8: Time series (1 hour intervals, 07:00 to 21:00 UTC+1) of BOA irradiance, below canopy measurements and DART simulated below canopy irradiance at location ‘woodland South’ for three days with predominantly direct irradiance representative of a) SOS (20 April 2019), b) MOG (23 May 2019) and c) SOP (9 July 2019).	206
Figure 7-9: a) RGB orthomosaic of study-site subset, b-d) difference of simulated DLI per pixel ($\text{mol d}^{-1} \text{ m}^{-2}$) between the reference model Sim_main and models b) Alt_sim_1, c) Alt_sim_2, d) Alt_sim_3 (see Table 7-2 for descriptions). Negative values show underestimation of the model versus Sim_main, positive values show overestimation.	207
Figure A 1: Sparse point cloud tie points resulting from Photoscan processing for LO_10yr (a) and HO1_10yr (b).....	285

Figure A 2: Simulated Sequoia and Sentinel 2A derived NDVI and CHL values for simulations of varying LAI and Chlorophyll a + b content respectively.	288
Figure A 3: Spring time-series of NDVI per species from 20 drone acquisitions, using the mean of all crown pixels (no brightest pixel extraction step as opposed to Figure 6-6 of the study). Lines represent the means, ribbons the standard deviation of all individual canopy NDVI means. Species names and number of individuals (n) are also reported.	291
Figure A 4: Temporal progression (DOY) of drone measured NDVI values (20 dates) and PAI values derived from hemispherical photography (9-10 dates) including fitted logistic functions and identified SOS, MOG and SOP (vertical dashed lines from left to right), across the 2019 period of spring green-up for 10 locations across the study site. A-D: oak (<i>Quercus spp.</i>), E-F: hawthorn (<i>Crataegus monogyna</i>), G-H: grey willow (<i>Salix cinerea</i>), I: goat willow (<i>Salix caprea</i>), J: elm (<i>Ulmus spp.</i>). All measurements represent individual crowns except I) which represents a closed stand of multiple individuals. The logistic fit to PAI values was not possible for G and omitted for E and I due to non-distinct SOS. The inset map shows the measurement locations across the study site.....	293
Figure A 5: Boxplots of SOS, MOG and SOP of all individual deciduous crowns grouped by species and ordered by median values. The bold line represents the median value, the lower and upper bounds of the boxes represent the 25 th and 75 th percentiles, the whiskers extend to the furthest values from the mean within 1.5 times the interquartile range and the circles are identified as outliers beyond this range.	296
Figure A 6: Boxplots of SOS, MOG and SOP of pine crowns. The bold line represents the mean value, the lower and upper bounds of the boxes represent the 25 th and 75 th percentiles, the whiskers extend to the furthest values from the mean within 1.5 times the interquartile range and the circles are identified as outliers beyond this range.	297
Figure A 7: Relationship between average hourly diffuse PAR fraction and the ratio of total PAR at BOA and modelled ET PAR.	300

Figure A 8: Crown locations and diameters manually identified from drone RGB orthomosaics. Low vegetation without clearly distinguishable crowns was omitted. The circular representation is consistent with the implementation in DART.	301
Figure A 9: Comparison of replicated PAI estimates from drone NDVI orthomosaics acquired during direct and diffuse irradiance conditions a) pre overstory green-up (31 March and 1 April) and b) post overstory green-up (22 July and 23 July).	303
Figure A 10: Graphs of hourly BOA PAR (black), simulated understory PAR (red) and true understory PAR (blue) for individual days pre- mid and post overstory green-up (leaf emergence to full expansion) and all measured locations below single trees and within the woodland. No results are presented for Hawthorn mid green-up due to flowering induced noise.	305
Figure A 11: Sensitivity analysis for DART simulations of direct and diffuse irradiance (sun at nadir) showing the relationship of the PAR fraction reaching the ground underneath a vegetated layer of given PAI.	306
Figure A 12: Sensitivity analysis for DART simulations of direct and diffuse irradiance (sun at nadir) showing the relative error in simulated PAR fraction reaching the ground underneath a vegetated layer of given PAI if leaf reflectance and transmittance is not modelled. For this comparison, the simulation was run with deciduous leaf optical properties available in the DART database.	306
Figure A 13: Sensitivity analysis for DART simulations of direct and diffuse irradiance at maximum solar elevation (63.24°), showing the relative error in simulated PAR fraction reaching the ground underneath a vegetated layer of given PAI if true leaf angle distribution is planophile but assumed spherical.	307
Figure A 14: HOBO logger locations (white crosses) in A) an RGB orthomosaic and B) the simulated DLI at ground level in $\text{mol d}^{-1} \text{ m}^{-2}$. C) Relationship between DART simulated DLI in $\text{PAR mol d}^{-1} \text{ m}^{-2}$ and HOBO logger recorded light in mean lux d^{-1} for two days at SOP with predominantly direct (15 July 2019) and diffuse (22 July 2019) irradiance respectively.....	307

Figure A 15: Left: Hemispherical flight plan displayed in Google Earth. Right: UAV image geotagged locations from the flight.....	309
Figure A 16: Left: Nadir view of oak tree canopy with SfM points in blue and TLS points in red. Right: Histograms of point counts per height (m) of the TLS (top) and SfM point cloud (bottom).	309
Figure A 17: Red: Sequoia normalised spectral response, Black: Simulated vegetation spectrum for illustration.....	313
Figure A 18: The grey card (a) and Spectralon panel on tripod (b) imaged pre-flight, and the five larger reference panels (c-g, with averaged reflectances of 0.2, 0.07, 0.39, 0.02 and 0.42 respectively) imaged at at 25 m altitude, displayed in the NIR band.....	314
Figure A 19: Reflectance values as derived from multispectral imagery using different calibration methods for five reference panels of different reflectance as well as a pseudo-invariant concrete surface (blue) and grass meadow (green). Results are plotted by band: a) Green, b) Red, c) Red edge and d) NIR bands.....	319
Figure A 20: HCRF values in the green wavelength band for a subset of the scene showing an oak tree canopy and cast shadow for a) the standard ELM, b) simplified ELM with grey card and c) simplified ELM with Spectralon panel.	320
Figure A 21: Spatial representations of the pseudo-irradiance values captured per image in the green band for the two drone acquisitions. Left: Flight 1 (F1), Right: Flight 2 (F2). The black dots represent the GPS position recorded for each captured image.	322
Figure A 22: Surface reflectance in the NIR band for the consecutive acquisitions F1 and F2, with and without accounting for measured irradiance information.....	322
Figure A 23: Boxplots of palm median NDVI (left) and CHL (right) values for acquisitions F1 and F2, with and without irradiance compensation (corr.). The bold central line represents the median, the lower and upper boundaries of the boxes are the 25th and 75th percentile respectively and the whiskers extend to the furthest data points within 1.5 times the interquartile range, outliers beyond are omitted.	323
Figure A 24: Per palm CHL and NDVI values for two replicate flights of varying illumination. Red: Irradiance considered during reflectance	

calibration, Blue: Irradiance not considered during reflectance calibration.....	324
Figure A 25: Main components of the illumination sensor system prototype and its drone mounting solution (inset) using 3D printed parts.....	330
Figure A 26: Indicative response of the SI1145 photodiodes as reported by the manufacturer (Silicon Labs, US).....	331
Figure A 27: Values recorded by the photodiodes in the absence of light (dark current).....	332
Figure A 28: Top: Pyranometer measurements of global irradiance during overcast conditions (12:04 to 12:19 UTC, 04.12.2017, Penryn, UK). Bottom: Concurrent measurements from the IR photodiode on the SI1145.....	333
Figure A 29: Typical CMOS RGB sensor relative sensitivity per wavelength, including region cut by IR-filter (Dworak et al., 2013)	334
Figure A 30: Top: An RGB image as acquired by the Pi-NoIR camera over a maize field with purple vegetation, green bare soil and dark cast-shadows. Below: Stretched representations of the red, green and blue bands along with their original histograms.....	335
Figure A 31: Nearest neighbour interpolated maps automatically generated upon flight completion. Top: DN values reported by the visible diode of the illumination sensor for overcast (left) and changing conditions (right). Bottom: Mean RPi-cam image pixel values in the red band for overcast (left) and changing conditions (right).....	339
Figure A 32: DN values reported by the visible photodiode of the illumination sensor for overcast (left) and changing conditions (right) displayed over time.....	339
Figure A 33: Nearest neighbour interpolated maps of point-based illumination measurements (in DNs) acquired from the drone. Left: Vis-photodiode, Right: IR-photodiode.....	340
Figure A 34: Nearest neighbour interpolated maps of image based metrics acquired from the drone. Left: Mean RPi-cam image pixel values in the red band, Right: RPi-cam image image entropy values in the red band.	340

Figure A 35: DN values reported by the visible (top) and IR (bottom) photodiode
for constant direct illumination conditions but varied sun-sensor
geometry displayed over time..... 341

Figure A 36: Relationship between the measured illumination values measured
by the IR diode and the cosine of the illumination angle derived from
vehicle attitude information (yaw, pitch, roll) and sun angles. 343

Abbreviations

AGB	Above-Ground Biomass
ALS	Airborne Laser Scanning
APAR	Absorbed Photochemically Active Radiation
ASD FieldSpec	Analytical Spectral Devices, Inc. Field Spectrometer
AVHRR	Advanced Very High Resolution Radiometer
BGB	Below-Ground Biomass
BOA	Bottom Of Atmosphere
BRDF	Bidirectional Reflectance Distribution Function
CAD	Computer Aided Design
CCD	Charge-Coupled Device
CHIME	Copernicus Hyperspectral Imaging Mission
CHL	CHLorophyll index
CHM	Canopy Height Model
CMOS	Complementary Metal-Oxide-Semiconductor
DART	Discrete Anisotropic Radiative Transfer
DBH	Diameter at Breast-Height
DGPS	Differential Global Positioning System
DGVM	Dynamic Global Vegetation Model
DHP	Digital Hemispherical Photography
DLI	Daily Light Integral
DN	Digital Number
DTM	Digital Terrain Model
DSM	Digital Surface Model
ELM	Empirical Line Model
EOS	End Of Season
ESA	European Space Agency
EVI	Enhanced Vegetation Index
EXIF	Exchangeable Image File Format
fAPAR	fraction of Absorbed Photosynthetically Active Radiation

FLEX	FLuorescence EXplorer (satellite mission)
FOV	Field Of View
GCC	Green Chromatic Coordinate
GCP	Ground Control Point
GNSS	Global Navigation Satellite System
GPP	Gross Primary Production
GPS	Global Positioning System
GSD	Ground Sampling Distance
HCRF	Hemispherical-Conical Reflectance Factor
IMU	Inertial Measurement Unit
IPAR	Incident Photosynthetically Active Radiation
ISO	International Standardisation Organisation (sensor sensitivity setting)
ITN	Innovative Training Network
LAI	Leaf Area Index
LiDAR	Light Detection And Ranging
LOOCV	Leave-One-Out Cross-Validation
LOS	Length Of Season
LUE	Light Use Efficiency
MA	Mapping Accuracy
MAD	Mean Absolute Deviation
MCA	Multi-Camera Array
MOG	Middle Of spring Green-up
MSAVI2	Modified Soil Adjusted Vegetation Index 2
MTVI2	Modified Triangular Vegetation Index 2
NDRE	Normalised Difference Red-Edge index
NDRI	Normalised Difference Red Index
NDVI	Normalised Difference Vegetation Index
NIR	Near-Infrared
NPP	Net Primary Production
PAD	Plant Area Density
PAI	Plant Area Index

PAR	Photosynthetically Active Radiation
PPFD	Photosynthetic Photon Flux Density
PPK	Post-Processing Kinematic
RGB	Red-Green-Blue (band combination)
RMSE	Root Mean Squared Error
RPi	Raspberry Pi computer
RSE	Residual Standard Error
RTK	Real-Time Kinematic
RTM	Radiative Transfer Model
SfM	Structure from Motion
SfM-MVS	Structure from Motion – Multi-View Stereopsis
SIFT	Scale-Invariant Feature Transform
SNR	Signal-to-Noise Ratio
SOP	Start Of Peak greenness
SOS	Start Of Spring / Start Of Season
SRF	Spectral Response Function
TCARI/OSAVI	Transformed Chlorophyll Absorption in Reflectance Index / Optimized Soil-Adjusted Vegetation Index
TFH	Top Frond Height
TIN	Triangulated Irregular Network
TLS	Terrestrial Laser Scanning
TRUSTEE	Training in Remote Sensing for Ecosystem Modelling (Marie-Curie innovative training network)
UAV	Unmanned Aerial Vehicle
VI	Vegetation Index
WAI	Wood Area Index

Statement of Contribution

I, Dominic Fawcett, declare that the work presented in this thesis entitled *Vegetation structure and function measurement and modelling using drone based sensing techniques* is my own. The work was undertaken while in candidature for a research degree at the University of Exeter. Where I have consulted the work of others the sources are given. This thesis and the publications included have been supported by contributions from various collaborators and these contributions have been clearly identified. Specific contributions of collaborators are summarised below in the list of published articles. My own contributions resulting in co-authorship of further articles are also stated.

I confirm that with the exception of the acknowledged contributions, this thesis represents my own work.

Published and accepted articles

Fawcett, D., Azlan, B., Hill, T.C., Kho, L.K., Bennie, J., Anderson, K., 2019.

Unmanned aerial vehicle (UAV) derived structure-from-motion photogrammetry point clouds for oil palm (*Elaeis guineensis*) canopy segmentation and height estimation. *Int. J. Remote Sens.* 40. doi:10.1080/01431161.2019.1591651

- This manuscript is presented in chapter 4 of this thesis. DF wrote the manuscript with inputs from all co-authors. DF, KA and TCH conceptualised the study and DF developed the experimental design. Fieldwork was carried out by DF, supported in part by AB. TCH and LKK administered the field campaign and provided support. DF performed the analysis.

Fawcett, D., Blanco-Sacristán, J., Benaud, P., 2019. Two decades of digital

photogrammetry: Revisiting Chandler's 1999 paper on "Effective application of automated digital photogrammetry for geomorphological research" – a synthesis. *Prog. Phys. Geogr.* 43. doi:10.1177/0309133319832863

- This review manuscript contains insights from preliminary work for chapter 4 of this thesis and is based in part on the introduction and methods sections dealing with structure-from-motion photogrammetry from drone platforms. DF led the writing of the manuscript with significant contributions from JBS and PB who wrote sections of the manuscript supported by their own datasets. This work also forms part of Javier Blanco-Sacristán's PhD thesis at the University of Milano-Bicocca since we collaboratively wrote this piece with Dr. Pia Benaud.

Fawcett, D., Panigada, C., Tagliabue, G., Boschetti, M., Celesti, M., Evdokimov,

A., Biriukova, K., Colombo, R., Miglietta, F., Rascher, U., Anderson, K., 2020. Multi-Scale Evaluation of Drone-Based Multispectral Surface Reflectance and Vegetation Indices in Operational Conditions. *Remote Sens.* 12. doi:10.3390/rs12030514

- This manuscript is presented in chapter 5 of this thesis. DF wrote the manuscript with inputs from all co-authors. DF, CP, MB and KA conceptualised parts of the study, DF developed the experimental design. Fieldwork was carried out by DF, CP, MB, GT, MC, AE, KB and RC with RC, MC, CP, MB, UR and FM administering the field campaign. HyPlant datasets and specific inputs were shared by UR. DF processed the drone data and performed the analysis.

Fawcett, D., Bennie, J., Anderson, K., 2020. Monitoring spring phenology of individual tree crowns using drone-acquired NDVI data. *Remote Sens. Ecol. Conserv.* In press.

- This manuscript is presented in chapter 6 of this thesis and has been accepted for publication. DF wrote the manuscript with inputs from JB and KA. DF and KA conceptualised the study. Fieldwork was carried out by DF, supported by KA and JB. DF performed the analysis.

Articles under review

Duffy, J., Anderson, K., **Fawcett, D.,** Curtis, R., Maclean, I. M. D. 2020. Drones provide scale-relevant spatial and volumetric data to deliver new microclimate insights.

- My contributions to this review manuscript are based on insights and preliminary results from chapter 7 of this thesis. I provided illustrations based on my own datasets and wrote a section on radiative transfer modelling. It is currently in review for publication in *Landscape Ecology*.

Articles in preparation

Fawcett, D., Bennie, J., Anderson, K., Modelling understory light availability in a heterogenous system using drone captured structural and spectral data. In prep.

- This manuscript is presented in its current form in chapter 7 of this thesis and is in preparation for submission to *Remote Sensing of Environment*. DF wrote the manuscript with inputs from JB and KA. DF, JB and KA conceptualised the study and DF developed the experimental design. Fieldwork was carried out by DF, supported by KA. DF performed the analysis.

Additional publications

Anderson, K., **Fawcett, D.**, Cuguliere, A., Benford, S., Jones, D., Leng, R., 2020. Vegetation expansion in the subnival Hindu Kush Himalaya. *Glob. Chang. Biol.* 26, 1608–1625. doi:10.1111/gcb.14919

- This article of which I am joint first author represents a collaboration with my PhD supervisor Dr. Karen Anderson who conceptualised the study. I led the practical implementation and coding for this work. It is not presented as part of this thesis but relates to reflectance index based monitoring of vegetation across scales which is an important element of chapter 5.

Contributions to scientific meetings

Work from this thesis was presented at the following scientific conferences:

Online presentation: "Modelling understory light availability in a heterogeneous landscape using drone-derived structural parameters and a 3D radiative transfer model" at EGU Sharing Geoscience Online 2020 (fully online conference due to COVID-19 restrictions).

Podium presentation: "Investigating impacts of calibration methodology and irradiance variations on lightweight drone-based sensor derived surface reflectance products" at SPIE Remote Sensing 2019 (Strasbourg, France).

Poster presentation: "Drone data based plant trait estimation and upscaling experiments over a heterogeneous corn field" at Living Planet Symposium 2019 (Milan, Italy).

Podium presentation: "UAV-based structural and spectral data for the assessment and monitoring of oil palm biomass" at EGU 2018 (Vienna, Austria).

Poster presentation: "Multispectral vegetation monitoring by drone: Surface reflectance accuracy and its influence on derived vegetation indices" at Kernow Conference: Postgraduate Research in Cornwall 2018 (Penryn, UK)

The TRUSTEE network



TRUSTEE
t r a i n i n g

training on Remote Sensing
for Ecosystem modelling

www.trusteenetwork.eu

This PhD project was part of a Marie Skłodowska Curie innovative training network “Training on Remote Sensing for Ecosystem Modelling” (TRUSTEE), funded by the European Commission under the Horizon 2020 program. The goal of the TRUSTEE network was to train a new generation of early-stage researchers to become experts in the field of vegetation remote sensing. Members took part in a number of training schools on theory and methods in remote sensing and ecosystem modelling (listed below), hosted by the participating institutions across Europe. This included working with image data, the planning of drone flights and performing relevant field measurements with a range of instruments. Further workshops focused on teaching transferable skills relevant for careers in academia and industry. Details on these events can be found in newsletters published on the TRUSTEE website linked above and certificates of attendance are attached in Appendix A8. The TRUSTEE project included deliverables for each institution. The report for deliverable 1.6 (design of a simple sensor to characterise in-flight illumination variations) which was developed for this project can be found in Appendix A7. International collaborations were fostered through secondments at partner institutions and I spent two months with the Remote Sensing of Environmental Dynamics Laboratory (DISAT) at the University of Milano-Bicocca in Italy. Collaborations within TRUSTEE provided valuable contributions to the work presented in this thesis, in particular for chapter 5 through a joint field campaign in Italy and for a review article published with fellow early stage researcher Javier Blanco-Sacristán.

TRUSTEE training events:

TC: Training Course, SS: Summer School

- Introduction to remote sensing and satellite data analysis, Milano, Italy (TC, 2017)
- Drone field operations for environmental monitoring, Penryn, UK (TC, 2017)
- Field experimental design and data acquisition, Majadas, Spain (SS, 2018)
- Sentinel 2 for agriculture monitoring activities and plant traits thematic workshop, Milano, Italy (TC, 2018)
- Remote sensing for traits mapping in agriculture, Juelich, Germany (SS, 2019)
- Remote sensing thematic workshop, Leuven, Belgium (TC, 2019)
- Transferable skills workshop, Trento, Italy (TC, 2020)

1 Introduction and Research Context

1.1 Introduction

A detailed quantitative understanding of vegetation ecosystems and their services is a priority in the face of concerns about global change as the terrestrial biosphere plays an important role in the carbon cycle through CO₂ fixation and storage (IPCC, 2014). The quantification of carbon storage in vegetation cover and the fluxes of carbon through uptake and emission influenced by environmental and anthropogenic factors is key for parameterising and benchmarking climate models (Clark et al., 2017; Lawrence et al., 2019; Scholze et al., 2017). Dynamic global vegetation models (DGVMs) which have been developed to study the interaction between vegetation and climate, as well as terrestrial carbon cycle models of which vegetation is a central element, show considerable discrepancies regarding carbon uptake and loss (Krause et al., 2018; Piao et al., 2013; Yang et al., 2020). In order to improve terrestrial carbon cycle modelling there is a need for more spatially replicated observations with high repeatability, as can be achieved by the construction of denser terrestrial sampling networks, but also for a better integration of spatial information from remote sensing systems (Ciais et al., 2014; Schimel et al., 2015).

Remote sensing has already proved to be an invaluable tool for monitoring vegetation dynamics over large extents by providing spatially contiguous measurements (Schimel et al., 2015). Optical satellite systems with global coverage enable the linking of global vegetation productivity with changing climate patterns (Guay et al., 2014; Nemani et al., 2003). Improvements in the spatial resolution of optical sensors has made remote monitoring of biodiversity possible and has led to the development of essential biodiversity variables to concentrate the efforts of the remote sensing community (Pettorelli et al., 2016; Turner et al., 2003). Remote sensing has now evolved to the point where the 3D structure and biomass of vegetation communities can be assessed using active technologies such as airborne laser scanning (ALS, light detection and ranging: LiDAR) (Casalegno et al., 2017; Lefsky et al., 2002). From space, vegetation structure can be monitored using radar and LiDAR technologies at a much larger

but coarser scale, with dedicated missions recently launched and in development (Dubayah et al., 2020; Quegan et al., 2019). Even chemical constituents of foliage which would otherwise have to be laboriously sampled from plants in the field can be determined from airborne imaging spectroscopy measurements covering wavelength ranges from the ultraviolet to shortwave infrared in hundreds of narrow spectral bands (Knyazikhin et al., 2013; Ustin et al., 2004; Wang et al., 2018). The fusion of hyperspectral and LiDAR technologies opens up new possibilities for the mapping of canopy functional diversity (Asner et al., 2017). Advancements in using hyperspectral measurements to detect sun-induced chlorophyll fluorescence will further reveal spatial variations in photosynthesis (Mohammed et al., 2019; Porcar-Castell et al., 2014) and with forthcoming missions such as the European Space Agency's (ESA) FLoorescence EXplorer (FLEX) (Drusch et al., 2017), there will be improved capabilities to measure chlorophyll fluorescence from space.

Remote sensing can thus permit characterization of vegetation ecosystems, but there are many platform-specific limitations which constrain understanding of vegetation dynamics in time and/or space. Satellite-based measurements have global coverage but there exists a trade-off between spatial resolution and revisit times due to fixed orbits, and optical missions suffer data interruptions due to cloud cover. The resolution of satellite based LiDAR and hyperspectral technologies are limited due to the Earth's atmosphere and the distance to the Earth's surface. For LiDAR this is due to beam divergence while atmospheric scattering results in a low signal-to-noise ratio (SNR) for hyperspectral measurements. Airborne platforms sacrifice areal coverage for state-of-the-art instruments, enabling small-footprint discrete return or waveform laser scanning and fine spatial resolution narrow-band hyperspectral measurements (Itten et al., 2008; Vane et al., 1993; Wagner et al., 2006), but acquisitions are financially costly (in the range of 10'000 to 100'000 GBP) and have limited flexibility due to aerospace regulations. Recently, a further method of airborne data acquisition has become possible with advances in autopilots and battery capacity of unmanned aerial vehicles (UAV) or drones. Popular in the private sector amongst videographers, drones have been gaining traction in science, as witnessed by a growing number of related publications (DeBell et al., 2016).

Drones are now widely adopted in the fields of remote sensing and photogrammetry (Colomina and Molina, 2014; Yao et al., 2019) as they offer a number of advantages over other platforms, which has allowed them to fill multiple niches. Low flight altitudes enable data capture at sub-decimetre scales, thus allowing to resolve many vegetation types at the fundamental ecological scale of individual plants (Marconi et al., 2019). They further allow the collection of data even during overcast conditions; although the latter depends on the types of data analysis required by the user. Revisit frequency can be much higher in practice than for large aircraft, where besides long delays due to weather conditions also campaign requirements in terms of manpower, flight planning and fuel are high. This large flexibility in timing allows drones to be used for multitemporal studies on diurnal and seasonal time-scales (e.g. Berra et al., 2019; Gonzalez-Dugo et al., 2013; Torres-Sánchez et al., 2014). Besides measurement advantages, drones are also attractive for researchers due to their low cost, applicability in challenging environments and possibility of operation and maintenance by research groups themselves, without reliance on third parties for data capture (Duffy et al., 2017).

These advantages make drones valuable assets for monitoring highly temporally dynamic and small scale processes within vegetation systems (D'Odorico et al., 2020; Houborg et al., 2015; Santesteban et al., 2016). The ability to resolve individual plants has led to the bulk of drone-related studies dealing with their application in precision agriculture, with multiple dedicated reviews (Maes and Steppe, 2019; Messina and Modica, 2020; Zhang and Kovacs, 2012). In contrast to agriculture, studies employing drones in natural ecosystems are fewer, but with considerable potential identified (Anderson and Gaston, 2013). The opportunities for ecologists consist in identifying small-scale processes such as competition (Silva et al., 2014) and variability in the biogeochemical and hydrological parameters through detailed mapping of vegetation types and plant traits (Cunliffe et al., 2016; Jensen et al., 2011) or improving understanding of large-scale processes by utilizing drone measurements to calibrate and validate models based on satellite observations (Fraser et al., 2017; Kattenborn et al., 2019; Puliti et al., 2017b), which is where drones can provide an important missing link between scales of observed vegetation dynamics.

A comprehensive review of drone sensors and experiments in the field of vegetation monitoring in general has been provided by Salamí et al. (2014), who focus primarily on systems and methodology. It is not the intention to replicate that work, yet as the field of drones is rapidly developing further inroads have been made since 2014 (*ibid.*), especially concerning hyperspectral measurements. Here an update on the current state of drone and sensor technology is provided, with a focus on vegetation characterisation in terms of plant structural and functional traits with relevance to quantifying carbon stocks and fluxes. We seek to highlight the potential of different drone based technologies and methods for plant trait retrievals and their role in bridging the gap between field-based and global measurements and the challenges this poses. However, many of the presented methodologies also have applications in monitoring biodiversity and precision agriculture.

1.2 Drone-based vegetation structure characterisation towards improved carbon stock estimations

Approximately 3.2 ± 0.6 Pg of CO₂ per year were taken up by the land surface on average between 2009 and 2018 (Friedlingstein et al., 2019). The largest proportion of this sink is attributed to vegetation storage, primarily tropical and boreal forests (Pan et al., 2011; Tagesson et al., 2020) but its distribution remains uncertain, especially the fluctuations in semi-arid ecosystems (Poulter et al., 2014). Therefore mapping the spatial distribution of these carbon stocks is valuable to understand where landcover change will have the largest impact and possible measures can be taken.

1.2.1 Established methods of remote biomass retrieval

The predominant scientific method for determining vegetation carbon stocks is to use destructive harvesting followed by measurements in the lab, to relate allometric measurements to above- and below-ground biomass (AGB and BGB). As this is a laborious and spatially constrained measurement, many studies on remote estimation of carbon stocks have been performed, on a variety of scales.

At coarse resolutions from satellites, there are multiple options for determining AGB, most relying on a combination of imaging spectroscopy and LiDAR. Imaging spectroscopy measures energy at multiple wavelength ranges (bands) of light and differences between these can be related to field measurements or finer-scale estimates of biomass through regression and machine learning models (see Figure 1-1 for example based on multispectral and LiDAR data) (Asner, 2009; Avitabile et al., 2016; Baccini et al., 2012), or through inversion of physically based canopy reflectance models (Soenen et al., 2010). Due to the nature of spectral measurements, these approaches often show saturation at higher biomass, which may be reduced by using narrower spectral bands (Mutanga and Skidmore, 2004). However, most current satellite-based instruments do not have this capacity. Undetected undergrowth vegetation as well as background reflectance cause further uncertainties in forest biomass estimates when using this method (Heiskanen, 2006). Identification of relationships between biomass and L-Band microwave emissions or radar backscatter provides an alternative for forests. It has the advantage of being cloud-cover independent and less prone to saturation, however prediction errors due to spatial variability, moisture conditions and topography are significant (Mialon et al., 2020; Mitchard et al., 2009). Despite the difficulties, forests remain at the centre of biomass related studies (Avitabile et al., 2016; Baccini et al., 2012; Zhang and Liang, 2020) while other types of ecosystems are neglected. This is in part due to forests representing a large and important part of terrestrial biomass, but is also due to challenges and poor understanding of relating satellite measurements of heterogeneous ecosystems to biomass. To retrieve forest biomass with high accuracy at finer spatial scales down to individual trees, airborne and terrestrial LiDAR has successfully been employed. LiDAR point-cloud derived height and width metrics are used to estimate biomass using allometric equations (Calders et al., 2015; Zhao et al., 2009). However, the lack of temporal flexibility and the high costs of airborne measurements are coupled with insufficient accuracies for low vegetation (Luscombe et al., 2015).

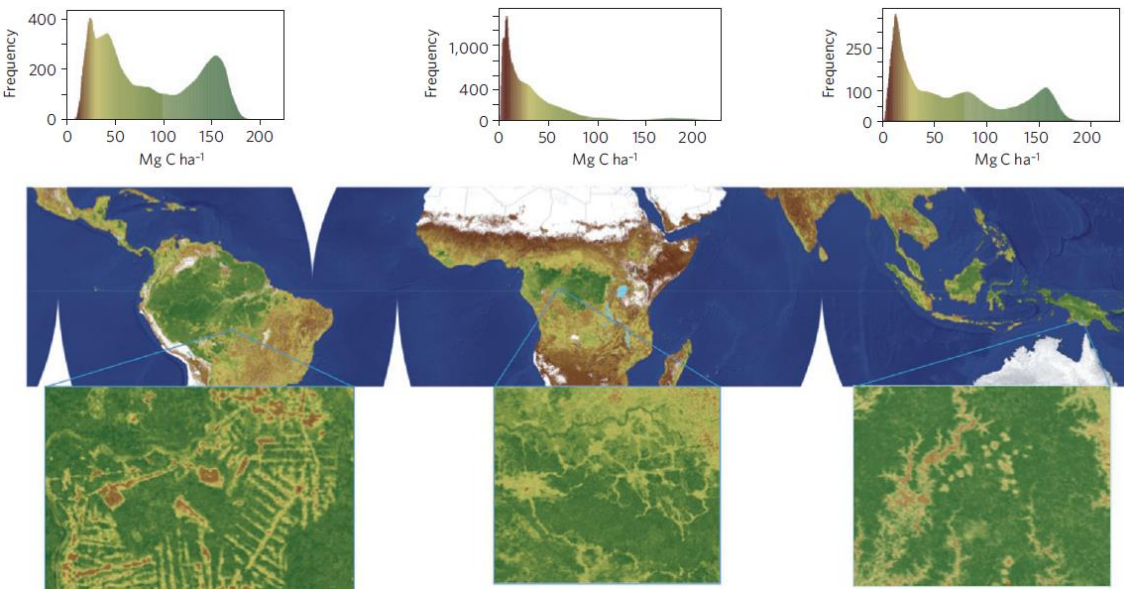


Figure 1-1: Pan-tropical aboveground carbon estimations based on GLAS and MODIS satellite data and field measurements (Baccini et al., 2012). The colour scheme from brown to green indicates the amount of carbon, see upper panels for numeric values.

1.2.2 *Drone based methods for vegetation structure and biomass estimation*

Drone systems offer a valuable alternative to retrieve biomass for smaller plant canopies and in more sparsely vegetated areas, to resolve smaller biomass related changes in structure and to differentiate growth and die-off related changes from noise.

1.2.2.1 *Drone LiDAR*

Drone-integrated LiDAR is a recent development arising from the miniaturisation of LiDAR sensors concurrent with improvements to drones and positioning systems. Currently, available lightweight LiDAR systems weighing in at around 0.5-3kg are commonly developed for automotive use but can be mounted on drones (e.g. Velodyne LiDAR). These payloads can be carried by relatively lightweight drone systems but still result in take-off weights above 7kg. The lightest configurations have extremely short flying times of up to 5 minutes (Tulldahl and Larsson, 2014; Wallace et al., 2012). Longer flight durations necessitate larger drones, however these often also optimize their payload with

more powerful LiDAR systems. RIEGL's RiCOPTER, a drone which carries their VUX-SYS lightweight scanner with 10 mm accuracy (approx. 5kg including control system, inertial measurement unit (IMU) and global navigation satellite system (GNSS)), has a take-off weight of 25 kg and up to half an hour flight time (RIEGL, 2017). Similar weights and times are reported by Tommaselli and Torres (2016) who mounted the IbeoLux 2010 system on a custom drone. Depending on point density and range, lightweight LiDAR systems are costed in the range of \$6'000 to \$100'000.

As the current drone mountable LiDAR systems are not designed with vegetation in mind, their limited range and number of returns (2 for Velodyne Systems, 3 for IbeoLux 2010) along with the restrictive flight durations and positioning uncertainties make them more suitable for proximal sensing and an efficient alternative to terrestrial laser scanning (TLS) for certain applications (Tulldahl and Larsson, 2014) as opposed to scanning large plots from greater height. Indeed, drone-based LiDAR acquisitions have proven capable of deriving TLS comparable estimates of diameter at breast height, a key metric for AGB estimation (Brede et al., 2017; Bruggisser et al., 2020). Current developments are further reducing restrictions, eventually making high accuracy multitemporal monitoring of carbon stocks at inventory plot scale (few hectares) possible.

1.2.2.2 *Drone-based structure from motion photogrammetry*

The other primary method of acquiring point-clouds representing vegetation structure from drones is structure-from-motion photogrammetry (henceforth: SfM). The typical workflow of SfM surveys for vegetation studies is displayed in Figure 1-2. This relies on the identification of tie-points from images with different geometries and derives 3D structure based on the relative differences (vectors). In contrast to multi- or hyperspectral imaging, the systems commonly used for image acquisition in the photogrammetric workflow are consumer-grade digital cameras which require minimal calibrations. Relative estimates of the camera locations and orientation can be precisely reconstructed from the images themselves using a bundle adjustment method (Remondino et al., 2011). The GNSS and IMU data acquired by the drone platform or camera aids in the tie-point extraction process and could potentially allow direct georeferencing of resultant models, but this requires high accuracies which can be delivered by real time kinematic (RTK) solutions to produce models with spatial accuracies equalling their sub-decimetre resolution (Tomaštík et al., 2019). An alternative method involves surveying ground-control point (GCP) markers identifiable in the acquired images using a high accuracy differential GPS (DGPS) system (~2 cm) *in situ*. This method is still commonplace as it can ensure high georeferencing accuracy while providing independent measurements to control for systematic errors (James et al., 2017a). Following image-orientation, features are extracted by using algorithms such as the scale-invariant feature transform (SIFT) (Lowe, 2004). This results in dense point-clouds as a predominantly 2.5 D representation of the imaged scene. The point clouds can then be filtered by removing redundant information in flat, uniform regions but preserving edges as well as possible. From this point cloud, ultra-high spatial resolution digital surface models (DSM) can be created. The described processing workflow is implemented in SfM processing software where the most popular solutions (Fawcett et al., 2019b) are proprietary (Agisoft Metashape, Pix4D mapper) but open-source alternatives are also available (MicMac). Agisoft Metashape is the most popular software solution.

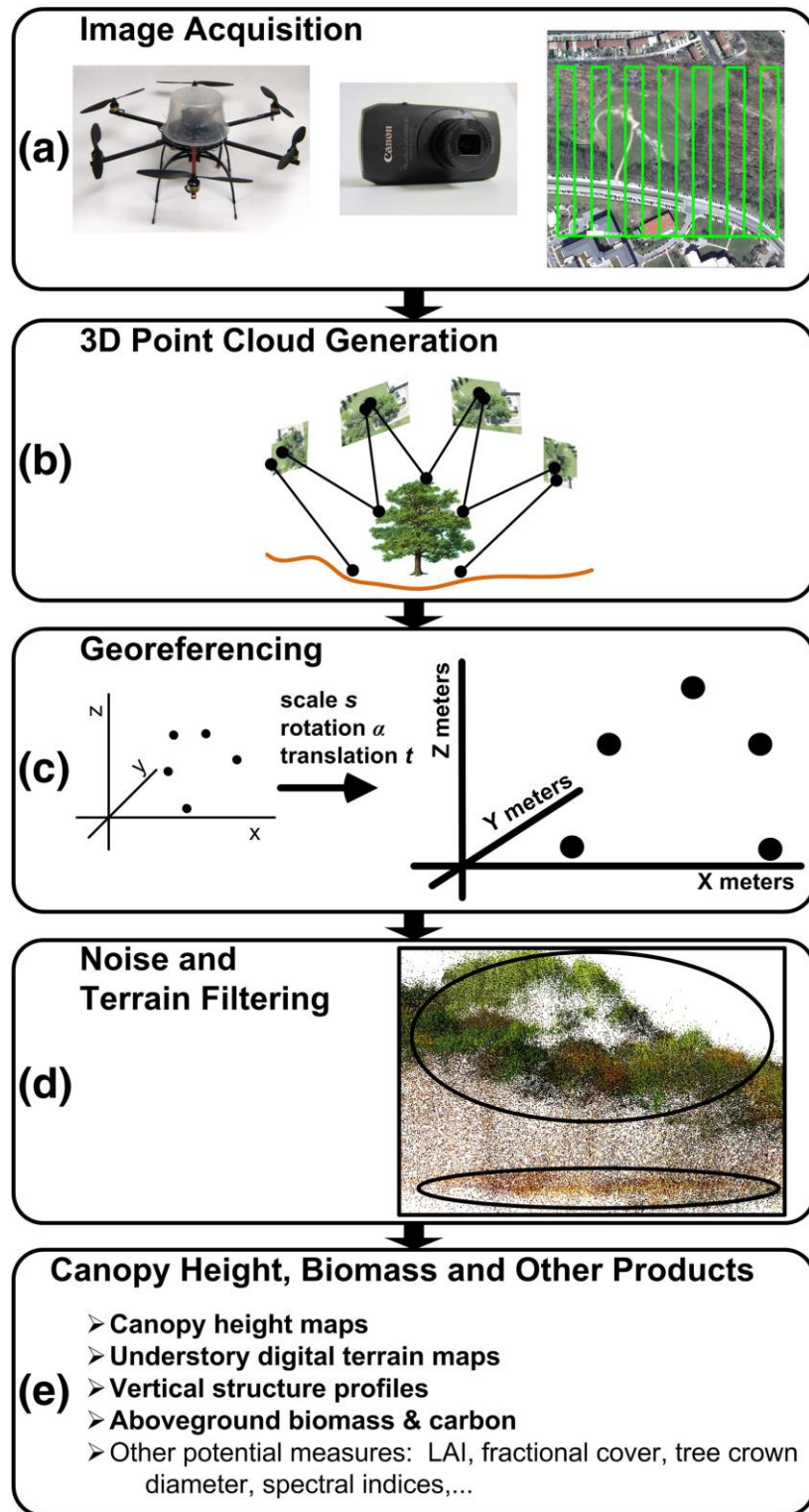


Figure 1-2: Overview of typical drone SfM photogrammetry workflows for vegetation studies (Dandois and Ellis, 2013). Letters (a) to (e) indicate the typical order of the steps in a standard workflow.

Multiple studies have been performed comparing drone SfM derived DSMs to DSMs from LiDAR (Cao et al., 2019; Puliti et al., 2015; Thiel and Schmullius, 2017; Wallace et al., 2016). In a study deploying both technologies from drones (Figure 1-3), LiDAR outperformed SfM for capturing ground surface points below dense vegetation canopies (only 1 point per m^2 for SfM) which propagated into errors when estimating tree height (root mean squared error (RMSE) 1.3 m vs 0.92). Differences in canopy cover estimates were also found (SfM: 50%, LiDAR: 63%) (Wallace et al., 2016). Comparing non-drone ALS results to those of drone SfM for boreal forest biophysical properties showed slightly smaller RMSEs for ALS (with 7.4 points per m^2) (Puliti et al., 2015). Comparisons using 4 points per m^2 ALS data found a higher single tree detection rate for drone SfM due to higher point density (93.2% with 10.7% commission error vs 78.0% with 9.8% commission error) and canopy heights were 0.85 m higher on average, indicating better capture of the highest point of tree crowns (spruce and pine dominant) (Thiel and Schmullius, 2017). These kind of comparisons are performed primarily in tree-dominated ecosystems. For lower vegetation, ALS has been shown to have limitations such as systematic underestimation of short sward height and volume (Luscombe et al., 2015). With good results in estimating height of cereal crops (Bendig et al., 2014), it can be expected that SfM can provide a more accurate alternative for tall grass and sward ecosystems.

In summary, the disadvantages of SfM for capturing vegetation structure is the lack of 3D canopy structure in point clouds, the reliance on identifiable tie-points between images, lower accuracy of on-board positioning systems compared to airborne acquisitions and limited spatial coverage per acquisition. Future work may seek to mitigate these drawbacks by utilizing the flexibility provided by small drone platforms in terms of dynamic flight planning and camera orientation.

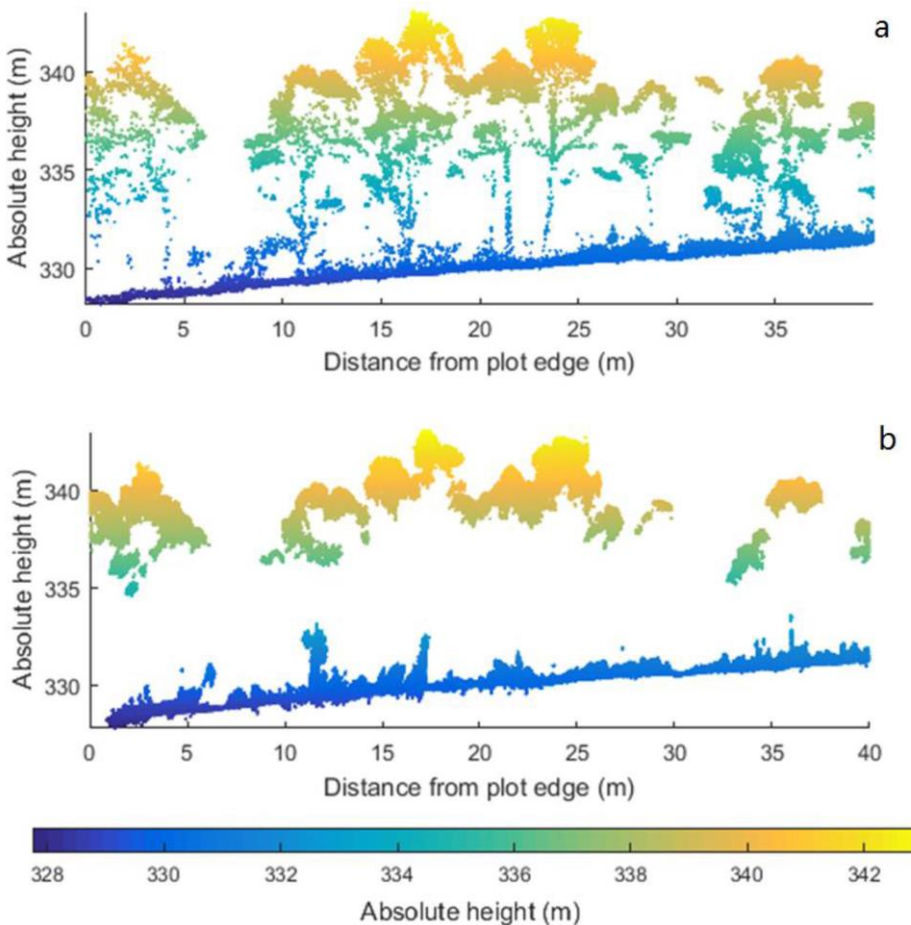


Figure 1-3: a) Side-view of a transect through a study plot containing eucalypt trees, generated from the point cloud of an ALS system and b) the same produced using RGB images and SfM photogrammetry (Wallace et al., 2016).

1.2.2.3 Biomass estimation from drone measurements

The applicability of drones for biomass estimation has been assessed in multiple recent studies. While for crops, plant height as derived from SfM can be sufficient to provide good estimations of biomass (Bendig et al., 2014; Roth and Streit, 2017), estimations for natural land-cover types are challenging due to complex and varying three dimensional structure. They are reliant on precise empirical relationships which should ideally be measured for each species (Cunliffe et al., 2016), but have been found to perform similarly to laborious point-framing methods for shrub tundra systems (Cunliffe et al., 2020). Some feasibility studies have shown that SfM based tree-height estimates are accurate enough to track tree growth and derive biomass (about 5 cm accuracy) (Karpina et al., 2016). Regression analysis using SfM point clouds as input (height percentiles and point

densities) allowed stem volume for boreal forests to be retrieved with 14.95% RMSE (Puliti et al., 2015). The same study estimated a range of different forest inventory variables such as mean height, dominant height, stem number and basal area through linear models using ground reference data. Further studies utilizing tree height and RGB spectral information to model biomass over more complex, non-uniform forests produced results with greater error. Over temperate deciduous forest sites, canopy height metrics were used to estimate biomass with RMSEs of 31-36% (Dandois and Ellis, 2013), while results for tropical forest were poorer with 46% RMSE, which the authors argue is down to more complex forest structure (Kachamba et al., 2016). The same study compared methods of DTM retrieval and found the best results were achieved using unsupervised ground filtering based on the progressive triangulated irregular network (TIN) algorithm. Deriving forest growing stock volume independently of DTM information has proven possible (Giannetti et al., 2018), however high DTM accuracy is still considered crucial for accurate biomass estimates and represents one of the major sources of uncertainty in purely SfM derived data. Other studies have relied on LiDAR generated DTMs for this purpose and found that SfM based estimates of aboveground carbon density were highly correlated to those from LiDAR (R^2 of 0.8) (Messinger et al., 2016).

Studies of diverse ecosystems with varied plant types represent a challenge when it comes to biomass estimation and its validation. For rangeland ecosystems, merely using plant height was not deemed adequate and foliar volume preferred due to the complex canopy architecture of shrubs. Evaluation of canopy height models (CHM), especially in this case, should not only focus on maximum plant height as this is often underestimated by SfM and is of limited importance for biomass (Cunliffe et al., 2016). Biomass retrievals in shrub ecosystems could be further improved by supplementing the CHM information with spectral information from RGB image data (Alonzo et al., 2020).

One forest-specific advantage which drones theoretically offer over airborne surveys is the ability to fly between and underneath high canopies to accurately characterize understory vegetation. This has not been made use of in any photogrammetric studies to the authors' knowledge, possibly due to a number of challenges which must be addressed. Amongst these are weak GPS signal and

generally difficult pathfinding, requiring advanced piloting skills but facilitated by first-person vision systems.

1.2.3 *Upscaling*

While drone-based estimates of vegetation structure and biomass can provide helpful information for finer-grained questions such as the plant growth environment, disturbance regimes and age structure, they also provide an excellent way of closing the gap between field-based sampling of single canopies and the coarse resolution measurements of satellite systems (Browning et al., 2010) (see Figure 1-4). Once sufficiently accurate models for all vegetation types of a biome have been established with the use of field data, drone plot-scale estimates could provide an adequate substitute for more intensive field sampling, as has been demonstrated successfully for forest volume estimates (Puliti et al., 2017a). This would lead to efficient collection of more representative, spatially contiguous data covering entire satellite pixel footprints as opposed to random or even preferential sampling which is a commonly practiced method in inaccessible terrain (e.g. Zandler et al., 2015). Ultimately, when using drones the challenge of heterogeneous surfaces and complex biomes can be addressed by identifying non-linear relationships between plot-scale information to spectral signatures or backscatter of individual pixels from satellite measurements. This has recently been demonstrated for mangrove biomass mapping by relating drone LiDAR based biomass estimates to Sentinel-2 data (Wang et al., 2020). This kind of upscaling methodology harbours potential not only for biomass estimates but for a large range of ecological questions which has been demonstrated for invasive species classification using drone RGB imagery derived maps of plant species related to Sentinel-1 and Sentinel-2 satellite data (Kattenborn et al., 2019). This avenue of using drone acquired data in the training and validation process of satellite-data based models is certain to be explored more in the near future.

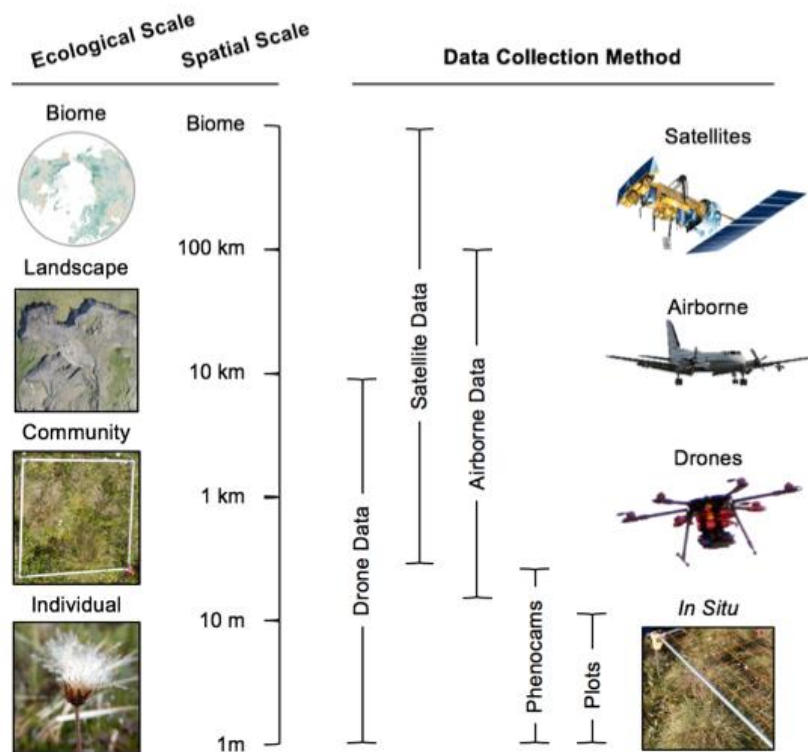


Figure 1-4: Platforms and spatial scales of data in remote sensing (HiLDEN, <https://arcticdrones.org/>, 2018)

1.3 Contribution of drone measurements to understanding and modelling fluxes

Changes in carbon stocks are termed carbon fluxes. These are a very dynamic part of the carbon cycle, and in the case of vegetation they are highly varying on a multitude of timescales from seconds to seasons and dominated by different processes respectively (Braswell et al., 2005; Damm et al., 2010). Of special interest is the mechanism of carbon sequestration, in which vegetation plays an important role. Uncertainties in land sequestration models are large for scenarios of rising CO₂, and in-depth understanding of fluxes must be developed to reduce these (Walker et al., 2015). In the vegetation context, the quantities of interest are gross and net primary production (GPP and NPP). GPP is the amount of CO₂ assimilated by photosynthesis, while NPP subtracts plant respiration. GPP representative of a limited spatial extent can be retrieved from flux-tower based measurements of CO₂ fluxes using the eddy covariance technique (Papale et al., 2006). GPP and NPP have also been derived from satellite measurements since the 1990s (Advanced Very High Resolution Radiometer (AVHRR) instrument), by assumptions based on the logic of Monteith (1972) that 1) NPP is directly related

to absorbed solar energy, 2) there is a connection between absorbed solar energy and vegetation indices (VIs) (e.g. normalised difference vegetation index (NDVI)) and 3) for biophysical reasons, the conversion efficiency of absorbed energy varies (Field et al., 1995; Potter et al., 1993; Running et al., 2004). GPP can be expressed as equation 1-1:

$$GPP = \epsilon \times fAPAR \times PAR \quad (1-1)$$

where ϵ is conversion or light use efficiency (LUE) ($gC\ MJ^{-1}$, grams carbon per megajoule), PAR is the incident photosynthetically active radiation and fAPAR is the fraction of absorbed PAR and can be related to NDVI (Sellers, 1987) (equation 1-2):

$$fAPAR = \frac{APAR}{PAR} \approx NDVI \quad (1-2)$$

Daily net photosynthesis is derived from GPP by subtracting 24 hour leaf maintenance respiration and yearly NPP is formed by summing daily net photosynthesis and subtracting annual growth respiration as well as woody tissue maintenance respiration. These respirations are estimated by using allometric relationships and satellite-derived leaf area index (LAI). LAI in turn follows from identified relationships with NDVI (Fensholt et al., 2004). The most uncertain term ϵ greatly varies between vegetation types and climatic conditions. For MODIS GPP and NPP estimates, the range of ϵ is constrained through biome-specific look-up tables (LUTs) resulting from a complex ecosystem model (Running et al., 2004). ϵ may also be quantified at higher spatial and temporal resolutions using narrow-band VIs and chlorophyll fluorescence with potential for GPP and NPP modelling (Damm et al., 2010; Gamon et al., 1997). *In-situ* and satellite-based retrievals of chlorophyll content have also been shown to have the potential to constrain GPP estimates (Houborg et al., 2013).

The ways in which vegetation carbon flux modelling, according to the scheme presented above, can profit from drone data are twofold. First, drone based

measurements may be used for proximal validation and uncertainty estimates of many of the presented input quantities, or, second, drone observations may provide higher quality inputs for small-scale high resolution modelling of carbon exchange.

1.3.1 Core canopy structural measurements from drones

Measurements from flux-towers are currently related to vegetation development by using phenocams and simple NDVI sensors, whereas drones could be employed for more precise fine-scale monitoring within a flux tower footprint (Anderson and Gaston, 2013; Gamon, 2015). Drone mountable instruments are capable of providing all the core canopy structural measurements or structural traits required for adequate flux-interpretation, listed by Baldocchi et al. (1996) as LAI, canopy height, biomass, species composition and seasonal change in leaf area. While drones have drawbacks in regards to constant monitoring compared to phenocams, they are useful for periodic site investigations and offer a nadir view unaffected by horizontal occlusion which is more closely comparable to satellite data. The use of drone observations to chart spring green-up phenology at individual tree level has recently been demonstrated (Berra et al., 2019). Their data could be used to explain part of the variability in flux measurements arising from footprint heterogeneity and current vegetation status, as well as to calibrate phenocam estimates which can be biased due to aforementioned occlusion but this has not yet been pursued. The impact of footprint heterogeneity (Figure 1-5) has previously been assessed using airborne data (Pacheco-Labrador et al., 2017), where the issue of lacking temporal resolution could be solved by utilizing multi- or hyperspectral sensors mounted on drones instead.

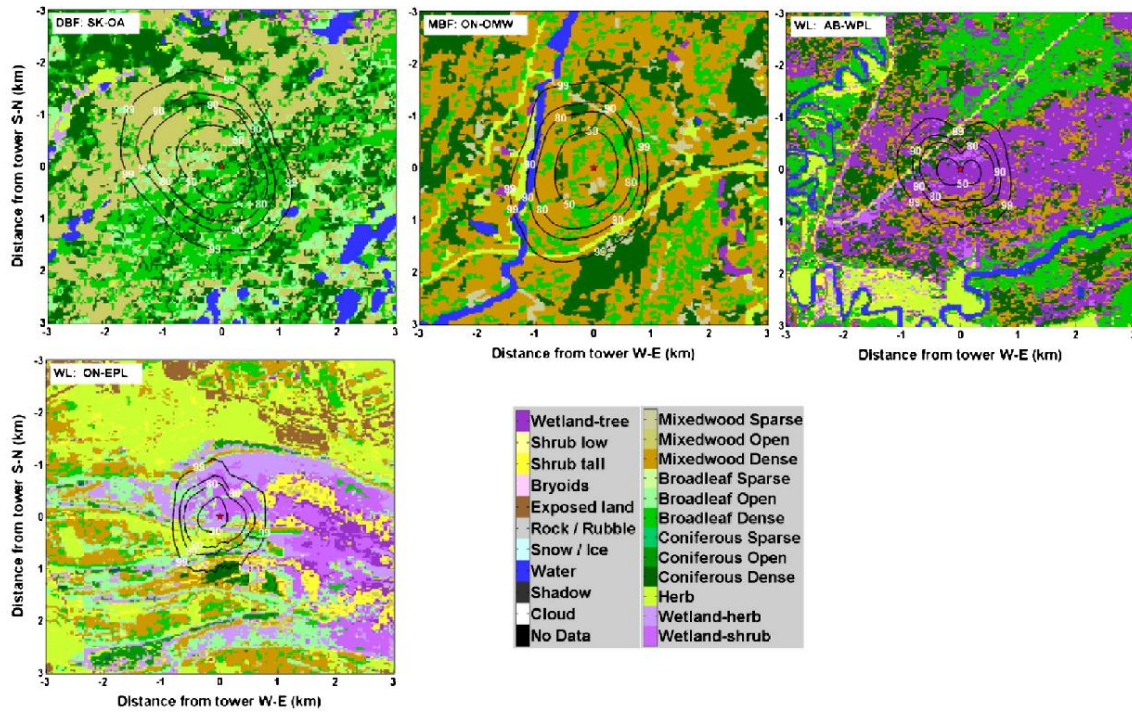


Figure 1-5: Example of modelled footprints (50-99%) and landcover classification of heterogenous flux-tower sites in Canada (Chen et al., 2012).

Capabilities to estimate the key variables of canopy height and biomass through SfM and drone-LiDAR were elaborated above (section 1.2.2.3). Some studies also attempt to predict LAI using structural parameters derived from the SfM point-cloud, with moderate success shown for vineyards (R^2 : 0.57, RMSE: 0.24 LAI) (Mathews and Jensen, 2013) as well as for maize canopies (R^2_{adj} : 0.74, RMSE: 0.23 LAI) (W. Li et al., 2016). But besides the structural information, a spectral component can provide further opportunities for vegetation characterisation. It is possible to determine LAI using only RGB images from consumer grade cameras. In one forest case study, canopy cover is estimated first through canopy classification based on RGB bands and a clumping index is derived further based on canopy gap sizes, the Beer-Lambert law can be utilized to estimate LAI with satisfactory results (R^2 : 0.7 for best estimate) (Chianucci et al., 2016). Additional information about vegetation health and structure can be revealed by utilizing VIs such as the NDVI. Following the model of satellite-based processing chains, specific empirical NDVI to LAI relationships can be identified and used to estimate mean LAI per canopy or plot from drone platforms (Berni et al., 2009; Tian et al., 2017; Yao et al., 2017). These VIs require spectral bands located around vegetation reflectance features such as the green-peak (550 nm)

and red edge (~710 nm), which can only be captured from drones by dedicated sensors such as multispectral cameras.

1.3.2 *Drone-based multispectral imaging*

The term multispectral is often only applied to systems whose bands differ from the RGB bands of commercial digital cameras, although these are per definition also multispectral. Spectral sampling width varies greatly between models. A commonly used, low-cost option is to modify conventional digital cameras by replacing the NIR-light blocking filter with a red light blocking filter, essentially replacing the red with a NIR band (e.g. Lu & He, 2017). As these are not science-grade instruments, the spectral response functions (SRF) are defined by the Bayer pattern colour filter array (Bayer, 1976) and vary greatly between bands. Bandwidths are generally large (around 100 nm) and the SRFs per band overlap, especially between green and blue (compare Lu and He (2017)). To derive spectral reflectance properties of the imaged surface, these sensors should be radiometrically calibrated using reference surfaces and empirical line correction (Lu and He, 2017; Von Bueren et al., 2015).

Dedicated multispectral cameras are more financially costly due to requiring model-specific calibration procedures during manufacture but improve upon RGB cameras by providing data over separate narrow wavelength bands (Aasen et al., 2018). A number of commercial systems are being offered for precision farming applications, providing 4 to 6 spectral bands, generally covering RGB, red-edge and NIR regions, with band-widths between 10 and 40 nm (e.g. Sequoia, Parrot, RedEdge, MicaSense and P4 Multispectral, DJI). Expert systems allow specifying the wavelength bands through exchangeable filters (Micro-MCA, Tetracam). Reflectance factors are calibrated using reference targets, while corrections for various noise and vignetting effects also need to be performed (Kelcey and Lucieer, 2012). In a study using the legacy Mini-MCA system by Tetracam, reflectance values appeared to deviate quite strongly from reference measurements. These differences are attributed to radiometric inconsistencies and calibration issues (only one calibration image acquired over reference targets for empirical line calibration) (Von Bueren et al., 2015). A contrasting study found very small RMSEs (1.17%) when comparing reflectance factors (Berni et al.,

2009). This illustrates the importance of pre- or post-flight calibration with well-characterized reference targets in the field which has since been highlighted by multiple studies (Aasen et al., 2018; Assmann et al., 2019), as well as using large uniform validation targets guaranteeing pure pixels visible in multiple acquisitions (personal comm. Field Spectroscopy Facility, Edinburgh UK).

1.3.3 Drone acquired indicators of light use efficiency

The potential for vegetation type specific remote monitoring of LUE could be granted by insights into foliar biochemistry. Multiple relationships between pigments and LUE have been identified. Gitelson et al. (2006) showed that a simple definition of $LUE = GPP/PAR$ was valid for maize canopies and chlorophyll content was directly related to this. Relationships between chlorophyll content and GPP over the season could also be identified in an olive orchard, while NDVI remained stable, which has implications for satellite derived GPP (Zarco-Tejada et al., 2013). If these relationships hold for other crops or even natural ecosystems has yet to be tested. Chlorophyll content as a supplemental indicator of LUE was also studied using a carbon, water and energy exchange model and very good fits were found, indicating the potential of using chlorophyll content as a proxy for LUE (Houborg et al., 2011). While other studies linked LUE development over the year primarily to foliar nitrogen (N), chlorophyll content is correlated with N but represents a more convenient measure. The study by Houborg et al. (2011) based its maps of chlorophyll content on only one airborne campaign and generated daily maps through adjusting values with field measurements and controlled studies. The uncertainties generated by this approach could be minimized by frequent drone measurements.

Chlorophyll and carotenoid pigment content estimation from drone platforms is possible by utilising spectral information and derived indices of varying representativeness, from NDVI to indices tailored for pigment retrieval (Gitelson et al., 2006a). Berni et al. (2009) related the TCARI/OSAVI multi-band VI to chlorophyll content using the FLIGHT radiative transfer model (RTM) and succeeded in retrieving chlorophyll for olive tree canopies with RMSE of $4.2 \mu\text{g cm}^{-1}$ (Figure 1-6). The capability of easily capturing multi-angular data with drones can also be leveraged for retrievals based on RTM inversions (Roosjen et al.,

2018). Using narrow-band indices related to carotenoid content, D'Odorico et al., (2020) were able to relate drone acquired information to photosynthetic phenology in spruce seedlings. Hyperspectral cameras also show good potential for monitoring chlorophyll. A summed green reflectance over the 500-599 nm region showed very high correlations with total chlorophyll content (Constantin et al., 2015) while Kanning et al. (2018) used partial least squares regression to successfully estimate chlorophyll.

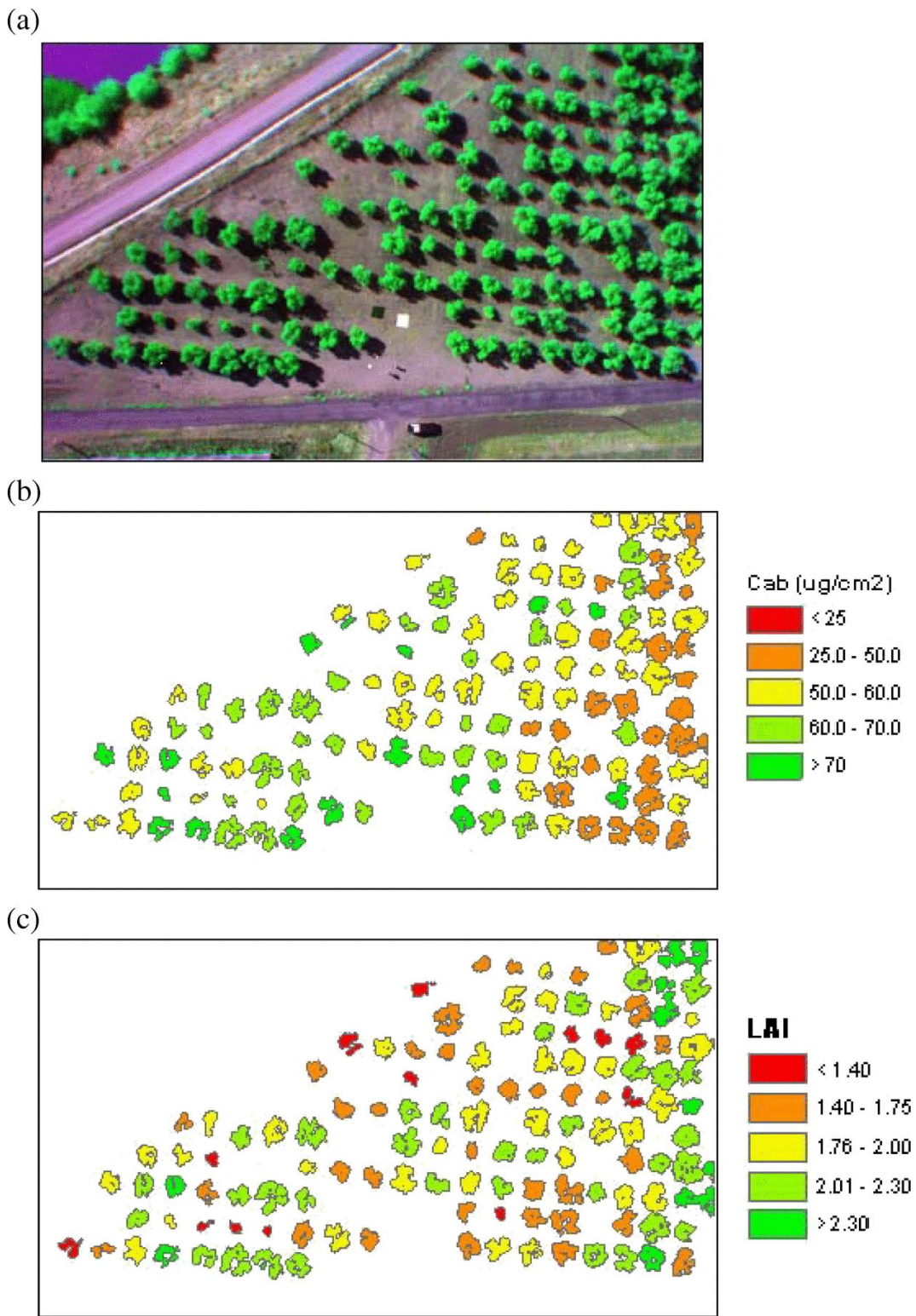


Figure 1-6: Drone Multispectral imagery (false colour) of an olive orchard acquired using an MCA-6 multispectral sensor (a) and derived chlorophyll content (b) and LAI (c) per canopy (Berni et al., 2009)

Pigment status directly related to LUE, such as the de-epoxidation state of xanthophylls due to the plant's need to dissipate excess energy, can be quantified by the photochemical reflectance index (PRI), if the corresponding narrow bands at 531 and 570 nm are available (Gamon et al., 1997). This is possible with the appropriate band combination for drone mounted sensors (Abdulridha et al., 2020; Berni et al., 2009).

Besides LUE related indices, a further method of assessing vegetation status and functioning is the very faint signal of chlorophyll fluorescence, an emission of light from the photosynthetic apparatus with peaks at 685 and 740 nm. It is the remotely measurable quantity which is the most directly related to the photosynthetic process (Porcar-Castell et al., 2014) and has recently become the focus of many vegetation remote sensing studies (Cendrero-Mateo et al., 2019; Cogliati et al., 2015; Damm et al., 2015a; Dannenberg et al., 2020; Rascher et al., 2015).

1.3.4 Drone-based hyperspectral imaging

The technology which lends itself to the retrieval of fluorescence as well as a multitude of narrowband indices and surface reflectance are hyperspectral measurements. Drone-based fluorescence retrieval has been demonstrated in proofs of concept using non-imaging spectrometers mounted on drones (Chang et al., 2020; Garzonio et al., 2017; Vargas et al., 2020) while hyperspectral imaging from drones is still in its infancy with most recent studies focusing on technical aspects (Arroyo-Mora et al., 2019; Banerjee et al., 2020) or utilising the additional information for species classification (Nezami et al., 2020; Sankey et al., 2018). An overview of some of the prototypes currently available is given in Table 1-1, following a classification by Aasen et al., (2015). Adão et al. (2017) and Zhong et al. (2018) provide a more in-depth review of sensors and example applications. In practice, drone based hyperspectral imaging is still fraught with operational concerns and demand a high initial financial investment. Further work to improve sensor design and to find the best solution which takes into account the drone platform's limitations is needed before this can become a truly operational methodology and able to deliver high quality observations of spectral properties of the imaged surface.

Table 1-1: Drone-mountable hyperspectral sensor technologies and examples

Technology	Example	Capabilities and limitations
Snapshot camera (capture all bands in one exposure using a segmented charge-coupled device (CCD) chip)	S 185-Firefly SE, (Cubert GmbH, Germany)	450 – 950 nm, 125 bands, segmented CCD results in well registered bands but lower resolution (approximately 10 cm at 100 m).
Image-frame camera (bands captured sequentially using a Fabry-Perot interferometer)	Hyperspectral imager (VTT Technical Research Centre of Finland Ltd) (Mäkynen et al., 2012)	500 – 900 nm, 10-30 nm spectral resolution. Band registration needed, introducing uncertainties.
Spatio-spectral imaging (combines frame imaging with hyperspectral filters for the CCD chip)	COSI (Vito, Belgium)(Livens et al., 2017)	600 – 900 nm, provides fine spatial ground resolutions of about 2 cm but requires stable platform and ideally constant flying speed, can introduce uncertainties due to the same point being imaged at different wavelengths from varying angles.
Pushbroom sensor (Acquires one row of spatial pixels sequentially)	Micro-Hyperspec VNIR scanner (NIR and SWIR available) (Headwall Inc., USA)	400 – 1000 nm, 324-369 bands at 4.5 nm spectral resolution, requires very high stability and GPS accuracy as rows cannot be photogrammetrically co-registered as in imaging systems.
Non-imaging high spectral resolution spectrometer	PICCOLO DOPPIO (MacArthur et al., 2014) based on e.g. USB2000+ (OceanInsight, Finland)	400 – 1000 nm, 0.1-10 nm spectral resolution, can be used for chlorophyll fluorescence retrieval. Highest spectral resolution but requiring high platform stability as movement introduces uncertainty of measured footprint.

1.3.5 Modelling radiation interaction with vegetation representations based on drone data

As introduced above, for satellite based GPP estimations, fAPAR is usually inferred from NDVI (Xiao et al., 2004), but there are uncertainties in this assumption which can be addressed by investigating the relationship at finer

spatial scales. Drones have previously been used to estimate the related measure of fraction of incident photosynthetically active radiation (fIPAR) at plot-level by linking NDVI to irradiance simulations using an RTM (Guillen-Climent et al., 2012). A further method to explore radiation propagation through vegetation canopies at fine scales could involve the use of drone acquired information on vegetation structure (SfM or LiDAR based methods to model crown shape, LAI, clumping and average leaf angle) to better represent vegetation in an RTM framework as has been demonstrated for ALS and TLS data (Calders et al., 2018; Schneider et al., 2014), but this has yet to be explored. Such models are also key for linking surface reflectance as acquired by optical remote sensing to functioning through model inversion, retrieving traits such as LAI and leaf pigment content (Kattenborn and Schmidlein, 2019).

1.3.6 Drones as a tool for studying vegetation phenology

Phenology describes the study of periodically recurring patterns of growth and development of plants and animals throughout the year (Lieth, 1974; Piao et al., 2019). The study of vegetation phenology is of particular interest in relation to climate change as it is directly impacted by changing temperatures and in turn influences the timing and duration of carbon sequestration among many other ecosystem processes. It can also affect ecological interactions with birds and insects which depend on the timing of bud-burst, leaf-out and leaf expansion dates (Körner and Basler, 2010; Polgar and Primack, 2011).

Remote observations usually track the timing of vegetation phenology using optical sensors and vegetation indices such as the green chromatic coordinate (GCC) or NDVI (Brown et al., 2017; White et al., 2014; X. Zhang et al., 2003). The metrics of interest relating to the start and duration of vegetation productivity that can be derived from time-series of observations include the start of season (SOS), end of season (EOS) and length of season (LOS), from first leaf expansion to senescence. The period of spring green-up can be further divided into start of spring (identical to SOS), middle of green-up (MOG) and start of peak greenness (SOP) (terminology changed from (Klosterman et al., 2018) to avoid confusion between ‘spring’ and ‘season’ in abbreviations). These are extracted using different methodologies, identifying the extremes of the rate of change of

index values being the most common (Berra et al., 2019; Klosterman et al., 2018; White et al., 2014).

Phenocams are the method of choice for proximal observations of phenology and for validating satellite-derived landscape scale phenology (Brown et al., 2016; Hufkens et al., 2012; Keenan et al., 2014). They can resolve individual trees and are relatively unaffected by cloud-cover but also suffer from occlusion due to oblique viewing angles. Drones provide an advantage as besides resolving individual plant crowns, allowing the separation of species specific phenology even in highly diverse systems such as mixed forests, they provide a birds-eye view which is more comparable to satellite observations. For studies at landscape or global scale using satellite data, drone observations can be applied to investigate the scaling of phenological parameters and address the mixed pixel effect of satellite-based retrievals (Berra et al., 2019; Chen et al., 2018; Klosterman et al., 2018).

1.4 Conclusions

By thorough review of literature on established methods for remote sensing of vegetation structure and functioning and the current state of drone sensor technologies, the potential to address key questions in vegetation ecosystem science have been presented. Drone acquisitions not only provide a low cost alternative for state-of-the-art methods but provide advantages in terms of flexible deployment and unparalleled spatial grain to complement *in situ* measurements. The carbon cycle modelling community can make use of drones to acquire fine-grained information on biomass, LAI and LUE related parameters for the calibration and evaluation of landscape and global scale models. The drone-based technologies illustrated here also have applications in many more overlapping branches of ecology which were not discussed, such as monitoring biodiversity. Some of the proposed applications are currently largely hypothetical, yet first realisations are emerging as drone remote sensing is being fully adopted for environmental monitoring. It remains to be shown precisely how established remote sensing workflows can optimally benefit from high resolution spatial

information as produced by drones, but early work on drone-derived information supplementing or mostly replacing *in situ* measurements shows promise.

Advanced applications of drone acquired information such as using spectral information to assess vegetation stress and pigment contents or using SfM methods to resolve subtle changes in vegetation structure however requires careful assessments of uncertainties related to the acquisition method and the miniaturised sensors. Further research must be undertaken to pin down these uncertainties and advise on best practice methods for data acquisition which in many drone related studies are still treated only briefly. Continuous improvements in both, acquisition practices and miniaturised system components ensures that that drone-based sensing is here to stay as a solution for fine spatial resolution vegetation characterisation and monitoring.

2 Overview of research aims

This project aims to evaluate the information content and accuracy of measurements from lightweight drone-based sensors to assess vegetation structure and function. The outcomes should lead to improved monitoring and understanding of vegetation related processes in the carbon cycle. Equipped with miniaturised versions of sensors commonly used on airborne and spaceborne platforms, drones can, in theory, observe identical quantities compared to such platforms but at much finer spatial scales. Such fine scale information enables the identification and monitoring of changes in plants at individual level which can also aid in simulating fine scale processes and in disentangling signals observed at coarse scales (Abdollahnejad et al., 2018; Berra et al., 2019; Brüllhardt et al., 2020; Klosterman et al., 2018). Acquired information can further serve as inputs for calibration and validation of models based on coarser scale data (Kattenborn et al., 2019; Revill et al., 2019; Wang et al., 2020).

However, the data acquired from small drone platforms are influenced by a large range of effects which include but are not limited to flight planning, environmental conditions and sensor related effects such as vignetting, lens distortion and dark current noise (Adler, 2018; Duffy et al., 2017; Kelcey and Lucieer, 2012; O'Connor et al., 2017). The impact of these uncertainties should first be understood in order to apply adequate methods for drone-based plant traits estimation. Against this background, the work presented in this thesis follows up on three overarching aims:

The first seeks to quantify uncertainties in drone acquired photogrammetric measurements with the goal of assessing the suitability of these technologies for retrieving vegetation height metrics. The question posed here is: To what extent can SfM photogrammetry-derived products deliver accurate information about vegetation height parameters?

The second seeks to quantify the accuracy and consistency of drone acquired surface reflectance and derived VI measurements and their implications for deriving structural vegetation parameters. The question posed here is: How accurate and consistent are surface reflectance and VI products acquired from drone-based sensors over vegetation canopies?

The third seeks to use the assessed methods of drone data acquisition to achieve a spatial and temporal representation of vegetation structure at a study site and to ingest this information into an RTM as a step towards fully functional ecosystem representations at fine scales. The question posed here is: Can drone-based data be used to constrain and drive models of radiative transfer for understanding photon-plant interactions in complex heterogeneous canopies?

These aims are pursued over four distinct experiments (chapters 4-7) of this thesis. The contributions of the presented studies to the research aims are synthesised in chapter 8 (thesis structure shown in Figure 2-1). The studies are self-contained, addressing individual research questions which are presented along with their rationale in the corresponding chapters. The research follows four major threads:

- A) Chapter 4: Investigation of drone-based SfM photogrammetry as a tool for delivering biomass related vegetation height metrics. Assessment of the impact of acquisition designs favouring areal coverage over high resolution and overlap on point cloud precision and derived metrics towards efficient flight planning.
- B) Chapter 5: Inter-comparison of calibration methods and assessment of the uncertainty in drone acquired multi-spectral surface reflectance and VI data. Investigation of their correspondence with coarser scale data acquired from airborne and satellite platforms.
- C) Chapter 6: Assessment of the suitability of drone-derived NDVI data for the phenological monitoring of deciduous tree species and its sensitivity to illumination conditions.
- D) Chapter 7: Description of a vegetated study site using a multi-temporal drone-dataset to simulate the radiative transfer of PAR under realistic conditions and assess PAR availability at the understory.

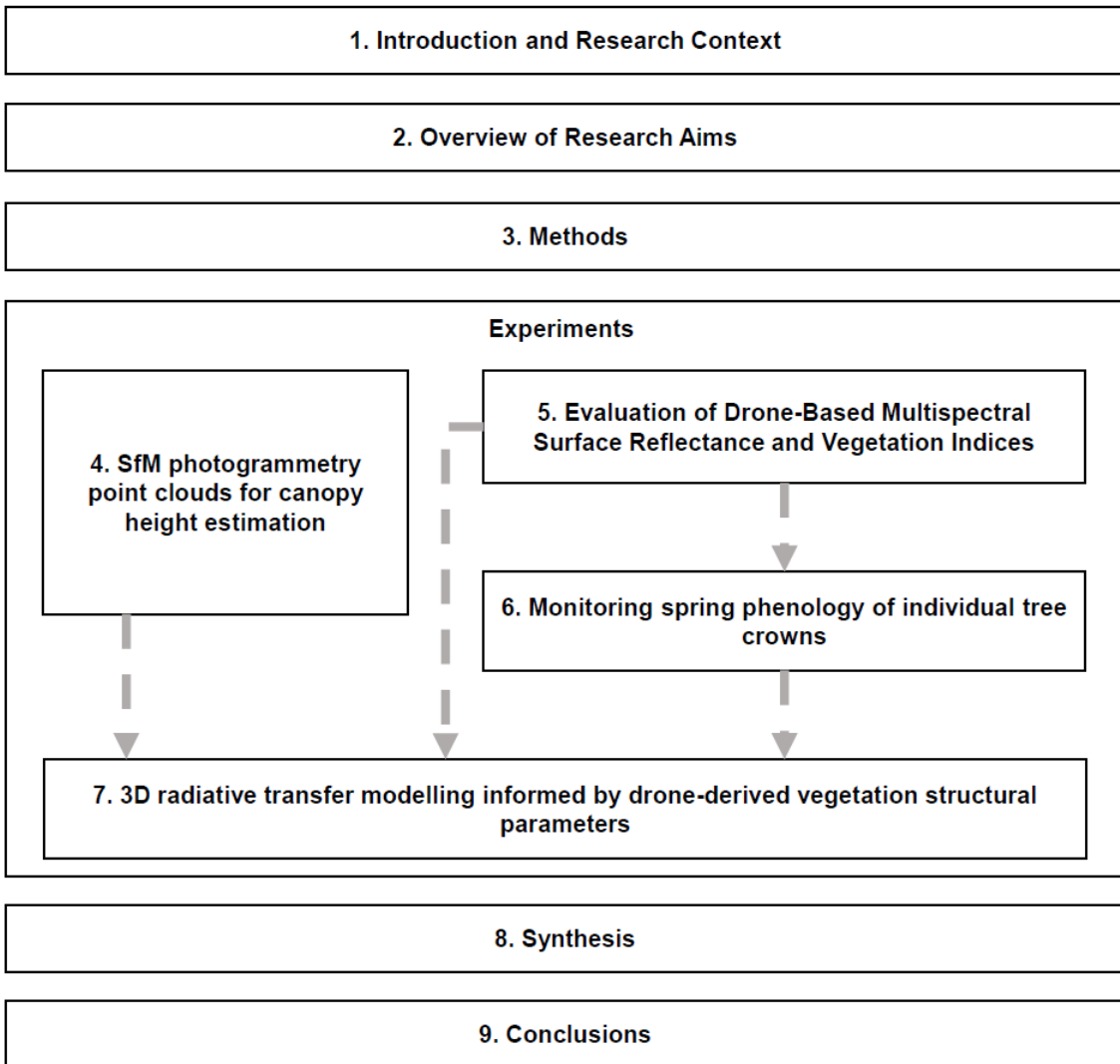


Figure 2-1: Structure of the presented thesis with numbers corresponding to chapters. The case studies or data chapters are presented with abridged titles and arrows indicating which studies are related and inform following studies in terms of data or methodology used.

3 Methods

3.1 Chapter overview

This chapter introduces the study sites, methods and materials used for the original research in chapters 4-7. The methodology is presented critically and given more context than can be provided in the shorter sections with chapters that follow. The development process and rationale for method selection over possible alternatives is included. For the application of the methods to case studies, including precise parameterisation, please refer to the individual chapters. The contents of this section are based in parts on the published work of Fawcett et al. (2019b) and Fawcett and Anderson (2019), attached in appendix A6.

3.2 Study systems

The studies conducted within this project made use of three very different vegetated study systems within three countries (Figure 3-1). These sites were selected for various reasons, primarily because they allowed the major science questions to be addressed and also because they allowed international collaborations to be explored. Brief site descriptions including the background for site selection are detailed in subsequent sections.

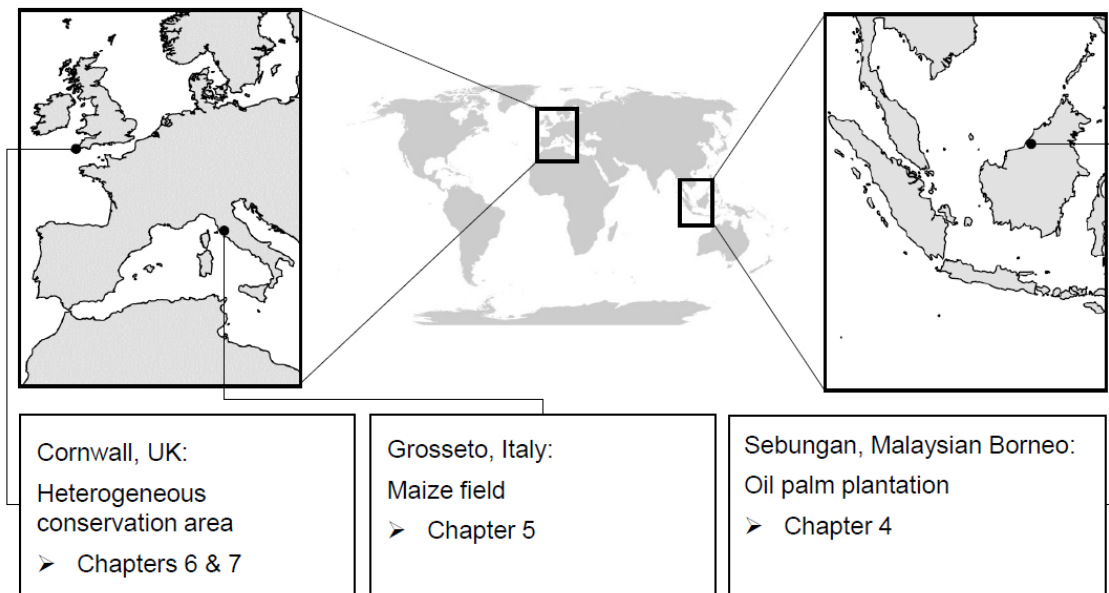


Figure 3-1: Study site locations shown in a global context, with indications of data chapters in which they are featured.

3.2.1 Oil palm plantation (Chapter 4)

To address research theme A, a study system was required where individual plant crowns could be clearly resolved and where underlying topographic variations could be described easily using SfM data alone. In collaboration with Dr. Tim Hill, the oil palm plantation of Sarawak Oil Palms Berhad in the state of Sarawak, Malaysian Borneo was identified as an ideal study system. Here, the application of drone-based SfM also allowed the development of further research questions of interest for both carbon accounting and plantation management, while addressing the main goal of developing drone-based SfM workflows for plant crown height retrieval and uncertainty estimates. The field data collection was supported both by Sarawak Oil Palms Berhad, its plantation workers and drone team, and Dr. Khoon Lip Kho of the Tropical Peat Research Institute, Selangor, Malaysia. The plantations of Sabaju ($3^{\circ}09'40.1"N\ 113^{\circ}25'09.1"E$) and Sebungan ($3^{\circ}09'58.1"N\ 113^{\circ}21'20.2"E$) were planted on tropical peat with smaller areas on clay dominated mineral soil and featured blocks of different palm ages, expressed as palms of different sizes and crown (frond) overlap. We selected blocks of 2, 7 and 10 years of age to include a size transect (Figure 3-2). The study areas for the 2 and 10 year-old blocks were selected to centre on two

flux-towers operated by Dr. Tim Hill to support wider research of the spatial and structural variation within the flux-tower footprint.

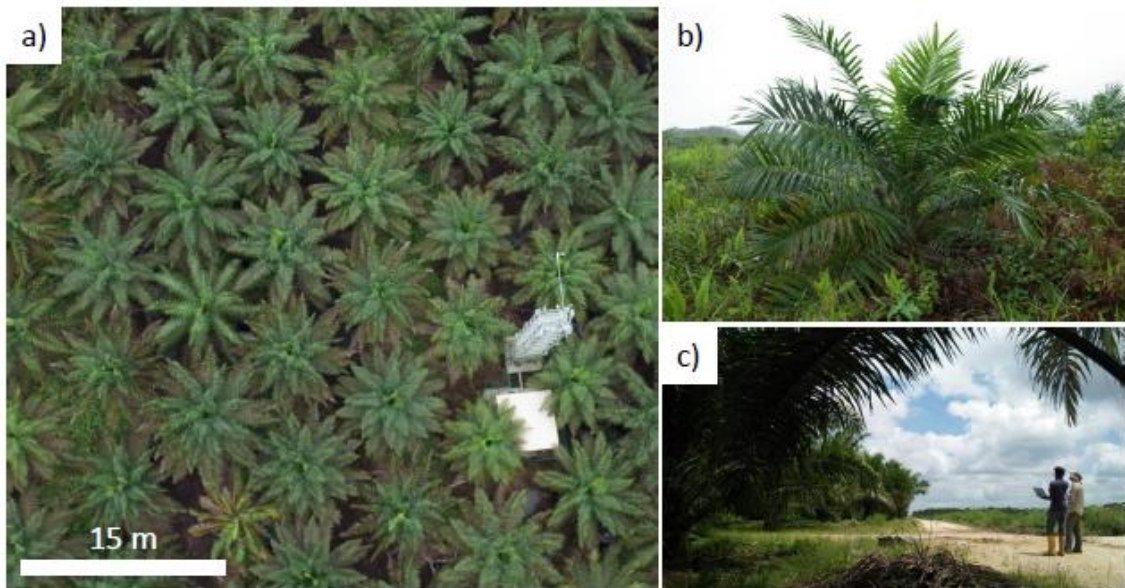


Figure 3-2: Images from the field campaign in the oil palm plantation in Sarawak, Malaysia: a) Drone image taken above the 10 year-old plantation including flux-tower, b) oil palm from the 2 year-old plantation, c) author and co-pilot standing between the 7 and 2 year-old plantation blocks while carrying out a drone flight.

3.2.2 Maize field (chapter 5)

A maize field study site (Figure 3-3) in the vicinity of Braccagni, a province of Grosseto, Italy ($N 42^{\circ}49'7.06''$, $E 11^{\circ}3'39.98'$, 3 m a.s.l.) was selected to address research theme B in an agricultural setting and focusing on a key crop type. The field was selected as it was the focus of a joint field campaign with researchers of the University of Milano-Bicocca (part of the TRUSTEE ITN network), where the author was on a two-month secondment. Field measurements of chlorophyll and LAI were being collected in conjunction with a hyperspectral airborne acquisition for the FLEXsense and CHIME projects (research in advance of the FLEX and Copernicus Hyperspectral Imaging Mission (CHIME)). Acquiring drone multispectral data at the same time as the airborne hyperspectral acquisition represented a unique opportunity for a multi-scale comparison of the two datasets, around which field efforts were coordinated.

The maize was planted on clay soil in north-south oriented rows and was drip irrigated. At the time of the study in early July 2018, the majority of the crop was in the tasselling stage (plant at full height and shedding pollen from extended

tassels, see Figure 3-3 d). The field showed considerable spatial heterogeneity and variability in plant density, likely due to soil characteristics and some localised irrigation issues. The area-of-interest to be covered by drone, airborne and satellite data was selected specifically to include a large range of LAI values.

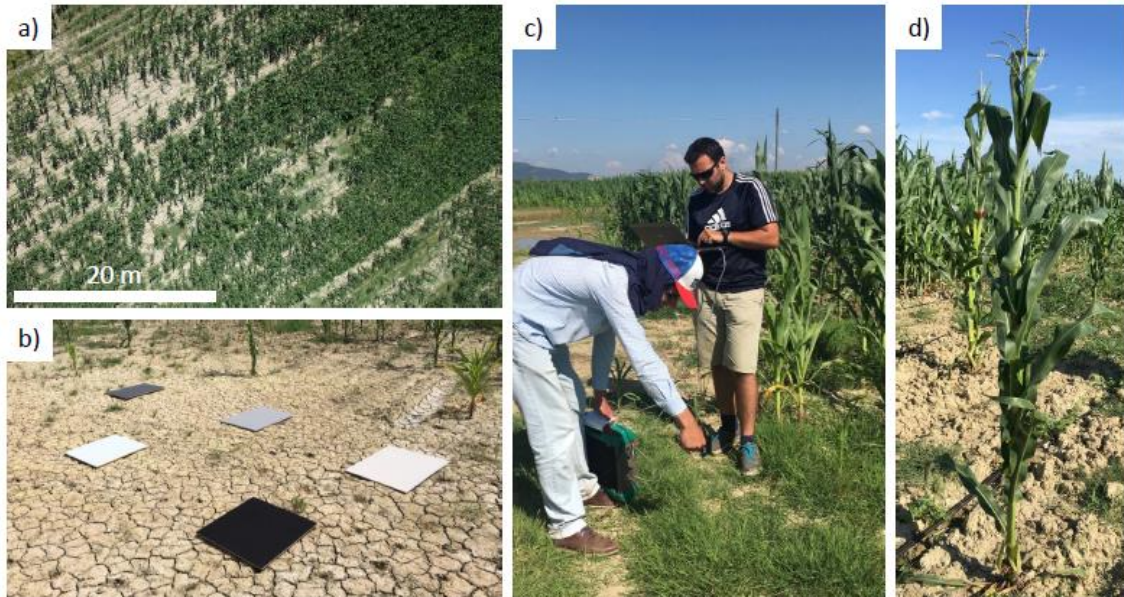
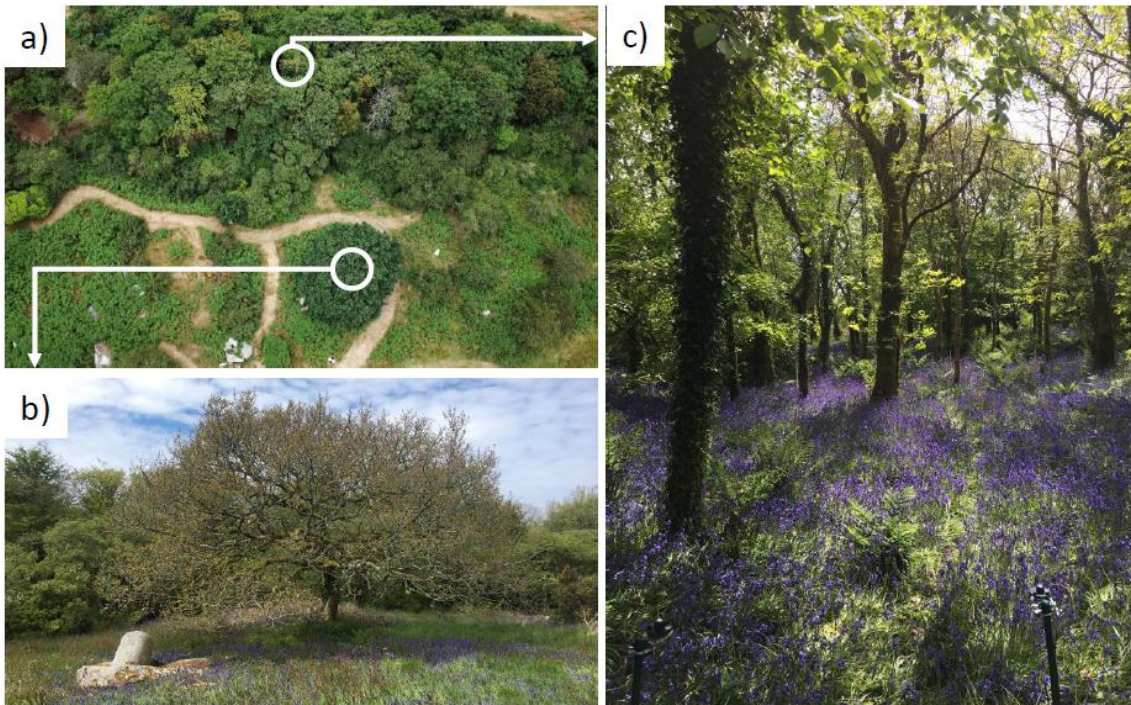


Figure 3-3: Images from the field campaign in Grosseto, Italy: a) drone image showing the heterogeneity of the studied maize field, b) reflectance panels for calibration and validation of multispectral images (dimensions: 50 x 50 cm and 40 x 60 cm), c) collaborators performing field spectral measurements, d) maize plant in tasselling stage.

3.2.3 Heterogeneous conservation area (Chapter 7 & 8)

The study site “Trelusback Farm” is located in West Cornwall, UK ($50^{\circ}12'10.0''N$ $5^{\circ}12'22.6''W$) close to the campus where the author was based. It is managed for the purpose of wildlife conservation, predominantly birds, moths and butterflies. It includes a small mixed woodland dominated by sweet chestnut (*Castanea sativa*), sycamore (*Acer pseudoplatanus*) and alder (*Alnus glutinosa*) as well as isolated free-standing trees and shrubs, mainly hawthorn (*Crataegus monogyna*), oak (*Quercus* spp.), grey willow (*Salix cinerea*) and gorse (*Ulex europeaus*) (Figure 3-4). The site was selected to address research themes C and D due to its tree species richness, accessibility and due to being a heterogeneous system with variation in canopy density which is a common feature of many natural and semi-natural ecosystems worldwide but represented only by mixed pixels at the coarser scales of freely available Earth observation satellite data (e.g. Landsat: 30 m, Sentinel 2: 10-20 m). The site accessibility (20 minutes drive from campus)

was a key consideration in selection of this site, which allowed for regular visits to capture data under acceptable illumination conditions.



*Figure 3-4: Images from the Trelusback Farm study site: a) drone image of a study site subset including the mixed woodland (c) and an isolated oak tree (b), b) oblique view of the oak tree shortly after budburst, c) image from within the woodland showing flowering of the understory (*Hyacinthoides non-scripta*) and quantum sensors mounted on posts (bottom).*

3.3 Drone data acquisition and processing

3.3.1 Drone platform

The main drone based acquisitions for all studies presented here were performed with a 3DR Solo quadcopter (3D Robotics, US), a multi-rotor (quad) drone system. From previous experiences within the research group this system was identified as a relatively low-cost yet capable platform for image data acquisitions (Duffy et al., 2018b, 2018a) and has since been the platform of choice for multiple drone remote sensing studies (e.g. Johansen et al., 2018; Tu et al., 2019). A multi-rotor drone was preferable over a fixed wing system for the experiments performed due to ease of deployment, greater control over flight parameters and no minimal flying altitude.

At a platform weight of 1.5 kg and payload capacity of 0.5 kg (3D Robotics, 2015), it can be used to deploy compact consumer grade cameras and small imaging sensors while falling within a low weight category which is important for operating within varied international restrictions. The Solo uses a Pixhawk 2 autopilot running open source software and thus provides more options for flight planning and accessing flight logs containing important flight parameter information such as GPS position and platform orientation. This is a key advantage over comparable systems such as the DJI Phantom series (DJI, China). Finally, the Solo airframe lends itself to customisation using 3D printed mounts which were the method of choice for attaching unique sensor payloads to a vibration damped plate (Figure 3-5). Mounts designed for this project have been made freely available online (<https://www.thingiverse.com/DomFawcett/designs>).



Figure 3-5: The 3DR Solo drone (a) used for this project, with 3D printed mounting solutions for a powerbank (b) and Parrot Sequoia irradiance (c) and multispectral imaging sensors (d).

3.3.2 Sensors

The two kinds of drone-based imaging sensors used within this project were chosen as to allow the acquisition of structural and spectral datasets respectively. Fine spatial resolution image data were required as inputs for photogrammetric processing to derive 2.5 D scene structure. For drone-based photogrammetry, the Ricoh-GRII compact consumer-grade camera has been advocated

(O'Connor et al., 2017) and was selected as it represents a trade-off between camera weight and image quality (i.e. minimal lens distortion). When acquiring images for use in SfM workflows a large dynamic range is desired (O'Connor et al., 2017). Following recommendations, camera settings such as f-stop and exposure were adjusted to illumination conditions and remained constant throughout acquisitions (automated exposure settings may be preferable for greatly changing illumination conditions). Focus was set to infinity which avoids out-of-focus images for drone acquisitions at higher altitudes (Dandois et al., 2015).

For the acquisition of spectral information on vegetation, a camera solution which can capture information over critical wavelength ranges where the amount of reflected light is indicative of vegetation's presence and status is desired. Desirable features to capture are the green peak of chlorophyll reflectance (550 nm), the dip of chlorophyll absorption (680 nm), the red-edge (740 nm) and NIR plateau (ca. 800 nm) (Figure 3-6). The Parrot Sequoia camera (Parrot, France) is a multi-camera array (MCA) system which features a camera with appropriate band-pass filters for each of these spectral bands (green: 550 nm, 40 nm bandwidth, red: 640 nm, 40 nm bandwidth, red-edge: 735 nm, 10 nm bandwidth and NIR: 790 nm, 40 nm bandwidth), while still being lightweight enough to be deployed on small drone systems, along with an independent power-source for straight forward integration (see Figure 3-5). A caveat is that the manufacturer only provides the wavelength-specific filter transmissivity but not the SRF, which is treated as confidential information by many manufacturers of consumer-grade MCAs. As the SRF is required to perform robust comparisons of spectral information, it is calculated by multiplying the filter transmissivities with an approximated CMOS (complementary metal-oxide-semiconductor) sensor response based on manufacturer published graphs (suggested by Parrot (Parrot, 2019, 2017a), and adopted by researchers of the Spanish National Research Council (CSIC, personal communication).

While the camera lenses of the Sequoia exhibit a stronger distortion effect compared to similar but heavier MCA systems (e.g. TetraCam, MicaSense RedEdge), these could feasibly be corrected using integrated software workflows. Each camera is triggered simultaneously and possesses a global shutter. This leads to increased consistency within individual images as opposed to cheaper

rolling-shutter type systems (e.g. Survey 3, MAPIR, USA) especially considering non-gimballed acquisitions (Candiago et al., 2015; Minařík et al., 2019).

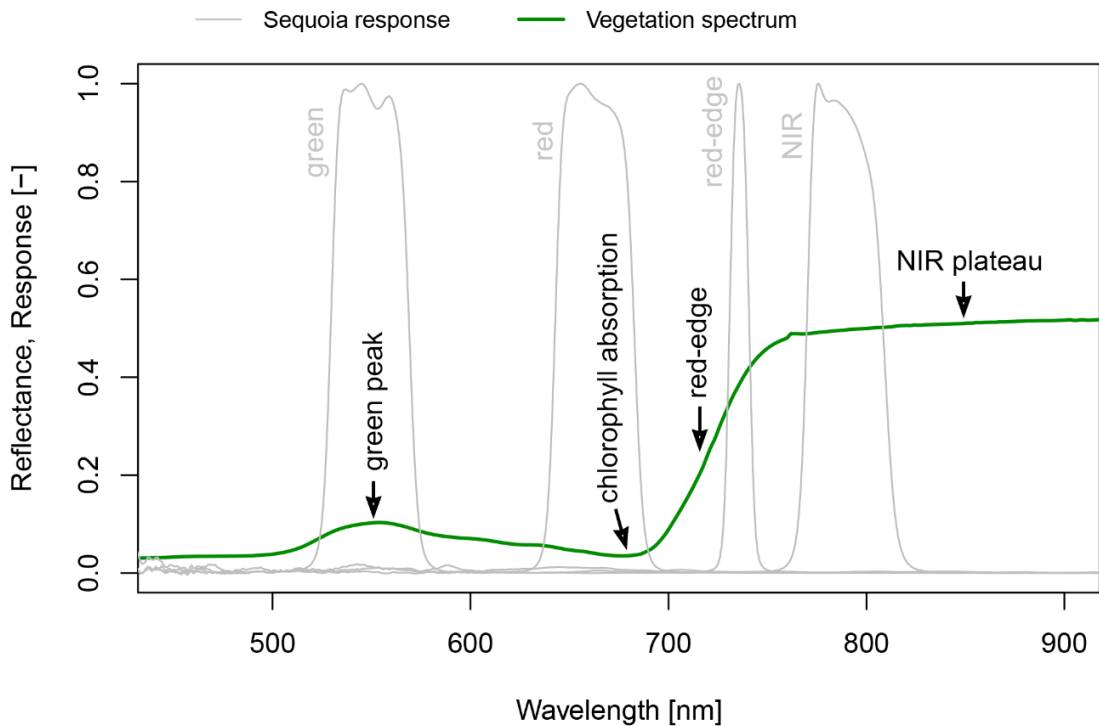


Figure 3-6: Reflectance spectrum of vegetation (grass, measured using an ASD spectrometer) with characteristic spectral features annotated. The spectral response curves of the four Sequoia cameras are overlaid.

Besides imaging sensors, methods of recording variations of incoming radiation are desired for quality control and correction of data captured by drones. High quality measurements which can be used for radiometric calibration can be acquired by stationary spectrometer or PAR sensors on the ground (Burkart et al., 2014; Hakala et al., 2010), while the ideal integrated solutions for drones are still being trialled (Suomalainen et al., 2018). Practical solutions focus on capturing relative changes in irradiance as is done by the integrated irradiance sensor of the Parrot Sequoia which was utilised here. Simple photoreceptors offer a defensible low-cost solution for the monitoring of relative irradiance variations during a flight (Hakala et al., 2013). As a deliverable for this PhD project required by the Marie-Curie grant agreement, a low-cost and lightweight illumination sensor system that can be easily mounted on drones was developed. More information on the implementation and the results of this deliverable can be found in appendix A7.

3.3.3 Flight planning

Advances in autopilot systems have allowed accurate automated flight planning including the specification of flight paths and drone flight speeds which are closely followed, given appropriate wind conditions and good GPS fix. Due to the variety of different camera systems for acquiring images as well the software solutions to process them, there are few general guidelines from previous studies which can be directly applied. Furthermore, most acquisition parameters including the amount of overlap required, acquisition angles and spatial resolution to be achieved are very study specific and thus require careful consideration on a case-by-case basis. Thus drone flight plans for the studies within this project were designed based on recommendations from the literature and adjusted according to sensors, study requirements and local restrictions. These parameters and their ranges are separated by sensor type and tabulated in Table 3-1 while parameters for specific experiments are listed in the corresponding chapters. It does not include environmental parameters such as wind speed and illumination, the latter of which is examined more closely in chapter 6.

For the successful photogrammetric processing based on drone acquired images a large amount of overlap is required. In general, greater overlap is always better for robust SfM-MVS processing but is limited due to coverage needs, time-critical factors and battery capacity. Previous studies have recommended a minimum of 60% overlap for a stable image network, while greater overlap is preferred (Dandois et al., 2015; James et al., 2020). Ensuring a minimum of 75% lateral overlap represented a good trade-off for the RGB data acquisitions performed, enabling the coverage of entire study sites or large subsets of these at 50 to 100 m altitudes. 60% overlap was used in a single comparison flight to investigate the trade-off between coverage and vegetation height product accuracy. Over forest canopies, it was found that greater flying altitude did not significantly increase vertical errors of the derived SfM point clouds, while the amount of forward image overlap had a greater effect (Dandois et al., 2015). Increasing acquisition altitude therefore represents the preferred way to optimise coverage, depending on the structural detail that must be resolved as the resulting lower ground sampling distance (GSD) will also result in sparser point clouds. Higher flight speeds may also be used to increase coverage while high forward overlap is guaranteed by

decreasing the image capture interval. To avoid any blurriness in acquired images the distance travelled during exposure time must however remain smaller than 1.5 GSD (O'Connor et al., 2017).

For multispectral image acquisition there were several further considerations which had to be taken into account during flight planning. Ideally the sun-object-sensor geometry should remain as consistent as possible during acquisitions to avoid viewing geometry effects visible in the data. This is nigh impossible with non-gimballed sensor mounting, but can be partially mitigated by reducing drone forward tilt by flying at lower speeds. Ideally, acquisitions should also be performed perpendicular to the solar principle plane to minimise the effect of the vegetation bidirectional reflectance distribution function (BRDF). Finally, multispectral acquisitions with frame camera systems should ensure a very high degree of overlap due to lens distortion and vignetting effects (Kelcey and Lucieer, 2012) affecting data towards the image boundaries and a high overlap ensures the resulting orthomosaic contains data primarily from central pixels. For all acquisitions with the Parrot Sequoia camera a forward and lateral overlap of at least 80% was ensured, based on prior recommendations (Johansen et al., 2018; Tu et al., 2019).

Table 3-1: Acquisition parameters set during flight planning for different studies, separated by sensor type: RGB primarily used for generating dense point clouds yielding structural information and multispectral primarily used for generating surface reflectance orthomosaics.

Acquisition parameter	RGB	Multispectral
Altitude	50-100 m	45-70 m
Ground sampling distance	1-4.43 cm	4.15-8.1 cm
Flying speed	5-11 m/s	< 5 m/s
Image capture interval	1-2 s	1.5 s
Forward overlap	60-85%	>80%
Lateral overlap	60-75%	80%
Camera angle	90° (nadir), 45° (oblique)	90° (nadir)

3.3.4 Ground control and georeferencing

In order to perform accurate georeferencing of drone image-based products as well as providing geometric constraints for photogrammetric processing, GCPs were used as the currently most reliable method of constraint and validation

(James et al., 2017a) given that the position of the drone platform could not be determined to centimetre accuracy. The GCPs must be clearly identifiable in the acquired images, which necessitated different GCP sizes (40-80 cm) and materials (PVC and canvas) for RGB or multispectral acquisitions to be visible at coarser resolutions (10 cm) and at NIR wavelengths in the case of the Parrot Sequoia (Figure 3-7). Good georeferencing can be achieved with relatively few GCPs (≥ 4) (Tonkin and Midgley, 2016) but their placement is important, favouring the boundaries of the surveyed area as well as the centre to eliminate systematic errors such as the so-called ‘bowl-effects’ is recommended (James et al., 2017). The accuracy at which GCP positions can be measured provide a lower bound for resulting product accuracies and it is therefore desirable to use solutions that allow post-processing GPS data with differential corrections to yield centimetre scale accuracies. For the studies within this project, two systems which provided centimetre-scale accuracy were used (1. Trimble Geo 7x GNSS system with a Zephyr Model 2 antenna, Trimble, US and 2. Topcon HiPer Pro, Japan).



Figure 3-7: Central GCP network being deployed in a Malaysian forest clearing by collaborators including (a) 40 x 40 cm painted PVC targets and (b) 80 x 80 cm canvas targets.

There are multiple methods for independent assessments of spatial errors of point cloud and orthomosaic outputs, all of which were applied in this project where the assessment of point cloud accuracy was amongst the primary goals. A common solution is to omit a subset of surveyed GCPs as check-points to

evaluate horizontal and vertical errors (Dandois and Ellis, 2013), which does however require the deployment of more GCPs. Measuring a larger number of replicates rapidly can be achieved with height validation points, provided the GPS surveying accuracy is sufficiently high (>10 cm), in order to assess vertical errors of drone-based DTM products (Cunliffe et al., 2016). Finally, a Monte Carlo method for assessing the precision of photogrammetric point-cloud outputs which was developed by James et al. (2017b) was applied to study the impact of georeferencing uncertainties on vegetation reconstruction.

3.3.5 Structure-from-motion photogrammetry and point cloud processing

SfM with Multi-View Stereopsis photogrammetry (SfM-MVS, often abbreviated to just ‘SfM’) represents a more flexible approach to photogrammetric scene reconstruction, as unlike conventional stereo photogrammetry, the camera pose and position can be derived using image data alone, without the explicit need for reference points of known 3D position in the imaged scene (Westoby et al., 2012). A great diversity of SfM photogrammetry software products are available and implement subtly different methods for tie-point detection and bundle adjustment (mostly proprietary and confidential but usually based on SIFT and Bundler) and product generation. While some cross-comparisons exist (Eltner and Schneider, 2015; Forsmoo et al., 2019; Fraser and Congalton, 2018; Turner et al., 2014b) they are case specific and there remains a need to clarify the advantages of each software for studies of different vegetation structural types.

Within this project two different software packages were used for the processing of RGB and multispectral image data respectively. With the main aim of generating dense point clouds and finely resolved DSMs, RGB image processing was performed using Agisoft Metashape (formerly Photoscan, versions 1.4.2 and 1.5) (St. Petersburg, Russia). This software was selected due to its successful use in vegetation focused applications such as forest inventories (Dandois and Ellis, 2013; Puliti et al., 2015), the ability to fine-tune many of the processing parameters (e.g. tie-point constraints) and the availability of previously developed Python scripts for spatial uncertainty estimation (James et al., 2017b). For the processing of multispectral data Pix4D (Pix4D, Switzerland) was used as an

alternative software solution. Initially this was primarily due to the limited capability of Agisoft Photoscan to handle multi-spectral data from the Parrot Sequoia camera. While this capability was later added (since version 1.4.1), the fact that the precise implementation of camera corrections and radiometric calibration (see section 3.2.6) remain black-box for both software solutions, Pix4D remained the preferred choice due to their official support and collaboration with the sensor manufacturers.

Further steps of dense point cloud processing and segmentation were handled interactively within CloudCompare (v. 2.9.1) or fully automated using functions of the lidR R package (Roussel and Auty, 2018). Besides automated statistical outlier filtering, CloudCompare enables investigation and manual deletion of point cloud areas which was necessary for eliminating artifacts originating e.g. from standing water, particularly when the DTM needed to be derived from classified ground points in the absence of LiDAR height information. The lidR package and its functions were originally developed for the further processing of LiDAR data but were found to also be applicable to SfM point clouds. It allows very straight forward generation of common structural products such as the DSM and CHM after point cloud normalisation with a DTM. Of the further functionality we made use primarily of the ground classification through a morphological filtering algorithm (based on K. Zhang et al., 2003 and previously applied to SfM data by Dandois and Ellis, 2013) for separating vegetation from ground points, and different crown segmentation approaches based on the identification of local maxima and application of a buffer (Silva et al., 2016) or a watershed region growing algorithm. It should be noted that due to computational limitations, dense point clouds needed to be subsampled to allow processing in R. The impact of this subsampling was deemed small considering the size and height variations of the studied vegetation canopies but may be limiting for studies focusing on smaller or complex vegetation and influencing height based point-cloud statistics.

3.3.6 Radiometric calibration

Converting the digital numbers (DNs) of multispectral drone imagery to a physically meaningful surface reflectance quantity is central to its further use and

the evaluation of different methodologies and their outputs was a focus of chapter 5. The following formulas for the calibration of Sequoia images using information recorded in image EXIF (Exchangeable Image File Format) tags are based on information provided by the manufacturer (Parrot, 2017b) and are fully integrated within the Pix4D software (with the exception of the standard empirical line method (ELM) based on multiple panels). However, the implementation of the full processing pipeline remains black-box and cannot be detailed here. Lens distortion and vignetting corrections are also applied within the software (see Pix4D, 2019).

The DNs (P) as recorded per pixel by the Sequoia sensor are converted to radiance-equivalent values, here termed pseudo-radiance R , following eq. (3-1) in Table 3-2. Here f is the focal ratio, γ the ISO and ϵ the exposure time in seconds whereas A , B and C are camera specific calibration factors provided by the manufacturer. These factors include a constant dark current correction, however it should be noted that the camera's internal temperature increases considerably during operation which has been found to increase dark current related noise within captured images (Adler, 2018). This was confirmed in preliminary experiments, which, consistent with Adler's, (2018) findings, showed a significant increase in mean image values with increasing temperature from 30 to 80 degrees Celsius (Figure 3-8). However, the impact appeared to vary considerably between camera pixels (both positive and negative) and resulted in no change in image median values.

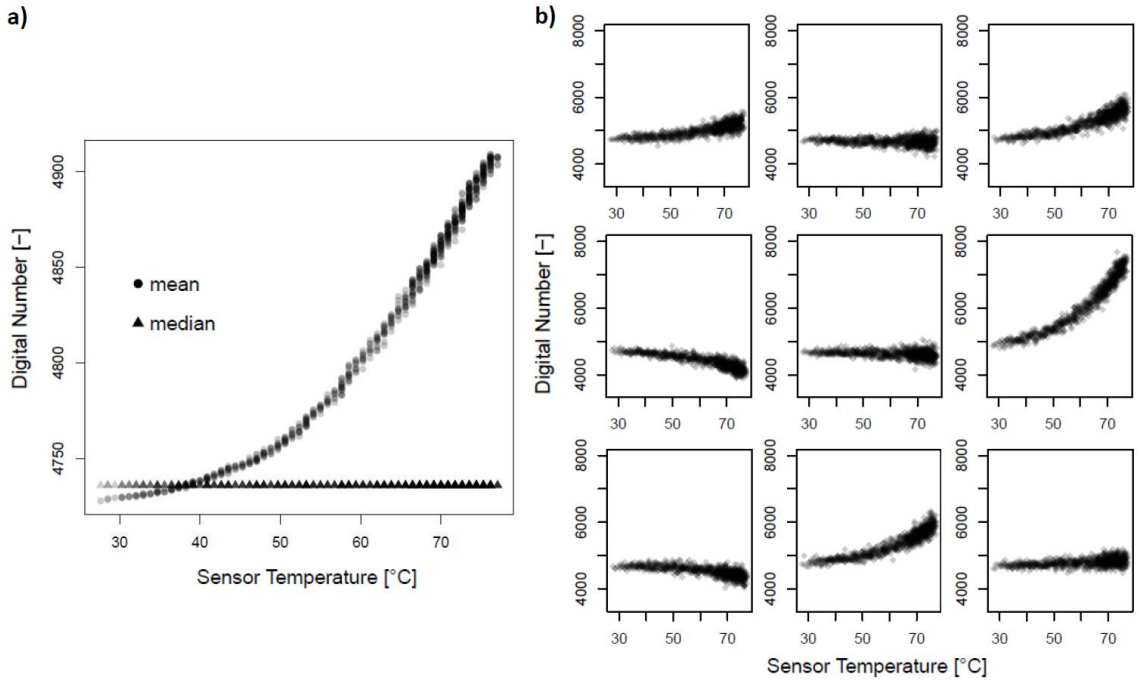


Figure 3-8: Results of a dark current experiment conducted with the Sequoia (lenses covered in dark room) depicting DN changes with increasing sensor temperature. a) mean and median DN values for images in the red band, b) DN values for a sequence of nine pixels (vertical downwards transect from image centre) for images in the red band.

For the single-panel simplified ELM calibration, R was converted to surface reflectance ρ (hemispherical-conical reflectance factor, following terminology by Schaepman-Strub et al. (2006) using calibration coefficient K (eq. 3-3, Table 1). K was derived from the calibrated reflectance value ρ_{ref} of a reference panel imaged prior to the flight, as well as the average R over the surface of the imaged panel, termed \overline{R}_{ref} (eq. 3-2, Table 1). ρ_{ref} for the Sequoia bands was calculated using the panel reflectance spectrum measured with high spectral resolution (< 1 nm) and the Sequoia SRF. The reference panel was imaged multiple times with bracketed exposure and the image per band with the longest exposure time was selected, unless there was oversaturation in which case a shorter exposure time was chosen.

Alternatively, the irradiance counts in DNs (C) recorded by the irradiance sensor were converted to pseudo-irradiance (R_{irr}) using eq. 3-4, where g is the gain and ε_{irr} is the exposure time of the irradiance sensor. R_{irr} could then be used to account for the variation in irradiance in respect to the single panel reference image and derive a ρ which was less susceptible to irradiance differences, using eq. (6) in Table 1. K' was derived similarly to K but included the irradiance

measured during the capture of the single panel calibration image R_{refirr} (eq. 3-5, Table 1). This factor also accounted for the differences in sensitivities and solid angles between the irradiance sensor and camera pixel measurements.

Table 3-2: Formulas used to convert DNs as measured by the Sequoia camera and irradiance sensor to hemispherical-conical reflectance factors (HCRF). Left column: reflectance calibration not considering irradiance, Right column: Reflectance calibration with irradiance compensation.

Pseudo-Radiance (R) from camera DNs (P): $R = f^2 \frac{P-B}{A\varepsilon\gamma+C} \quad (3-1)$ Calibration coefficient using reference panel (simplified ELM): $K = \frac{\rho_{ref}}{R_{ref}} \quad (3-2)$ $\rho = KR \quad (3-3)$	Pseudo-Irradiance (R_{irr}) from irradiance sensor DNs (C): $R_{irr} = \frac{C}{g\varepsilon_{irr}} \quad (3-4)$ Calibration coefficient using reference panel and measured irradiance (simplified ELM): $K' = \rho_{ref} \frac{R_{refirr}}{R_{ref}} \quad (3-5)$ $\rho = K' \frac{R}{R_{irr}} \quad (3-6)$
--	---

3.4 Supporting *in situ* measurements

Independent Field measurements are required to assess the quality and consistency of remotely sensed data and products derived from them. They enable the calibration of data to physical quantities of interest and the generation of empirical models to derive information which cannot be directly observed, such as relating VIs to structural and biochemical parameters (Heiskanen, 2006; Kang et al., 2016; Tillack et al., 2014). *In situ* observations also serve as critical validation measurements for products based on remotely sensed data and associated models, such as biomass, LAI and fAPAR (Bendig et al., 2014; Cheng

et al., 2006; Fensholt et al., 2004; Haboudane et al., 2004). However, despite being acquired *in situ*, many methods used to collect validation measurements are themselves indirect with inherent uncertainties which should be discussed and accounted for (Yan et al., 2019). In the following, the purpose and methodology of key *in situ* measurements acquired for this project are presented.

3.4.1 *Vegetation structural measurements*

3.4.1.1 *Height metrics*

The height of plant crowns were measured primarily for the validation of photogrammetric height models (CHMs, point cloud max heights). Due to the size of the studied vegetation (trees mostly between 5 to 12 m height), we opted for a laser rangefinder (integrated in Trimble GEO 7x, 0.05 m accuracy reported by the manufacturer (Trimble, 2018)) as a commonly used height measuring tool in forestry research with previous applications for the validation of drone-derived height metrics (Dandois et al., 2015; Marques et al., 2019; Wallace et al., 2016). The implemented three-shot method of height measurement allows the rapid measurement of tree heights but introduces a number of uncertainties related to the identification of the tree top (or top frond for oil palms). Combined with the <5 cm accuracy of these systems, replicates of height measurements showed standard deviations of 5-17 cm for tree crowns, which was discussed within the studies herein.

3.4.1.2 *Leaf and plant area index*

The leaf and plant area indices (LAI and PAI) represent structural metrics of vegetation canopies reporting the one-sided area of foliage elements per square metre of ground. The direct measurement of this quantity is possible only through destructive harvesting or the extrapolation of leaves caught in litterfall traps (Bréda, 2003). For the purpose of relating LAI or PAI to drone acquired data, time-critical snapshots of these metrics are required and therefore an indirect

technique was needed. We made use of two common solutions in remote sensing of plant traits, the LAI-2000 instrument (Li-Cor, USA) as well as digital hemispherical photography (DHP), depending on availability and suitability for different vegetation canopy types. For the study focusing on a maize-field, LAI information was collected by collaborators with the LAI-2000 based on an established sampling protocol (Baret et al., 2005). This instrument is well suited for application in continuous crops of limited height. For the local study site in a heterogeneous ecosystem dominated by open and closed tree stands, an LAI-2000 instrument was not available and DHP was selected as an alternative indirect method. Hemispherical photography has a long history of use in forest systems (Anderson, 1964; Thimonier et al., 2010) and DHP has the advantage of being able to critically analyse captured data post-acquisition and performing exposure related adjustments on raw file formats if required. Images were acquired using a Nikon D7000 with a Sigma 4.5mm F2.8 EX DC HSM Fisheye lens, along transects throughout closed tree stands as well as in four cardinal directions beneath free-standing trees (Figure 3-9).

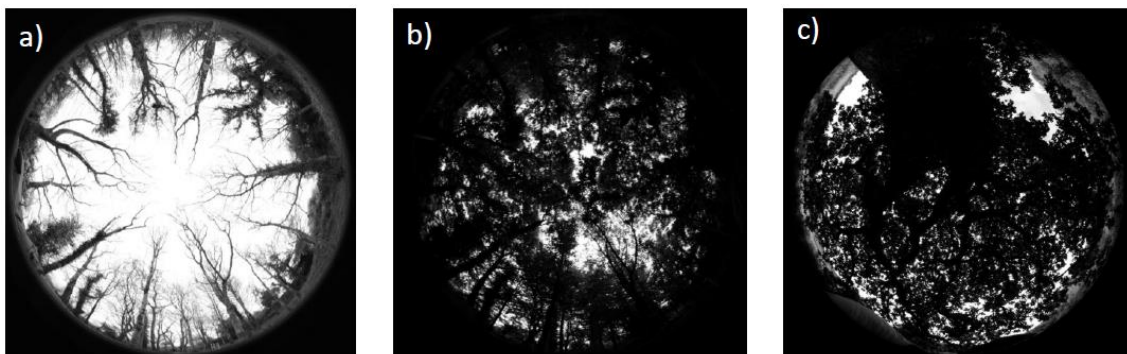


Figure 3-9: DHP images of a) woodland pre green-up, b) woodland post green-up, c) single oak tree post green-up.

In closed stands, PAI was estimated per image using the image processing software Hemisfer (version 2.2, WSL, Switzerland) which implements a formula for average foliage density (Miller, 1967) as used for LAI-2000 (Li-Cor, USA). For individual tree crowns the method required adjustments as they do not fulfil the assumption of continuous vegetated layers and must take into account the crown geometry (Bréda, 2003). An according workflow is implemented for LAI-2000 systems using a view-cap and requiring multiple measurements per crown as well

as field-measured representations of crown geometry (Li-Cor, 1992). This has been successfully applied for free-standing trees (Cutini and Varallo, 2006). DHP images for single crowns were divided into four sectors and one sector per image and direction used to estimate plant area density (PAD, plant area per 1 m volume of canopy). The LAI-2000 method of estimating PAI (L) is based on a discrete version of Miller's integration (Miller, 1967), using five rings (i) of equivalent width (eq. 3-7).

$$L = 2 \sum_{i=1}^5 K(\theta_i) \sin(\theta_i) \Delta\theta_i \quad (3-7)$$

In (eq. 3-7), θ_i is the midpoint of the ring in radians, $K(\theta_i)$ is the contact frequency per ring, $\Delta\theta_i$ is the angular width of the ring and $\sin(\theta_i)\Delta\theta_i$ represents the ring weighting factor (Thimonier et al., 2010). By integrating measurements from zenith to the horizon, the impact of the unknown leaf angular distribution is removed. However, often the outermost rings cannot be used, either in case of topography and particularly in the case of single crowns. For the LAI-2000 algorithm, the weight of the ignored ring is added to the adjacent ring while within Hemisfer the number of rings, $\Delta\theta_i$, and as a result θ_i can be defined for each case. In all cases this reintroduces some uncertainties based on leaf angular distribution as the outermost ring is extrapolated to the horizon while effectively measuring only an angular subset.

When incorporating crown geometry, L represents PAD instead of PAI and $K(\theta_i)$ is estimated by taking into account the path length through the canopy (Welles and Cohen, 1996):

$$K(\theta_i) = -\ln(T(\theta_i))/S(\theta_i) \quad (3-8)$$

Where $T(\theta_i)$ is the transmittance of vegetation and $S(\theta_i)$ is the path length through the canopy. $T(\theta_i)$ is reported by Hemisfer for each sector based on the ratio of vegetation versus sky pixels in the image. $S(\theta_i)$ is derived using the approximate position of the camera, the height of the top of the crown extracted from the CHM and the bottom of the crown based on field measurements (see Figure 3-10). The mean PAD per crown is extracted by applying (eq. 3-7) in the

four cardinal directions from the crown centre. A representative PAI value for the crown can then be derived by multiplying PAD with mean crown height (derived from CHM and field measurements).

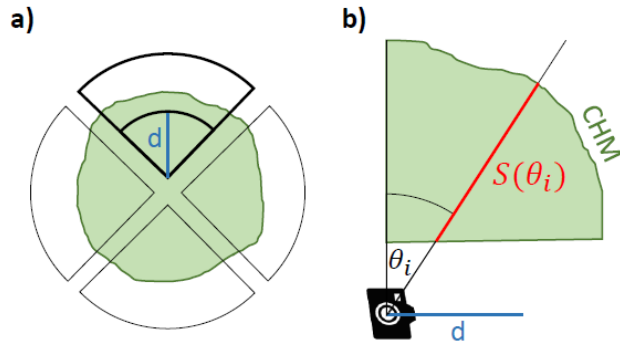


Figure 3-10: a) Schematic of 90° sectors extracted from four hemispherical images taken below the tree crown. d is the distance of ring i from the image centre. b) Schematic showing the path length $S(\theta_i)$ as approximated for each crown, ring and sector in this study.

3.4.2 Spectral measurements

Field spectral measurements were required for the calibration and validation of multispectral image mosaics and surface reflectance products. As the four spectral bands of the Parrot Sequoia camera used here lie within the visible to NIR range, smaller spectrometers such as the OceanOptics USB2000 and FLAME series (now OceanInsight) measuring from 350 nm to 1000 nm at approx. 1 nm spectral resolution can be used and offer an acceptable signal-to-noise ratio (SNR) for measurements in natural direct sunlight conditions. When available (through collaborations with TRUSTEE project partners), an ASD FieldSpec Pro instrument was preferred due to higher SNR and automated dark current measurements resulting in higher quality spectral information.

The measurements with field spectrometers followed best practice procedures (MacArthur and Anderson, 2007). They consisted of alternating and repeated measurements of reflected light from a Spectralon® white reference panel and the target of interest. All measurements were performed using a bare optical fibre with 23° field-of-view (FOV). The distance above the target was adjusted according to the instantaneous FOV and size of the target. When measuring, the

instrument operator was always positioned at 90° to the solar principal plane to minimise multiple scattering of light onto the target.

The relative reflectance formed by the ratio of the target and white reference measurements was post-processed to absolute reflectance using reference panel specific calibration files. The resulting datasets of hemispherical-conical reflectance factor (HCRF) reflectance spectra could be further used in combination with the Parrot Sequoia sensor response function for calibration and validation of surface reflectance orthomosaics.

3.4.3 Photosynthetically active radiation measurements

PAR is defined as radiation within the 400 – 700 nm wavelengths that plants can absorb and utilise for photosynthesis (McCree, 1972). It is commonly measured using quantum sensors which are calibrated to report the photosynthetic photon flux density (PPFD) in $\mu\text{mol m}^{-2} \text{s}^{-1}$. Above canopy measurements of incoming PAR at the bottom of the atmosphere (BOA) are essential for a number of applications relating to vegetation functioning and are an inherent part of the flux tower sensor assemblages alongside instruments to measure eddy covariance (Jenkins et al., 2007). When seeking representative measurements of PAR below canopies, point based measurements from single quantum sensors are highly variable in space and time due to overstory structure and sunflecks under direct irradiance conditions. This is addressed either by manual measurements over a constant sampling grid (Gendron et al., 1998), by using replicate sensors, e.g. as multiple single sensors or integrated within a sensor bar (Comeau et al., 1998; Fladeland et al., 2003), or by automated moving sensors (Lafleur and Farnsworth, 2008), in order to yield more spatially integrated metrics or capture spatial variation.

For the below-canopy PAR measurements as required for Chapter 7 of this project, the need for replication was recognised. As manual measurements were not feasible to capture daily variations of PAR, this was implemented by placing multiple (3-4) single levelled quantum sensors on poles at 75 cm above ground in 0.5-1.5 m distance from each other, connected to a FieldScout data logger. Measurements were taken at 1 minute intervals which required data download

every 7 days due to limited internal storage. Combined with averaging over 1 hour time steps, this configuration was deemed sufficient for compensating for the influence of small-scale structural variations. Due to requiring a total of 8 sensors, the LightScout quantum sensor (Spectrum technologies Inc., US) was selected over the more financially expensive but widely adopted Li-Cor sensors (Li-Cor, US) (Figure 3-11). The spectral response of the LightScout sensor deviates more strongly from an ideal response over the PAR wavelengths when compared to higher quality quantum sensors, particularly also recording a small fraction of photons below 400 nm (Spectrum Technologies, 2011). However, given the recording of reference above-canopy PAR with an identical sensor, this wavelength-specific effect should not have large implications for the results.

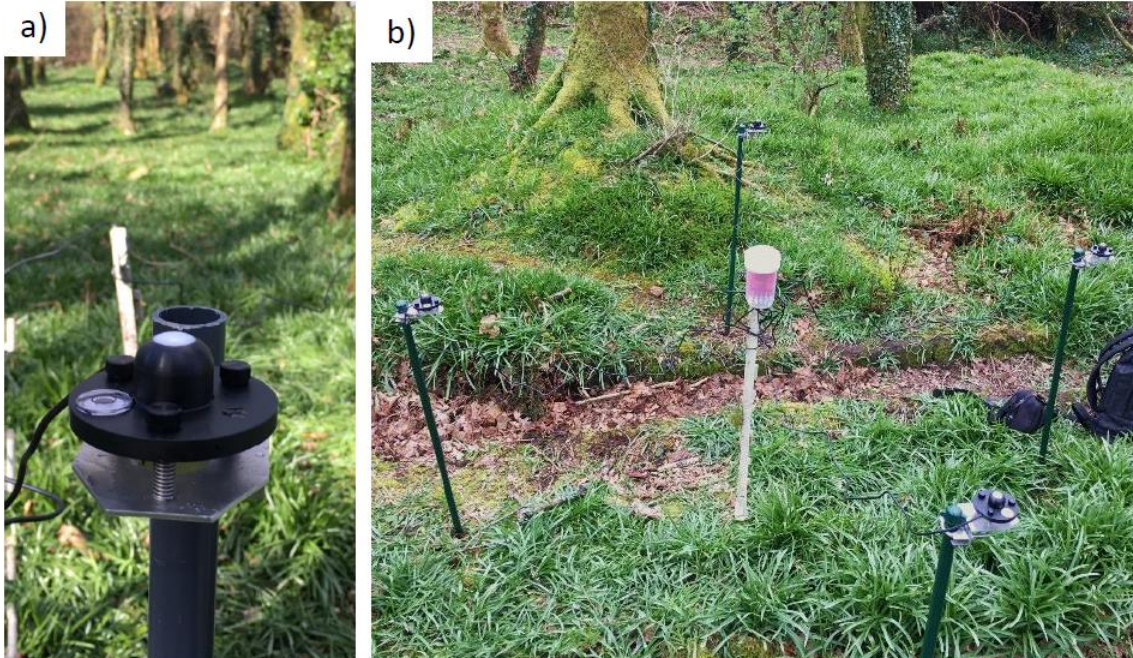


Figure 3-11: a) Levelled LightScout quantum sensor (Spectrum Technologies Inc.) for measuring PAR, b) woodland understory sensor arrangement with data logger (centre).

3.5 Radiative transfer modelling

RTMs allow simulating the interaction of radiation with 3D objects or within turbid media. In remote sensing of vegetation they are most commonly used to simulate radiation propagation through vegetation canopies represented with different levels of complexity, in order to invert optical signals and derive information on structural and biochemical vegetation properties such as LAI and chlorophyll content (Jacquemoud et al., 2000; Koetz et al., 2005; Myneni et al., 1997). This represents a widely applicable physical methodology as an alternative to empirical models which are reliant on case-specific relationships of field measurements to remotely sensed information (Darvishzadeh et al., 2008). We here distinguish between 1-D and 3-D RTMs and elaborate on their choice to answer specific questions in this project.

3.5.1 1-D radiative transfer modelling

As the inversion of RTMs is computationally intensive, particularly when using iterative optimisation, doing so over large scales requires reducing the problem to a very simple representation with a small number of input parameters. For vegetation, the solutions are 1-D RTMs which combine a leaf model of optical properties with a simple representation of a canopy as a leaf-filled layer of constant height over a ground surface (Jacquemoud et al., 2000). At leaf level, the PROSPECT model is by far the most widely adopted model which combines leaf structural parameters, pigments and water content into a representation of wavelength specific leaf reflectance and transmittance (Féret et al., 2017; Jacquemoud and Baret, 1990). At canopy level, the SAIL model (Verhoef, 1984) was the first and still most widely used to represent light scattering within the canopy, in combination with PROSPECT as PROSAIL and further extensions (Jacquemoud et al., 2009). In SAIL, the leaf layer is described by its LAI and leaf-inclination distribution function and the soil reflectance is also modelled.

PROSAIL was used here for a sensitivity analysis of the response of Parrot Sequoia and HyPlant NDVI and chlorophyll index to changing chlorophyll content and LAI of a maize crop, for the purpose of investigating errors introduced by

resampling spectral information (Chapter 5, Appendix A2). PROSAIL could in theory be used to retrieve maize LAI and chlorophyll content from Parrot Sequoia and Hyplant data, but for this purpose would need to be critically evaluated due to issues in modelling row crops (Atzberger and Richter, 2012).

3.5.2 3-D radiative transfer modelling

3-D RTMs allow modelling the interaction of light within complex scenes made up of geometric shapes. For many 3-D RTMs there is no limit to the level of detail that can be modelled, allowing the use of realistic 3-D objects such as trees with detailed branch structure and representations of each individual leaf. 3-D RTMs have common input parameters with 1-D models such as optical properties and LAI, with the difference that these can vary for each vegetated element within a 3-D scene. Additionally, they require 3-D descriptions of terrain and objects within the scene which can be formed by geometric primitives, voxels or fully 3-D object meshes. These object descriptions can make use of auxiliary 3-D datasets such as ALS and TLS point clouds (Calders et al., 2018; Schneider et al., 2014), but have not previously been described using estimations of crown shapes from SfM photogrammetry.

Most 3-D RTM models use ray tracing where each ray is scattered in a number of predefined directions with each surface interaction which is very computationally intensive. Despite the increased computational resources available today, ray tracing based 3-D RTMs with high level of detail remain unsuitable for large-scale applications. They are used to model radiation interaction within landscapes of limited spatial extent where spatial heterogeneities have a considerable effect on the studied quantity, be it directional radiometric quantities or properties of small areas (grid cells <10 m) where greater spatial variations that depend on adjacent scene elements are resolved. Examples include studies of row-crop BRDF (Duthoit et al., 2008), orchards (Guillen-Climent et al., 2012) and most commonly forest systems (Hernández-Clemente et al., 2017; Kötz et al., 2004a; Schneider et al., 2014). Besides being used to simulate remote sensing observations for inversion purposes, 3-D RTMs have been used successfully to model light interception and transmission through vegetation canopies for precise estimates of IPAR and

APAR at different levels (Damm et al., 2020; Guillen-Climent et al., 2012). This aligns with our goal of modelling understory PAR availability using drone-acquired datasets as inputs.

For our study we required a 3-D RTM which could describe terrain and precise tree crown shapes, each with specific PAD values. The discrete anisotropic radiative transfer (DART) model (Gastellu-Etchegorry et al., 2015) was selected for its ability to represent complex vegetated landscapes as voxels of turbid media (Figure 3-12) and simulate 3D radiative budget products. DART was preferred to forest stand RTMs as used within forest research (Ligot et al., 2014a) due to its ability to prescribe vegetation properties at voxel level without the need for crown shape approximation using geometric primitives. It also allows modelling scene reflectance. Modelling scattering as opposed to simply light attenuation was considered important for upscaling considerations which would involve linking the transmitted radiation to top-of-canopy reflected radiation as is observed e.g. by satellite, however this aspect was not pursued further within this project. Compared to the similar Forest Light Interaction (FLIGHT) model (North, 1996), DART inputs could be more readily modified to represent complex crown shapes based on drone CHM datasets. The methods of DART model parameterisation based on drone-derived products for simulations of the Trelusback study site are described in chapter 7, section 7.2.7.

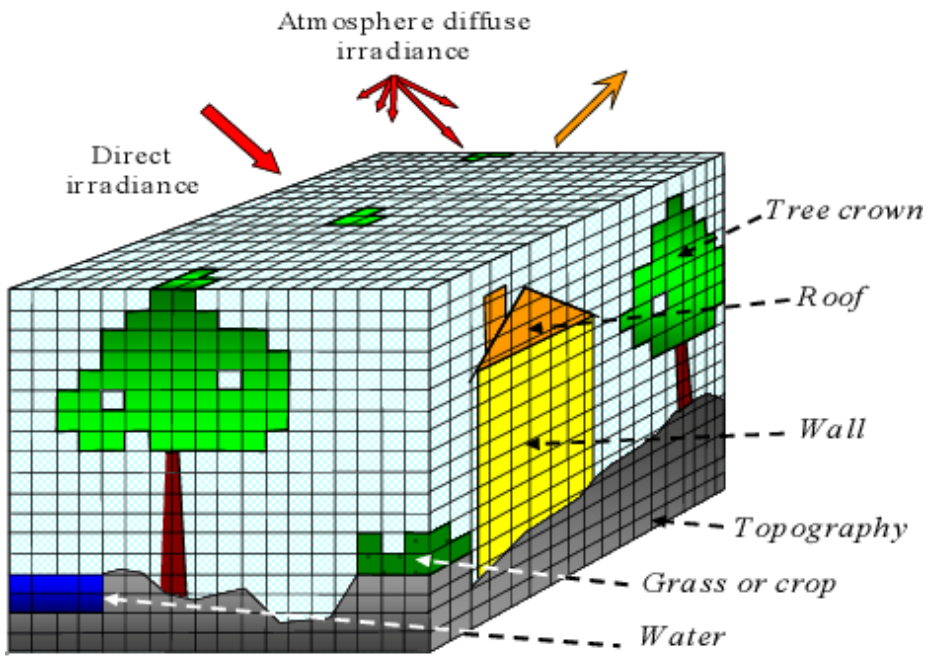


Figure 3-12: Figure representing a 3D scene cell matrix as can be simulated by DART, including parameterised voxels and 3D objects. Modified from (Gastellu-Etchegorry et al., 2012)

3.6 Statistical methods

3.6.1 Linear and non-linear regression models

Ordinary least squares (OLS) regressions were used to investigate the relationship between independent variables derived from drone acquired datasets (height metrics and spectral index values) and dependent variables derived from field measurements (vegetation height and PAI/LAI), using the coefficient of determination (R^2) and RMSE. When supported by observations and backed up by previous studies, non-linear models were fitted to the data. This was the case for the NDVI-PAI relationship used for prediction (linear, logarithmic and exponential, see Kang et al., 2016; Potithip et al., 2013), as well as logistic fits for spring NDVI increase over time, in order to derive phenological metrics related to “rate of change” (Klosterman et al., 2018). All regressions were performed using the “lm” and “nls” functions in R (version 3.4.3). Non-linear regressions required starting values which roughly correspond to the expected shape of the fitted model.

Where derived models are used to predict values (stem height, PAI) based on drone-derived datasets, leave-one-out cross validation (LOOCV) was employed in order to quantify errors, a common approach when dealing with a limited number of field samples (Li et al., 2016). In LOOCV, the model is fitted n times based on n-1 samples and the mean error of the predicted value for the omitted samples is reported.

3.6.2 Monte Carlo approach for point cloud uncertainty estimation

While photogrammetric processing software such as Agisoft Metashape and Pix4D can give indications of reconstruction quality based on the approximated versus the marked 3D locations of check points, it is often not feasible to include sufficient check points to assess local uncertainties across a landscape. To do this, check points would need to cover the entire horizontal and vertical range of the imaged scene, which is difficult in practice. However, information about the precision of each identified tie-point (sparse point cloud) between images can be derived through the ‘bundle adjustment’ process where camera parameters and 3D point locations are adjusted based on least-squares global optimisation. James et al. (2017b) developed a workflow to extract tie-point precision estimates using a Monte Carlo method by performing repeated bundle adjustment while adding random offsets to GCP and image measurement precisions (Python plugin for Agisoft Metashape). The output sparse point clouds could be processed to point coordinate precision estimates using the SfM_georef software (version 3.1); (James and Robson, 2012). It should be stressed that these precision estimates do not represent absolute accuracy which can only be verified by check points, but give a good interpretation of local reconstruction quality.

We used the Monte Carlo approach with tools provided by Mike James in order to compare estimates of point cloud uncertainties for two different acquisition methods over the oil palm plantation study site. Previously, this approach had only been applied to study vegetation-free surfaces, primarily for robust difference estimates for geomorphological studies (Duffy et al., 2018b; James et al., 2017b). Nevertheless, the approach should also be applicable to studies of vegetation canopies (personal communication with Mike James), despite expected precisions being much lower.

4 Drone derived structure-from-motion photogrammetry point clouds for oil palm (*Elaeis guineensis*) canopy segmentation and height estimation

Chapter context:

Since the early work of Dandois and Ellis, (2010) who pioneered the application of drone-acquired SfM photogrammetry to the characterisation of vegetation canopies, drone-based SfM has found wide application over vegetated ecosystems worldwide for characterising the height and volume of grasses, crops, shrubs and trees (Cunliffe et al., 2016; Forsmoo et al., 2018; Holman et al., 2016; Wallace et al., 2016). However, due to increased reliance on black-box processing workflows there is often insufficient understanding of the accuracy and precision of drone-acquired SfM point clouds of vegetation, and the relationship between spatial/volumetric accuracy and data acquisition parameters. Whilst considerable work has been done on this in the field of geomorphology (James et al., 2017b; James and Robson, 2014), it is relatively unexplored in ecological domains. Resultantly there is little known about how these uncertainties translate into uncertainties in derived height metrics of individual plants. Further research in this area is needed in order to develop best practice methods in terms of drone data acquisition for vegetation height studies as well as for spatial and volumetric uncertainty assessment.

This chapter presents an experiment that investigates drone-based SfM photogrammetry methodologies for the segmentation and height estimation of individual plant crowns, the impact of different data acquisition plans, and trials a point cloud uncertainty estimation method over vegetation. The opportunity to focus this work on an oil palm plantation arose from a collaboration with Dr. Tim Hill from the University of Exeter and Dr. Khoon Lip Kho from the Malaysian Tropical Peat Research Institute. The study site was selected as the homogeneous plantation with minimal topographic variation lent itself to investigations of acquisition related uncertainties in derived height metrics. As this also represented the first application of drone SfM methodologies in such a

system, the results were of further interest for plantation management practices. A focus is also put on the use of SfM derived height metrics for the quantification of AGB as this is of particular interest for carbon budget calculations in the context of rainforest conversions to plantations.

This chapter has been published as: Fawcett, D., Azlan, B., Hill, T.C., Kho, L.K., Bennie, J., Anderson, K., 2019. Unmanned aerial vehicle (UAV) derived structure-from-motion photogrammetry point clouds for oil palm (*Elaeis guineensis*) canopy segmentation and height estimation. *Int. J. Remote Sens.* 40. doi:10.1080/01431161.2019.1591651

Research aims:

- 1) To demonstrate a workflow for the retrieval of single palm canopies from SfM point clouds.
- 2) To quantify the uncertainties introduced by steps in the SfM-based workflow as well as in the retrieved metrics.
- 3) To derive and assess top-frond-height (TFH) and stem height metrics from single palm SfM point clouds.

Abstract

The vast size of oil palm (*Elaeis guineensis*) plantations has led to lightweight drones being identified as cost effective tools to generate inventories for improved plantation management, with proximal aerial data capable of resolving single palm canopies at fine resolution. If acquired with sufficient overlap, aerial data from drones can be processed using SfM photogrammetry to yield volumetric point cloud representations of the scene. Point cloud-derived structural information on individual plants can benefit not only plantation management but is also of environmental research interest, given its potential to yield spatially contiguous quantifications of aboveground biomass. In this study the uncertainties in SfM derived point clouds are assessed, for plots containing palms of different ages (2, 7 and 10 years) on peat soil in a plantation located in Sarawak,

Malaysia. Further, the use of the derived CHMs for palm identification using local height maxima and the derivation of maximum canopy height and stem height from segmented single palm point clouds are demonstrated. Point cloud precisions were found to be in the decimetre range (mean of 0.27 m) for a 10 year old plantation plot. Local maximum identification performed best (98.2% mapping accuracy) for palms which were taller than surrounding undergrowth but whose fronds did not overlap significantly. Stem heights could be predicted from point cloud derived metrics with RMSEs of 0.27 m ($R^2= 0.63$) for 7 year old and 0.45 m ($R^2=0.69$) for 10 year old palms. It was also found that an acquisition designed to yield the minimal required overlap between images (60%) performed almost as well as higher overlap acquisitions (>75%) for palm identification and basic height metrics which is promising for operational implementations seeking to maximise coverage.

4.1 Introduction

The oil palm (*Elaeis guineensis* Jacq.) can yield considerably more oil per hectare than any other crop, which explains its large-scale expansion over the last century, to meet the global demand for food and biofuel (Corley and Tinker, 2016). As a result the conversion of forest ecosystems to oil palm plantations has been the topic of much international research and also controversy due to concerns regarding its impact on biodiversity, carbon storage and ecosystem services (Butler and Laurance, 2009; Carlson et al., 2012; Fitzherbert et al., 2008; Germer and Sauerborn, 2008; Koh and Wilcove, 2008).

The global demand for oil palm products means that plantations now cover large tracts of land in the tropics – for example, in Malaysia 58,100 km² is taken up by commercial oil palm plantations (as of December 2017, Malaysian Palm Oil Board (MPOB) statistics retrieved from <http://bepi.mpopb.gov.my>). Both at national and plantation block scale, remote sensing is a valuable tool both for stakeholders and researchers. To provide an example, remote sensing data offers a means by which plantation management can be performed in a more profitable and arguably more sustainable manner because plantation inventories can be generated to inform targeted fertiliser and pesticide application (Chong et al.,

2017). Beyond the commercial sector, remote sensing data have been applied on a state-wide scale to monitor and quantify the impact of the land-use change due to the establishment of new plantations. These analyses are predominantly based on satellite data, and various studies have utilised optical in addition to radar capabilities to differentiate oil palm from other land cover classes (Cheng et al., 2018; Koh et al., 2011; L. Li et al., 2015; Morel et al., 2011). The challenge with using readily available satellite data for oil palm science is the limited spatial and/or temporal resolution of such data. The demand for finer resolution data is motivated by the ability to resolve individual palm canopies, which allows for automated identification and parameter retrieval to inform on palm structure and status. These parameters are not only of interest for plantation management but are central to the estimation of plantation carbon stocks, e.g. through the use of allometric equations (Corley and Tinker, 2016), which is critical if the carbon implications of forest conversion to oil palm are to be quantified (Morel et al., 2011). Furthermore, patterns relating to local soil nutrient deficiency or disease could also be better identified (Shafri and Hamdan, 2009).

For inventory generation, fine spatial resolution satellite data (e.g. WoldView 4 at 0.31 m resolution) provides high spatial resolution while retaining large imagery extent and has been successfully used for palm identification (Li et al., 2016; Srestasathiern and Rakwatin, 2014). For practical considerations, fine spatial resolution satellite data have known limitations, for example – they are financially costly and for countries with frequent cloud cover, acquiring a cloud-free acquisition at the desired time can be challenging. Improved accessibility and ease of use has recently led to lightweight drones being identified as a useful tool in oil palm plantation management, with major commercial oil palm companies establishing dedicated drone-teams for the routine acquisition of aerial imagery.

Currently the primary application of drone acquired data in oil palm management is the generation of orthomosaics for inventory purposes (Rokhmana, 2015). To generate inventories, manual counting based on spatial data products is still considered the most accurate and cost-effective method, however there are promising first demonstrations of machine learning techniques on both fine spatial resolution satellite and drone image data (Li et al., 2016; Malek et al., 2014) as well as software packages for the operational implementation of object-based segmentation (eCognition, Trimble, California, USA) for palm identification.

In these workflows, the third spatial dimension (i.e. height) has to date been largely disregarded, however, it opens up many possibilities at low opportunity cost. The acquisition of overlapping images from drone platforms can be used both to generate fine spatial resolution orthomosaics, and point clouds representing the height structure of the scene. Coupled with precise georeferencing information, resultant point clouds can be used to spatially separate objects and determine their spatial and volumetric dimensions. Such methods are now being used extensively to derive canopy metrics of individual vegetation canopies of varying sizes and structure (Cunliffe et al., 2016; Puliti et al., 2015; Zarco-Tejada et al., 2014), so it is a natural step to consider the utility of such approaches for oil palm surveys. Doing so would deliver new understanding of the spatial characteristics of oil palm plantations, which would be useful for carbon assessment. Currently such aspects of oil palm plantations lack sufficient data from which to quantify the environmental effects of tropical forest conversion (Kho and Jepsen, 2015). Information on palm height and its distribution is desirable as it can be an indicator of palm age and growing conditions. While some variations between individuals may be attributed to age difference due to re-planting, more spatially contiguous variations can be the result of unequal fertiliser application or other variation of soil nutrient availability. In previous work, drone based photogrammetry derived top-of-canopy height metrics were found to be comparable with LiDAR derived heights (Thiel and Schmullius, 2017; Wallace et al., 2016), while being much more affordable (relying only on consumer grade sensors and platforms) and easy to deploy (so long as the aircraft and payload are lighter than the low weight categories defined by civil aviation classifications (Duffy et al., 2017)). First efforts in applying the drone-based SfM methodology to palm plantations have demonstrated its potential for palm identification and retrieval of structural parameters (Kattenborn et al., 2014), however further investigation into uncertainties within generated products as well as the influence of acquisition schemes which allow to cover greater area at the cost of data quality is required for the operational implementation of these workflows.

Presented in this study is the first investigation of drone SfM point clouds for oil palm plantation physical assessment. This application of drone data extends beyond identification and counting of individual palms and presents a workflow

for the segmentation of individual palm point clouds to explore their application for retrieving height-related structural parameters, as well as assess uncertainties. Specific aims of this study are:

- a) To demonstrate a workflow for the retrieval of single palm canopies from SfM point clouds.
- b) To quantify the uncertainties introduced by steps in the SfM-based workflow as well as in the retrieved metrics.
- c) To derive and assess top-frond-height (TFH) and stem height metrics from single palm SfM point clouds.

Aim b) is key to understanding the potential and limitations of our methodology for oil palm science. This is especially important when considering the possible further usage of the retrieved structural parameters (aim c)) to inform larger scale models, as has been successfully demonstrated for forestry (Puliti et al., 2017a), to quantify error propagation. Aim c) provides an important step towards deriving per-palm AGB (Corley and Tinker, 2016; Thenkabail et al., 2004).

4.2 Materials and Methods

4.2.1 Study site

The study sites were located in the state of Sarawak, Malaysian Borneo, on the Sarawak Oil Palms Berhad plantations of Sabaju ($3^{\circ}09'40.1"N\ 113^{\circ}25'09.1"E$) and Sebungan ($3^{\circ}09'58.1"N\ 113^{\circ}21'20.2"E$). The majority of the plantation area was planted on tropical peat with smaller areas on clay dominated mineral soil. Three peat soil plantation sub-plots of 2, 7 and 10 years of age and covering approx. 4, 6 and 6 ha respectively were selected for this study. Plot sizes were chosen based on the maximal area which could be safely covered with one flight battery and fulfilling the desired image acquisition parameters (see section 4.2.2.2). The locations of the subsets are depicted in Figure 4-1. The peat soil plantations possess only slightly varying topography. The 2 year old palms consisted mainly of fronds with the above-ground stems being negligible. Besides the young palms, the 2 year old plot also contained stacking rows of woody material which were overgrown by vegetation and were higher than the top frond heights of the palms. The 7 year old plot contained significant undergrowth and the same heaped rows of timber between every other palm row, though here the palms had grown higher than this topographic variation. In the 10 year old plot there was significantly less undergrowth, likely due to light limitation as the fronds of neighbouring palms begin to overlap, as well as a very high water table due to a difference in local topography. Undergrowth here occurred mainly along drainage channels dug between every other palm row.

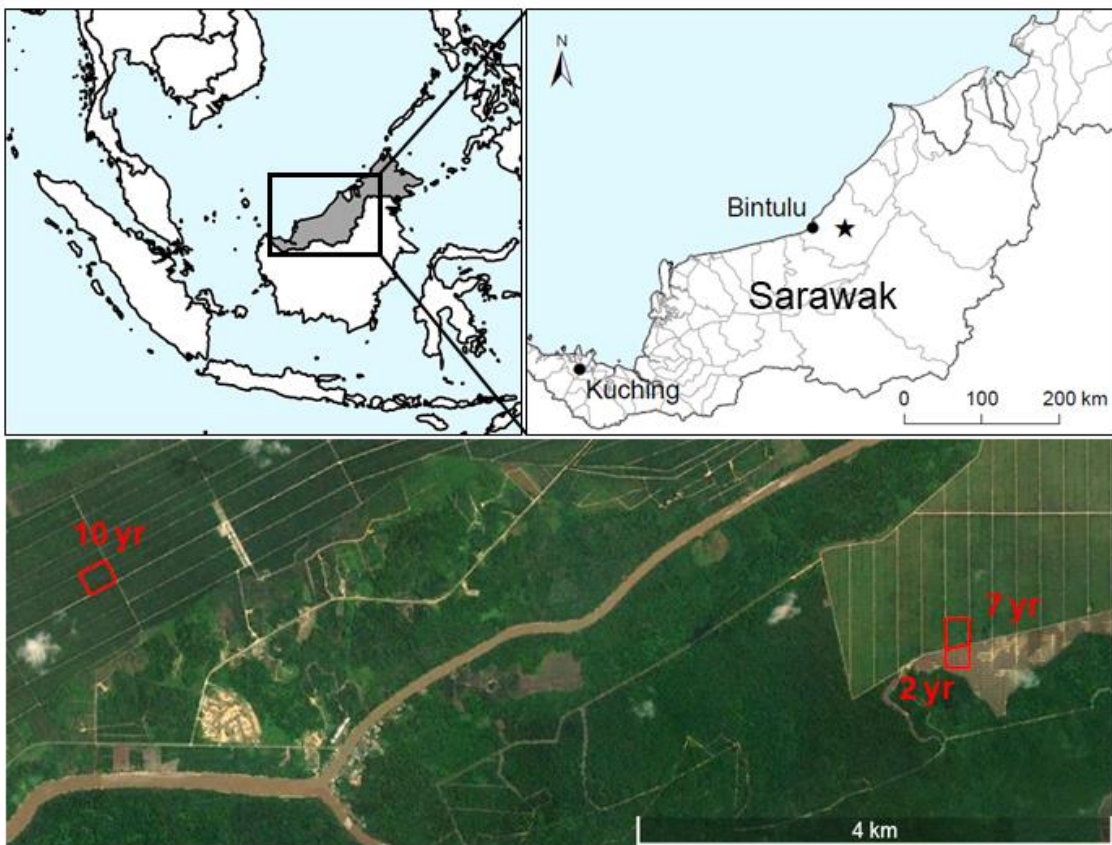


Figure 4-1: Top: The state of Sarawak in Malaysian Borneo with a star marking the location of the studied plantation (shapefiles from www.diva-gis.org, last accessed 01.11.2020). Bottom: Satellite imagery with the location, extent and age in years of the studied plots (Google Earth).

4.2.2 Data acquisition

4.2.2.1 Field sampling

Measurements in the field were conducted on a per-palm basis. Within the boundaries of existing 1 ha carbon sampling plots, palms were sampled in a grid pattern in accordance with the subdivided squares of the plot. Outside of carbon plots, palms were sampled following a random sampling scheme. 33, 22 and 37 palms were selected for measurement in the 2, 7 and 10 year old plots respectively, with the number of samples varying due to sampling time constraints and accessibility of the plots. TFH as a metric representing canopy height was measured as the distance between the apex of the highest frond and ground level, to provide a validation for SfM photogrammetry derived heights. The stem height was also measured as the distance between the petiole base of the lowest intact

frond and ground level. Due to the size of the older palms, both heights were consistently measured using a laser rangefinder in all plots. These systems typically possess decimetre accuracy.

4.2.2.2 *Drone flights and GPS data*

The drone used for this study was a 3DR Solo quadcopter containing a pixhawk 2.0 flight controller. Including payloads it weighs under 2 kg and is capable of approximately 15 minutes flying time. The system was selected due to its ease of use and flexibility. Flights were programmed in the ArduPilot Mission Planner software by drawing a polygon per plot to be reused for all flights. Flights were conducted at an altitude of 100 m and a speed of 5 m/s, with the exception of the 2 year old plot which was flown at 70 m to better resolve the significantly smaller palms. The minimum frontal and side overlap was defined as 75%. For the 10 year old plot, a replicate was flown using identical flight parameters. Drone flights were conducted close to solar noon for all acquisitions when lighting conditions are optimal for later photogrammetric reconstruction (Dandois et al., 2015), and wind speeds at ground level were below 4.5 m/s. Flight details are summarised in Table 4-1.

The sensor mounted on the drone was a consumer-grade RGB camera (Ricoh GRII). The ground sampling distance (GSD) at 70 and 100 m altitude was 1.19 and 1.71 cm respectively. The camera was triggered by intervalometer every 2 seconds during the flight – chosen since the flight planning software suggested that this would ensure the desired 75% front and side overlap (with higher effective frontal overlap of 82%), close to the optimal overlap of 80% recommended by Dandois et al., (2015) for vegetation SfM photogrammetry workflows. The focus was set to infinity, white balance to automatic and exposure time (1/1250 s – 1/1600 s) as well as aperture (f2.8-f3.2) and ISO (100-200) were varied based on the illumination conditions and site characteristics (direct/diffuse and amount of shadow) but kept constant throughout each flight, following recommendations of previous studies (Cunliffe et al., 2016; O'Connor et al., 2017).

For georeferencing, a total of 10-15 GCPs were surveyed per site. These allow SfM generated DSMs to be adequately constrained (Tonkin and Midgley, 2016)

and can be used to validate georeferencing accuracies utilising unused GCPs as check-points. GCP distribution followed recommendations from previous work on drone SfM survey accuracies (James et al., 2017a) by ensuring placements around the boundaries of the region of interest as well as close to the centre of each plot.

Additionally, >10 height validation points were measured for each plot. GCPs and validation points were measured using a Trimble Geo 7x GNSS system coupled with a Zephyr Model 2 antenna. GPS data was post-processed using RINEX data acquired from the Department of Survey and Mapping Malaysia (JUPEM) to yield 3 cm horizontal and 5 cm vertical precision.

A replicate of the 10 year old plot using the same flight parameters was flown as a traditional way of assessing the consistency of the photogrammetric reconstruction (Dandois et al., 2017).

In addition to the main data acquisition described above, an additional RGB image dataset covering the entirety of the studied 10 year old plantation block was acquired by the Mapping Unit of Sarawak Oil Palms Berhad. The system used was a DJI Phantom 4 with integrated camera, flying at 150 m and 11 m/s resulting in a GSD of 4.43 cm/pixel and aiming at acquiring images with 60% frontal and side overlap. This acquisition plan allowed covering one entire plantation block using a single DJI flight battery.

Table 4-1: List of drone flights used in this study, indicating the flight parameters, the palm age plot site (including the replicate for the 10 year old plot) and date of acquisition.

System	Sensor	Altitude	Speed	Overlap	Site	Date
3DR Solo	Ricoh GR II	70 m AGL	5 m/s	>75%	2 yr	30.01.2018
3DR Solo	Ricoh GR II	100 m AGL	5 m/s	>75%	7 yr	09.02.2018
3DR Solo	Ricoh GR II	100 m AGL	5 m/s	>75%	10 yr	02.02.2018
3DR Solo	Ricoh GR II	100 m AGL	5 m/s	>75%	10 yr (repl.)	02.02.2018
DJI Phantom 4	Integrated camera	150 m AGL	11 m/s	60%	10 yr	05.02.2018

4.2.3 Photogrammetric processing

The photogrammetric processing of drone-acquired images was performed in Agisoft Photoscan Professional V1.4.2 (St. Petersburg, Russia). There are a number of software options available for photogrammetric processing and Photoscan was selected here due to its successful use in similar applications such as forest inventories (Dandois and Ellis, 2013; Puliti et al., 2015), and the ability to use previously developed Python scripts (James et al., 2017b). Palms differ considerably from coniferous or broadleaf trees, however no inter-comparison of software options and algorithms exists for this canopy type. Images per flight and plot were input into the software, upon which tie-points within images are identified and used for image matching (algorithms used are proprietary, but a common method is the SIFT algorithm (Lowe, 2004)). An automatic aerial triangulation followed by a bundle block adjustment is performed, reconstructing scene geometry while accounting for camera orientation and distortion. The resulting sparse point cloud representing the tie-points in 3D space is used to generate a rough mesh of the scene. After this initial processing, GCP coordinates are imported and their position manually identified within the images. To evaluate the geometric accuracy of the resulting model, $\approx 25\%$ of measured GCPs per site were omitted from the photogrammetric processing and used as independent check points. The initial processing was re-run on the highest setting (with key point limit: 80'000, tie point limit: 8000), followed by depth-map and dense point cloud generation on high settings. Depth filtering was disabled as even mild depth-filtering appeared to remove points of vertical palm fronds. A full

list of settings to reproduce the workflow can be found in appendix A1 Supplementary information for chapter 4.

While geometric uncertainties of the resulting model are reported by the software, these only represent errors in relation to the measured GCPs and check points at ground level, which are clearly identifiable within the image. At the top of the canopy, errors can be expected to be considerably higher, as the Z dimension cannot be adequately constrained by the measured GCPs and values are more heavily dependent on the non-reproducible tie point identification. To quantify the precision of the photogrammetric processing as outlined in aim b), which is impacted by varying camera geometry and GCP uncertainties, we utilised a Monte Carlo method developed by James et al. (2017b) to derive point precisions representing the expected one standard deviation in X, Y and Z directions by running many simulations of the sparse point cloud generation including GCP information while randomly varying parameters within reported precision thresholds. Precision estimation is performed based on the sparse point cloud as the dense matching does not optimise the image network and, while it can introduce additional smaller errors, does therefore not affect the underlying precision (James et al., 2017b). This method was primarily developed for the assessment of SfM based surveys of non-vegetated landforms but the precision estimates it generates can also prove useful for vegetation focused studies. 1000 simulations proved sufficient, assessed by the difference between the Monte Carlo means and the initial error free values. Per-point precision estimates in each dimension were generated based on the simulations, using the ‘sfm-georef’ software (James and Robson, 2012).

4.2.4 *Point cloud processing and parameter retrieval*

The processing workflow for oil palm segmentation and derivation of TFH and stem height is demonstrated in Figure 4-2. After generating the dense point cloud representing the volumetric structure of the scene, a statistical outlier filtering was performed (CloudCompare, V2.9.1), removing points far above or below the scene which are considered as noise, likely attributed to movements of palm fronds between images. As most scenes contained water, either as standing

water or in drainage channels, this caused errors in the photogrammetric processing due to reflections and larger negative outlying point clusters were found, an effect described by Duffy et al., (2017). The majority of these outliers were removed by eliminating points below a feasible threshold, informed by GCP heights. A minimal amount of manual clipping of the point cloud in CloudCompare (V2.9.1) was therefore required.

Due to the lack of detailed topographical data of the sites, the DTM had to be derived from the SfM point cloud. Ground points in each plot were classified by excluding the vegetation through a morphological filtering procedure, originally developed for airborne laser scanning (K. Zhang et al., 2003) and implemented in the R lidR package (Roussel and Auty, 2018). This method has previously been applied for SfM-based DTM generation (Dandois and Ellis, 2013) and was selected as it provided more control over the filtering process and appeared to perform better for sparse ground points as opposed to PhotoScan's own implementation of ground classification which has been used for DTM generation in more recent SfM based studies where more ground information was available (e.g. Cunliffe et al., 2016). It did however require the point cloud to be subsampled with a 0.1 m distance constraint between points for efficient processing. The parameters for morphological filtering had to be adjusted for each plot due to the varying height and density of palm crowns. The classified ground points were interpolated using k-nearest-neighbour inverse distance weighting. The noise filtered original point clouds were normalised using the derived DTM, yielding height above ground for the remaining vegetation points and CHM. For palm identification, the CHM was first smoothed using a mean filter after which local-maximum filtering was applied with a window size informed by the known planting distance between palms (approx. 9 m, an established planting pattern for oil palm (Chong et al., 2017)). Individual palms were then segmented from the point cloud using a crown delineation method by Silva et al., (2016) and adjusted by Roussel and Auty, (2018), using the identified palm points as centroids and CHM as input. This particular delineation method was selected due to its suitability for the simple circular footprint of oil palm crowns and as the impact of overlapping fronds can be reduced by constraining the buffer radius used. Other methods based on watershed analysis or region-growing (Dalponte and Coomes, 2016) proved to have issues where overlap occurred.

The TFH values for each segmented palm were retrieved by selecting the maximum point within the cloud, the sensitivity to erroneous outliers reduced by the previous statistical outlier filtering. Derived TFH was assessed against field measured TFH for measured palms. To test the consistency of TFH for two independent builds, TFH was also derived from a replicate dataset over the 10 year old plot and the values compared for the same palms.

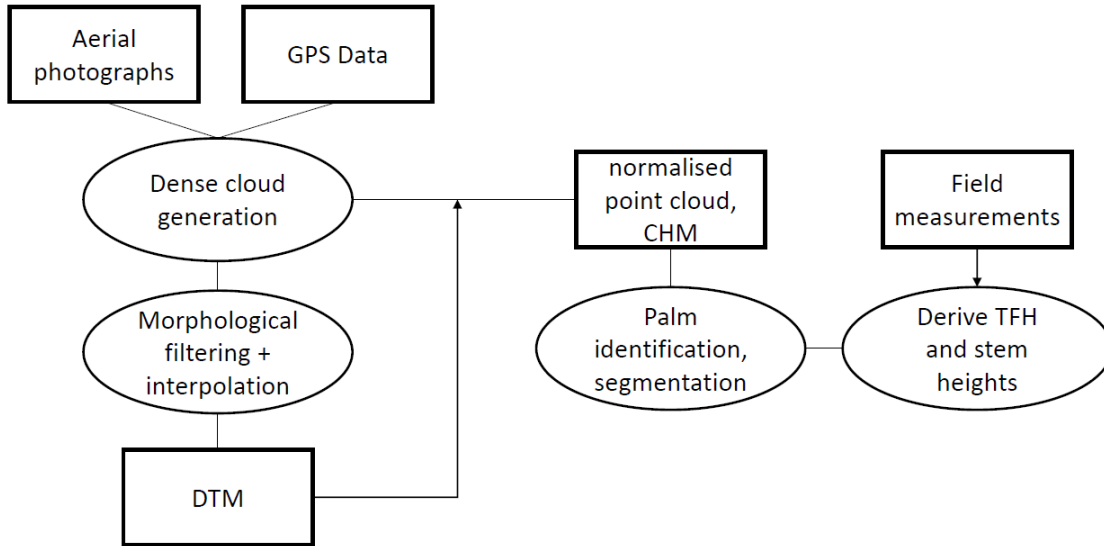


Figure 4-2: Processing workflow for deriving per-palm height metrics from drone data.

Using linear regression, the correlations of different height percentiles (30 to 90% in 10% steps), and the mean and maximum point height with field measured stem height were assessed for the samples of the 7 and 10 year old plantation. Due to a limited number of samples, prediction accuracy was assessed using LOOCV as used in similar studies (Li et al., 2016). Two separate models depending on plot age were assessed as the relationship between point cloud metrics and stem heights can be expected to differ slightly between palms of different age classes. This does not avoid the issue of younger, re-planted palms within the same plots. The relationships with highest R^2 were then applied to all identified palm point clouds to derive stem heights.

4.3 Results

4.3.1 Photogrammetric dense clouds

Drone image data averaged around 350 images per plot and acquisition, from which dense point clouds were generated for each plot through photogrammetric processing. For the 10 year old plot, a replicate dataset using the same acquisition parameters was generated, as well as a coarser resolution sparser dataset for the entire plantation block.

Subsets of the point clouds from the three different aged plots are displayed in Figure 4-3. Initial visual inspections of the generated dense point clouds per plot showed reconstructions of individual palm fronds. Noise increased for higher, vertical fronds. The point density decreased towards the apical stem as fronds overlapped. No information on the trunk was captured as it was entirely obscured by fronds in all images. The 10 year old plot contained fewer points from the ground and bottom fronds due to the denseness of the canopies.

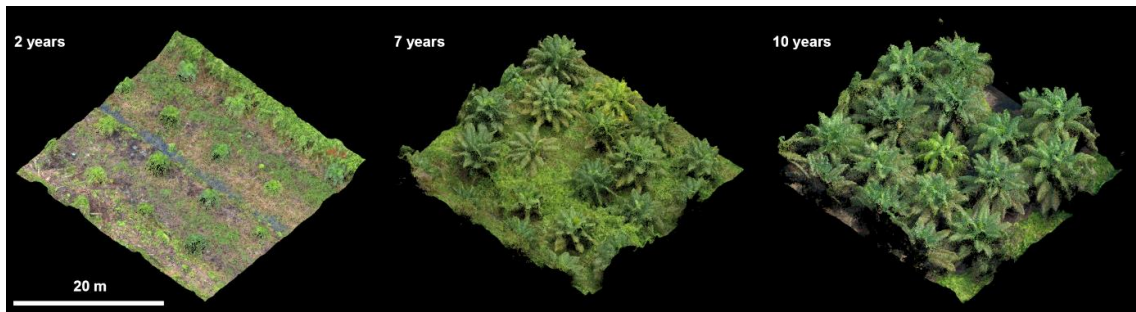


Figure 4-3: RGB dense point cloud subsets (33 x 33 m) of the 2, 7 and 10 year old plantation datasets.

The geometric accuracies of the scene reconstructions, assessed by check points which were not used for the photogrammetric processing ($\approx 25\%$ of total GCPs per site), were high with mean horizontal errors (xy) of 2.29 cm and mean vertical errors (z) of 3.4 cm.

The low overlap dataset showed significantly lower point density (a 1 ha square extracted from the dense clouds contained 10.26 Mio points for the high overlap

and 1.69 Mio points for low overlap) but still appeared to represent finer details and individual fronds of single palms. At the higher altitude and speed of this flight, surface points were imaged 8 times and the ground resolution was 3.94 cm per pixel. The average of 8 images per ground point indicated that the overlap was slightly below the targeted 60% recommended for photogrammetric surveys (Dandois et al., 2015). This may have been due to acquisition conditions on the day of the flight, or imperfect flight planning.

Geometric accuracies reported by check points for the full coverage flight were lower than the subset flights with horizontal error (xy) of 12.9 cm and vertical error (z) of 39.1 cm. Point precisions for the varying acquisitions of the 10 year old plot were generated as described above. For the generation of maps from the sparse point cloud precision estimates, values were interpolated for the dense point locations using nearest-neighbour inverse distance weighting. Due to the reduced overlap for the full coverage flight, there were considerably fewer tie points within the sparse point cloud. The resulting map therefore included a higher amount of interpolation and the precision estimates were less resolved spatially.

The mean precisions did not exhibit large differences between low and high overlap acquisitions. Horizontal precisions in X and Y were very slightly larger for the higher overlap acquisition, while vertical precisions (Z) were slightly lower on average (Table 4-2). When displaying point precisions spatially (Figure 4-4), it is apparent that precisions were higher for the flat ground surface on which GCPs were placed as opposed to the vegetation canopy. The acquisition with lower overlap displayed larger patches of lower precision, due to the sparser tie points. Additionally, ground point precisions were lower overall with some stretches of the road between plots showing discontinuities in precisions. Such patches of low precision may influence the reliability of the derived DTM. For the higher overlap acquisition, precisions were higher for resolved ground points. Vertical precisions appeared lower but more uniform for the vegetation canopy, with some edge effects at the north-eastern border.

Table 4-2: Parameters for the two different acquisitions over the 10 year old plot along with mean precision estimates in X, Y and Z directions.

Acquisition overlap	GSD	Mean X precision	Mean Y precision	Mean Z precision
<60%	4.43 cm/pixel	77.35 mm	89.86 mm	247.90 mm
>75%	1.71 cm/pixel	68.34 mm	80.29 mm	267.39 mm

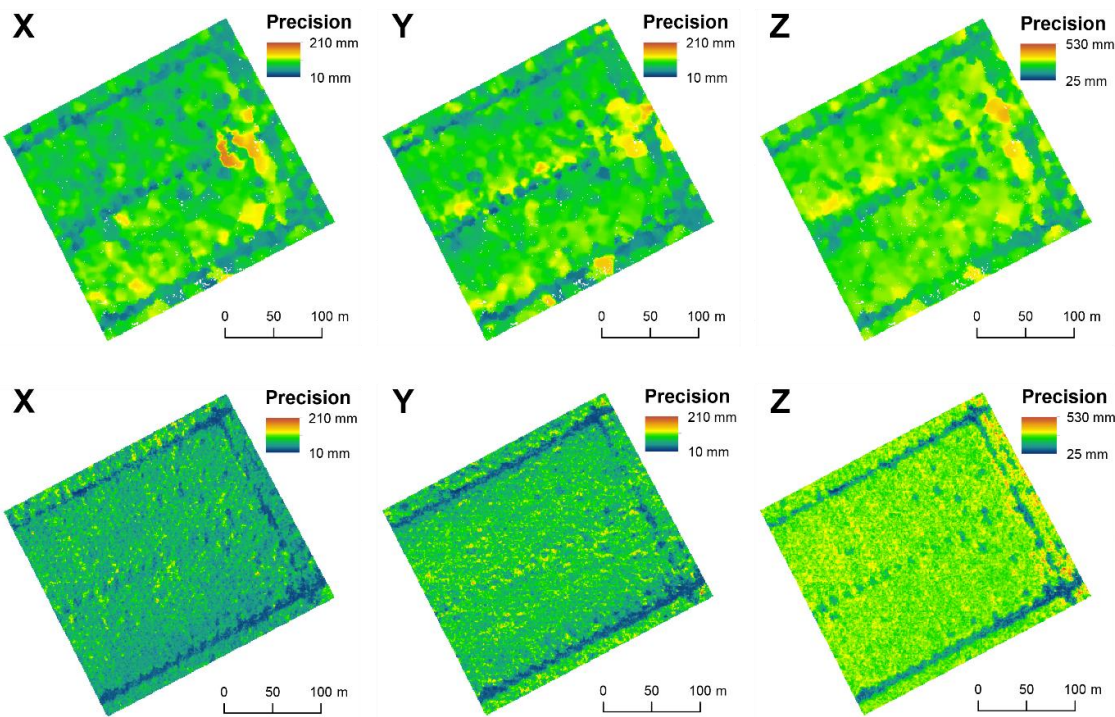


Figure 4-4: Maps of interpolated point precisions in X, Y and Z direction for the 10 year old palm plot. Top row: Acquisition with 4.43 cm/pixel GSD and 60% nominal overlap. Bottom row: Acquisition with 1.71 cm/pixel GSD and 75% nominal overlap.

4.3.2 Digital terrain models

After filtering out non-ground points the remaining points were interpolated to derive a DTM per site. The DTM accuracy was assessed using height validation points measured between palms in the field with reported mean measurement horizontal precisions of 3.23 cm and vertical precisions of 5.74 cm. Mean vertical absolute errors assessed for height validation points were 9.1 cm for the 2 year old, 12.4 cm for the 7 year old and 12.12 cm for the 10 year old plot. The full

coverage flight resulted in errors of 31.62 cm. The increase in errors from the 2 year old to the older plots was due to less visible ground within the imagery and thus non-uniformly distributed ground points within the dense cloud. For the 2 and 7 year old plots, DTM heights were generally over-estimated Figure 4-5.

This overestimation is assumed to be related to undergrowth which obscured the ground beneath. While there was very little undergrowth present in the 10 year old plot, the reason for the underestimation of ground height is unclear but likely due to interpolation related uncertainties as well as the larger amount of drainage channels in this plot.

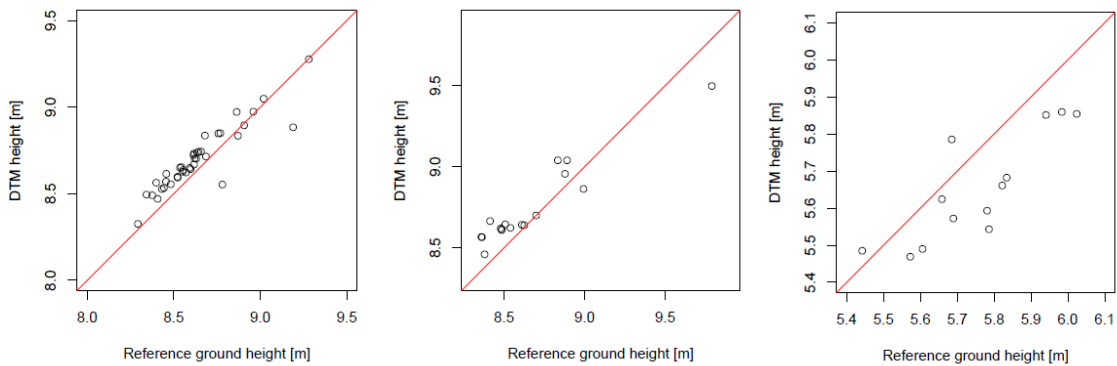


Figure 4-5: Interpolated DTM heights above mean sea-level versus GPS measured reference ground heights. Left: 2 year old plot, Middle: 7 year old plot, Right: 10 year old plot.

4.3.3 Palm identification

The local maximum palm identification algorithm performed relatively well for the 7 and 10 year old palm plots (containing 776 and 654 palms total), with a mapping accuracy (MA: correctly identified/(true total + commissions)) of 98.2% and 94.9% respectively. The identified palm locations for the 10 year old plot are illustrated in Figure 4-6, along with a subset showing an example of omitted palms. For the 2 year old plot, this method caused a large amount of omission and commission errors in the vicinity of the overgrown stacks of woody material between the palm rows, as the vegetation is higher than the palm canopies. Neglecting these stacks and immediately adjacent palms, the method showed a MA of 80.4% for 238 palms total. The MA for the same region of the 10 year old plot using data from the lower overlap flight was 94.0%.

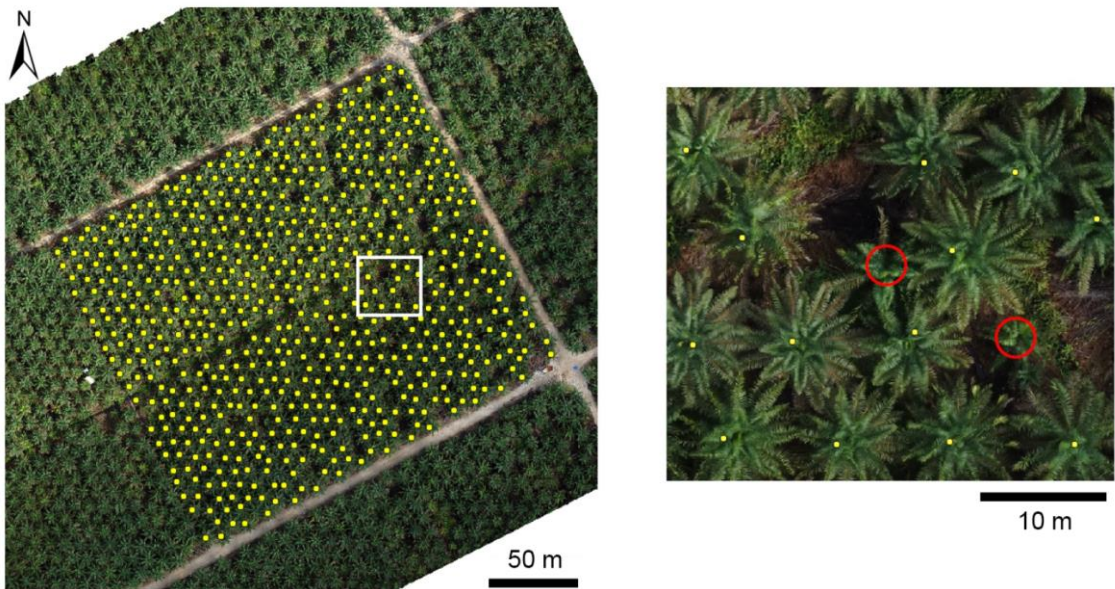


Figure 4-6: Left: Resulting palm locations (yellow points) for the 10 year old plot and subset location (white rectangle), right: Subset illustrating omitted palms (red circles).

4.3.4 Height metrics

Maximum values of the individual palm point clouds were assessed against the TFH measured in the field. Results showed relatively large deviations between TFH measurements and maximum point cloud values with mean absolute errors of 0.383 m for the 2 year, 0.968 m for the 7 year and 1.246 m for the 10 year old plot, which represent 18.9%, 13.7% and 11.7% of the mean measured heights respectively (Figure 4-7). The full coverage flight showed lower mean absolute errors of 1.099 m for TFH of the 10 year old plot.

When comparing the maximum values between replicates of the 10 year old plot for the field measured palms (Figure 4-8), this resulted in a mean absolute error of 0.199 m. Deviations between the values appeared independent of field-measured height. One obvious outlier was visible, caused by overlap resulting in a different segmentation of the palm. The magnitude of this deviation between replicates is consistent with values generated by the Monte Carlo point precision analysis on the sparse point cloud (Table 4-2).

To establish the optimal metrics for deriving stem height from the point cloud it was necessary to establish separate linear relationships between basic point cloud height metrics of the segmented palm point clouds and the structural metric

of stem height using LOOCV for different age stands (Table 4-3). For the 2 year old plot, the stem height above ground was negligible. The strongest relationships (according to R^2 values) with stem heights of the 7 year old plot was shown by the maximum value ($R^2 = 0.63$; Table 4-3), while for the 10 year old plot the 80th percentile of elevations performed better ($R^2 = 0.69$; Table 4-3). The MAEs represented 12.2% and 30.9% of mean stem heights respectively. Results for the low overlap acquisition showed overall lower R^2 values compared to the high overlap dataset, but was consistent in showing the best relationship for the 80th elevation percentile ($R^2 = 0.59$).

Using these linear models to derive stem heights for the 7 and 10 year old plots yielded the distributions displayed as histograms in Figure 4-9. For the 7 year old plot, negative values for predicted stem heights were set to 0 which resulted in high counts for this bin.

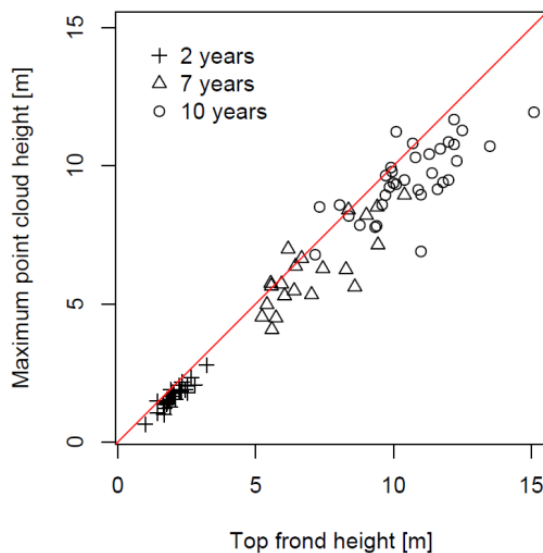


Figure 4-7: Maximum point cloud heights plotted against field measured TFHs for 2 year, 7 year and 10 year old palms.

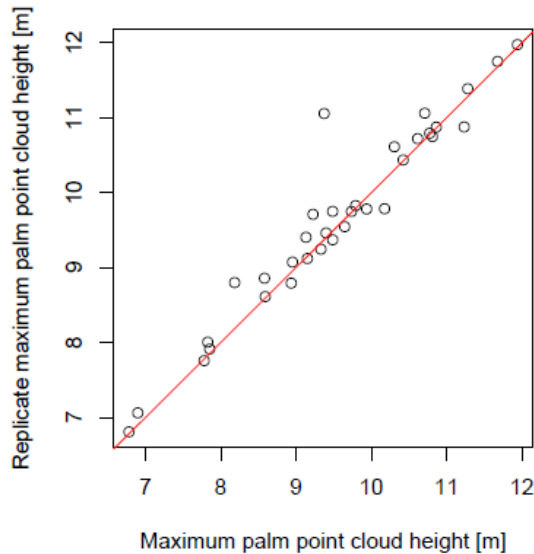


Figure 4-8: Maximum point cloud height compared for the same palms between replicates of the 10 year old plot.

Table 4-3: Linear stem height model strength and errors for the 30th -90th point cloud height percentiles as well as the maximum and mean values. Reported for the 7 year old plot and the 10 year old plot with high and low quality acquisitions. The highlighted rows show the models with the highest R² values which are used subsequently for stem height estimation.

	7 yr plot (high), n = 22			10 yr plot (high), n = 37			10 yr plot (low), n = 37		
	R ²	RMSE [m]	MAE [m]	R ²	RMSE [m]	MAE [m]	R ²	RMSE [m]	MAE [m]
30%	0.56	0.30	0.24	0.64	0.48	0.40	0.52	0.50	0.42
40%	0.62	0.28	0.21	0.64	0.48	0.40	0.54	0.49	0.41
50%	0.61	0.28	0.21	0.64	0.48	0.39	0.55	0.48	0.39
60%	0.60	0.29	0.21	0.66	0.47	0.38	0.55	0.49	0.38
70%	0.58	0.29	0.21	0.68	0.45	0.36	0.54	0.49	0.38
80%	0.58	0.29	0.22	0.69	0.45	0.34	0.59	0.46	0.37
90%	0.57	0.30	0.22	0.68	0.45	0.34	0.57	0.47	0.38
Max	0.63	0.27	0.22	0.52	0.55	0.39	0.41	0.56	0.45
Mean	0.61	0.28	0.21	0.48	0.58	0.43	0.54	0.49	0.39

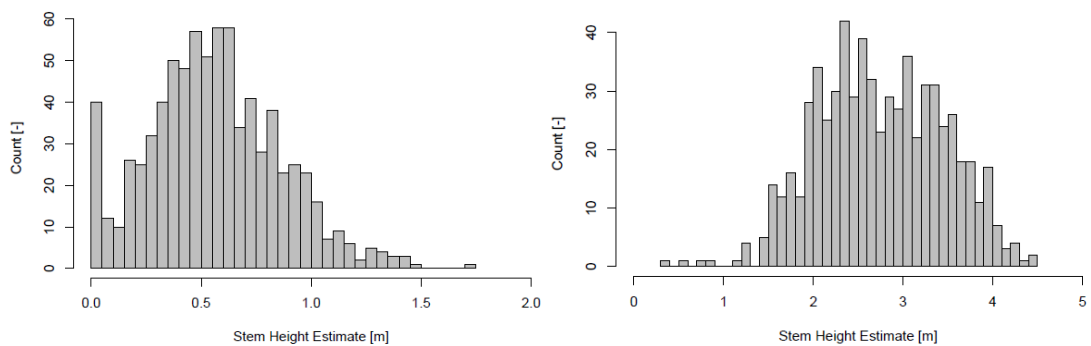


Figure 4-9: Histograms of estimated stem heights for the 7 year old plot (left) and 10 year old plot (right).

4.4 Discussion

This study presented a processing workflow for deriving per-palm height metrics from drone imagery while quantifying method-inherent uncertainties introduced at different stages. As demonstrated, it is possible to successfully segment single palms from SfM based datasets and derive TFH and stem height. Subsequent sections of this discussion will address precision estimates and accuracies of the generated results, and their implications for the application of this method in management and research of oil palm plantations.

4.4.1 Uncertainties within resulting SfM point clouds

Uncertainties resulting from SfM processing were estimated using a method which has not previously been applied to a vegetation focused study. If correctly parameterised, this method may reduce the need for time consuming replicates from independent acquisitions which are commonly advocated in SfM based studies (Dandois et al., 2017, 2015). Overall, the precision maps provide a better spatial indication of the SfM method's inherent uncertainties than relying on values reported by GCPs and check points as a measure of reconstruction quality, which due to the limited number of surveyed GCPs and the lack of GCPs at canopy level do not adequately represent uncertainties across the scene (James

et al., 2017b). Sparse point precisions at ground level were higher (<10 cm) than for the vegetation canopy (20-50 cm). The contrast between precisions of the lower (60%) versus higher (>75%) overlap acquisition highlighted that ground information resulting from higher overlap flights appears more reliable, an observation which has previously been made for forested areas (Dandois et al., 2015). These uncertainties were confirmed at the dense point cloud level by comparing per palm maximum values from a replicate dataset.

4.4.2 Quality of derived DTM

Retrieving accurate ground elevations from SfM can introduce considerable uncertainties but doing so is a necessity when lacking LiDAR coverage of the studied area, for point cloud normalisation and CHM determination. We found that undergrowth caused an overestimation of identified ground points, while dense canopies lead to very limited ground information. Interpolating between sparse ground points as was required in this study for the 10 year old plantation was only feasible for regions of very slightly varying topography as is the case for peat-soil plantations. Although the MAE of the measured ground points did not exceed 20 cm for all the studied areas, it can be expected that uncertainties in the DTM remain a major limiting factor in the quality of resulting canopy height metrics. An increase in DTM errors resulting from fewer ground points was observed for the lower overlap (60%) acquisition, suggesting that higher overlap is recommended if CHMs must be derived from SfM point clouds alone.

4.4.3 CHM-based palm identification

Local maxima based palm identification informed by planting distance performed very well (98.2% MA) for palms of intermediate ages (here 7 years), when they were taller than surrounding vegetation and other topographic variations (e.g. mounds of overgrown timber) and when their fronds did not yet overlap considerably. This mapping accuracy is identical to that reported by Kattenborn et al., (2014) for dense palm stands without overlap. The performance of height based identification of young palms (2 years) was heavily dependent on the

plantation structure and undergrowth. Excluding areas with large local topographic variations it performed moderately well with 80.4% mapping accuracy, influenced predominantly by false positives from tall undergrowth. In the plot studied here, the application of the method to the entire plot was complicated by the overgrown stacks of organic material which resulted in false positives and sometimes obscured adjacent young palms. Local maximum methods should therefore not be applied directly to plantation blocks showing such topographic variations. For older plantations (10 years), the resulting MA of 94.9% was due to issues with overlap and smaller palms which were surrounded by taller ones not being identified as local maxima. This could be partly addressed by decreasing the window size of the local maximum filtering, which would however introduce more false positives.

4.4.4 Assessing maximum point cloud height against TFH

Comparing the maximum point cloud height with field-measured TFH showed a high uncertainty but also an apparent negative bias for the drone-derived metric (Figure 4-7). The large deviations between field measurements and point cloud metrics are likely due to uncertainties related to the field measurements which include the manual identification of the highest frond, selection of its highest part and a possible horizontal discrepancy between the reference point on the ground and the highest measured frond point. Their suitability for the assessment of the SfM result is therefore questionable. The difficulty of validating SfM-derived height metrics for higher vegetation such as trees has been identified in previous studies (Lisein et al., 2013), as they can only be compared to field measurements or LiDAR data which must be concurrent and themselves possess considerable uncertainty or coarser spatial resolution. Here this issue was not solved but addressed by the generation of tie-point precision estimates which provide further insight into the method-inherent uncertainties, which we showed to be low for ground points and higher at canopy level, averaging around 30 cm as visible in Figure 4-4.

Expected to be independent of the above uncertainties, the negative bias apparent in the results (Figure 4-7) can be partially explained by the effect of

undergrowth on the interpolated DTM surface. For the 10 year old palm plot this is however not consistent with height validation measurements where the DTM values were below the reference. Further bias may originate from an inherent smoothing effect of the dense matching process, observed in previous studies where SfM point clouds were compared to LiDAR reference data (Lisein et al., 2013), but this is contradictory to the fact that the lower resolution and overlap acquisition produced maximum height values closer to field measured TFH.

Overall, the errors resulting for the TFH (or top-of-canopy height) estimation were very close to those reported by other studies applying SfM methodologies to vegetated systems of similar height range (Panagiotidis et al., 2017; Wallace et al., 2016). Better results can be achieved when employing a LiDAR-derived DTM (Lisein et al., 2013; Puliti et al., 2015), though this represents a considerable operational constraint. The inclusion of convergent imagery at non-nadir angles (e.g. 45°) has also been advocated as besides strengthening the image network for reconstruction it can result in more ground points being visible to aid in DTM generation (Cunliffe et al., 2016). The latter aspect may be negligible for dense canopy cover but could yield better results for younger palms. The impact on point precisions and DTM error would benefit from further study, especially in relation to the cost of additional acquisitions and processing time.

4.4.5 Point cloud height metric based stem height estimation

Assessing the relationship between different point cloud height metrics and field measured stem height did not show very large differences between the metrics used. Nevertheless, the metric with the strongest relationship differed between the two different aged plots analysed, which can likely be attributed to different point cloud characteristics as a result of canopy density. For 7 year old palms where little to no overlap occurs, a greater portion of the fronds were resolved in the point cloud while for the 10 year old palms the lower fronds were obscured. When applying the resulting models to generate estimates of stem height distributions throughout the plots, it is striking that there are relatively large value ranges for plots of the same age, considerably larger than the resulting MAEs. For the 7 year old plot, there are however a considerable number of negative

values, set to zero for the analysis. The two primary causes for this were local DTM errors caused by undergrowth as well as the fact that younger, later planted replacement palms have significantly smaller fronds which will result in underestimation of stem height by the linear model. Due to the amount of palms affected, a solution should be sought before applying this model for stem height estimations. Given a large amount of field samples across multiple palm ages, it may be possible to identify a robust non-linear relationship which accounts for age-dependent differences. This would allow efficient and accurate retrieval of per-palm trunk biomass from SfM point cloud data using allometric equations, given assumptions about diameter at breast-height (DBH) (Corley and Tinker, 2016).

4.4.6 Implications for oil palm plantation management and research

The methods for palm identification, TFH and stem height retrieval presented here are applicable to imagery from consumer grade drone systems, provided it is acquired with sufficient overlap, and can thus be of interest for improved plantation management by generating maps indicative of plantation status at relatively low additional cost. Repeat acquisitions would further allow the identification of height increments over time and local variations in height could possibly be correlated with oil palm yield, for example by influencing the light regime (Corley and Tinker, 2016). The retrieval of height metrics appeared to work almost as well for lower resolution, lower overlap acquisitions as they did for acquisitions focused on retrieving a higher quality point cloud. This is an important insight when seeking to maximise the coverage of flight plans and reduce the time required for acquisitions. A constraining factor regarding both time and cost of drone acquisitions, following the survey designs presented here, is the reliance on high precision GCP measurements. If the absolute geographic locations are not a necessity, an alternative may be the use of a total station to measure distances between markers. The installation of adequately spaced permanent GCPs would also greatly facilitate repeat acquisitions. Furthermore, with the improvement of on-board real-time kinematic systems, direct high precision georeferencing of the acquired imagery may become an affordable option in the future (Turner et al., 2014a).

The demonstrated usefulness of even low overlap acquisitions to derive height metrics and the increased application of drones for plantation management means that there may be an untapped data source of interest for research and a potential for a closer collaboration between researchers and innovative palm oil companies.

Despite similar results for higher and lower overlap acquisitions it can be assumed that for deriving information on younger palm canopies and for finer scale structural information such as frond rachis length and number, utilizing advanced point cloud metrics, higher overlap and finer resolution are required. The ability to derive advanced metrics with higher reliability may also prove useful in predicting per palm biomass, given adequate training and validation data derived from destructive harvesting or estimated AGB derived from allometric measurements of stem height, DBH, petiole cross-section and frond number in the field (Corley and Tinker, 2016). Coupled with further concurrent field sampling efforts, drone SfM photogrammetry derived metrics may be robust enough to provide much needed information to address one aspect of the lack of data for oil palm carbon stock estimates and the impact of the conversion of different land cover to oil palm plantations (Kho and Jepsen, 2015).

Previous work on automated palm detection from drone imagery has been largely focused on computer vision and object based detection. Malek et al., (2014) achieved an overall accuracy of 96.4% for classification of date palms using a SIFT-keypoint based machine learning approach. Their study however represented a simple case where the soil background was homogenous and clearly distinguishable from the canopies and no overlapping occurred. In a further image based approach, the characteristic radial pattern of oil palm fronds was exploited through circular autocorrelation of the polar shape matrix over a more complex site with overall detection accuracy of 84% (Manandhar et al., 2016). Further work is needed to demonstrate the applicability of these methods in plots with larger undergrowth. It stands to reason that object based and height based detection possess a number of contrasting advantages and that a hybrid approach including height information and image-based segmentation may yield the most accurate solution. As a DSM typically results from the workflow for orthomosaic generation, no additional data acquisition is required. Therefore this

would be a promising direction for future research aiming at developing palm identification methods with sufficient accuracy for commercial application.

4.5 Conclusions

This study demonstrated the use of SfM point clouds derived from drone imagery for the identification of single palm canopies and the retrieval of basic structural information based on height metrics from segmented palms. In plantation plots with flat topography as studied here a DTM interpolated from classified SfM ground points proved sufficiently accurate (~10 cm for high overlap acquisitions) for height based studies of oil palm without requiring LiDAR based information, which is key for the operational implementation at similar sites. Employing a Monte Carlo approach for generating point precision estimates allowed a spatially resolved assessment of SfM data quality which can inform on its robustness and suitability for vegetation structure related studies. Local maximum methods for CHM based palm identification performed best for intermediate palm ages (7 years) but showed more errors where large undergrowth and overlapping between palm canopies was common. Further it was shown that reliable inventories of the number of palms per plantation block could be generated with acquisition plans which favour coverage over high overlap, which provides an important benchmark for applying this methodology while maximising the efficiency of data acquisition. However, more highly resolved per-palm point clouds allowed for better estimation of stem height using height percentiles, and enabled the generation of stem height distributions for the studied plots. Due to the amount of detail resolved, it can be assumed that more complex point cloud based metrics could be identified which correlate with other aspects of palm structure and therefore warrant further research. These derived per-palm metrics, besides giving detailed information on plantation status, may prove useful for predicting per-palm AGB and ultimately mapping oil palm carbon stocks, providing an affordable and widely applicable method for carbon accounting.

5 Multi-Scale Evaluation of Drone-Based Multispectral Surface Reflectance and Vegetation Indices in Operational Conditions

Chapter context:

Miniaturised multispectral imagers flown on drone systems offer the unique ability to generate maps of surface reflectance and VIs with a spatial resolution fine enough to resolve individual plants and provide important indicators of their health (Anderson and Gaston, 2013; Gitelson et al., 2006a; Schlemmer et al., 2013). Such drone acquisitions provide data at an intermediate scale between field-based and airborne/spaceborne measurements, which is important for relating processes observed in individual plants to patterns observed from coarser scale data (Gamon, 2015). However, such data have still not been widely used, or assimilated into broader remote sensing workflows for scaling up since the technology is still at an early stage of adoption. To evaluate the capacity for integrating data from such sensors and workflows into broader upscaling or assimilation studies, high accuracy and consistency within the drone-acquired products are likely to be required. Unlike airborne or satellite sensors, drones fly low enough that atmospheric correction of the data is generally considered unnecessary (Hakala, Suomalainen, & Peltoniemi, 2010). However, data from lightweight multi-spectral sensors are influenced by a range of acquisition- and sensor-related effects (Kelcey and Lucieer, 2012). The accuracy of these data have previously been assessed over reference surfaces *in-situ* (Deng et al., 2018; Von Bueren et al., 2015), but there are a lack of studies investigating the impact of such uncertainties spatially, over variable vegetation cover and how they may influence the retrieval of biochemical and structural parameters.

This chapter presents two experiments which sought to:

1. investigate the accuracy and impact of different calibration methods on surface reflectance estimates from the four bands of the Parrot Sequoia MCA;

2. compare surface reflectance and VIs over a maize field to concurrent acquisitions from airborne and spaceborne sensors to understand the impact of uncertainties over space and for plots of different LAI.

The conceptual idea for these experiments and their design originated from collaborations within the TRUSTEE Network. During the author's secondment at University of Milano-Bicocca he took part in a joint field campaign (see section 3.2.2 for further details). In particular the HyPlant hyperspectral imaging acquisition was identified as a unique opportunity to generate an independent reference dataset at fine spectral and spatial resolutions for comparison with data from the Parrot Sequoia.

This chapter has been published as: Fawcett, D., Panigada, C., Tagliabue, G., Boschetti, M., Celesti, M., Evdokimov, A., Biriukova, K., Colombo, R., Miglietta, F., Rascher, U., Anderson, K., 2020. Multi-Scale Evaluation of Drone-Based Multispectral Surface Reflectance and Vegetation Indices in Operational Conditions. *Remote Sens.* 12. doi:10.3390/rs12030514

Research questions:

1. What is the performance of MCA sensors with regards to measuring surface reflectance?
 - a) What is the accuracy of MCA derived hemispherical-conical reflectance factors (HCRF, following the terminology by Schaepman-Strub et al. (2006))?
 - b) How is HCRF accuracy influenced by the type of calibration procedure followed?
 - c) How consistent are HCRF products spatially and over varying vegetation cover?
2. What is the performance of MCA sensors with regards to deriving VIs?
 - a) How consistent are VI products spatially and over varying vegetation cover?

- b) Are the MCA derived VIs comparable to VIs derived from similar bands of coarser spatial resolution data captured close in time (HyPlant, Sentinel 2)?

Abstract

Compact multi-spectral sensors that can be mounted on lightweight drones are now widely available and applied within the geo- and environmental sciences. However; the spatial consistency and radiometric quality of data from such sensors is relatively poorly explored beyond the lab; in operational settings and against other sensors. This study explores the extent to which accurate HCRF and VIs (specifically: NDVI and chlorophyll red-edge index (CHL)) can be derived from a low-cost multispectral drone-mounted sensor (Parrot Sequoia). The drone datasets were assessed using reference panels and a high quality 1 m resolution reference dataset collected near-simultaneously by an airborne imaging spectrometer (HyPlant). Relative errors relating to the radiometric calibration to HCRF values were in the 4 to 15% range whereas deviations assessed for a maize field case study were larger (5 to 28%). Drone-derived VIs showed relatively good agreement for NDVI with both HyPlant and Sentinel 2 products ($R^2 = 0.91$). The HCRF; NDVI and CHL products from the Sequoia showed bias for high and low reflective surfaces. The spatial consistency of the products was high with minimal view angle effects in visible bands. In summary; compact multi-spectral sensors such as the Parrot Sequoia show good potential for use in index-based vegetation monitoring studies across scales but care must be taken when assuming derived HCRF to represent the true optical properties of the imaged surface.

5.1 Introduction

Spectral information and derived VIs are at the core of a wide array of methodologies for the monitoring of vegetation. How vegetation reflects light at different wavelengths is indicative of its structure, biochemical composition as well as status and function in terms of photosynthesis and carbon dioxide assimilation (Gamon et al., 2019; Gitelson et al., 2005; Tucker et al., 1985). Deriving spectral information at fine spatial and temporal resolutions was identified as being critical for relating processes measured at local scale to coarser spatial resolution global measurements, for example, to bridge the scaling gap between flux-tower based eddy-covariance measurements and satellite observations (Gamon, 2015). The practicalities of sampling detailed ecosystem optical properties at fine scales previously relied on elaborate and financially costly infrastructure such as *in situ* spectral measurement tramways (Gamon et al., 2006) or motorised flux-tower mounted cameras (Hilker et al., 2007).

Recently, the use of drones as proximal acquisition platforms has revolutionised the way in which these finely resolved datasets can be collected (Anderson and Gaston, 2013; Berni et al., 2009; Garzonio et al., 2017). Lightweight drones have the further benefit of low financial cost, flexibility and enable deployment also in remote and harsh environments (Assmann et al., 2019; Duffy et al., 2017). In tandem with the development and production of compact and lightweight turnkey multispectral sensors, there has been a surge in drone-based multispectral data applications during recent years which make use of the fine spatial resolution or frequent revisit capabilities (Johansen et al., 2018; Manuel Fernández-Guisuraga et al., 2018; Nebiker et al., 2016; Wang et al., 2019). Popular sensor solutions are MCA systems such as the Parrot Sequoia (Parrot SA, France) and Micasense RedEdge (Micasense, US) which consist of individual cameras with different band-pass filters to record reflected light at specific narrow (10-40 nm) wavelength intervals. The individual camera images are then co-registered to provide a single image with multiple spectral bands. Designed primarily for applications in precision agriculture, these sensors exhibit a number of qualities which have also made them attractive to the scientific community, primarily their low financial cost, simple integration into lightweight drone systems and accompanying software options.

However, data from lightweight MCAs are susceptible to a considerable amount of geometric and radiometric effects which require an extensive workflow of corrections such as dark current, lens distortion and vignetting compensation, as detailed by Kelcey and Lucieer, (2012). These corrections are increasingly handled by commercial, mostly black-box software packages (e.g. Pix4D and Agisoft Metashape) which generate fully mosaicked, orthorectified outputs and include the option of radiometrically calibrating orthomosaics to provide surface reflectance and VI maps.

The impact of correction and calibration methodologies as well as viewing-angle effects for non-gimbaled acquisitions on the final surface reflectance and derived VI maps can be considerable (Bendig et al., 2015; Damm et al., 2015b) and is relatively poorly explored beyond the lab, in comparison against other optical remote sensing instruments (e.g. onboard satellites or in airplanes) in operational settings. These effects have potential implications for the spatial consistency and sensitivity of the products to the desired plant trait to be monitored (Miura et al., 2000). Yet, these uncertainties are not reported to the end-user by the software and the direct integration of products in further processing workflows without critical assessment can potentially lead to bias in the results. Understanding the extent to which these uncertainties influence outputs is important in a precision agriculture context where VIs serve as indicators of local vegetation status. Ensuring that there is sufficient consistency between datasets is also crucial when integrating drone-based data with other remote sensing and *in situ* data sources, for improved temporal monitoring (Easterday et al., 2019; Gevaert et al., 2015; Van Leeuwen et al., 2006). For scaling studies, surface reflectance values should further be traceable and comparable between sensors (Padró et al., 2018).

Due to the large interest from a diverse user base and the many potential applications of low-cost MCA systems, there is now a need for rigorous data assessments in an applied context. This can determine whether the sensors are able to deliver physical quantities (e.g. surface reflectance) with the required accuracy for scientific research and whether derived VIs are sufficiently consistent to provide useful relative information as sought after for agricultural applications. To this end we planned a field campaign based on a section of heterogeneous maize field with multi-sensor acquisitions and accompanying spectroscopy field-measurements and sampling of biophysical parameters. The

presented study sought to provide a thorough assessment of MCA-derived surface reflectance and derived VI products and to answer the following research questions:

1. What is the performance of MCA sensors with regards to measuring surface reflectance?
 - a) What is the accuracy of MCA derived HCRF?
 - b) How is HCRF accuracy influenced by the type of calibration procedure followed?
 - c) How consistent are HCRF products spatially and over varying vegetation cover?
2. What is the performance of MCA sensors with regards to deriving VIs?
 - a) How consistent are VI products spatially and over varying vegetation cover?
 - b) Are the MCA derived VIs comparable to VIs derived from similar bands of coarser spatial resolution data captured close in time (*HyPlant*, Sentinel 2)?

Question 1 a) and b) were addressed by a calibration-validation experiment using reference panels imaged in-flight. Both software (Pix4D) implemented proximal panel calibration and empirical line models (ELMs) based on in-flight imagery are compared in their ability to deliver accurate HCRFs. For question 1 c), a spatially contiguous, pixel-wise HCRF comparison over a heterogeneous maize field LAI ranging from 0 to 4) was performed utilising a reference dataset from a simultaneous airborne hyperspectral imager acquisition (*HyPlant*). Question 2 was answered using field measured LAI values and vegetation indices derived from comparable acquisitions by drone-based, airborne (*HyPlant*) and spaceborne (Sentinel 2 multi-spectral satellite) instruments over the same study area.

5.2 Materials and Methods

The object of study, datasets and comparisons performed are presented in the following sections. An overview of the study highlighting the different scales and the datasets compared is presented in Figure 5-1

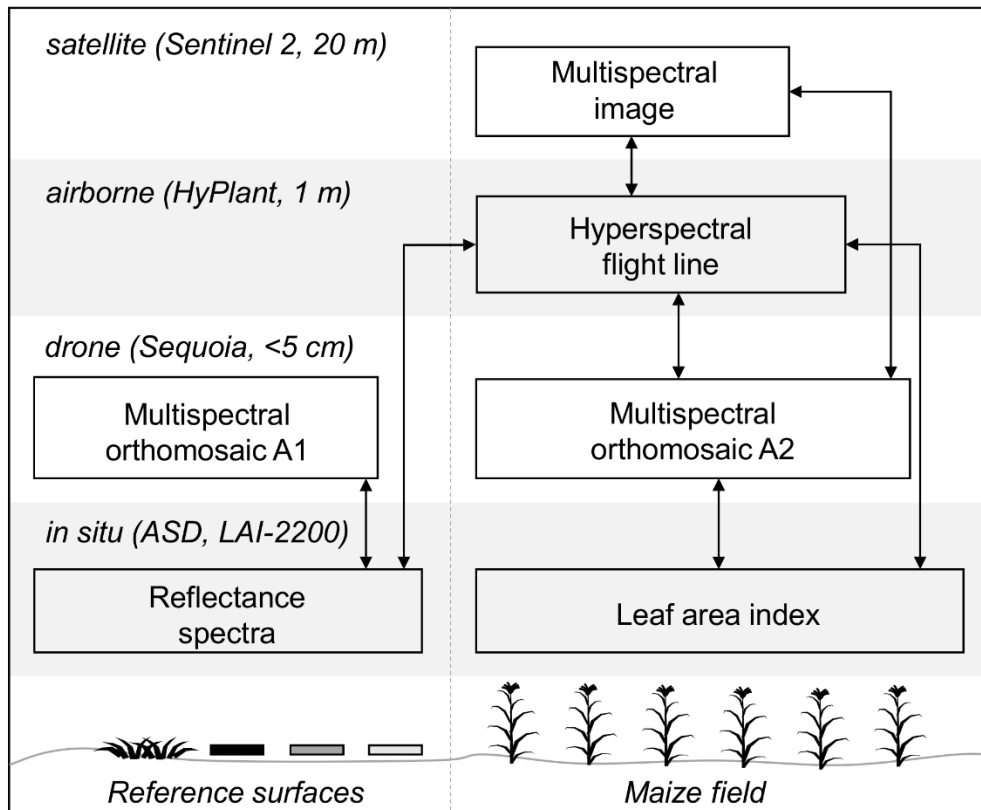


Figure 5-1: Overview of the multisource datasets, including details on spatial resolution, and comparison experiments performed. Arrows indicate which datasets are compared within this study.

5.2.1 Study Site

The study was carried out over a maize field in the vicinity of Braccagni, province of Grosseto, Italy ($N 42^{\circ}49'7.06''$, $E 11^{\circ}3'39.98'$, 3 m a.s.l.) (Figure 5-2). This region has a temperate climate according to the Köppen-Geiger classification (Csa) (Beck et al., 2018) and experiences dry and hot summers. The maize was planted on clay soil in north-south oriented rows and was drip irrigated. At the time of the study in early July 2018 the majority of the crop was in tasselling stage. The field showed considerable heterogeneity and variability in plant density, likely due to soil characteristics and some irrigation issues. The region of interest covered parts of

two fields with the same sowing date with a spatial extent of 3.4 hectares, limited by drone flying height restrictions and battery capacity.



Figure 5-2: The studied maize field in the province of Grosseto, Italy is depicted along with its location (inset map). The flight lines and coverage of the drone (Sequoia, red) and airborne (HyPlant, blue) datasets are also shown. Image data licensed by ESRI, © DigitalGlobe.

5.2.2 Image Data

Multi-source remote sensing data were used for this study and are described in Table 5-1. Drone image data were acquired using the Parrot Sequoia (Parrot, France) MCA mounted on a 3DR Solo quadcopter. The Sequoia sensor has four monochrome cameras with band-pass filters to record light in different wavelength regions (sensor response depicted in Figure 5-3, centre wavelengths: 550, 660, 735 and 790 nm, bandwidths: 40, 40, 10 and 40 nm). The mount was custom designed to fix the camera at a 3 degree angle to offset average in-flight forward tilt. The flying altitude for the drone acquisitions was 45 and 50 m above ground, resulting in a GSD of 4.15 cm and 4.71 cm respectively. The flying speed was constant at 4 m/s and the camera was triggered every 1.5 s by intervalometer, guaranteeing 85% forward image overlap. The lawnmower-pattern flight plan (Figure 5-2) was designed with a distance between flight lines resulting in 80% lateral image overlap. Initial georeferencing of the images with a camera internal

GPS was refined using 6 GCP markers clearly visible within the imagery and surveyed using a high accuracy DGPS (Topcon HiPer Pro, Japan).

Acquisition 1 (A1) (Table 5-1) denotes an acquisition for the validation of drone derived surface reflectance factors for panels and natural targets. Acquisition 2 (A2) consisted of two subsequent flights (F2A and F2B) to cover the entire region of interest (Figure 5-2), each with a duration of approximately 10 minutes and 10 minutes intermission between flights.

Hyperspectral image data over the same area was acquired by the HyPlant airborne imaging spectrometer (Rascher et al., 2015). The HyPlant instrument consists of two modules (the FLUO and DUAL module) and was mounted on an aircraft flying at 680 m height resulting in a GSD of 1 m and a swath of 390 m. Data were geometrically and radiometrically corrected. The georeferencing accuracy of the images was 1 pixel, i.e. 1 m. For this study only data of the DUAL module, which covers the spectral range of 380 – 2500 nm, was used. Top-of-canopy radiances and relative reflectance was calculated using the laboratory calibration with the GalliGeo software package (SPECIM, Oulu, Finland) and radiative transfer modelling using MODTRAN 5 (for details on the processing of HyPlant imagery see Siegmann et al., (2019)). Both drone and airborne data were acquired during cloud free conditions over the study site, though isolated cumulus clouds were passing in the vicinity.

The study site was imaged by Sentinel-2A (S2) during cloud-free conditions at noon the following day. The Level 2A atmospherically corrected surface reflectance data were downloaded from the Copernicus Open Access Hub (<https://scihub.copernicus.eu/>). Due to the lower resolution of the red edge bands, all bands used were resampled to 20 m pixel resolution. S2 bands 3, 4, 6 and 7 show the best correspondence with the Sequoia bands (Figure 5-3, centre wavelengths: 560, 665, 740 and 780 nm, bandwidths: 36, 31, 15 and 20 nm).

Table 5-1: Description of image datasets used within this study, including sensor, acquisition time, GSD (spatial resolution) and spectral bandwidths (spectral resolution).

Dataset Descriptor	Sensor	Acquisition Time	GSD	Bandwidth	Spectral Range
Sequoia A1	Parrot Sequoia	6th July 2018 16:07 (UTC+2)	4.15 cm	10–40 nm	550–790 nm
Sequoia A2 (F2A + F2B)	Parrot Sequoia	7th July 2018 11:50 to 12:20 (UTC+2)	4.71 cm	10–40 nm	550–790 nm
HyPlant	HyPlant dual-channel module	7th July 2018 12:32 (UTC+2)	1 m	3–4 nm	380–2500 nm
S2	Sentinel 2A MultiSpectral Instrument	8th July 2018 12:10 (UTC+2)	20 m	18–45 nm	440–2200 nm

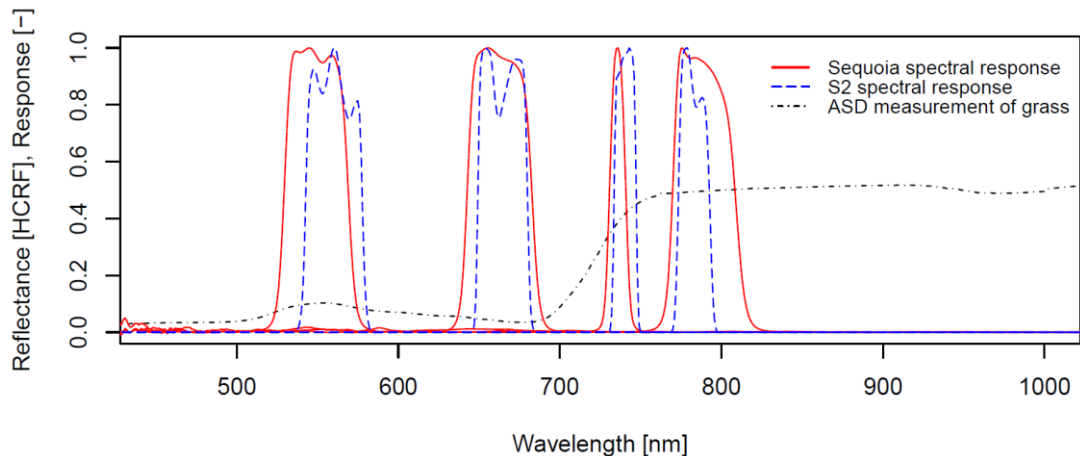


Figure 5-3: Relative spectral responses of the four Parrot Sequoia cameras as well as the most closely corresponding Sentinel 2A bands (bands 3, 4, 6 and 7), overlaid on a measured grass reflectance spectrum.

5.2.3 Field Measurements

5.2.3.1 Field Spectral Measurements for Calibration and Validation

Concurrently with A1, five reference panels of varying reflectance as well as a dry bare soil and a grass target were measured using an ASD FieldSpec Pro spectrometer and calibrated to HCRF using a 99% Spectralon® white panel as

reference. The brightest and darkest panel of 50 x 50 cm dimensions and 2% and 44% nominal reflectance across bands were manufactured by MosaicMill (Finland), consisting of a fabric applied to plywood. Three 40 x 60 cm panels of intermediate reflectance (means of 8%, 21% and 39% across Sequoia bands) were manufactured using RustOleum® matte primer and paint on plywood. The target sizes were selected based on targets used in similar studies (Padró et al., 2018).

For the validation of the HyPlant DUAL derived hyperspectral HCRF product, three tarps of different reflectance (approx. 5%, 40% and 70% average reflectance in the 400 to 1000 nm wavelength range) made of PVC-coated canvas material (Kayospruce Ltd., UK) were measured using the ASD. It should be noted that these tarps were imaged in a different flight line acquired approx. 20 minutes prior to the one used further within this study, however the atmospheric conditions are assumed to remain similar and therefore the HCRF resulting from atmospheric correction are comparable.

5.2.3.2 Leaf Area Index Measurements

In the associated field campaign carried out on the same date as the overflights, LAI was estimated using a LAI-2200 (LI-COR, US) instrument. LAI-2200 measurements are a good proxy of real LAI data in maize (Facchi et al., 2010). Measurements were taken within 20 10 x 10 m plots corresponding to elementary sampling units (ESU) as suggested by the VALERI protocol (Baret et al., 2005) (Figure 5-4 a). Each ESU was selected to be approximately spatially homogenous in terms of LAI. LAI measurements protocol for the LAI-2200 device consisted of two Above canopy (A) and six Below canopy (B) readings acquired along a transect that crossed maize crop rows (ABBBBBBA sequence, Figure 5-4 b). A 270° cap was used to restrict the azimuthal field of view (FOV), so that the operator was not in view and the open portion of the sensor was pointed north-west along the rows. The spatial subset analysed for this study contains 20 ESUs with mean LAI values ranging from 0.85 to 3.83.

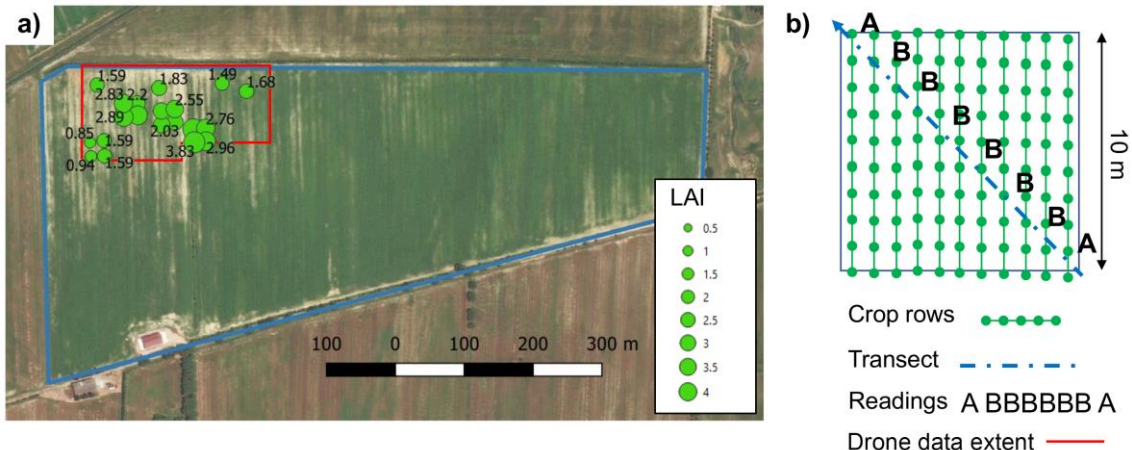


Figure 5-4: Position and values of LAI measurements available for the analysis (a), acquired along a transect on 10 × 10 m plots (b).

5.2.4 Image Data Processing

5.2.4.1 Surface Reflectance from Drone Image Data

Image processing from individual four band images to multispectral HCRF orthomosaics was performed in Pix4D (Pix4D, Switzerland). This included the geometric correction and stitching of images which employs photogrammetric algorithms as well as the radiometric calibration to surface reflectance. The precise methodology employed in both workflows is not disseminated due to the black-box nature of the proprietary software, however the radiometric calibration procedure for Sequoia imagery has been shared in application notes by the manufacturer (Parrot, 2017b), and is documented here.

For each spectral band (individual camera), the DN (P) recorded within Sequoia image data can be converted to a pseudo-radiance in arbitrary units R homogeneous to $\text{W sr}^{-1} \text{m}^{-1}$ according to equation (5-1), where ε is the exposure time in seconds, γ is the ISO, f is the f-number ($f = 2.2$) and A , B and C are camera specific calibration coefficients which model the non-linear behaviour of the CMOS sensor and are measured in production for each camera (Fallet and Domenzain, 2018).

$$R = f^2 \frac{P - B}{A\varepsilon\gamma + C} \quad (5-1)$$

There are several options for deriving HCRF (ρ) from the measured pseudo-radiance R . One commonly applied to drone-based data is the use of a single reference target with a known reflectance factor, imaged proximally before or after the acquisition. This is essentially a one-point simplified ELM (Smith and Milton, 1999) with zero intercept where the band specific calibration coefficient for converting R to ρ is the ratio of known HCRF of the target (ρ_{ref}) and the spatially averaged R over the target (\overline{R}_{ref}) (eq. (5-2)). This simplified correction procedure is part of the default workflow for reflectance map generations in photogrammetry softwares such as Pix4D and Agisoft Metashape. Irradiance information which is recorded by the upward facing sunshine sensor is not used here and the irradiance assumed constant throughout the acquisition.

$$\rho = R \frac{\rho_{ref}}{\overline{R}_{ref}} \quad (5-2)$$

White (100% reflective) reference targets are unsuited for use with many current drone-based sensors, as the integration times needed to achieve a satisfactory signal-to-noise ratio in the rest of the scene lead to oversaturation over very bright surfaces (Jakob et al., 2017; Manuel Fernández-Guisuraga et al., 2018). The reference panel used in this study was a Kodak grey-card, an inexpensive reference panel common in photography, with an approximate 20% reflectance across bands. In a previous study, the difference between the use of a grey card reference and an assumed Lambertian Spectralon® panel of higher (40%) reflectance was shown to be minimal within this calibration procedure (Fawcett and Anderson, 2019).

An alternative to the proximal panel calibration is the use of the ELM using reference targets imaged in-flight. A linear model formed by ordinary least squares regression against multiple reference targets or merely one dark and bright target is used to relate R to ρ . Adjacency effects due to diffuse scattering have previously been observed influencing the reflectance of dark reference panels and leading to erroneous negative values in shaded or dense canopy areas (Tu et al., 2018), which was also found in a preliminary analysis for this study. Therefore, two alternate versions of the ELM approach were tested using 1) one bright reference panel and the intercept set to zero, 2) one bright reference panel with the intercept

set to zero and the lowest value occurring within the vegetated scene subtracted from the data, following recommendations by Tu et al. (2018).

5.2.4.2 Vegetation Index Products

The four bands of the Sequoia sensor allow the calculation of several VIs which are indicative of vegetation vigour and status. Two commonly employed indices were selected for this analysis, the NDVI (eq. 5-3) and the red-edge chlorophyll index (CHL) (eq. 5-4). The NDVI has been used successfully as an indicator of LAI in crops (Gitelson et al., 2007), while CHL is sensitive to canopy chlorophyll content (Gitelson et al., 2005).

$$NDVI = \frac{\rho_{NIR} - \rho_{red}}{\rho_{NIR} + \rho_{red}} \quad (5-3)$$

$$CHL = \frac{\rho_{NIR}}{\rho_{red\ edge}} - 1 \quad (5-4)$$

5.2.4.3 Multi-Scale HCRF and VI Intercomparison

In order to compare HCRF measurements between data sources, they must be resampled to common spectral and spatial resolutions. To derive panel validation HCRF corresponding to the Sequoia bands, the ASD measured HCRF values were convolved with the Sequoia relative sensor SRF (Figure 5-3). In A1 at a GSD of 4.15 cm, approximately 140 pixels per reference panel were resolved in the stitched orthomosaic. However, due to concerns of adjacency effects/stray light influencing the values towards the panel edges, only the mean of the central 16 pixels per panel were used and very small inter-pixel differences verified by analysing their standard deviation. If canvas targets are used, a larger number of pixels would be required to account for variability due to surface unevenness.

For an intercomparison of Sequoia derived HCRF values with HyPlant HCRF, the drone derived HCRF orthomosaic was spatially resampled to 1 m spatial resolution. The hyperspectral reflectance values were convolved with the Sequoia

SRF, following the basic procedure described by D'Odorico et al. (2013) to yield HCRF comparable with the Sequoia bands.

Relative offsets between the image datasets were reduced by updating the georeferencing of the HyPlant image with a 2D polynomial in ArcMap (ESRI, US) using clearly identifiable tie-points between datasets and nearest-neighbour resampling. After spectral resampling, Sequoia comparable VIs were derived from the HyPlant dataset. The resampled HCRF and VI datasets were compared pixel-wise for the entire extent of A2. NDVI values over the sampled ESUs were also compared, and a non-linear regression of the NDVI mean values versus estimated LAI was performed.

VIs were further compared to those derived from S2 data (utilising bands 4 and 7 for NDVI, bands 6 and 7 for CHL). For this comparison, Sequoia and HyPlant data were spatially resampled to 20 m resolution and HyPlant bands spectrally resampled to the target S2 bands.

Deviations between datasets are assessed using the mean absolute deviation (MAD) and relative error metrics. MAD was selected as an unambiguous metric which weighs all differences between the datasets equally.

5.3 Results

5.3.1 HCRF Products

The HCRF products were derived from the Sequoia, HyPlant and S2 image data and georeferenced and clipped to the extent of the drone dataset. The georeferencing RMSE error for the Sequoia A2 orthomosaic was 0.007 m. A visual comparison of false-colour infrared composites (Figure 5-5 a) as well as representative spectra are presented (Figure 5-5 b). It is evident that the drone data can resolve the row structure of the crop and small patches of bare ground. The detailed information on the spatial heterogeneity of the field is partially lost at the comparatively coarse resolution of S2. At this resolution it is furthermore impossible to extract pure spectral information on soil due to mixed pixels. The HyPlant dataset is able to well represent the variability of vegetation cover while the reflectance spectra provide an additional wealth of information, particularly by finely resolving the green-peak (550 nm), the chlorophyll absorption in the red

wavelength regions (600-700 nm) as well as the sharp red-edge increase in reflectance of healthy vegetation (730 nm). These wavelength regions are all covered by the Sequoia and S2 sensors resolving the same features but at a much coarser spectral resolution.

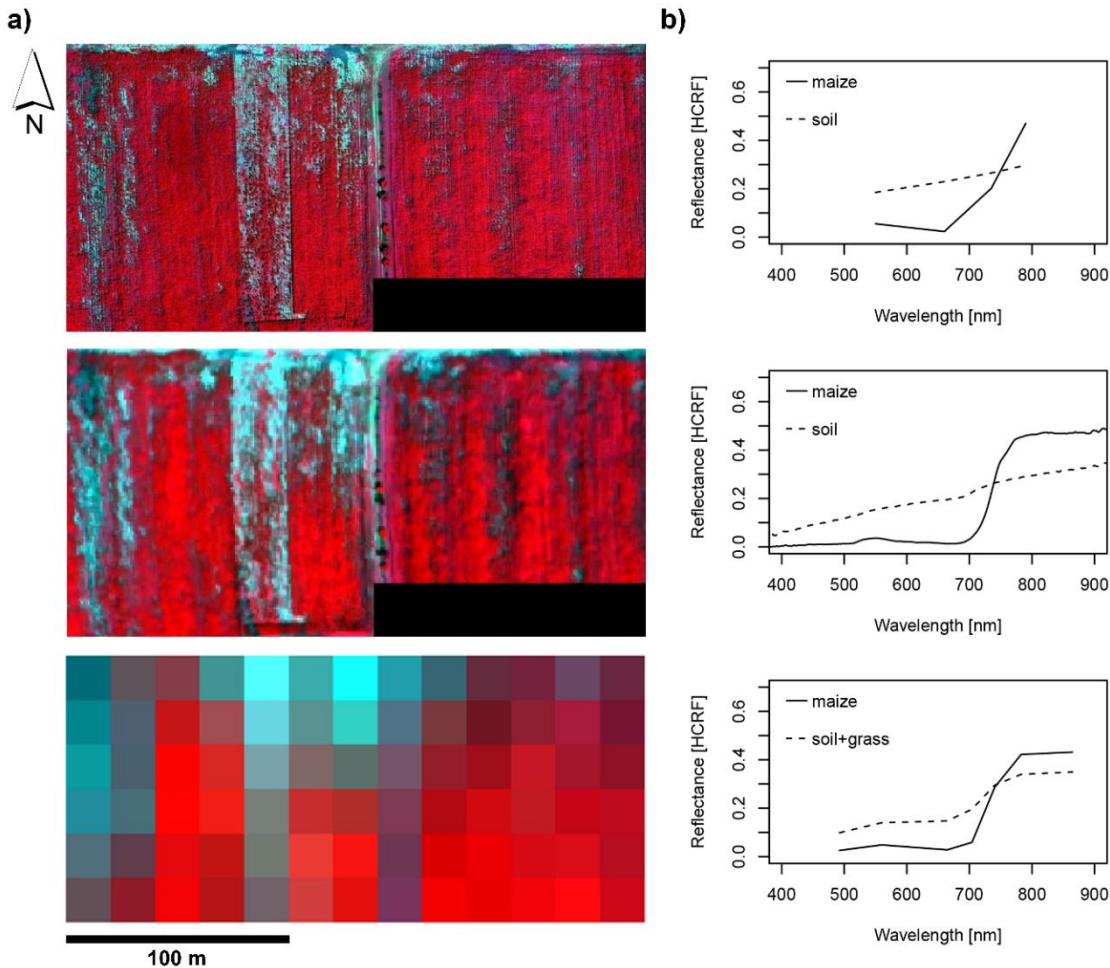


Figure 5-5: False-colour infrared representations (a) and representative HCRF spectra (b) of the Sequoia (top), HyPlant (middle) and S2 (bottom) surface reflectance products over the maize field study site (no pure soil pixel for S2). The subsets shown are the extents analysed. Aerosol and water vapour bands of S2 were omitted.

5.3.1.1. Reference Target Validation of Drone Derived HCRF

The Sequoia derived HCRF values extracted from the mean of the central pixels of the reference panels imaged in-flight, as well as for a grass and soil target, were compared against *in situ* ASD-measured HCRF using MAD (Figure 5-6,

Table 5-2). For the green band, the two brightest panels (>39% reflectance) were saturated and therefore excluded from the analysis. This sensor inherent issue for the visible bands has been verified by previous studies (Gilliot et al., 2018; Tu et al., 2018) and limits its applicability to surfaces of intermediate brightness.

The standard deviations between the individual pixel values of the panels, assessed for the single panel approach, were small (green: 0.0015, red: 0.0023, red edge: 0.0028, NIR: 0.0020).

Overall, errors per band are in the 2-4% reflectance range which equals 4-15% relative error (Table 5-2). The largest errors are most apparent for the lower reflective panels in the NIR band, while there is a general over-estimation of reflectance values across all bands. The only exceptions are the grass target which is underestimated in the red edge band as well as the brightest reference panels imaged in the red band. The performance of the single panel calibration and the 0 intercept ELM is similar while the subtraction of the minimum value within the image leads to considerably smaller errors for the green band but largest errors within the NIR band. Therefore, the error does not appear to be a simple offset but shows a wavelength-dependent behaviour as well as being related to the magnitude of the target reflectance, which is clearly visible for the NIR band (Figure 5-6).

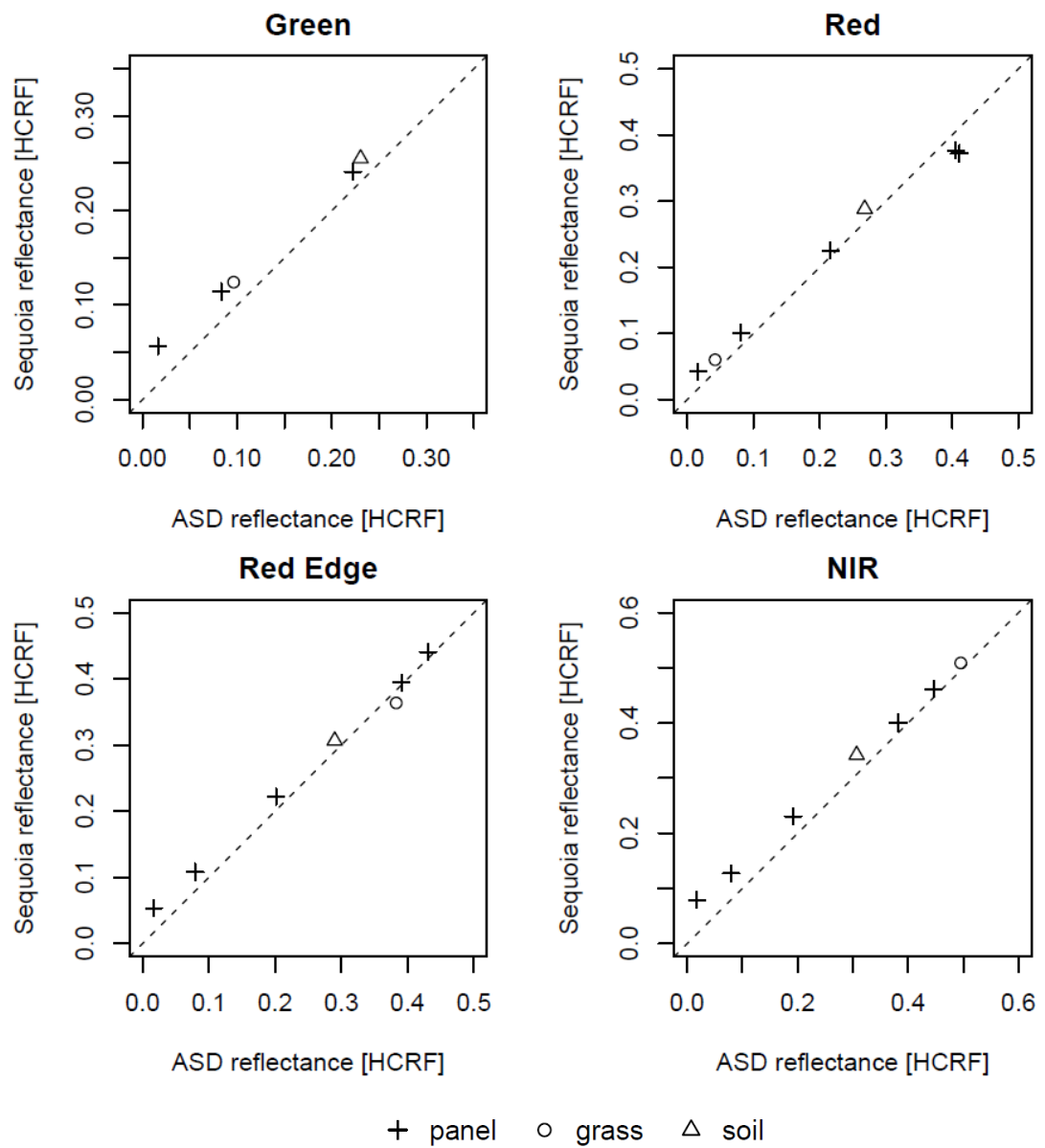


Figure 5-6: Sequoia multispectral image data-derived HCRF of validation targets compared to ASD measurements.

Table 5-2: MAD of Sequoia derived HCRF values per band for the three calibration approaches, estimated from the comparison with field measured reference panels and surfaces.

Calibration Method	MAD Green	MAD Red	MAD Red Edge	MAD NIR
Single panel calibration	0.029 (13.63%*)	0.023 (11.11%*)	0.019 (7.53%*)	0.033 (11.95%*)
ELM with 0 intercept	0.02 (9.69%*)	0.027 (13.18%*)	0.023 (8.76%*)	0.027 (11.21%*)
ELM with modified 0 intercept	0.009 (4.19%*)	0.025 (12.29%*)	0.02 (8.87%*)	0.036 (14.75%*)

* relative error.

5.3.1.2. Spatial Comparison between Airborne and Drone Derived Surface Reflectance

The spatial comparison of the HCRF values was performed for all three reflectance calibration approaches by computing MAD between Sequoia and HyPlant HCRF (Table 5-3). The HCRFs from the proximal panel approach are visualised as scatterplots per band (Figure 5-7), as well as difference images between the HCRF values (Figure 5-8). The relative errors for HyPlant HCRF over the Sequoia band ranges for the three validation tarps were also computed (Table 5-4).

It is apparent that for the visible bands, pixels which contain dense vegetation were over-estimated in terms of HCRF by the Sequoia by approximately 0.03 while the higher reflective bare-ground pixels were underestimated by a similar amount (Figure 5-7, Figure 5-8). For more mixed pixels, the differences compensated each other and the reflectance was much closer to the HyPlant derived values. As observed for the panel validation experiment, the single panel calibration and 0 intercept ELM based on in-field panels resulted in similar deviations. The minimum subtraction method greatly increased deviations for the infrared bands.

The difference images (Figure 5-8) did not exhibit strong surface cover independent spatial bias, except for some spatial variation in the red-edge and NIR bands. For the red-edge, the area covered by F2B (eastern field) was closer

to the HyPlant HCRF (mean bias: -0.0135) while the area covered by F2A (western field) was significantly lower (mean bias: -0.0417). This also explained the larger variation of Sequoia red-edge HCRF as opposed to HyPlant values in the scatterplot (Figure 5-7). Possible view-angle related effects were visible in the difference image of the NIR band (Figure 5-8) as faint horizontal striping parallel to the drone flight path and perpendicular to the vertical striping from variable vegetation cover.

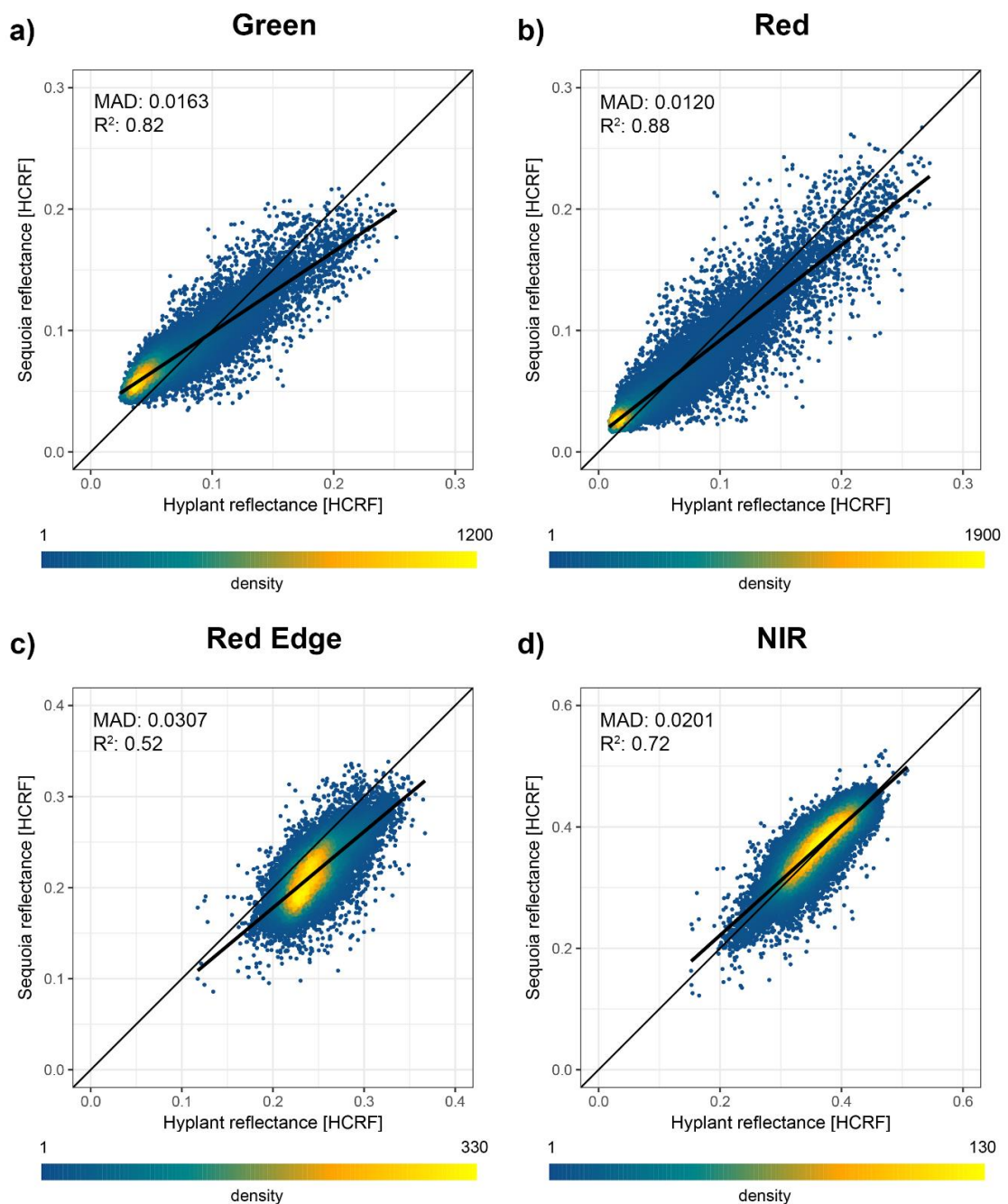


Figure 5-7: Scatterplot comparisons of Sequoia and HyPlant based HCRF values for the four bands analysed over the region of interest with an ordinary least squares regression line (bold), the R^2 and the MAD.

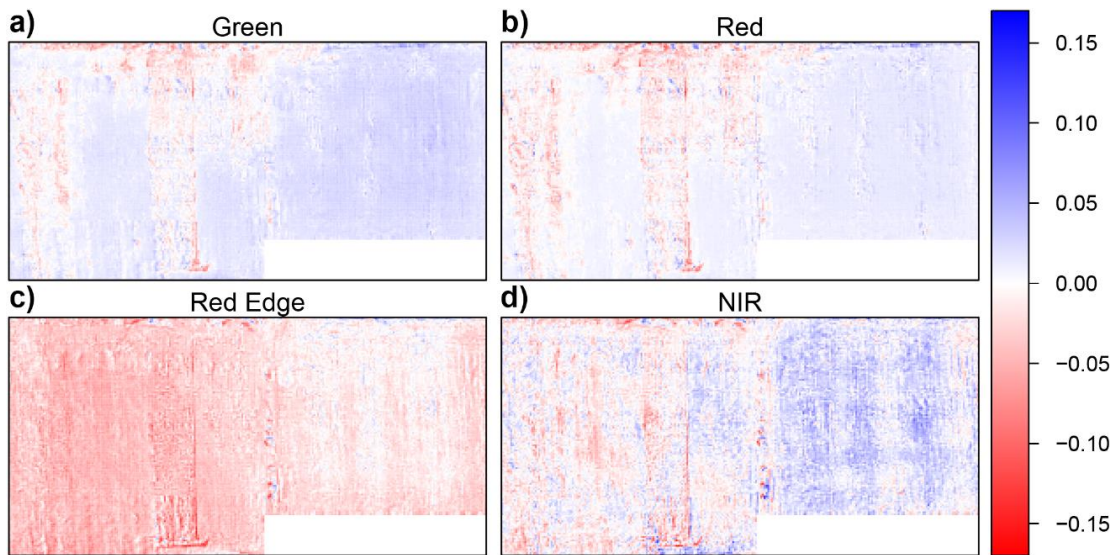


Figure 5-8: Difference images (Sequoia A2 minus HyPlant) of the HCRF values of the four analysed bands over the studied maize fields.

Table 5-3: MAD of Sequoia derived HCRF values per band for the three calibration approaches, estimated from the comparison with HyPlant HCRF values.

Calibration Method	MAD Green	MAD Red	MAD Red Edge	MAD NIR
Single panel calibration	0.0163 (25.39%*)	0.0120 (26.10%*)	0.0307 (12.56%*)	0.0201 (5.61%*)
ELM, 0 intercept	0.0177 (27.58%*)	0.0117 (25.45%*)	0.0194 (7.94%*)	0.0360 (10.05%*)
ELM, modified 0 intercept	0.0118 (18.38%*)	0.0110 (23.93%*)	0.0539 (22.05%*)	0.0479 (13.37%*)

* relative error.

Table 5-4: Bias and relative errors of the HyPlant HCRF for the Sequoia band spectral ranges over three differently reflective validation surfaces (tarps).

Validation surface	Error Green	Error Red	Error Red Edge	Error NIR
0.05 HCRF (Black)	0.0044 (9.61%*)	0.0045 (10.19%*)	0.0036 (7.95%*)	0.0038 (8.35%*)
0.4 HCRF (Grey)	0.0097 (2.20%*)	0.0071 (1.62%*)	0.0017 (0.39%*)	0.0001 (0.03%*)
0.7 HCRF (White)	-0.0181 (-2.53%*)	-0.0155 (-2.22%*)	-0.0178 (-2.58%*)	-0.0152 (-2.24%*)

* relative error.

5.3.2 Vegetation indices

VI_s derived from Sequoia and HyPlant data, as well as S2 data were compared pixel-wise across the same extent as HCRF (Figure 5-9 and Figure 5-10) and the MADs for different calibration methods reported (Table 5-5). Finally, Histograms of Sequoia and HyPlant NDVI values and their model fits were compared for 10 x 10 m ESUs of varying LAI (Figure 5-11).

While NDVI appeared in relatively good agreement across the range for all datasets (Figure 5-9 a, Figure 5-10 a and Figure 5-10 c), it was evident from the scatterplots, histograms and LAI models (Figure 5-11) that lower NDVI values due to low vegetation fraction and higher soil contribution were overestimated by the Sequoia data while high NDVI values stemming from purely vegetated pixels were slightly underestimated.

For the CHL index, there was a good linear relationship between the datasets but a very clear offset which increased with higher values of CHL (Figure 5-9 b, Figure 5-10 b). For the Sequoia comparison with S2 (Figure 5-10 b), this was to be expected due to a slight difference in red-edge band positions (Figure 5-3, Figure A 2) but does not explain the offset in comparison to HyPlant (Figure 5-9 b). The impact of HyPlant band spacing was tested using simulated data, the methodology and results of which can be found in the appendix A2. Mean estimated errors for all bands were very small across a variation of LAI and chlorophyll content values, the largest of which were found for the red-edge band (0.00037 for LAI 0.5 to 10 and 0.00018 for chlorophyll from 0 to 100 µg/cm², Table A 1).

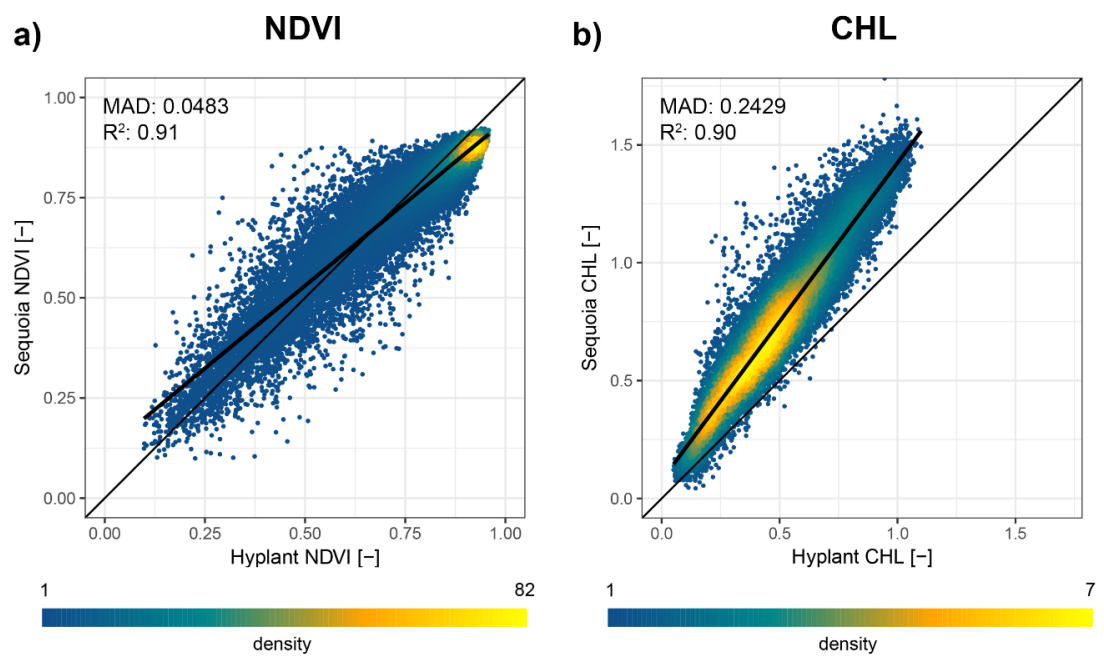


Figure 5-9: Scatterplot comparisons of Sequoia and HyPlant based NDVI (a) and CHL (b) values for the region of interest with an ordinary least squares regression line (bold) and the MAD.

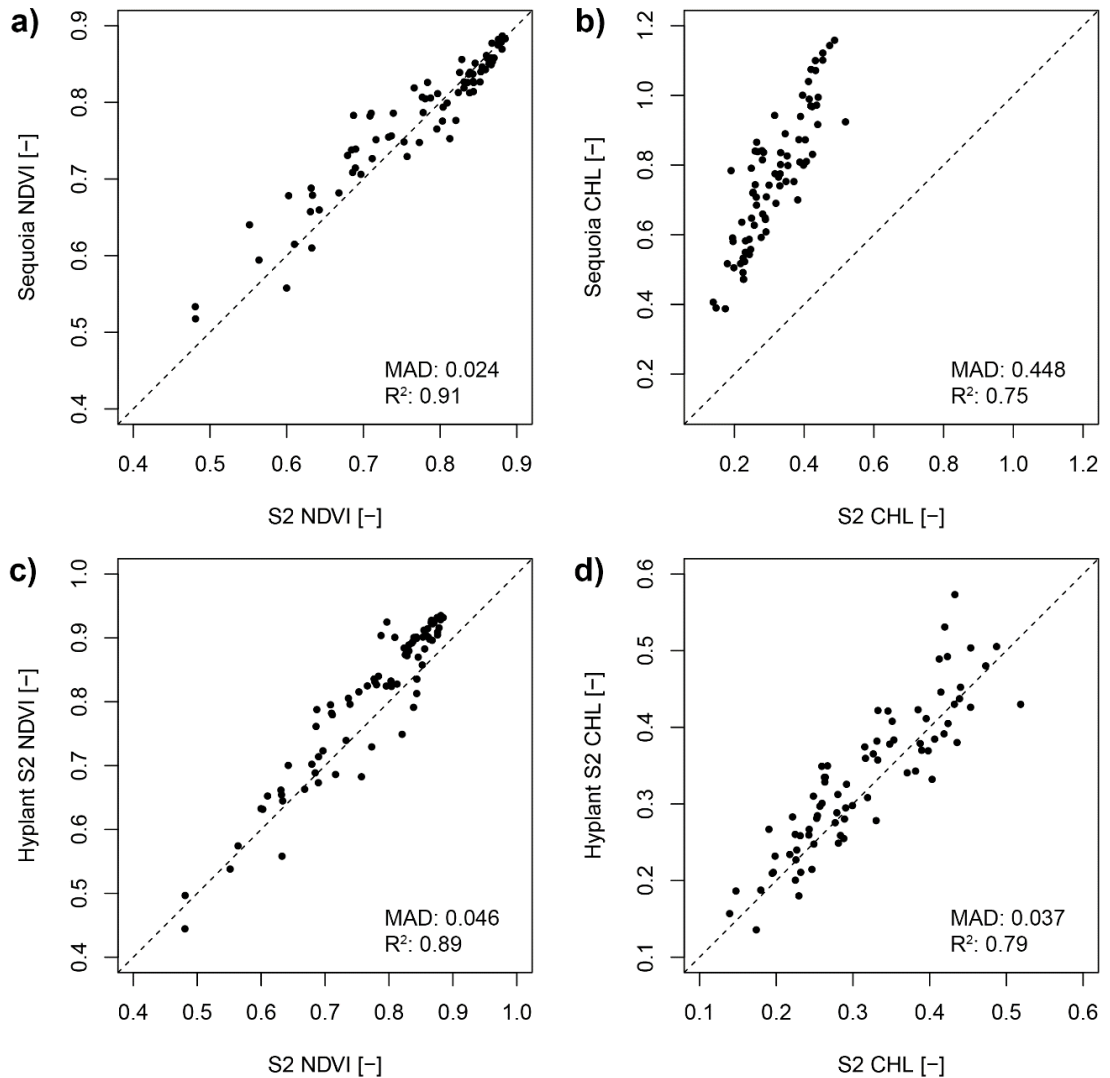


Figure 5-10: Top: Scatterplots of NDVI (a) and CHL values (b) derived from S2 and Sequoia imagery (resampled to 20 m spatial resolution). Bottom: Scatterplots of NDVI (c) and CHL values (d) derived from S2 and HyPlant imagery (resampled to 20 m spatial resolution).

Table 5-5: MAD of Sequoia derived VI values (NDVI and CHL) for the three calibration approaches, estimated from the comparison with HyPlant derived index values.

Calibration Method	MAD NDVI	MAD CHL
Single panel calibration	0.0483 (6.20%*)	0.2429 (50.97%*)
ELM, 0 intercept	0.0468 (6.01%*)	0.2227 (46.73%*)
ELM, 0 intercept, minimum subtracted	0.0387 (4.97%*)	0.2069 (43.42%*)

* relative error.

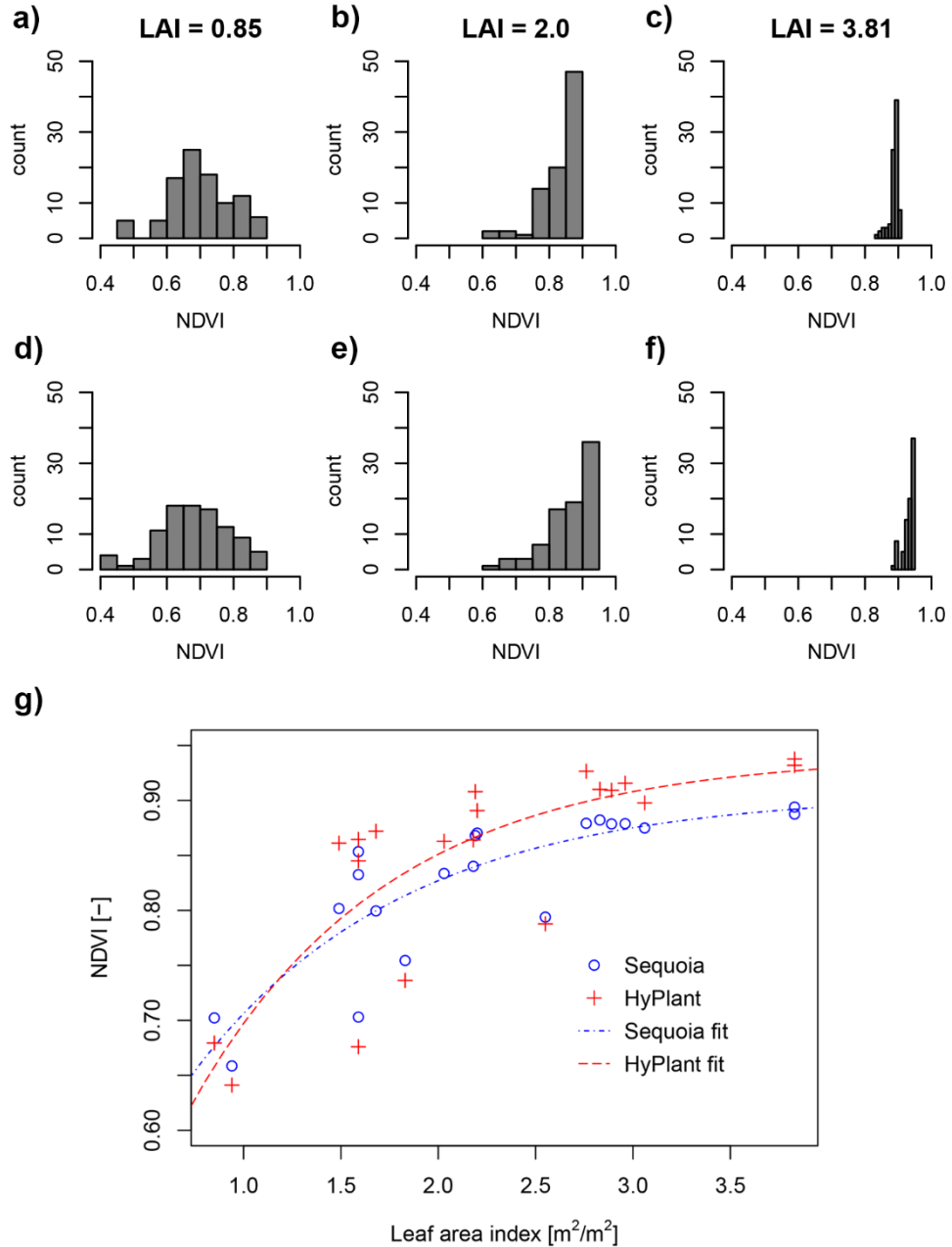


Figure 5-11: Histograms of Sequoia (a–c) and HyPlant (d–f) NDVI values for three 10 × 10 m ESUs of varying LAI. g) NDVI values averaged over ESU extents and the corresponding LAI value measured in the field. Non-linear model fits are provided for illustrative purposes.

5.4 Discussion

5.4.1 HCRF Accuracy

The reference panel validation analysis of HCRF factors showed that Sequoia values tended to overestimate panel reflectance by 4-15% (Figure 5-6, Table 5-2), and that this effect was most severe for lower reflective panels. The magnitude of deviations from field measurements were comparable to those of other vegetation-focused studies using an identical or similar sensor (Padró et al., 2018; Stow et al., 2019). Going further, this study allowed an assessment of HCRF over varied maize canopy cover at high spatial resolutions (1 m) using the HyPlant dataset, where the same trend of overestimated HCRF in the visible bands was observed for densely vegetated pixels (Figure 5-7). The HyPlant dataset itself was shown to be sufficiently accurate to serve as reference for the purpose of this comparison (Table 5-4).

The reason for the overestimation of HCRF for the low reflective panels was likely due to the influence of diffuse scattering and adjacency effects, as pointed out by Tu et al. (2018). Additional spatial smoothing, also affecting the vegetated scene, is caused by projection and stitching which represents an aggregation of pixel values from multiple images during orthomosaic generation. This reduces detector noise but may also lead to bias in measured HCRF. Compensation of this effect could involve kernel-based sharpening/deblurring (Ji and Wang, 2012) but restoring original pure spectral responses is not trivial and there have been no studies investigating methods to be used at centimetre scale spatial resolutions where contamination of multiple neighbouring pixels prevails. For panel-based comparisons and calibration, these forms of adjacency effects can be avoided by resolving a greater amount of pure pixels per target which means flying at lower altitude or deploying larger targets relative to the sensor GSD (Stow et al., 2019).

In addition to adjacency effects, increased temperatures during operation lead to a considerable influence of dark current on measurements (Adler, 2018). Insufficient compensation of this effect as well as the non-linearity of the CMOS sensor during software internal calibration to pseudo-radiance (Eq. 5-1) are further sources of uncertainty (Fallet and Domenzain, 2018; Tu et al., 2018) which may have led to the zero-intercept and modified ELM calibration not yielding

overall improvements. Nevertheless, the strong linear relationships observed for the visible bands in comparison with HyPlant HCRF (green R^2 : 0.82, red R^2 : 0.88, Figure 5-7) highlight potential for improvements of the ELM calibration procedure. The largest deviations between the image datasets of Sequoia and HyPlant HCRF were found over the red-edge band (Figure 5-7, Figure 5-8) and an offset was also observed for the ASD-measured grass target in the field (Figure 5-6). As vegetation reflectance increases sharply within the red-edge spectral region, uncertainties within the SRF and the spectral resampling between HCRF products can be expected to have a large impact on derived Sequoia HCRF. The approximated Sequoia SRF for the red-edge band derived from manufacturer information on filter transmission and CMOS sensitivity may be insufficient. This would explain why no strong offsets were observed for the validation panels with spectrally flatter reflectance responses across the measured wavelength range (Figure 5-6).

Overall, the observed errors are large in an imaging spectroscopy context, indicating that there is still progress to be made in terms of calibration and the implementation of drone MCA data processing and correction procedures within commercial software such as Agisoft Metashape and Pix4D as well as the radiometric calibration reliant on manufacturer calibration coefficients (A, B and C in Eq. 5-1) which result from high-throughput processes (Fallet and Domenzain, 2018). This software implemented workflow is not currently designed with the goal of delivering reproducible scientific data as there is a lack of transparency considering some key processing steps due to commercially sensitive information. The sensor itself is designed for out-of-the box operation in an agricultural context. In order to guarantee robust HCRF from drones, full lab-based characterisation of sensors and absolute radiometric calibration methodology remains a necessity (Hakala et al., 2018), which however comes at considerable financial cost.

The applications of accurate HCRF data from drone platforms are only beginning to be explored. Opportunities include the evaluation of satellite HCRF products and the performance of atmospheric correction (Padró et al., 2018), commonly reliant on point-based measurements of uniform surfaces (Thome et al., 2001) which drone-based measurements can extend to larger, more varied systems. Work towards accurate band-specific HCRFs is further motivated by the ability to provide more information in the context of vegetation biophysical parameter

retrieval for the identification of best suited models e.g. by means of gaussian process regressions (Revill et al., 2019).

While this work showed the current limitations of accurate drone based HCRF retrieval using compact MCA sensors, potential applications motivate the further characterisation of sensor uncertainties and identification of optimal calibration procedures.

5.4.2 Multi-Scale VI Consistency and Sensitivity

Comparisons with the spatially consistent HyPlant product could provide an assessment of orthomosaic product consistency at unprecedented spatial resolution. Spatial variabilities related to acquisition artefacts have been known to influence stitched orthomosaic drone data products (Aasen and Bolten, 2018), but have previously only been evaluated with repeat measurements at different viewing or solar angles (Hakala et al., 2010; Stow et al., 2019). Our findings based on near-simultaneous reference data show that a high level of consistency can be expected even from non-gimbaled drone multispectral measurements which are the default for low-cost practical implementations, e.g. in precision agriculture. However, as directional effects vary greatly depending on plant structural type (Román et al., 2011), there is further need for assessing the impacts on drone-derived VIs over different crops.

The analysis over field-sampled 10 x 10 m ESU plots showed that uncertainties in calibration and radiometry express themselves in a reduced sensitivity of Sequoia NDVI to LAI, assessed against HyPlant NDVI values (Figure 5-11). This demonstrates that efforts towards reliable calibration are important and can yield improvements even for studies only seeking to derive empirical relationships between VIs and biophysical parameters or where relative VI information is used, such as in guided fertiliser application (Toulios et al., 2017).

Despite these observed biases, there was a strong correspondence between drone-derived VIs and the coarser grained HyPlant and S2 datasets (NDVI $R^2 = 0.91$, CHL $R^2 = 0.75-0.9$, Figure 5-9, Figure 5-10), indicating that the drone VIs can reflect variations within maize canopy cover and can be compared across scales. This highlights the potential for integrating drone-based VI measurements within or as alternative to coarser resolution workflows either as validation or

additional measurements at desired time steps for monitoring purposes, such as identifying water limitation or phenology of vegetation canopies (Berra et al., 2019; Easterday et al., 2019). This remains feasible and cost effective for study areas <5 ha (Matese et al., 2015). However, for multi-temporal monitoring, the stability of derived indices to slightly different acquisition conditions (solar angles, atmospheric composition) is of similar importance to spatial consistency and warrants further investigation as particularly solar angle variations have been shown to have a potentially large effect (Stow et al., 2019). This was highlighted by results for the red-edge band in this study, where these temporal changes were visible even between the two drone acquisitions needed to cover the study area (Figure 5-8 c). The long duration of acquisitions during changing illumination conditions represents a major shortcoming of drone-based monitoring (Hakala et al., 2013). The results presented in this study represent an ideal case based off almost-concurrent acquisitions during constant illumination conditions.

Current developments in drone sensor technology will aid in improving within-product consistency and comparability between drone and satellite measurements. Introducing band-pass filters for MCA sensors which closely match those of satellite sensors, such as the MAIA camera with S2 equivalent bands (Revill et al., 2019) will reduce band-position based offset effects. Efforts towards fully gimbaled integrations of cameras and irradiance sensors even on lightweight drones may further remove viewing angle and illumination effects and lead to improved product consistency.

5.5 Conclusions

This study focused on the assessment of accuracy and spatial consistency of drone-based HCRF acquired during ideal illumination conditions, as well as the accuracy of VIs and their comparability to products from other sensors which included a fine-resolution HCRF comparison with simulated spectral bands using the HyPlant DUAL hyperspectral imaging sensor.

MCA derived individual band HCRF values exhibited bias when compared to ASD *in situ* measurements, particularly over lower reflective surfaces with HCRF < 20% and none of the assessed simple calibration procedures (proximal panel calibration, 0 intercept ELM and minimum subtracted 0 intercept ELM) performed consistently better over all spectral bands. HCRF outputs from simplified

calibration procedures should therefore be used with caution and independent assessments using high quality HCRF measurements over large reference targets are encouraged for studies seeking to identify optical properties from drones. Thorough lab-based sensor calibration remains a requirement for reliable physical measurements.

Conversely, the good level of spatial consistency of the drone mounted MCA-derived products and comparability of NDVI values to those of airborne and spaceborne sensors found in this study mean that drone derived VIs show promise for vegetation monitoring at high spatial resolutions as well as improving temporal resolutions of time series for dedicated study sites (e.g. flux tower footprints), in addition to satellite datasets.

While this study mainly assessed HCRF and VIs from drone MCAs in context of coarser spatial resolutions (1 and 20 m GSD), the ability of drone sensors to resolve individual canopies and even leaves, separating them from background and shading effects, harbours great potential for mapping biochemical plant traits at high resolutions. Once reliable solutions for operational calibration of drone MCA HCRF have been found, the investigation of methods and uncertainties in linking HCRF at the centimetre pixel scale to field measured optical properties of individual leaves and canopies is anticipated to be at the forefront of drone-based vegetation research.

6 Monitoring spring phenology of individual tree crowns using drone-acquired NDVI data

Chapter context:

The temporal consistency of drone-derived VI products is important if such sensors are to be useful for multi-temporal monitoring applications at the individual plant level (e.g. identifying changes due to water stress or the timing of spring green-up phenology (Berra et al., 2019; Easterday et al., 2019)). In chapter 5, the accuracy and spatial consistency of VIs derived from drone MCA data were assessed, however, these assessments represent a snapshot in time and don't necessarily inform how well such indices can track changes in vegetation parameters. Studies have shown that time-varying factors such as illumination geometry (which varies based on acquisition time and conditions) can have a measurable effect on VI products (Stow et al., 2019). This calls for further investigation of factors influencing the drone data derived VIs and how these relate to the magnitude of changes to be observed.

This chapter presents two experiments which focus on:

1. investigating the impact of different illumination conditions on drone NDVI data which is considered to be one of the key differences between acquisitions in time;
and
2. demonstrating the use of the drone NDVI time-series to track spring phenology and derive common metrics of green-up timing per tree species.

This study arose rather opportunistically from the identified potential to track spring green-up timing using the NDVI time-series resulting from frequent drone acquisitions performed for chapter 7. This explains the lack of dedicated *in situ* phenological observations to validate individual crown green-up, but differences between species could be investigated using citizen science databases and DHP observations.

This chapter has been accepted for publication as: Fawcett, D., Bennie, J., Anderson, K., 2020. Monitoring spring phenology of individual tree crowns using drone-acquired NDVI data. *Remote Sens. Ecol. Conserv.*

Research questions:

- 1) Are NDVI orthomosaics derived from multi-spectral drone imagery sufficiently robust over time to track changes at individual crown level?
 - a. Is the georeferencing accuracy following standard georeferencing procedures sufficiently high to ensure data are co-registered well enough for time-series reconstruction for individual crowns?
 - b. How large are NDVI variations due to different atmospheric conditions during acquisition?
- 2) Can the drone derived NDVI data reveal phenological differences at the species and individual crown level?
 - a. What species-specific features can be identified from the NDVI time-series?
 - b. How plausible are derived phenological metrics (start-of-spring, middle-of-spring green-up and start-of-peak greenness) and what do they reveal about intra and inter-species variability?

Abstract

Quantifying the timing of vegetation phenology is critical for monitoring and modelling ecosystem responses to environmental change. Phenological processes have been studied from landscape to global scales using Earth observing satellite data, and at local scale by *in situ* surveys of individual plants. Now, data acquired from multi-spectral sensors on drone platforms provide flexible opportunities for monitoring phenology from individual plants to small ecosystem scales efficiently, allowing community and species level information to be derived. We captured a time-series of drone-acquired NDVI data with a multi-spectral sensor (Parrot Sequoia, (Parrot, France)) over a highly heterogeneous ecosystem in Cornwall, UK, during a period of spring green-up. We monitored NDVI trajectories at the individual crown and species' level. For deciduous crowns we derived metrics representative of spring phenological stages: Start-of-spring (SOS), middle-of-spring green-up (MOG) and start-of-peak greenness (SOP) using a logistic function. While the exact timing of SOS, MOG and SOP appeared susceptible to understory effects and saturation of the NDVI, relative timing of green-up for a subset of species was plausible in relation to phenological observations from an extended geographic region and in-situ PAI measurements. In evergreen vegetation (*Pinus* spp.) subtle changes were also detected through the growing season. The impact of illumination differences was analysed for image pairs during leaf-off and leaf-on conditions. While significant, these effects were small (mean absolute NDVI deviation of up to 0.034 for leaf-off, 0.013 for leaf-on conditions), meaning that data captured under both constant direct and diffuse irradiance conditions can be used together and that cloudy conditions should not lead to data gaps. We conclude that the capability of drone-mounted multi-spectral instruments for spatio-temporal characterisation of crown-level phenology shows great promise for improving the understanding of intra- and inter-species differences in strategy, and offers an efficient means of doing so over areas of a few hectares.

6.1 Introduction

The advantage of centimetre scale spatial resolution remote sensing in the vegetation context lies within its ability to resolve the fundamental ecological unit: individual plants (Marconi et al., 2019). In mixed species ecosystems, resolving individual plant crowns is necessary if seeking to analyse species-specific phenological trends, plasticity and responses to extreme events, e.g. the earlier green-up of some species in response to shifts in temperature and consequently growing degree days (Vitasse et al., 2010), or the expression of stress (Adams et al., 2015). It has previously been concluded that satellite-based data are not suitable for monitoring the phenology of individuals or species (Polgar and Primack, 2011). A wealth of satellite based studies on tree phenology has predominantly focused on the ecosystem, landscape or forest stand scale (Melaas et al., 2013; Pastor-Guzman et al., 2018; Pennec et al., 2011; Walker et al., 2012). While studying species-level phenology using satellite data is possible, it requires larger mono-species regions due to spatial resolutions which are too coarse (>10 m) to resolve individuals in mixed species systems (Berra et al., 2019; Delbart et al., 2005; Han et al., 2013; Liu et al., 2017). In order to investigate species specific phenology, to relate this to local conditions as well as quantify the effect of landscape heterogeneity on large-scale satellite derived metrics efficient monitoring at the individual level is required (Klosterman et al., 2014). The lack of ecosystem-scale ground phenological data which can serve as reference over adequately large spatial extents (e.g. 250 m pixels) has previously been highlighted as a major limiting factor for the validation of satellite derived estimates (Cleland et al., 2007). The use of fine spatial resolution satellite data (e.g. WorldView, PlanetScope) is limited due to their financial cost and missing observations in areas with frequent cloud cover (Bolton et al., 2020; Hufkens et al., 2012). The remote observations which best enable phenological monitoring at the species and individual level are cameras mounted *in-situ*, such as the global network of phenocams providing daily measurements (Brown et al., 2016; Polgar and Primack, 2011). However, phenocam images suffer limitations due to oblique viewing angles such as measurement saturation at low leaf-area-index (Keenan et al., 2014) and canopy occlusion resulting in limited spatial coverage.

Recently, the acquisition of crown time-series data over areas of multiple hectares in extent has become a possibility through drone platforms. Drones provide advantages over phenocams by covering larger areas with close to nadir view angles enabling calibrated reflectance based metrics (Piao et al., 2019) and unlike optical satellite instruments can acquire useful data during overcast conditions. Coverage limitations of drones (approx. 5 ha according to a cost-benefit analysis of acquisitions by multi-rotor (Matese et al., 2015)) means that drone-based surveys are best suited to capture data over plot scales that are broadly representative of a larger region, e.g. exhibiting similar species composition and climatic conditions. As compared to surveys using piloted aircraft or commercial satellite imagery, drone-based acquisitions can be lower cost (dependant on the size of the study site, accessibility and cost of labour) with the only limitations to revisit times for data acquisitions being meteorological conditions and accessibility of the study site (Duffy et al., 2017).

Drone-based monitoring of phenological transitions of individual tree and shrub crowns has recently been proven possible (Berra et al., 2019; D'Odorico et al., 2020; Klosterman et al., 2018; Park et al., 2019). Most such studies use primarily RGB (red, green and blue band) photography from consumer-grade cameras (Berra et al., 2019; Klosterman et al., 2018; Park et al., 2019). Supplementing RGB with information from the near-infrared (NIR) where healthy green vegetation is highly reflective allows the derivation of plant indicators such as the NDVI which shows the presence and measures the photosynthetic capacity of the canopy (Tucker, 1979). It has previously been shown that NDVI remains more sensitive to leaf development beyond the saturation point of RGB based indices (Brown et al., 2017). NDVI from modified consumer-grade cameras proved poor at crown scale (Berra et al., 2019), but compact radiometric, multi-spectral sensors are now widely available for lightweight drones and allow for simultaneous narrow-band NIR measurements enabling potentially, more robust NDVI-based monitoring of changes in vegetation (Aasen et al., 2018; Duan et al., 2017), and which can also be customised to monitor evergreen species phenology using pigment indices (D'Odorico et al., 2020)

Data from drone-based multi-spectral sensors thus appear promising for the reliable monitoring of leaf development from budburst to senescence and the subsequent derivation of phenological stages. Knowledge of the robustness of

this data and its sensitivity to changes over time is however crucial and as yet, untested. Specifically, the geometric consistency (Marques et al., 2019) and the reproducibility of vegetation products under varying illumination conditions (Damm et al., 2015b; Gamon et al., 2006; Lee and Kaufman, 1986) should be assessed, which leads to specific questions that are posed in this study.

We investigated the robustness of the NDVI time-series and sought to extract phenological indicators of spring green-up at the individual level from drone-based radiometric, multi-spectral data captured through a spring green-up time-series. In particular, we set out to answer the following research questions:

- 1) Are NDVI orthomosaics derived from multi-spectral drone imagery sufficiently robust over time to track changes at individual crown level?
 - a. Is the georeferencing accuracy following standard georeferencing procedures sufficiently high to ensure data are co-registered well enough for time-series reconstruction for individual crowns?
 - b. How large are NDVI variations due to different atmospheric conditions during acquisition?
- 2) Can the drone derived NDVI data reveal phenological differences at the species and individual crown level?
 - a. What species-specific features can be identified from the NDVI time-series?
 - b. How plausible are derived phenological metrics (start-of-spring, middle-of-spring green-up and start-of-peak greenness) and what do they reveal about intra and inter-species variability?

Answering these questions represents an important step towards the operational drone-based monitoring of phenology at the individual crown level.

6.2 Materials and Methods

6.2.1 Study site

The study site “Trelusback Farm” is located in west Cornwall, UK ($50^{\circ}12'10.0''N$ $5^{\circ}12'22.6''W$) with the studied area covering 4.5 ha. It is managed for the purpose of wildlife conservation and includes a small mixed woodland of predominantly sweet chestnut (*Castanea sativa*), sycamore (*Acer pseudoplatanus*) and alder (*Alnus glutinosa*) as well as isolated free-standing trees and shrubs, mainly hawthorn (*Crataegus monogyna*), oak (*Quercus spp.*), grey willow (*Salix cinerea*) and gorse (*Ulex europeaus*). The site was selected due to its tree species richness, accessibility and due to being a heterogeneous system with variation in canopy density which is a common feature of many natural and semi-natural ecosystems worldwide.

6.2.2 Drone data acquisition and processing

Data were acquired between 22 March 2019 and 23 July 2019 using the Parrot Sequoia MCA (Parrot, France), which possesses four cameras with different band-pass filters in order to record light in the green (550 nm, 40 nm bandwidth), red (640 nm, 40 nm bandwidth), red-edge (735 nm, 10 nm bandwidth) and NIR (790 nm, 40 nm bandwidth) wavelength regions. The Sequoia also records irradiance in equivalent bands with an upward-facing irradiance sensor. The camera was mounted on a 3DR-Solo lightweight quadcopter. For multi-spectral data acquisition, the drone was flown in a pre-programmed north-south lawnmower pattern at 5 m/s ground speed and 70 m altitude in order to be able to cover the entire study site within a single flight with approx. 9 minutes acquisition time. This resulted in 8.1 cm mean GSD and >80% frontal and lateral image overlap as advocated by other studies using the Parrot Sequoia sensor (Assmann et al., 2019; Tu et al., 2018). Visual reference datasets for crown discrimination were acquired using a consumer-grade RGB camera (Ricoh GR II), mounted on the same platform and flown at 6 m/s ground speed and 60 m altitude. Six GCPs were deployed in the field (see Figure 6-1 for reference), distributed following recommendations by James and Robson, (2014) to minimize systematic error within the photogrammetric processing. Two GCPs were

redeployed in slightly different locations on 19 April 2019 and 19 May 2019 respectively due to sub-optimal coverage and plant over-growth. Due to the limited number of GCPs, all were used within the photogrammetric processing workflow to guarantee the best possible georeferencing of the output. For an independent investigation of georeferencing accuracy, a subset of three datasets (22 March 2019, 19 April 2019, 23 July 2019) were assessed by excluding a GCP as check-point and processed using the Pix4D (version 4.4.12, Pix4D, Switzerland) photogrammetric software. Pix4D was then used to generate a multi-band orthomosaic for each date from single band images, using the “Ag Multispectral” processing template. Noise filtering and medium surface smoothing were enabled. Keypoints image scale was set to full with a targeted number of 10'000 keypoints. Half image scale was used for densification and point density was set to “optimal”. Pix4D applies camera specific corrections (lens distortion and vignetting), the conversion of DNs to pseudo-radiance (values homogenous to actual radiance (Parrot, 2017b)) and the further calibration to surface reflectance using reference images of a levelled 50 x 50 cm panel of 44% nominal reflectance across all four bands of the Sequoia sensor (MosaicMill, Finland) taken prior to or post-flight (see Fawcett and Anderson, (2019) for more details on the calibration method). The panel reflected pseudo-radiance in the red and NIR bands was derived from calibration images and reported in Tab. SI1 as an indicator of irradiance conditions. Data from the irradiance sensor were used to eliminate possible small differences for data acquired during diffuse conditions but could not be applied to two diffuse acquisitions following 11 July 2019 due to malfunctioning of the irradiance sensor connection. The impact of this is expected to be small due to homogeneously overcast skies. The described workflow allows a more straight-forward calibration of the data to surface reflectance compared to modified off-the shelf digital cameras (Holman et al., 2019).

Acquisitions were conducted when weather and illumination conditions were suitable with more frequent (approx. twice per week) sampling around the start of green-up for the majority of crowns in the study site and aiming at weekly sampling thereafter with longer intervals when conditions were not suitable (see Table A 2 for dates). Data were acquired during either homogeneously overcast diffuse (9 observations) or clear sky direct (11 observations) illumination conditions. Requiring homogeneous conditions throughout single acquisitions

limited the sampling frequency but was considered essential due to direct/diffuse irradiance transitions introducing considerable bias in VI estimates which can not be fully compensated by the use of unstabilised irradiance sensor measurements (Fawcett and Anderson, 2019; Suomalainen et al., 2018). Finally, the surface reflectance (ρ) product of the red and NIR bands were used to generate the NDVI (Eq. 6-1).

$$NDVI = \frac{\rho_{NIR} - \rho_{red}}{\rho_{NIR} + \rho_{red}} \quad (6-1)$$

The NDVI as a metric of choice for vegetation monitoring over time is merited due to its sensitivity to the physical parameters of interest as well as greater consistency compared to common metrics derived from uncalibrated RGB photography (Yao et al., 2017).

6.2.3 Field reference data

A sample of individual trees (206 total) was manually digitised from the RGB orthomosaic and the species determined following a GPS-assisted field survey and visual interpretation of the RGB data. A 1.5 x 1.5 m concrete surface within the study site served as unvegetated reference to control for erroneous NDVI variability over the duration of the study (Figure 6-1).

To investigate the relationship of crown NDVI values with PAI during spring green-up, a transect of DHPs through the woodland and DHPs at 10 locations below individual crowns were taken on 10 dates from pre budburst of most species to full leafing out. 6 dates corresponded directly to drone acquisitions during diffuse conditions and the maximum difference in time between drone and DHP acquisition dates was 5 days. DHPs were taken using a Nikon D7000 with a Sigma 4.5mm F2.8 EX DC HSM Fisheye lens, along north-south transects with 5 m spacing during periods of no direct sunlight (mostly overcast, some with scattered clouds). For individual crowns, DHPs were taken close to the stem and the image sector containing the stem was masked. Each image was processed using the Hemisfer software (version 2.2, WSL, Switzerland), applying the LAI-2000 algorithm as implemented by Li-Cor (USA), and the Li-Cor recommended

adjustments for individual crowns (Cutini and Varallo, 2006), detailed in the supplementary information. Areas of interest with the transects at their centre of approx. 17 m width and 75 m total length for the woodland and manually delineated individual crowns were extracted from the NDVI raster datasets to yield a time-series of NDVI mean and standard deviation. For direct comparison with PAI observations of non-matching dates, linear interpolation of the NDVI observations was performed.

Dates of budburst and emergence of the first leaf were extracted for 7 of the analysed species from the Woodland Trust's "Nature's Calendar" which displays data collected by the UK Phenology Network (UKPN), for comparison with identified phenological metrics. This analysis was constrained to the counties of Cornwall and Devon (South West England) and the same year (2019) to account for climatic variations.

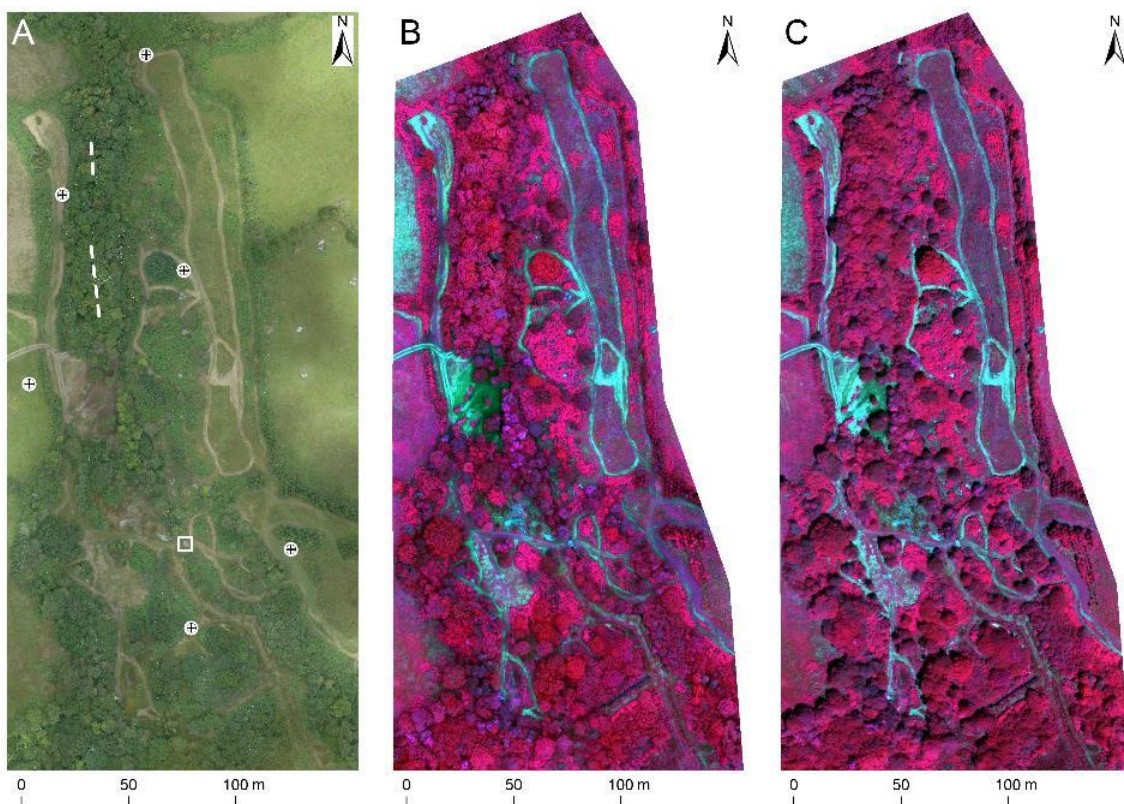


Figure 6-1: A: RGB orthomosaic from consumer-grade camera images as overview of the Trelusback Farm study site in Cornwall, UK ($50^{\circ}12'10.0"N$ $5^{\circ}12'22.6"W$) on 22 July 2019, with crosses indicating GCP locations, dashed lines the locations of DHP transects and the square showing the location of the concrete reference surface. B and C: False-colour orthomosaics from Parrot Sequoia image data (red: NIR band, green: red band, blue: green band) of the study site, B: on 22 July 2019 with overcast conditions resulting in diffuse illumination and C: on 23 July 2019 with cloud free conditions resulting in direct illumination with clearly visible cast shadows.

6.2.4 Assessment of crown NDVI values in direct versus diffuse conditions

At opposite ends of the time-series, during leaf-off and leaf-on conditions, repeat acquisitions during contrasting illumination conditions with only 1-2 day time difference were acquired (22 March and 24 March, 31 March and 1 April, 22 July and 23 July 2019). These were used to assess the impact of differing illumination conditions on retrieved crown NDVI.

NDVI density distributions for all crown pixels were generated. Furthermore, the coefficient of determination (R^2), MAD and bias between the direct and diffuse NDVI values were compared for different crown aggregation metrics. The metrics assessed were the mean, median, and the mean after masking all but the 20% brightest pixels in the green band, per crown, a recommended method for mitigating the influence of the crown background (Berra et al., 2019). A two sample t-test was performed with the null hypothesis that the means of the direct and diffuse per-crown NDVI values were identical.

6.2.5 Green-up modelling and phenophase estimation

Established methods for extracting start-of-spring green-up (SOS), middle-of-spring green-up (MOG) and start-of-peak greenness (SOP) were applied to the NDVI time-series data spatially aggregated at crown-level. Per-crown data was extracted based on the digitised crown extents and using the 20% brightest pixel method described in section 2.4. As this analysis only covered vegetation green-up, NDVI progression was modelled by a single logistic function (Liu et al., 2019; X. Zhang et al., 2003). We used the following generalised logistic function:

$$y(t) = \frac{c}{1 + e^{-b(t-a)}} + d \quad (6-2)$$

Where a through d are fitting parameters representing a : the value of t at the inflection point, b : the growth rate, c : the amplitude of increase and d : the lower asymptote. Eq. 6-2 was fitted to the data using the “nls” function in the R stats package. After successful fitting of the model, the minima and maxima of the rate of change of curvature, calculated using the first and second derivatives of Eq. 6-

2 could be used to identify SOS, MOG and SOP (Klosterman et al., 2014) (Figure 6-2).

In a preliminary analysis it was observed that the flowering of hawthorn resulted in a period of low NDVI within the time-series which led to failure during model fitting. As the flowering event does not represent the spring green-up modelled here (obscuring the signal of leaves), four hawthorn observations during this period (May to mid June) were excluded from the data used to fit the logistic function.

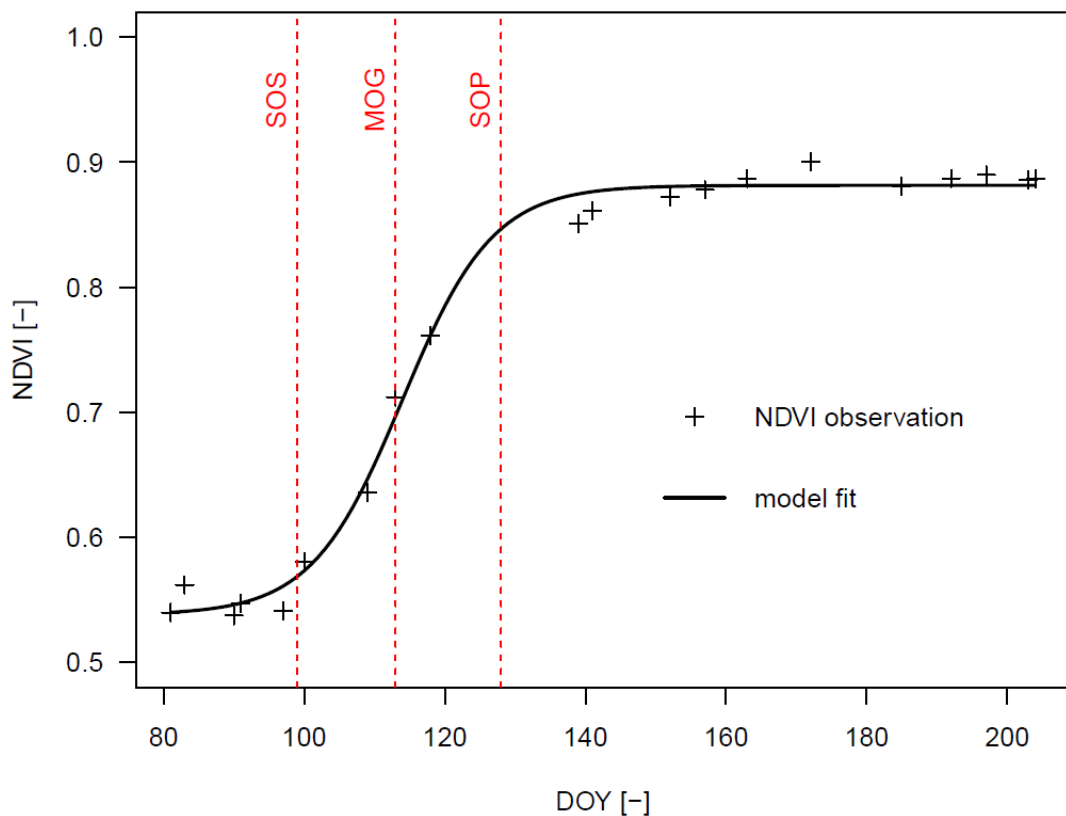


Figure 6-2: Example of a sigmoid model fitted to NDVI data of a grey willow crown from this study, with vertical lines indicating the timing of SOS, MOG and SOP, determined based on the rate of change of curvature.

6.3 Results

6.3.1 *Surface reflectance and NDVI orthomosaics*

20 surface reflectance orthomosaics (Figure 6-3, irradiance conditions for each are given in Table A 2) were generated with a mean reported georeferencing error of 0.023 m (standard deviation: 0.012 m). When using one GCP as check-point, assessed for three datasets, the mean horizontal error (XY) was 0.023 m, while the mean vertical error (Z) was 0.149 m. As the horizontal error was lower than 1 GSD, the orthomosaic products had minimal visual spatial offset.

For the cloud-free acquisitions pre green-up, there were a lack of identified tie-points within sparse tree crowns and an increased number of points identified on the ground below resulting in an incorrect representation of some crowns within the generated DSM and consequently in the NDVI orthomosaics due to mosaicking issues. This could not be mitigated by disabling surface smoothing and noise filtering in Pix4D. For overcast acquisitions and post-green-up, crown shapes were found to be highly consistent.

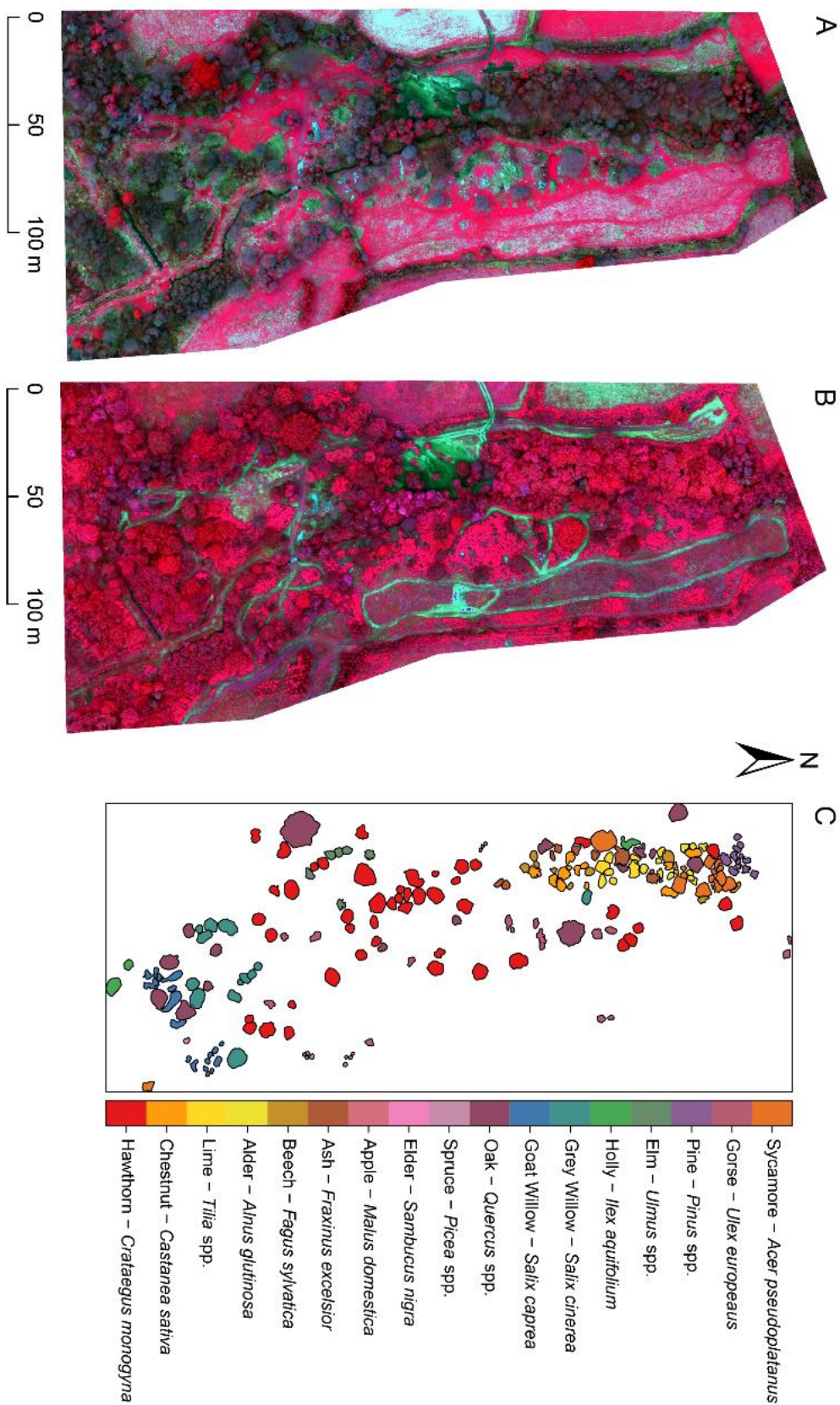


Figure 6-3: False-colour infrared representations (red: NIR band, green: red band, blue: green band) of surface reflectance orthomosaics of the study site generated from drone acquired multispectral images during a) leaf-off (22.03.2019) and b) leaf-on (22.07.2019) conditions. (colour range scaled to better match reflectance value range of leaf-off image) c) A map of the digitised tree samples colour coded by species.

6.3.2 NDVI sensitivity to illumination and aggregation metrics

Visual evaluations of surface reflectance products resulting from acquisitions during contrasting direct and diffuse illumination conditions showed that direct illumination resulted in cast shadows, either from the crowns on the ground or within crowns due to their structure. These shadowed areas were not as apparent in the NDVI product as it is formed by band ratios but fine-scale variations were visible within single crowns if scaled appropriately (Figure 6-4).

The density distributions of all crown NDVI values for two leaf-off and one leaf-on snapshot (Figure 6-5) revealed that direct illumination conditions led to a larger spread in values both pre and post green-up. The differences for leaf-off conditions were assessed using two pairs of dates and ranged from 3.4% to 5.4% for the first, depending on aggregation metric, to no significant differences for the second image pair (Table 6-1). The differences in red to NIR band ratios of the calibration panel reflected pseudo radiance (Table A 2) for the three pairs were 0.42, 0.27 and 0.25 (a, b and c in Figure 6-5). The mean and median metrics did not show large differences in terms of R^2 , MAD and bias. R^2 values were however lower if only the 20% brightest pixels were considered.

For the concrete reference surface, the standard deviation of NDVI over the entire time-series was 0.0403. A two-sample t-test showed that there was no significant difference between the means of the diffuse and direct measurements for this surface (p -value = 0.216, 95 percent confidence interval: [-0.0635, 0.0157]).

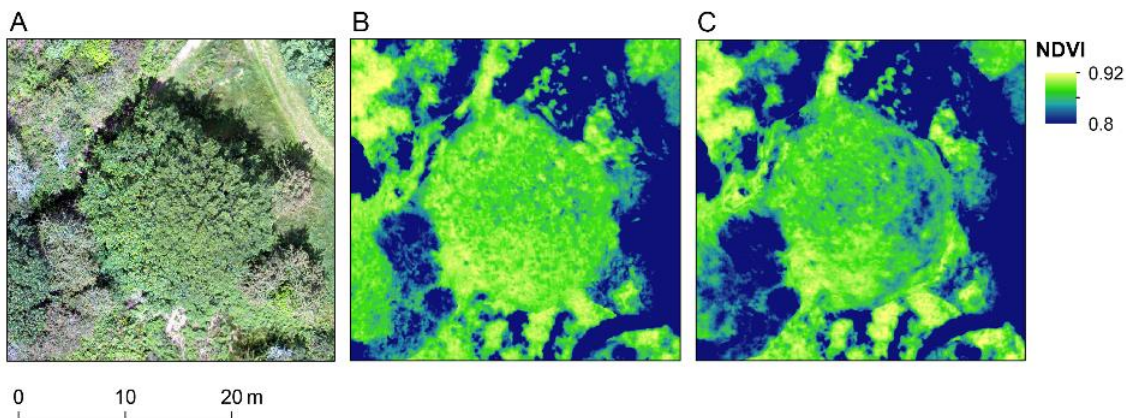


Figure 6-4: A fully greened-up single oak tree crown on the study site ($50^{\circ}12'07.6''\text{N}$ $5^{\circ}12'23.6''\text{W}$), imaged a) in true-colour using a consumer grade camera and its NDVI derived from multi-spectral imagery during b) overcast (10:51, 22 July 2019) and c) cloud-free conditions (11:48, 23 July 2019). The colour scale is scaled between 0.8 and 0.92 to reveal small NDVI differences within the crown between acquisitions.

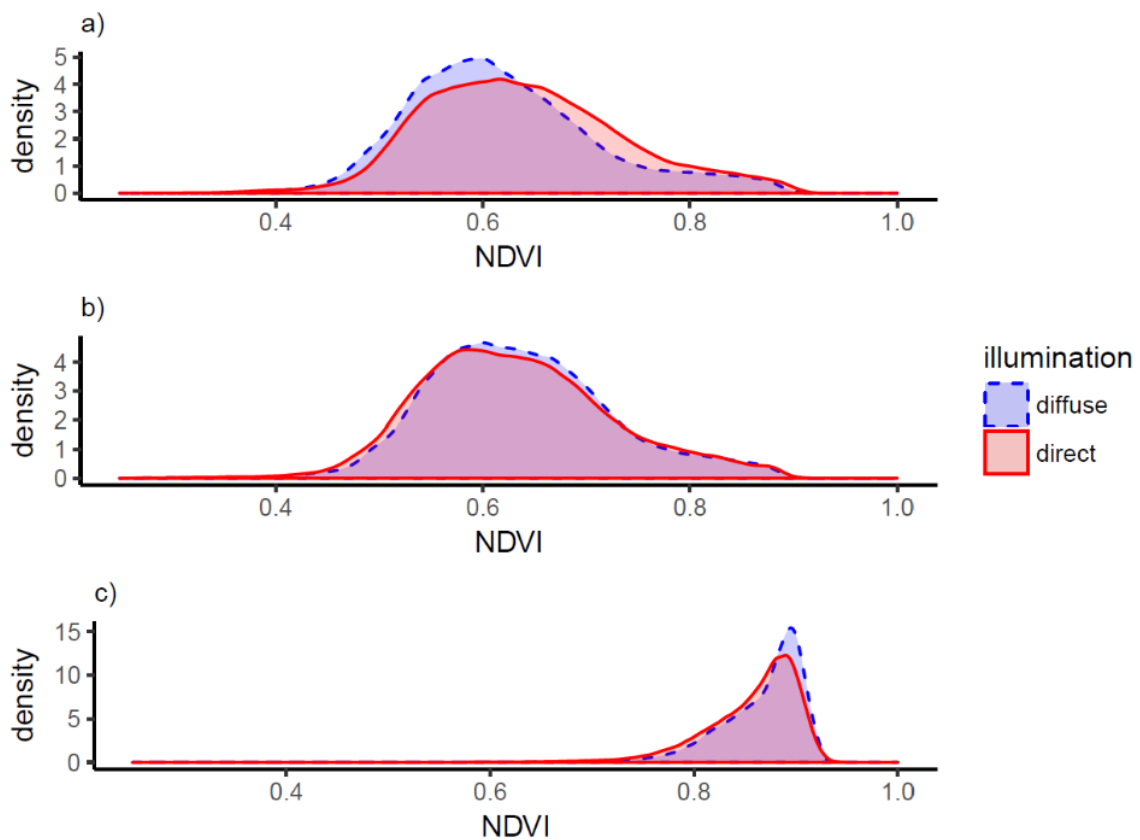


Figure 6-5: Density distributions of crown pixel NDVI values (all pixels of delineated crowns, see Figure 6-3 c), for leaf-off and leaf-on stages during contrasting illumination conditions (direct and diffuse). a) leaf-off NDVI values for 22 March 2019 (diffuse) and 24 March 2019 (direct), b) leaf-off NDVI values for 31 March 2019 (direct) and 1 April 2019 (diffuse) and c) leaf-on NDVI values for 22 July 2019 (diffuse) and 23 July 2019 (direct).

Table 6-1: Relationship between crown NDVI values extracted from drone orthomosaics acquired during direct and diffuse illumination conditions for leaf-off and leaf-on stages. The dates included in this analysis for leaf-off are a) 22 March 2019 (diffuse) and 24 March 2019 (direct), b) 31 March 2019 (direct) and 1 April 2019 (diffuse), and c) for leaf-on are 22 July 2019 (diffuse) and 23 July 2019 (direct). This relationship is assessed for different aggregation metrics to derive crown NDVI values: Median, mean, and the mean of the 20% brightest pixel method. (assessed using R², MAD, bias and a t-test for significant differences between aggregated values for direct and diffuse acquisitions).

a) Leaf Off	Median	Mean	Mean, 20% brightest
R ²	0.957	0.957	0.863
MAD	0.0236 (3.6 %)	0.0226 (3.4 %)	0.0344 (5.4%)
Bias (Direct-Diffuse)	+0.0220	+0.0211	+0.0292
t-test (p-val)	0.0047	0.0041	0.0002
b) Leaf Off	Median	Mean	Mean, 20% brightest
R ²	0.979	0.976	0.895
MAD	0.01 (1.5%)	0.0097 (1.5%)	0.0203 (3.25%)
Bias (Direct-Diffuse)	-0.0034	-0.0027	+0.0017
t-test (p-val)	0.6392	0.6974	0.8249
c) Leaf On	Median	Mean	Mean, 20% brightest
R ²	0.946	0.941	0.774
MAD	0.0096 (1.1 %)	0.0099 (1.2 %)	0.0125 (1.5%)
Bias (Direct-Diffuse)	-0.0086	-0.0090	-0.0093
t-test (p-val)	0.0088	0.008	0.0232

6.3.3 NDVI time-series

Individual crown mean NDVI values of the 20% brightest pixels in the green band were extracted from all drone orthomosaics based on the digitised extents (Figure 6-3 c). These were combined to represent the mean NDVI and standard deviation time-series per species within the study site (Figure 6-6). There was one observation less for spruce (*Picea* spp.) due to incomplete coverage of one acquisition, indicated by a gap in the time-series. Results from an identical analysis which did not include the brightest pixel extraction step and instead aggregated all crown NDVI values are included in the supplementary information (Figure A 3). The concrete reference surface revealed some significant variability between acquisitions. Some of these effects were visible in crown NDVI time-

series, such as a slight dip and subsequent spike in NDVI at DOYs 157 and 163, most prominent for gorse and goat willow (*Salix caprea*). Further variability was visible pre green-up (approx. DOY 80 to 100) which was related to different illumination conditions. This was not as evident when averaging over all crown pixels (Figure A 3). The reduced contribution of the understory for the brightest pixels method was expressed as lower NDVI prior to the green-up (or baseline NDVI) of the overstory for most species (Figure 6-6, Figure A 3). The mean difference between NDVI pre green-up and post green-up (using means of the first three and last three acquisitions) for deciduous crowns was 0.252 for the brightest pixels method and slightly lower when using the mean of all pixels (0.234).

The time-series of PAI and mean NDVI for the woodland revealed that the NDVI increased prior to any significant leaf expansion, as PAI remained low (Figure 6-7). The NDVI plateaued around DOY 160 while PAI continued to rise. This behaviour is reproduced at the individual crown scale (Figure A 4), though there is more variability in the NDVI-PAI relationship between species.

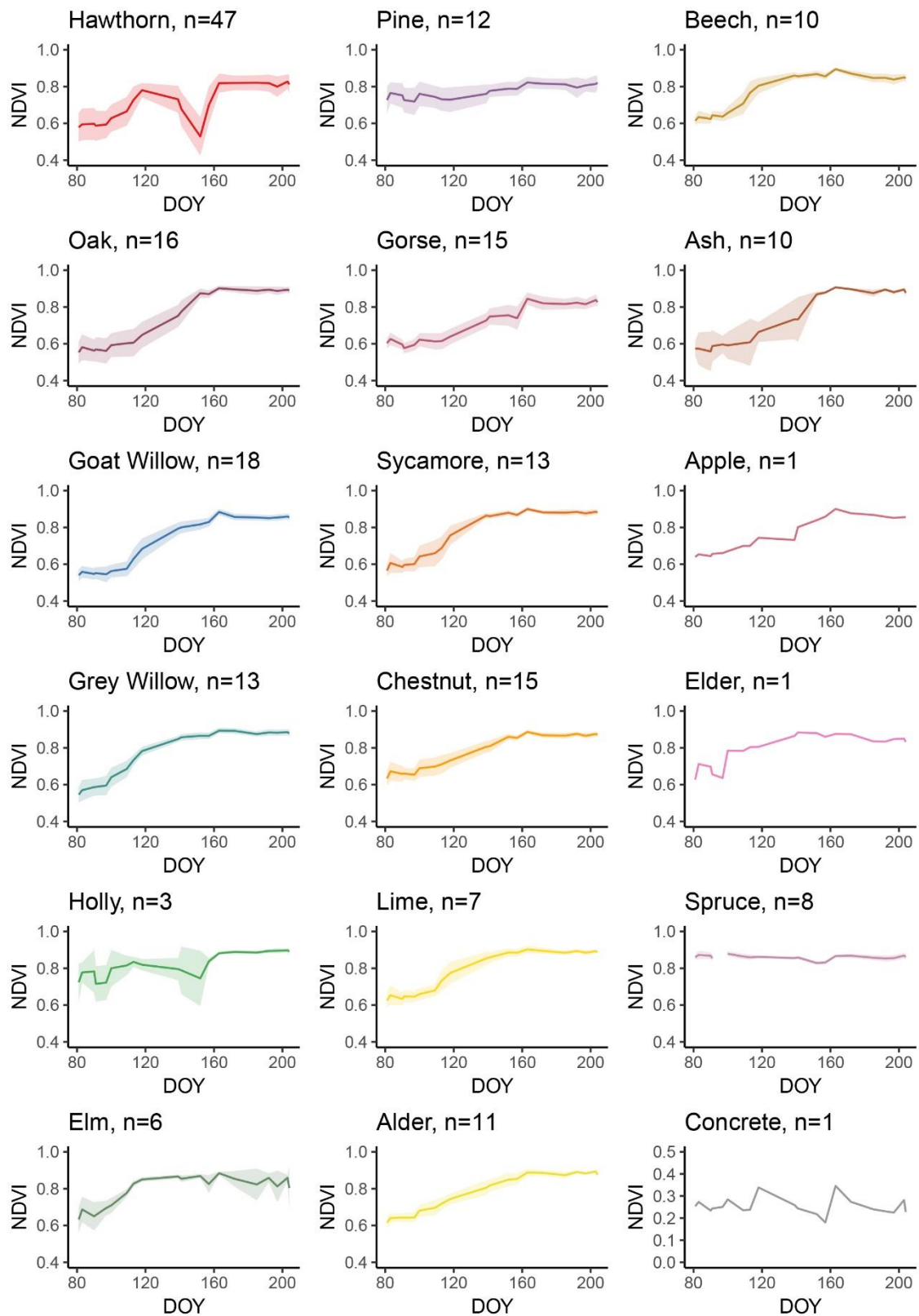


Figure 6-6: Time-series of NDVI per species from 20 drone acquisitions, covering the period of spring green-up. NDVI values are aggregated per crown using the mean of the 20% brightest pixels in the green band. Lines represent the means and ribbons the standard deviation of all individual crown NDVI values per species. The NDVI time series of the concrete reference surface is also included. Species names and number of individuals (n) are reported.

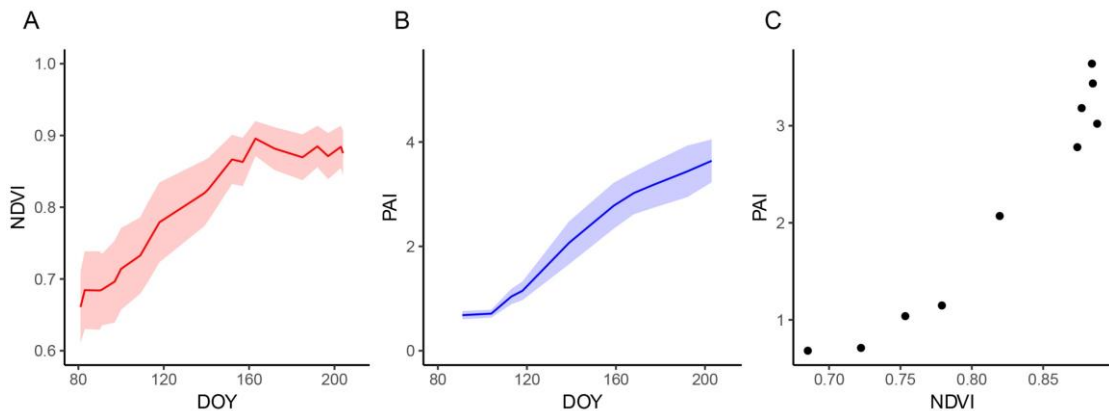


Figure 6-7: Time-series of a) NDVI from drone acquisitions ($n = 20$) and b) PAI from DHP ($n = 10$) averaged over the woodland transects (see Figure 6-1). The ribbons represent \pm one standard deviation in NDVI and PAI respectively, c) depicts the NDVI-PAI relationship with NDVI values linearly interpolated where they don't correspond to PAI observation dates.

6.3.4 Extracted species phenophases

For deciduous species, the logistic function was successfully fitted to most of the individual crown NDVI time-series (164 out of 168). Fitting failed for four crowns due to noisy NDVI time-series including outliers, caused by differences in image orthorectification due to complex crown geometry. Mean residual standard errors (RSE) per species are reported in the supplementary information (Table A 3). The SOS, MOG and SOP DOYs were extracted from the fitted function (Figure 6-8). In 14 individual cases (mostly grey willow and sweet chestnut) the SOS could not be extracted due to the first maximum in rate-of-change of the curvature of the fitted model lying beyond the bounds of the analysed time-span (prior to DOY 80) and the corresponding MOG and SOP values were excluded due to poorly constrained fits. The largest within-species variation of metrics could be observed for SOS, particularly for ash (*Fraxinus excelsior*), oak, and chestnut. A comparison of the same metrics extracted using the mean NDVI of all crown pixels (Figure A 5) showed that there were differences in green-up timing depending on the method used. SOS was found to be approx. 1.5 days later, MOG 1 day earlier and SOP 3 days earlier averaged over all classes when using the 20% brightest pixels (Table A 5). Comparisons of the median identified SOS date with mean budburst and first leaf dates of 7 species from UKPN observations

in South West England revealed that SOS was closer in time to first leaf than to budburst for all species except alder and ash, which were close to budburst (8.4 and 1.11 days difference) (Table A 4). All median SOS dates were within ± 1 standard deviation from the mean first leaf dates except for hawthorn and elder where reported dates fall prior to the first drone acquisition.

For evergreen species the changes in NDVI were very small and the extraction of phenological metrics based on the logistic function are expected to be uncertain. The function could not be fitted to spruce and holly time series due to no consistent NDVI increase. Pines exhibited a small NDVI increase and phenological metrics could be extracted which are reported in the supplementary information (Figure A 6). Gorse was excluded from this analysis due to flowering-related variations throughout the spring.

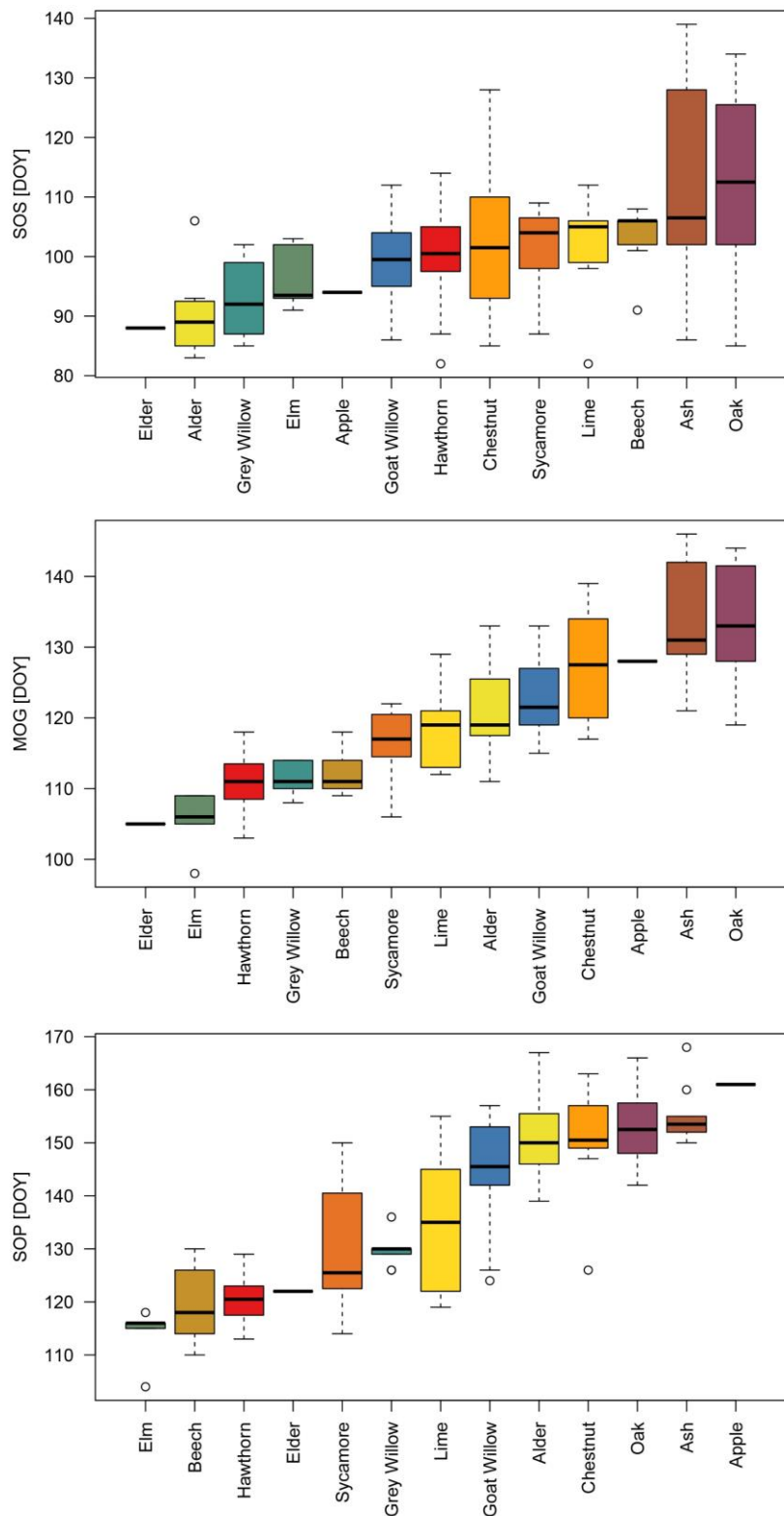


Figure 6-8: Boxplots of SOS, MOG and SOP of all individual deciduous crowns grouped by species and ordered by mean values. The bold line represents the mean value, the lower and upper bounds of the boxes represent the 25th and 75th percentiles, the whiskers extend to the furthest values from the mean within 1.5 times the interquartile range and the circles are identified as outliers beyond this range.

6.4 Discussion

6.4.1 Robustness of drone based NDVI time-series

NDVI data from drone based multi-spectral images can effectively track seasonal changes at crown level. Visual assessments of extracted time-series separated by species (Figure 6-6) showed clear differentiation between many species with feasible, gradual increase of NDVI for deciduous crowns starting at different times throughout the spring while evergreen crowns such as the spruce showed very little variation.

While optical satellite data has proven effective for classifications of tree species from landscape scale to individual level by incorporating information from different phenological stages or sensors with fine spatial resolution (Immritzer et al., 2019; Persson et al., 2018; Wagner et al., 2018) as well as for monitoring forest phenology (Han et al., 2013; Pastor-Guzman et al., 2018; Prabakaran et al., 2013; Walker et al., 2012), the latter is predominantly based on medium to coarse resolution data (e.g. Sentinel 2: 10-20 m, Landsat: 30 m, MODIS: 250 m) which results in mixed pixels for heterogeneous ecosystems such as the study site presented here and are influenced by soil background effects and understory vegetation (Boyd et al., 2011; Ryu et al., 2014). The ability to resolve individuals and separate species phenology even within small mixed tree stands overcomes these limitations. Drone data however include different uncertainties related to platform, acquisition and data processing, which our results suggest should be assessed robustly by users to confirm time-series reliability.

A prerequisite for the time-series analysis at individual crown level is a high georeferencing accuracy of the drone-based products. Here a horizontal error smaller than one GSD was achieved through the use of 6 well-distributed GCPs which proved sufficient without requiring further co-registration of the datasets. The GCP approach remains the method of choice for multi-temporal studies from drone platforms (Berra et al., 2017; Van Iersel et al., 2018), yet in forest environments with canopy occlusion doing so remains a challenge (Wallace et al., 2016). Developments of direct georeferencing using RTK or post-processing kinematic (PPK) solutions show promise to facilitate high accuracy drone surveys

of these systems (Forlani et al., 2018; H. Zhang et al., 2019) and marker-free co-registration approaches may be applied if absolute geolocation is not necessary to further reduce equipment and survey costs (Poblete et al., 2018; Scheffler et al., 2017).

A further constraint on drone-based time-series monitoring is the impact of different illumination conditions on data quality. The effects of dominantly direct or diffuse illumination are challenging to correct (Hakala et al., 2013) and lead to major impacts in band-ratio indices if individual bands are not perfectly aligned (Berra et al., 2019). The alignment issues were mitigated by the MCA sensor and software-based workflow utilised in this study as the red and NIR spectral bands were co-registered during pre-processing. Assessed over calibration targets, illumination conditions have been shown to have a small impact (differences of 1-3%) on the reflectance of the red and NIR bands of the Parrot Sequoia (Deng et al., 2018). Differences are expected to be amplified over vegetation due to structural influences on reflectance anisotropy (Sandmeier and Itten, 1999).

We identified a small but significant impact of contrasting illumination on NDVI values for vegetation crowns for a leaf-off and a leaf-on direct-diffuse image pair, while a third image pair during leaf-off conditions showed no significant difference (Figure 6-5, Table 6-1). The different findings for the two leaf-off image pairs could relate to greater wavelength-specific differences in irradiance inferred from calibration panel reflected radiance (red to NIR band ratios differed by 0.42 and 0.27 between images) and differences in reconstruction quality of tree crowns. In images of the leaf-off canopy acquired under direct irradiance conditions, background features were more visible which besides implicitly affecting the radiometry also influenced the DSM and mosaicking algorithm of the photogrammetric software due to issues with crown reconstruction (influencing image projection and prioritising ground pixels visible within multiple images in some cases). To minimize visible understory in gaps which can lead to bias in retrieved crown NDVI metrics, acquiring data during overcast conditions is recommended prior to leaf development.

After tree crown green-up, a small but significant decrease of NDVI could be observed when imaged during direct illumination conditions (bias = ca. -0.01) (Figure 6-5, Table 6-1). This may relate to shading effects within the crown due to its structure, leaf angular distributions and solar illumination angles, which other

studies have noted can have a significant effect on index products (Aboutalebi et al., 2019; Damm et al., 2015b; Gamon et al., 2006; Schläpfer et al., 2013).

Overall, the identified illumination-based uncertainties were roughly an order of magnitude smaller (up to 0.034 for leaf-off, 0.013 for leaf-on) than the NDVI difference pre- and post green-up of deciduous trees (0.252). Therefore, for the study of spring phenology of deciduous crowns, observations from contrasting illumination conditions can be included. Illumination-based uncertainties must be revisited for the monitoring of photosynthetic phenology in evergreen species as the pigment indices commonly used are much more sensitive to these effects (D'Odorico et al., 2020; Möttus et al., 2015; Takala and Möttus, 2016).

6.4.2 Drone derived phenology metrics

The high spatial and temporal resolutions that can be achieved with drone-based NDVI information makes resolving seasonal changes at the individual and species level possible, but their potential for phenological monitoring needs to be assessed critically. Based on the NDVI time-series, for deciduous crowns, a logistic function could be fitted in most cases and SOS, MOG and SOP metrics derived. Based on a comparison with PAI values for the woodland NDVI was found to mirror the increase in PAI, with some non-linearity arising from NDVI increase prior to overstory green-up due to understory effects which are known to influence both satellite and *in-situ* sensor derived phenology estimates (Ahl et al., 2006; Ryu et al., 2014; Soudani et al., 2012; White et al., 2014), as well as NDVI saturation prior to maximum PAI (Figure 6-7). The latter is a previously identified limitation of VIs such as NDVI due to ratioing and the reflectance at red wavelengths experiencing little change over denser canopies (Birky, 2001; Wang et al., 2005; Zhu and Liu, 2015). Changes in the enhanced vegetation index (EVI) have been found to better reflect vegetation phenology (Kowalski et al., 2020) but could not be calculated from Sequoia data due to requiring spectral information at blue wavelengths (Huete et al., 2002). It should be stressed that these conclusions are from satellite based studies at coarser resolutions and further work is needed to explore these dynamics in drone acquired data. For specific species, the relative timing of the phenological stages matched well with previous

observations, such as the early green-up of alder and hawthorn, the slower progression and late peak greenness of alder and late but rapid green-up of ash and oak tree crowns (Kuster et al., 2014; Leslie et al., 2017; Mijnsbrugge and Janssens, 2019; Vilhar et al., 2013). On the basis of individual crown PAI measurements (Figure A 4), differences in green-up timing between oak and hawthorn could be verified and UKPN observations of species phenology in the same geographic region (counties Cornwall and Devon in South West England) confirmed a late green-up of beech, ash and oak through mean budburst dates (Table A 4). The median identified SOS date was closer to the date of first leaf emergence and later than budburst for most species, though it should be considered that regional variations of the reported events may occur at smaller spatial scales than the county level. In contrast, Berra et al., (2019) found that SOS identified from drone acquired RGB data was generally earlier than SOS derived from field observations (defined as >90% of bud open) in North East England. Differences could arise due to understory vegetation growth, the VI used or observation timing and fitted model. Here, further observations pre green-up would enable a more robust model fit and SOS extraction as some species showed increasing NDVI shortly after the first drone acquisitions. The intra-species variation of phenological metrics were relatively large, particularly for SOS and MOG (Figure 6-8), and include outliers. For some species such as oaks, regional differences in photoperiod response have been observed (Basler and Körner, 2012). Erroneous early green-up and variability may be influenced by growth of understory vegetation, particularly bluebells (*Hyacinthoides non-scripta*) within the woodland and further uncertainties arose in this experiment from observation gaps in the dataset, caused primarily by adverse weather conditions which did not permit safe drone flights.

From inspecting species-specific NDVI time-series (Figure 6-6) it was evident that increase in greenness for evergreen species could also be distinguished. NDVI increased slightly in pine species (*Pinus spp.*) in early summer which may indicate phenological changes as has previously been observed for pine species using satellite based NDVI (Aragones et al., 2019). However, NDVI is not a good indicator of leaf-level photosynthetic phenology in evergreen species (D'Odorico et al., 2020; Wong et al., 2019). Flowering events reduced NDVI (by increasing reflectance in both red and NIR) in hawthorn (mid-May) and evergreen gorse

(Bowman et al., 2008). These species specific effects could be better represented and analysed with dedicated models and masking, for example the 20% brightest pixel method here showed to be much more sensitive to the hawthorn blooming than the mean of all pixels (Figure 6-6, Figure A 3). Mapping of flowering phenology has also been achieved using drone acquired RGB imagery (Neumann et al., 2020) and further comparisons are required to identify which spectral bands can yield the best indicators.

6.4.3 The future of drone-based phenological studies

In order for the presented methodology to be scalable to larger study areas, some logistical concerns must be addressed. The manual digitising of individual crowns should ideally be replaced either by object-based segmentation of crowns and automated species classification making use of the fine spatial resolution textural and multi-temporal dataset (Xu et al., 2020, example of workflows which could be modified for drone datasets: Guirado et al., 2019; Qiu et al., 2020; Sheeren et al., 2016; Wagner et al., 2018), or auxiliary datasets such as detailed forest inventories, e.g. based on laser scanning data (Burt et al., 2019; Duncanson et al., 2014). A further limiting factor for the deployment of drones to improve upon phenocam-based monitoring of phenology is their timely deployment and operational costs considering the fieldwork effort involved for reaching remote sites and the susceptibility to weather conditions. While this study showed that both, direct and diffuse illumination conditions are conducive to the acquisition of useable datasets, gaps in time-series result from too changeable conditions, too high wind-speeds and other limitations. For dedicated study sites, fully automated deployment informed e.g. by weather-station data from a hub including battery recharging station as is being pioneered in robotics and smart-cities research (Byun et al., 2016; Galkin et al., 2019; Menouar et al., 2017) may soon offer the desired solution.

With sensor technology as well as associated workflows still rapidly evolving, the ideal payload for phenological monitoring has yet to be determined. Saturation and understory influences as were observed in this study could be addressed by performing leaf-cover classification at the pixel level (Park et al., 2019). Crucial

information on phenology also includes processes such as pigment changes at leaf-scale, which cannot easily be decoupled from changes in crown leaf area when using merely the NDVI. Including further spectral bands, particularly the red-edge, in phenological analysis could improve this separation (D'Odorico et al., 2020; Delegido et al., 2011). Finally, new opportunities are arising with the development of drone sensors which exhibit identical bandsets to those of satellite sensors (Revill et al., 2019). These will aid in understanding and validating studies based on coarser resolution time-series from satellites where multiple crowns are aggregated and mixed pixels will show a combination of individual canopy phenology, scaling differently depending on phenological stage (Chen et al., 2018; Klosterman et al., 2018).

6.5 Conclusions

Recent studies using drone-mounted consumer-grade cameras revealed that tree-specific phenological monitoring is possible. Here, we showed that the NDVI derived from a calibrated drone mounted multi-spectral sensor can provide the basis for deriving and comparing phenological metrics for many species in a heterogeneous ecosystem. This finely resolved spatial information holds great potential for revealing adaptations in species specific phenology to changing local conditions such as the micro-climate, as well as the possible identification of flowering events with high relevance to pollinator research. The signal from the vegetated understory however exerts an influence, even at the fine spatial resolutions of drone-based datasets, and should be addressed. Furthermore, we demonstrated that observations from contrasting illumination conditions can introduce bias, but this was relatively small when compared to the NDVI change during spring green-up. Given conditions throughout each flight are still consistent, data from overcast or clear-sky acquisitions can be used together for NDVI-based time-series analysis which greatly increases the feasibility of these studies in temperate climates with variable weather conditions.

7 Modelling understory light availability in a heterogeneous system using drone captured structural and spectral data

Chapter context:

Modelling spatially varying radiation interactions with vegetated landscapes is important for understanding light availability as a limiting factor for photosynthesis and for the inversion of coarse-grained remotely sensed products e.g. to extract leaf structural and biochemical parameters (Damm et al., 2020; Laurent et al., 2014). For tree dominated ecosystems, state-of-the-art methods rely on 3D RT models (Ligot et al., 2014a). However, in order for 3D RT models to be able to simulate radiation propagation accurately, they require a great number of parameters describing vegetation structure and their optical properties at fine spatial scales, which have so far been acquired by *in situ* sampling or ALS acquisitions (Gastellu-Etchegorry et al., 2015, 1999; Schneider et al., 2014). Now that drones provide a cost effective method for acquiring fine grained structural and spectral information, the use of these datasets to describe vegetated scenes within RT models represent an unexplored opportunity to enable the wider application of 3D RT methods for a variety of ecosystems at low financial cost.

This chapter brings together and is informed by insights gained from work in chapters 4, 5 and 6 in that it seeks a fully structural and spectrally multi-temporal description of a heterogenous vegetated study site. The presented experiment focuses on understory PAR availability at different stages of spring green-up to investigate the extent to which the spatio-temporal dynamics of radiation can be modelled through the use of drone acquired datasets. Understory PAR was selected as, besides being an important parameter, it enabled a feasible independent validation of the modelled outputs to be performed. The presented methodology provides options for extension of model and application, e.g. for the forward modelling of surface reflectance or APAR given adequate optical properties.

Research questions:

- 1) Can drone acquired SfM point clouds and VI data be used to accurately represent the vegetation height and PAD variations for a heterogenous scene within a 3D RT model?
- 2) Can the drone-data parameterised RT model accurately simulate understory PAR and daily light integrals (DLI) across a period of spring green-up?
- 3) Can the drone-data parameterised RT model resolve fine-grained spatial variations in understory PAR more accurately than models using geometric primitives or constant PAD values?

Abstract

The light environment within vegetated landscapes is a key driver of microclimate, creating varied habitats over small spatial extents, and it controls the distribution of understory plant species. Modelling spatial variations of light within heterogenous systems requires finely resolved (< 1 m grain) information on topography and canopy properties. We demonstrate a 3D radiative transfer based approach to modelling spatial distributions and temporal progression of understory PAR for a wildlife conservation site in the south-west UK. Our method used canopy structural data acquired from drone-borne sensors (consumer-grade camera and Parrot Sequoia) and the discrete anisotropic RTM DART. The spatial and vertical extent of the vegetation canopy was described using SfM photogrammetry-derived DSMs. The PAD was informed by relating drone acquired spectral data to hemispherical photography-based estimates of PAD. Understory PAR was simulated for multiple dates across Spring 2019 and showed plausible spatial variations across the site (DLI ranging from 0.5 to 16 mol d⁻¹ m⁻²) and reduction in accordance with increasing PAD from start to end of spring green-up (68.9% for a woodland subset). The errors in hourly PAR fractions compared to *in-situ* measurements (RMSEs 0.116-0.333) are related to the empirical PAD model and RT model simplifications (particularly spherical leaf angles). Comparing model outputs against those from simpler parameterisations using geometric primitives and constant PAD showed that representing the vegetated scene using drone acquired data did not yield improvements in resolving fine scale spatial variations of PAR under a dense woodland canopy subset. The presented workflow, while computationally expensive, represents a physically based method for mapping PAR at fine spatial resolutions and during changing illumination conditions throughout a period of spring green-up. Further potential applications of such drone-data based representations of vegetation in 3D RTMs include the simulation of relevant quantities for microclimate modelling and inversion of spectral signals to yield crown and leaf-scale information, given additional optical and thermal properties as inputs.

7.1 Introduction

Light is one of the spatially most variable resources for plant growth (Bazzaz, 1996), and the understory light environment is a key determinant of vegetation pattern and influences biodiversity (Gehlhausen et al., 2000; Martens et al., 2000). Duration and intensity of light affects microclimate which has ramifications for plants and insect species and leads to variability in ecosystem functioning (Chen et al., 1999; Pincebourde et al., 2007). PAR, which describes the range of light between 400 and 700 nm that plants can use for photosynthesis, is the quantity of interest when assessing light availability (Alados et al., 1996; Möttus et al., 2011). Its drivers have been most extensively studied in relation to forest management (Ligot et al., 2014b), but it is also important for carbon cycle modelling and biodiversity which has received comparatively less attention. Characterising understory PAR has been achieved predominantly through field measurements, based on gridded measurements using quantum sensors (Fladeland et al., 2003), elaborate tram systems (Baldocchi et al., 1984) or estimations derived from DHP (Cannon et al., 2019; Fournier et al., 1996), including DHP height profiles captured by drones (Brüllhardt et al., 2020). PAR has also been simulated using RTMs based on representations of forest structure, predominantly at stand level (Ligot et al., 2014a). To accurately simulate PAR transmission in heterogenous forests or tree stands, 3D RTMs and adequate representations of trees are required (Knyazikhin et al., 1997; Stadt et al., 2005). The determination of key tree structural parameters such as crown geometry and PAD, range from forest inventory based allometric estimates (Ligot et al., 2014b) to exhaustive measurements of individual trees in the field (Brunner, 1998; Gastellu-Etchegorry et al., 1999). Structural parameters derived from LiDAR remote sensing have also shown potential for modelling PAR transmission through realistic forest representations (Lee et al., 2008; Zeng et al., 2019).

Sensors mounted on lightweight drones along with SfM photogrammetry processing pipelines have emerged as a low-cost alternative option for acquiring structural and spectral information on vegetation canopies (Aasen et al., 2018; Anderson and Gaston, 2013; Dandois and Ellis, 2013; Salamí et al., 2014). This allows deriving vegetation heights and leaf or PAI at fine spatial resolutions (Cunliffe et al., 2016; Panagiotidis et al., 2017; Tian et al., 2017). The relative

ease of drone data acquisition also allows for multi-temporal characterisation of canopy properties – e.g. charting the development of vegetation over a season, which is a recognised limitation of ALS-derived vegetation structural information due to prohibitive costs (Mlambo et al., 2017). Drone-derived SfM point clouds and CHM representations of vegetation have previously been used for energy balance modelling in orchards (Aboutalebi et al., 2020) as well as for modelling solar irradiance in plantations (Abdollahnejad et al., 2018). There is clear potential for using similar representations to simulate PAR propagation, particularly in complex systems with discontinuous vegetation cover and shrubs. This can be achieved in theory, by using drone acquired spatial and volumetric information for parameterising vegetation canopies in 3D RTMs. The goal of this work was to develop a workflow for doing so, and therefore within this paper, we present our new approach based on the DART model (Gastellu-Etchegorry et al., 2015).

For this study, we make use of a time-series of drone derived photogrammetric point clouds coupled with concomitantly captured multispectral imagery and field measurements acquired over a heterogenous vegetated study site to assesses whether:

- 1) Drone acquired SfM point clouds and VI data can be used to accurately represent the vegetation height and PAD variations for a heterogenous scene within a 3D RT model.
- 2) The drone-data parameterised RT model can accurately simulate understory PAR and daily light integrals (DLI) across a period of spring green-up.
- 3) The drone-data parameterised RT model can resolve fine-grained spatial variations in understory PAR more accurately than models using geometric primitives or constant PAD values.

7.2 Materials and Methods

7.2.1 Study site

The study site “Trelusback Farm” (Figure 7-1 a) is located in west Cornwall, UK (50°12'10.0"N 5°12'22.6"W). It is managed for the purpose of wildlife conservation and includes a small mixed woodland with the predominant species being alder (*Alnus glutinosa*), sycamore (*Acer pseudoplatanus*) and sweet chestnut (*Castanea sativa*) as well as isolated free-standing trees and shrubs (see Figure 7-2 for a studied subset of trees). The site was selected due to having good accessibility for regular revisit surveys, structural complexity and species richness.

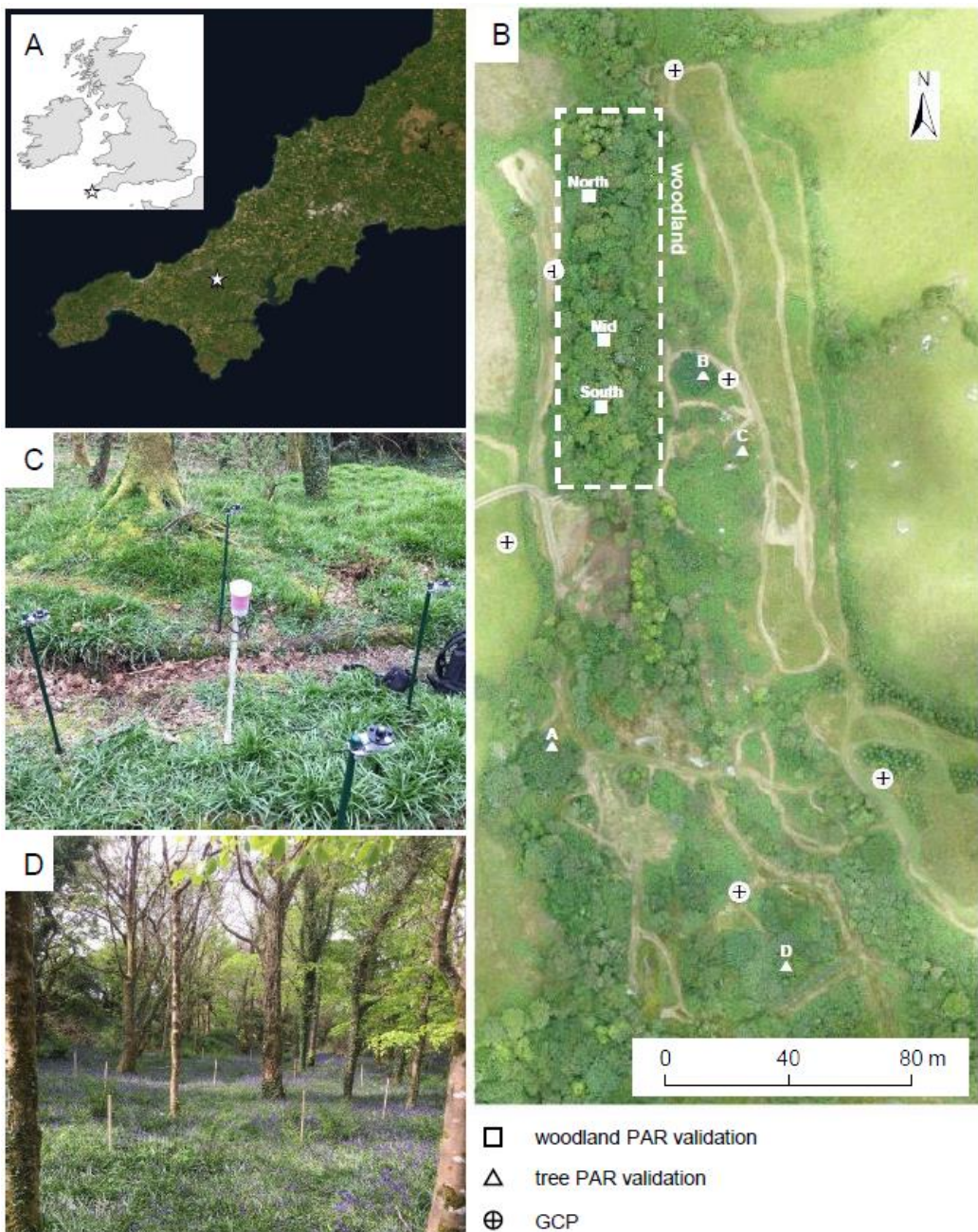


Figure 7-1: A) Location of the study site in Cornwall, UK, marked by star, B) RGB orthomosaic of the study site on 22 July 2019, indicating locations of PAR validation measurements and GCPs for georeferencing multispectral drone images. The woodland area subset is indicated by a dashed line. C) quantum sensor configuration for PAR validation measurement in woodland locations, D) woodland with posts indicating HOBO light logger locations. Satellite image source: Esri, Maxar Technologies, DigitalGlobe.

7.2.2 Field measurements

A total of 12 GCPs were deployed on-site, 6 of which were large canvas markers (80 x 80 cm) used to georeference the coarser spatial resolution multispectral products. Six further smaller GCPs (40 x 40 cm) were added to ensure better geometric constraint for the photogrammetric processing of finer spatial resolution RGB images. Most GCPs were left in place for the duration of the experiment (one was redeployed to improve coverage). They were surveyed using a Trimble Mobile Mapping system and the data post-processed for differential correction.

DHPs were taken on up to 10 dates for a total of 21 trees and for a North-South transect through the woodland. For each free-standing tree, an image was taken in each cardinal direction with the camera approx. 0.4 m from the central stem and 0.5 m above the ground, levelled manually. For the transect singular images were taken with 5 m interspacing. The height of the top and bottom of crowns above ground was measured using a laser rangefinder for a total of 74 trees and shrubs across 14 species identified on the study site.

Direct measurements of PAR in different measurement configurations are a common method for assessing understory light availability (Fladeland et al., 2003; Lafleur and Farnsworth, 2008; Rosati et al., 2020) and were used here for validation instead of simulations based on DHPs to provide independent measures and avoid circularity as DHPs were also used for model parameterisation. Below canopy PAR was measured below four free-standing tree crowns (Figure 7-2) and at three locations within the mixed woodland (Figure 7-1 b) by rotating sensor installation locations approximately every 7 days. Measurements represent the average of 3 (single tree) or 4 (woodland) replicate quantum sensors which measure PPFD (LightScout, Spectrum technologies Ltd.) placed 0.75 m above ground and within 0.5-1.5 m distance to each other (see Figure 7-1 c). Additionally, 11 HOBO light loggers (Onset, US) measuring uncalibrated incoming light (lux) (Onset, 2018) were deployed at different locations throughout the woodland (Figure 7-1 d) to assess the spatial and temporal variability of understory light conditions in this system.

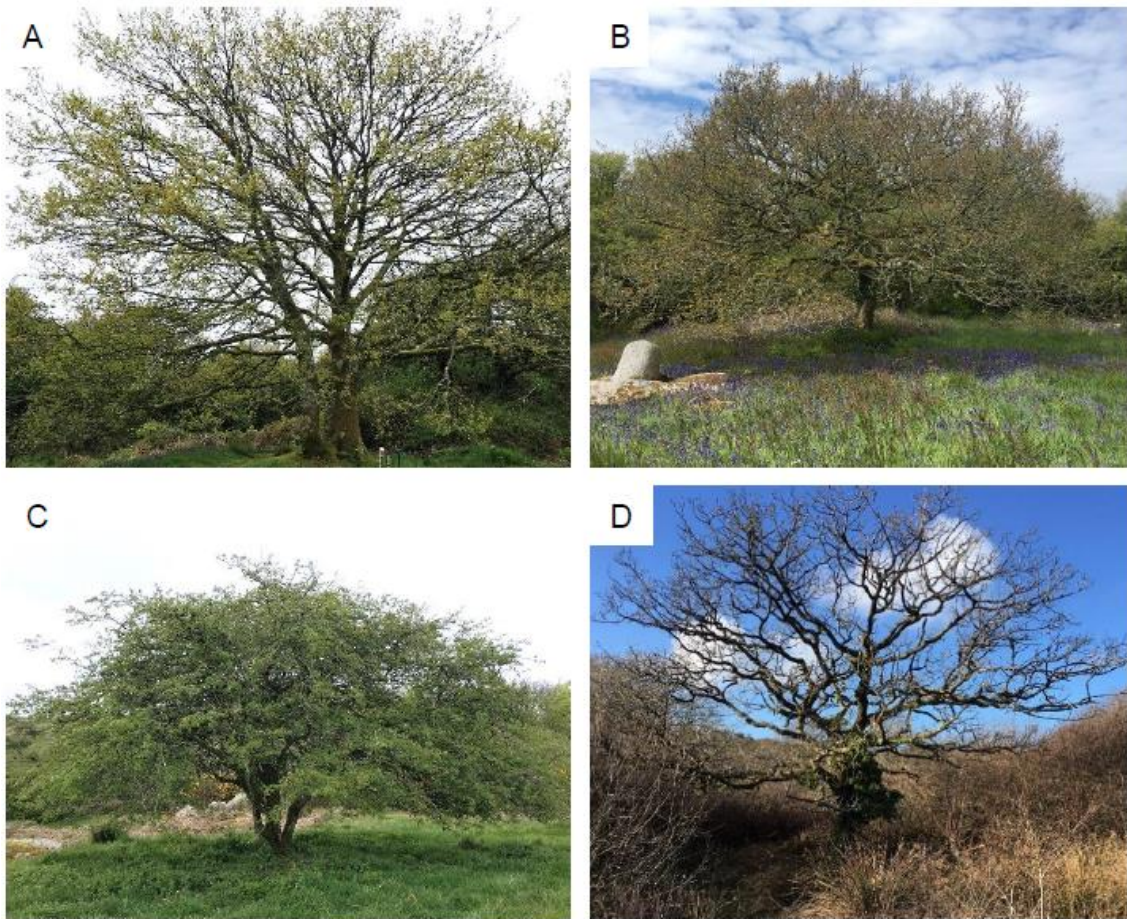


Figure 7-2: Isolated trees for which PAR validation measurements were taken (letters corresponding to locations in *Figure 7-1*). A, B and D are oak trees (*Quercus spp.*) in order of decreasing crown size, C is a hawthorn tree (*Crataegus monogyna*).

7.2.3 Drone datasets

7.2.3.1 Vegetation index orthomosaics

Multispectral drone images were acquired over the study site on 20 dates from 22 March to 23 July 2019 during cloud free or homogeneously overcast conditions. Images were captured with a Parrot Sequoia MCA mounted on a 3DR-Solo drone. The Parrot Sequoia records image data in four spectral bands (550, 640, 735 and 790 nm) and an accompanying irradiance sensor records downwelling radiance in four corresponding bands. The drone was flown at 70 m altitude with 5 m/s in a north-south lawnmower pattern flight plan which ensured >80% forward and lateral image overlap, as recommended for the Parrot Sequoia sensor (Tu et al., 2019). Images of a panel of known reflectance (50 x

50 cm panel with 44% nominal reflectance across Sequoia bands (MosaicMill, Finland)) were taken on the ground prior-to and post-flight for calibration. The multi-spectral drone images were processed using Pix4Dmapper (version 4.4.12, Pix4D, Switzerland). Within the Pix4D workflow, lens distortion and vignetting were corrected and photogrammetric processing was performed followed by radiometric calibration to produce a four-band surface reflectance orthomosaic of the study site. Further details on the calibration procedure can be found in Fawcett and Anderson, (2019), see appendix A6. Irradiance data were used within the calibration procedure to correct for differences in data acquired during diffuse conditions. It could not be applied to two diffuse acquisitions following 11 July 2019 due to sensor failure.

A range of VIs sensitive to LAI which use surface reflectance values in the four available spectral bands (ρ_{green} , ρ_{red} , ρ_{r_edge} , ρ_{NIR}) were identified from previous studies and computed (Table A 7). The indices assessed are the NDVI, the normalised difference red-edge index (NDRE), the normalised difference red-red edge index (NDRI), the modified soil adjusted vegetation index (MSAVI2) and the modified triangular vegetation index (MTVI2) (Delegido et al., 2013; Gitelson and Merzlyak, 1994; Haboudane et al., 2004; Heiskanen, 2006; Qi et al., 1994; Tucker, 1979; Yao et al., 2017). These indices were compared due to accounting for different influences (e.g. soil background) as well as making use of different bands of spectral information available.

7.2.3.2 Photogrammetric point cloud

RGB images of the study site were acquired on 28 April 2019 during mostly leaf-off/early green-up and 22 July 2019 during leaf-on conditions with a Ricoh-GRII camera. The drone was flown at 60 m altitude with 6 m/s and the camera triggered with 1 s intervals and a flight plan which guaranteed 75% lateral overlap and >80% forward overlap for robust photogrammetric processing. For 22 July, the north-south nadir acquisition was supplemented with an east-west oblique acquisition to optimize the accurate reconstruction of vegetation canopy structure (Cunliffe et al., 2016).

The drone RGB images were processed with Agisoft MetaShape (v1.5.0, Agisoft, Russia) using a total of 12 GCPs for georeferencing, 3 of which were used solely for the assessment of georeferencing accuracy. Depth filtering was disabled to yield a dense 3D point cloud representing vegetation structure. For the most accurate representations of crown shapes, the RGB data acquired on 22 July representing the fully leafed out crowns was selected for further processing as leaf-off acquisitions were found to result in greater within-crown variability of the point cloud due to a lack of identified tie-points for finer branches.

7.2.4 Irradiance measurement and modelling

The BOA irradiance over the PAR wavelengths was measured at the site as PPFD using a quantum sensor (Spectrum Technologies Inc., US). The fraction of direct/diffuse radiation which is a required input parameter for the DART model was estimated by an empirical model relating measured global PAR ($R_s(0)$) to extraterrestrial PAR R_0 (Hassika and Berbigier, 1998; Spitters et al., 1986), modified for local conditions (see appendix A4 for details) based on direct and diffuse PAR measurements from a representative weather station (approx. 10 km from the study site):

$$\frac{R_d(0)}{R_s(0)} = \begin{cases} 1, & \frac{R_s(0)}{R_0} < 0.25 \\ 1.35 - 1.41 \frac{R_s(0)}{R_0}, & 0.25 \leq \frac{R_s(0)}{R_0} \leq 0.8 \\ 0.15, & 0.8 < \frac{R_s(0)}{R_0} \end{cases} \quad (7-2)$$

7.2.5 Scene 3D structure

The 3D structure of the scene was described using ALS and drone based SfM photogrammetry data products. The DTM was derived from LiDAR data acquired for the Tellus South West project in Summer 2013 (Ferraccioli et al., 2014). These data had a 1 m spatial resolution with a 0.25 m vertical accuracy, though possible local changes in the terrain since 2013 could not be accounted for.

The photogrammetric point cloud resulting from drone RGB data processing was subsampled (10 cm) and statistical outlier filtering was applied. The point cloud was normalised to elevation above ground using the LiDAR DTM (resampled using bilinear interpolation to the higher DSM resolution of 0.03 m) and a CHM was calculated. The accuracy of the CHM was assessed by comparing the 90th height percentile per tree crown (to remove outliers) with laser rangefinder height measurements of 15 trees across the study site. Areas representative of individual tree and shrub crowns were segmented from the dense point cloud. Using algorithms implemented in the lidR package (Roussel and Auty, 2018), the point cloud was first classified into points representing overstory vegetation and ground (including grass and shrubs less than 1 m in height) which was excluded. Then, local maximum filtering was applied to identify tree tops and a watershed filter was used to segment areas based on height, representative of tree crowns. Distance constraints between identified tree tops were set in order to avoid subdivision of clearly identifiable large tree-crowns (7 m). As this led to aggregation of smaller crowns, the impact of this on PAR modelling results was investigated by using a reference segmentation with a smaller distance constraint (4 m) which oversegmented larger crowns.

As the CHM is a 2.5 dimensional representation of vegetation structure, the base of tree and shrub crowns had to be estimated using an empirical model based on the crown measurements acquired *in situ* (section 7.2.2). The height-based method which was used in favour of a constant crown ratio is detailed in appendix A4, eq. 1. The model was applied to each segmented crown to derive the crown base height (constant per crown).

An alternate reference dataset representing tree crowns as geometric primitives was also created to serve as alternative geometric input data for the DART model to compare and assess the performance of the drone-derived crown geometries. As a detailed tree inventory was not available for this site, this was created for the woodland by manual identification of crown locations and extents based on leaf-off and leaf-on drone orthomosaics and representing them by ellipsoids (Figure A 8). The vertical crown dimensions were extracted from the SfM DSM (top) and crown ratio model (bottom).

7.2.6 Plant area index

PAI which includes LAI and wood area index (WAI) was estimated at the level of 21 individual crowns and for three subsets of the woodland using the captured DHPs (section 7.2.2). For the woodland transect, PAI was estimated per image using the image processing software Hemisfer (WSL, Switzerland) which implements a formula for average foliage density (Miller, 1967) as used for LAI-2000 (Li-Cor, USA). For individual tree crowns the method required adjustments (see section 3.4.1.2 and Figure 3-10) as they do not fulfil the assumption of continuous vegetated layers and must take into account the crown geometry (Bréda, 2003).

Empirical models relating PAI to the derived VIs were established by including all PAI observations throughout spring green-up and linearly interpolating the 20 drone NDVI observations at the corresponding level (crown or woodland plot means) for these dates. Both linear and exponential regressions were compared in terms of LOOCV RMSE to determine the most suitable model (Table A 8). An exponential regression was found most suitable to model PAI from NDVI (as observed in previous studies (Kang et al., 2016; Potithep et al., 2013)). NDVI has previously been widely used to retrieve LAI for similar systems (Tian et al., 2017), while our model includes an offset to account for PAI including WAI. This model was applied to estimate PAI at crown level based on the NDVI datasets and downsampled to a 1 m spatial resolution grid for model parameterization using the derived crown geometry information. Within DART, the PAI information is converted to PAD per 3D voxel based on crown height information. The uncertainty arising from applying this model to drone NDVI observations acquired during contrasting illumination conditions (overcast and cloud-free sky) was also assessed for subsequent days during leaf-off and leaf-on conditions.

7.2.7 Understory PAR simulation experiments with DART

DART was created and extended by Gastellu-Etchegorry et al., (2015) for the simulation of radiative transfer within complex 3D scenes for the primary purpose of simulating an array of different remote sensing measurements, from airborne and satellite images to LiDAR waveforms. DART allows the description of scene

elements in the form of bespoke 3D objects and facets or as turbid medium voxels which possess specific properties determining the transmittance and scattering of light within. DART has previously been used to simulate the PAR regime in tropical and boreal forests (Guillevic and Gastellu-Etchegorry, 1999) in order to derive physical laws (modified Beer's law) of PAR transmission through these canopies. While it is not the most computationally efficient option, the DART model was selected for this study due to its capability in voxel based representation of the vegetation canopy. This allows representing varying canopy surface height, as is provided by drone SfM estimates, rather than simplified geometric models as have been used in many studies of understory light availability (Ligot et al., 2014a; Martens et al., 2000; Stadt et al., 2005).

For the purpose of simulating PAR availability at ground level, a number of simplifying assumptions concerning scene elements were made and few iterations (scattering) were required (Tab. 1). Due to the low reflectivity of vegetation in the PAR wavelength range (400 to 700 nm), it is common for models simulating understory PAR to not simulate reflectance or transmission of light at leaf level and focus exclusively on gap fraction (Ligot et al., 2014a; Stadt et al., 2005). We assessed the impact of this simplification for varying PAI in a sensitivity analysis using deciduous leaf optical properties from the DART database.

The DART scene topography was prescribed using the LiDAR DTM while vegetated scene elements were derived using drone-based NDVI and CHM datasets and empirical models. Vegetation was represented using voxels containing turbid medium (foliage elements). The 3D resolution of the simulation was set to 1 m as a trade-off between processing time and adequately representing the structural complexity of the scene. For the primary simulation (herein referred to as "Sim_main"), the horizontal distribution of voxels was constrained by the crown delineation dataset while vertical distribution was informed by CHM height and the crown ratio value derived per tree. PAD was assigned for the voxels of each tree based on the crown geometry and NDVI-PAI model.

Sim_main was compared with four alternative methods of PAD or crown geometry representation (Table 7-2) by simulating understory light availability for a single day (predominantly direct irradiance) and evaluating the result for the woodland subset (see Figure 7-1). Using geometric primitives and/or constant

PAD values is a common approach for understory PAR modelling (Gastellu-Etchegorry et al., 1996; Ligot et al., 2014b). Ellipsoids were used to represent crowns for Alt_sim_1 and Alt_sim_2. The constant PAD value used for Alt_sim_1 and Alt_sim_3 represented the mean of all drone NDVI derived PAD values estimated for this date. Alt_sim_4 represented an assessment of CHM-based crown segmentation as described in Section 7.2.5.

For all simulations a spherical leaf angle distribution was assumed for all voxels, a common assumption made for similar studies where species specific angular distribution can't be obtained (Gastellu-Etchegorry et al., 1999; Kushida and Yoshino, 2010). The differences to a planophile assumption (which may be more appropriate for some deciduous species) were investigated in a further sensitivity analysis. Woody elements such as tree stems and branches were not simulated explicitly, but the latter included within the PAI. Within-crown clumping (gaps) was also not simulated. It was previously found that its influence is much smaller than the between-tree variability including the 3D distribution and shape of crowns themselves (Guillevic and Gastellu-Etchegorry, 1999).

Simulations (Sim_main) of understory PAR were performed for 22 single days during the spring green-up transition period, grouped into three time periods representing SOS, MOG and SOP (see Table A 6 for dates and positioning of sensors for validation). It should be noted that this division is not based on any particular phenological metric due to large differences between individual species phenology. Budburst for some species (incl. hawthorn and grey willow) occurred during or prior to SOS while all species were fully leafed out by SOP. For each time-step and logger location configuration, two dates with predominantly direct or diffuse irradiance were selected. PAI values were retrieved from the drone observation which was closest to the simulated date (Table A 6, maximum 3 day and mean 1.18 day difference). Simulations were performed in 1 hour time intervals and for each hour, irradiance information from the *in situ* quantum sensor and the derived diffuse fraction model were used to parameterise average BOA irradiance. Sun zenith and azimuth angles were also adjusted hourly. The intercepted energy at ground level as output by DART is used as representation of understory PAR. Finally, the ground radiative budget products representing average PPFD per hour were combined into estimates of the DLI in mol PAR photons per day ($\text{mol d}^{-1} \text{ m}^{-2}$). The hourly and DLI outputs were assessed using

PAR measurements below single trees and the woodland canopy (Figure 7-1). The ability of the model to represent small spatial variations within the woodland was assessed using the distributed HOBO light loggers deployed towards SOP. The agreement between HOBO irradiance data (lux) and simulated DLI at these locations was assessed for two days at SOP with predominantly direct (15 July 2019) and diffuse (22 July 2019) irradiance, using Pearson's r. The same correlation was investigated for all alternative DART parameterisations for 15 July 2019.

Table 7-1: Input parameters for the DART model to perform simulations of radiative transfer in the PAR wavelength range and the data sources used to derive them in this study.

Parameter	Data Source
<i>Scene</i>	
Terrain	DTM (LiDAR)
Canopy voxels	CHM, crown ratio model
Leaf area density	PAI from empirical NDVI model, CHM, crown ratio model
<i>Optical properties</i>	
Leaf optical properties (LOP)	No reflectance or transmittance / LOP database
Leaf angular distribution	Spherical
<i>Irradiance</i>	
BOA irradiance	Quantum sensor
Direct/Diffuse fraction	Empirical model, quantum sensor

Table 7-2: A reference list of the DART simulations compared, with different combinations of PAD and crown geometry information. PAD is defined as the mean for all vegetation or varied at crown level informed by drone NDVI data. Crown geometry is informed either by DSM-based segmentation or manually identified crown ellipsoids.

Simulation name	PAD	Crown geometry
Sim_main	Crown-level (drone NDVI)	DSM (drone SfM)
Alt_sim_1	Constant	Ellipsoids
Alt_sim_2	Crown-level (drone NDVI)	Ellipsoids
Alt_sim_3	Constant	DSM (drone SfM)
Alt_sim_4	Crown-level (drone NDVI)	DSM, higher segmentation (drone SfM)

7.3 Results

7.3.1 Photogrammetry products and scene 3D structure

The georeferencing accuracy for the point-cloud product was high with 0.031 m horizontal RMSE and 0.123 m vertical RMSE. The CHM (Figure 7-3 a) resulting from rasterising the LiDAR DTM normalised point-cloud heights was assessed for 17 individual trees revealing a MAD of 0.71 m compared to laser rangefinder height estimates (11.8% relative to mean tree height). This represents a combination of uncertainties from the interpolated LiDAR DTM product, the photogrammetric point cloud product and the laser range-finder measurements in the field.

The CHM-based tree-identification algorithm showed some accuracy issues for dense tree stands and the woodland (Figure 7-3 b). Due to the dense canopy there is little height-based differentiation and the segmentation is driven largely by crown extent constraints set for the algorithm. Nevertheless, the segmented crown extents were used for further processing (for Sim_main) as feasible spatial units for RTM parameterization, while the impact of greater segmentation was

tested and discussed below. The CHM heights and computed base height per tree finally informed the 3D voxel representation of overstory vegetation in the DART model (Figure 7-3 c).

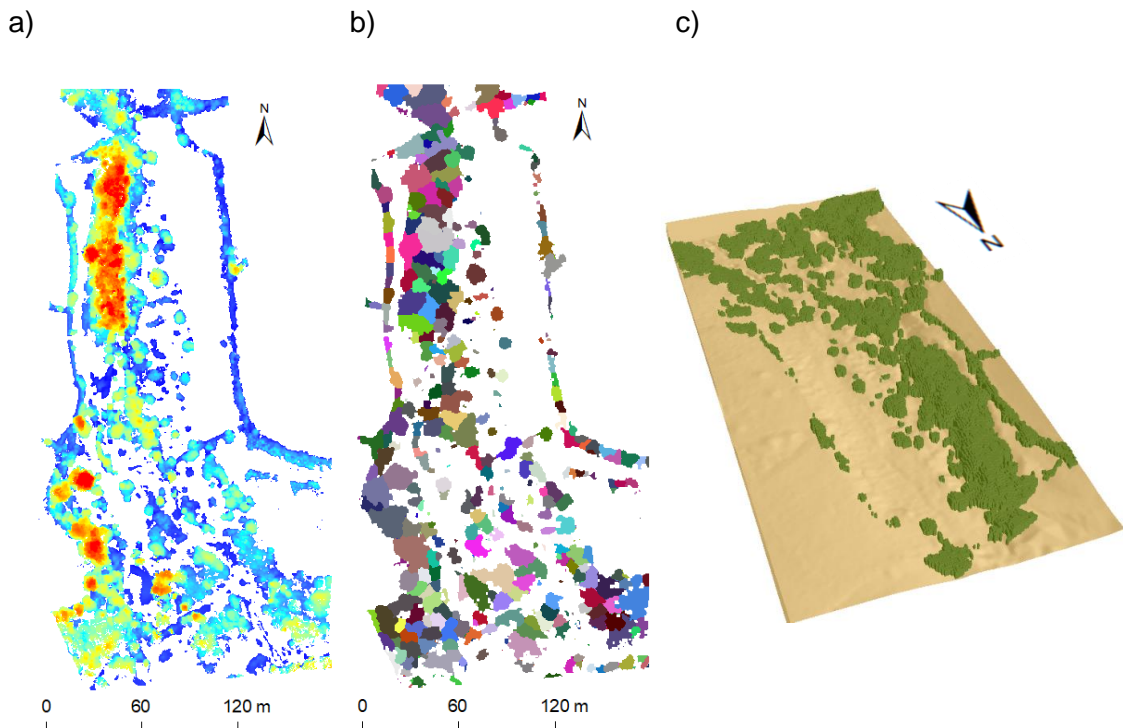


Figure 7-3: a) CHM generated from points classified as vegetation. b) segmented crown extents. c) visualisation of vegetated voxels and DTM as input for the DART model.

7.3.2 Vegetation index mosaics and PAI modelling

20 surface reflectance orthomosaics were generated with a mean horizontal error of 0.023 m and a vertical error of 0.149 m. As the horizontal error was smaller than the GSD there was no visible offset between orthomosaic products of different dates.

The linear and quadratic relationship between PAI estimated from DHP and different VIs (NDVI, NDRE, NDRI, MSAVI2, MTVI2) derived from surface reflectance was investigated (Table A 7 and Table A 8). The MSAVI showed the strongest linear relationship ($R^2 = 0.66$) while the quadratic model showed lowest LOOCV errors for NDVI (RMSE: 0.885) (Figure 7-4) as it enabled modelling the

baseline PAI and gradual PAI increase with NDVI up to large changes around the level of NDVI saturation.

Using this model had implications for slight variations in surface reflectance resulting from calibration uncertainties and different illumination conditions. The impact of using data acquired during fully direct versus diffuse irradiance conditions on retrieved PAI was small pre green-up (RMSE = 0.05) due to deciduous crowns dominating the overstory while the slight illumination dependent differences post green-up led to larger deviations (RMSE = 0.48) (Figure A 9).

Comparing outputs of PAI at crown level derived from three drone observations at different times throughout spring green-up (SOS, MOG and SOP), showed that the increase in PAI throughout the season as well as spatial variations between crowns were captured (Figure 7-5). At SOS, PAI was consistently low with few outliers representing evergreen spruce stands and early stages of beech green-up. At MOG, there was greater variability between crown PAI as species are in different stages of leafing out. Some exceptions were due to flowering induced NDVI reduction as in hawthorn. At SOP all species were fully leafed out and many crowns reached PAI values greater than 3.

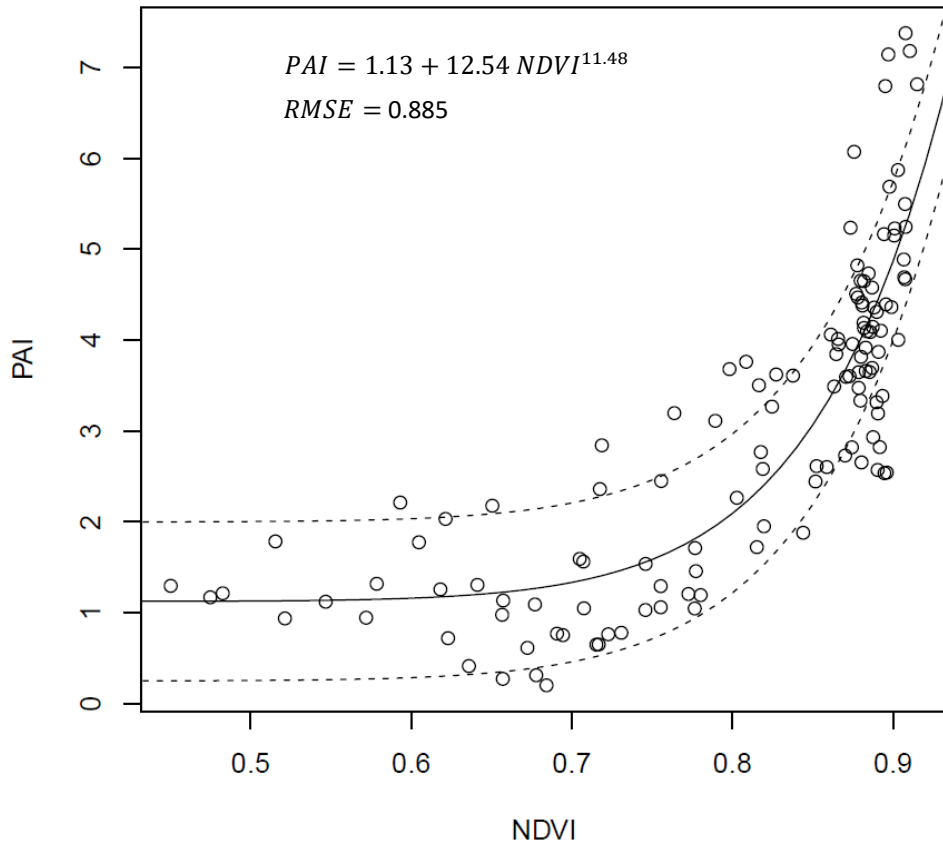


Figure 7-4: Exponential regression model between drone-derived NDVI values and estimated PAI from hemispherical photography at crown and subplot level. Dashed lines indicate ± 1 standard deviation of the residuals.

7.3.3 PAR simulation outputs and validation

The DART simulation outputs displayed considerable spatial variation of PAR reaching understory vegetation as was expected due to the discontinuous overstory on this heterogeneous study site (Figure 7-5). For both isolated trees and the woodland, the spatial transition from low to higher PAR regimes close to the edges of the canopy were visible. Over the period of spring green-up, the contrast in DLI between shaded and unshaded areas greatly increased due to both an increase in incoming PAR (given similar sky conditions) as well as increasing crown PAI. At SOP, DLI values across the site varied from 0.4 to 16 mol m⁻² d⁻¹. For validation locations in the woodland, the simulated hourly fraction of incoming BOA PAR reaching the understory decreased by 68.9% from 0.46 at SOS to 0.14 at SOP (Figure 7-6 a).

Assessing hourly simulations of understory PAR fraction using quantum sensor measurements at a total of 7 measurement locations (Figure 7-6 b and Figure 7-7) revealed that for woodland locations and two of the individual trees, PAR is simulated well at SOS, both for predominantly cloud free or overcast days (5.2% mean relative error in understory PAR). With increase in PAI, woodland PAR was however overestimated by a consistent fraction of 0.11 (Figure 7-6 b) which resulted in mean relative errors of 85.8% at MOG and 256.5% at SOP due to the very small measured PAR fraction. A sensitivity analysis (Figure A 12) showed that the relative underestimation introduced by not simulating leaf reflectance and transmittance was between 10 and 15% depending on diffuse fraction for the highest estimated PAI values of the site (5.5). For the same PAI value, another sensitivity analysis (Figure A 13) demonstrated that assuming spherical leaf angle distribution if the true distribution was planophile would lead to overestimations of up to 372% (direct irradiance, maximum solar elevation angle).

Across the season, the performance for individual trees was quite varied with RMSEs ranging from 0.116 for oak D (predominantly underestimated) to 0.333 for oak A (predominantly overestimated). When investigating the daily progression of simulated versus measured understory PAR for a woodland location (woodland south) for three days with predominantly direct irradiance (Figure 7-8) it was evident that location specific variability which is related to overstory features is not captured. This can be expected due to hourly mean values still being influenced by specific stem, branch and gap locations which are not explicitly modelled. Further daily graphs for comparison can be found in Figure A 10.

The correlation of DART simulated DLI (Sim_main) with HOBO logger recorded values at 11 locations throughout the woodland, for two days with predominantly direct and diffuse irradiance, was not significant (p -value > 0.05) (Figure 7-8). Correlations with HOBO logger readings and deviations in DLI at one validation location were further assessed for four alternative models of crown geometry and PAI representation for 15 July 2019 (direct irradiance; Table 7-3), however none of the models showed a significant correlation. For a single validation location (woodland north), simulations using ellipsoid crowns performed better in terms of absolute DLI values, though correlations of hourly simulated PAR fractions with measured PAR fractions were poorer.

The differences between Sim_main and alternative models (Alt_sim_1 to Alt_sim_4) were also investigated spatially (Figure 7-9). Spatial differences in simulated DLI for different crown representations were larger towards the edge of the woodland ($\sim 5 \text{ mol d}^{-1} \text{ m}^{-2}$) and decreasing to zero difference at the centre (Figure 7-9 b and c). The use of constant PAD across the scene decreased DLI for most of the woodland by 1-2 $\text{mol d}^{-1} \text{ m}^{-2}$, while differences were larger for isolated crowns (up to $4.5 \text{ mol d}^{-1} \text{ m}^{-2}$) (Figure 7-9 d).

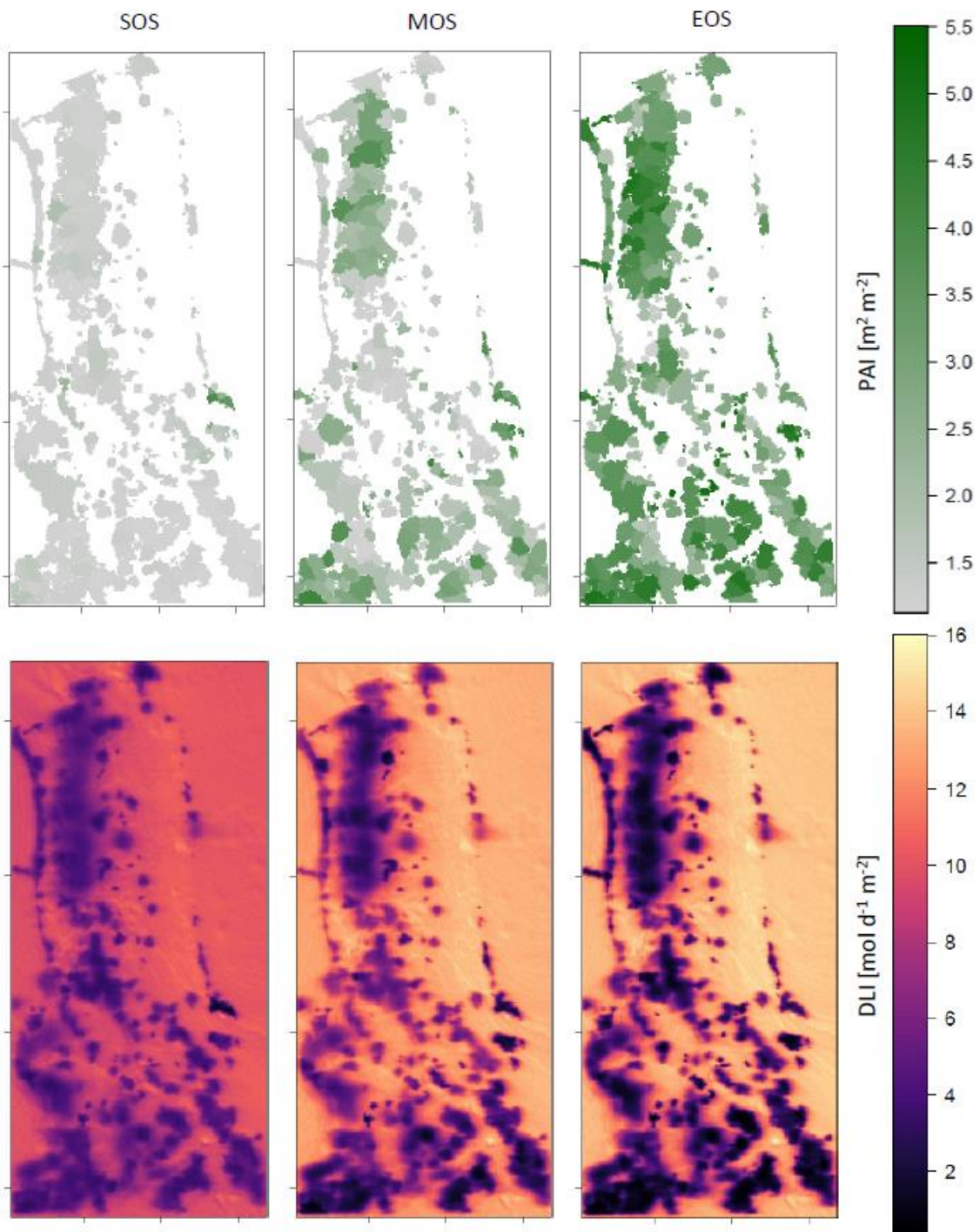


Figure 7-5: Modelled PAI per segmented crown (top) and DART simulated DLI at 1×1 m resolution for three cloud-free days (predominantly direct irradiance) representing SOS (20 April 2019), MOG (21 May 2019), and SOP (9 July 2019).

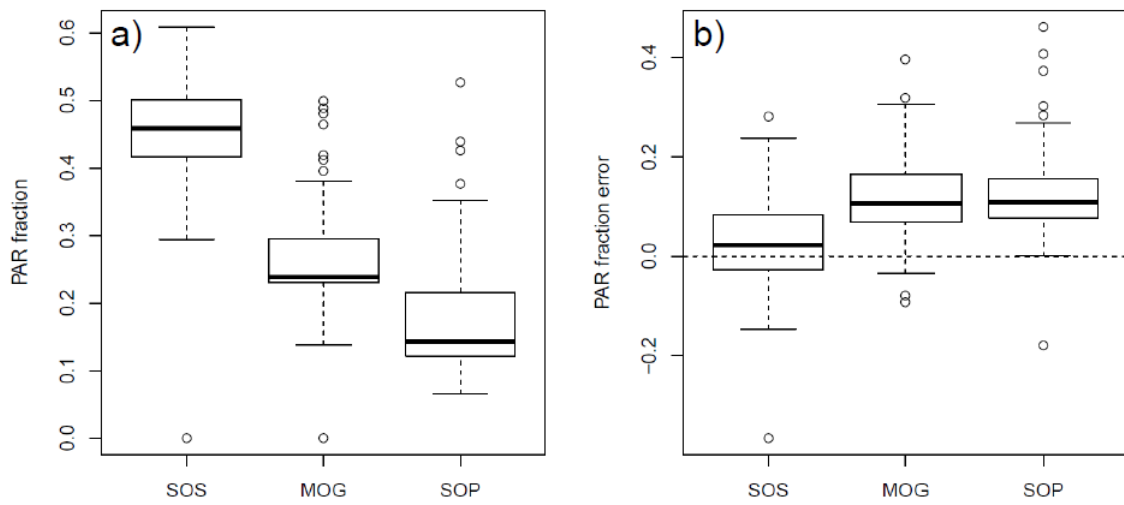


Figure 7-6: Boxplots of a) hourly understory PAR fraction and b) error in hourly understory PAR fraction for three stages of spring green-up (SOS, MOG, SOP) at woodland validation locations. The bold line represents the median value, the lower and upper bounds of the boxes represent the 25th and 75th percentiles, the whiskers extend to the furthest values from the mean within 1.5 times the interquartile range and the circles are identified as outliers beyond this range.

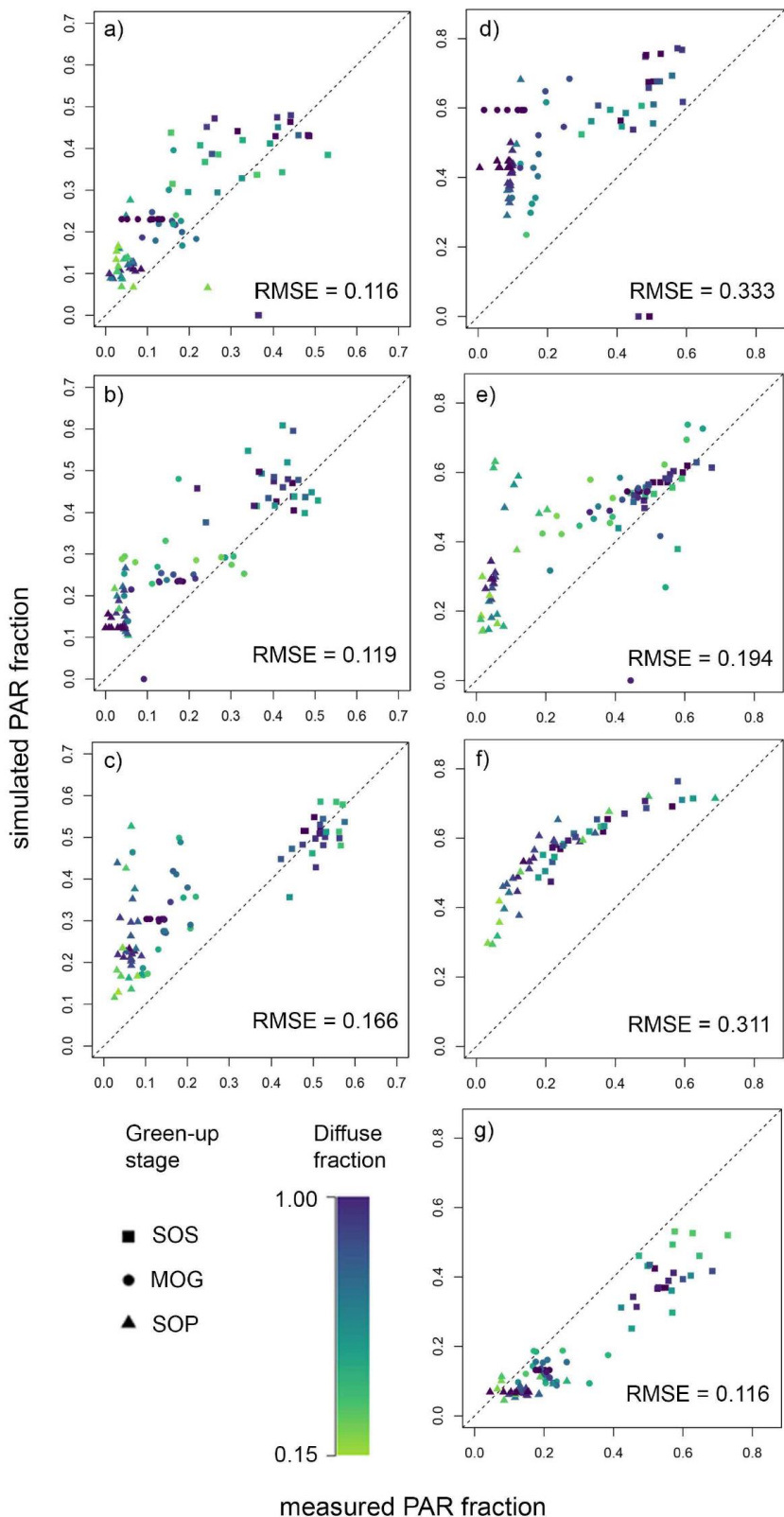


Figure 7-7: Comparisons of measured versus simulated hourly below canopy PAR fractions for the three woodland validation sites (a) South, b) Mid, c) North) as well as the four individual trees (d) oak tree A, e) oak tree B, f) hawthorn tree C, g) oak tree D). For each site, hourly values for a total of 6 days are displayed which represent two days per green-up stage (SOS, MOG, SOP) with contrasting illumination conditions (predominantly direct or diffuse, diffuse fractions ranging from 0.15 to 1). RMSE values show the error in simulated PAR fraction.

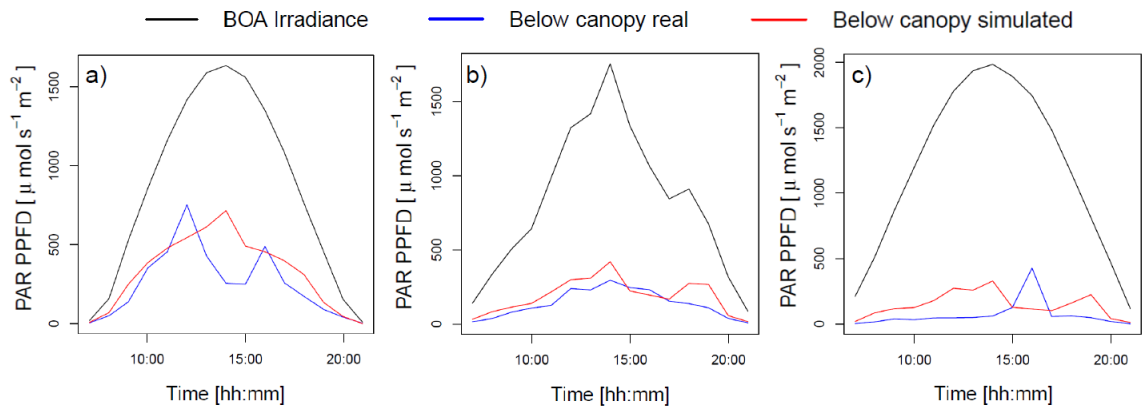


Figure 7-8: Time series (1 hour intervals, 07:00 to 21:00 UTC+1) of BOA irradiance, below canopy measurements and DART simulated below canopy irradiance at location ‘woodland South’ for three days with predominantly direct irradiance representative of a) SOS (20 April 2019), b) MOG (23 May 2019) and c) SOP (9 July 2019).

Table 7-3: Correlation of understory simulated DLI values with HOBO logger measurements as well as differences (total and relative) to quantum sensor measured DLI and correlations with true hourly PAR fractions at the “woodland north” location for the cloud-free conditions of 15 July 2019. Simulations are described in Table 7-2.

Simulation	Spatial correlation (pearson’s r, simulation vs HOBO logger measurements)	Modelled – measured DLI (woodland north)	Hourly PAR fraction correlation (pearson’s r, woodland north)
Sim_main	0.252	10.475 (350%)	0.231
Alt_sim_1	-0.115	5.136 (171%)	-0.084
Alt_sim_2	-0.042	5.308 (177%)	-0.103
Alt_sim_3	-0.002	8.001 (267%)	0.299
Alt_sim_4	0.197	10.131 (338%)	0.260

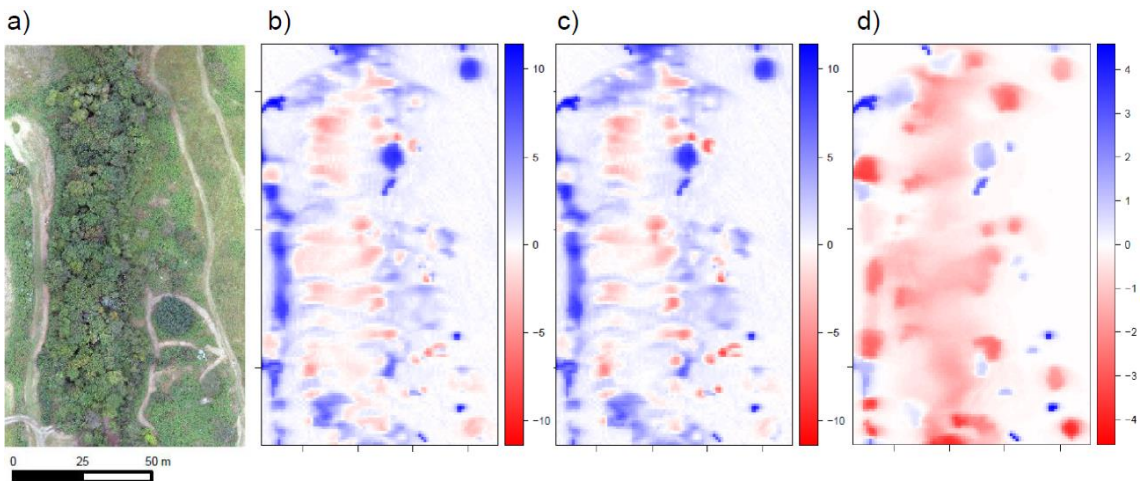


Figure 7-9: a) RGB orthomosaic of study-site subset, b-d) difference of simulated DLI per pixel ($\text{mol d}^{-1} \text{m}^{-2}$) between the reference model Sim_main and models b) Alt_sim_1, c) Alt_sim_2, d) Alt_sim_3 (see Table 7-2 for descriptions). Negative values show underestimation of the model versus Sim_main, positive values show overestimation.

7.4 Discussion

7.4.1 Capability of drone SfM and multispectral data for representing complex vegetated landscapes

SfM point clouds generated from nadir and oblique viewing RGB imagery over the study site allowed the extraction and volumetric representation of taller vegetation (shrubs and trees) efficiently compared to taking measurements in the field and with sufficient accuracy in terms of vegetation height. The crown extents of isolated trees were well represented by the point cloud based on visual comparisons with RGB orthomosaics while for overlapping tree crowns in the woodland, height based segmentation showed limitations. While applicable for plantations (Fawcett et al., 2019a; Torres-Sánchez et al., 2018) or predominantly coniferous forests with clearly identifiable tops (Nevalainen et al., 2017; St-Onge et al., 2015), crown segmentation studies in deciduous forests previously identified limitations of using photogrammetric point cloud data (Nuijten et al., 2019) which has recently been addressed by using both orthomosaics and CHM

data as inputs for machine learning segmentation algorithms (Qiu et al., 2020; Xu et al., 2020).

Vegetation height estimates were satisfactory for the purpose and resolution of the simulation (MAD of 0.71 m while simulation resolution was 1 m). Uncertainties arose primarily from the mismatch in accuracy and spatial detail between the SfM point cloud and the LiDAR DTM used. The crown base height on the other hand is a more important geometric parameter for modelling PAR in the vicinity of isolated trees and could not be retrieved by drone SfM and instead we relied on an empirical crown-ratio model with relatively high uncertainty (RMSE: 0.12).

Similarly, the errors in the empirical model to estimate PAI based on NDVI (RMSE: 0.89) were likely due to representing a large variety of different species, particularly their variable woody structure. The model also showed a sensitivity to small illumination-related changes in NDVI at SOP. Overall, the errors were comparable to those in LAI estimates from NDVI at stand level derived from various satellite sensors in other studies (Soudani et al., 2006).

Introducing structural-type specific models should greatly improve PAI estimates but additionally, such models require the development of accurate canopy classifications as well as extensive field sampling, the latter greatly reducing the benefit of rapid drone based acquisitions for model parameterisation. Due to the PAI and NDVI measurements covering different phenological stages, there is potential for splitting the model into similar stages, covering e.g. bud burst to canopy closure and leaf growth post canopy closure (Tillack et al., 2014), though species specific variation remains an issue for this differentiation. While the other VIs examined here did not outperform NDVI for PAI retrieval, there is potential for improving the model by including spectral bands beyond the range of the Parrot Sequoia camera used. Particularly the EVI (including blue band) could address the issue of saturation (Huete et al., 1997), while information in the shortwave infrared (SWIR) has also been shown to provide added value for LAI estimation (Gong et al., 2003; Nemani et al., 1993). A final option for retrieving PAI from optical data is through RTM inversion, previously applied for LAI retrieval from drone acquisitions over crop canopies (Roosjen et al., 2018; Zhu et al., 2019). The structures of tree crowns, variations in background vegetation and leaf pigment changes throughout the season would complicate such inversions,

however these are similarly limiting factors for the empirically-based estimation attempted here.

The most direct option for addressing the issues in both crown geometry and PAI estimation discussed above is to use exclusively highly resolved structural measurements such as from terrestrial laser-scanning (TLS) or drone-based LiDAR which can additionally provide more accurate DTM information and allow to explicitly model layering and larger woody structures such as stems (Brede et al., 2019; Disney, 2019; Kuželka et al., 2020; Wallace et al., 2014). While TLS surveys are time-consuming, particularly when repeat acquisitions over larger areas are required, the potential for drone-based LiDAR is high. However, drone LiDAR currently remains a financially much more costly solution, motivating alternatives (Mlambo et al., 2017).

Despite the uncertainties in crown geometry and PAI estimation from drone image data alone, it represents a viable novel approach for rapid parameterisation and representation of spatial variation compared to common approaches in forest radiative transfer modelling which infer both crown shape and leaf area metrics from inventory information (e.g. DBH) or use stand averaged values (Ligot et al., 2014b).

7.4.2 Accuracy of understory PAR simulations across Spring green-up using DART informed by drone data

PAR simulations with DART throughout the spring green-up period captured the spatial variability of DLI across discontinuously vegetated landscapes in addition to the temporal progression and reduction of available PAR at the understory with increasing canopy closure. Validation measurements at locations within the mixed woodland and under single trees showed that PAR fraction and absolute values were well simulated at SOS, prior to major leafing out of the canopy, but were considerably overestimated for most locations towards SOP (256.5% for woodland, Figure 7-6). While some errors are clearly related to variations in woody crown structure which was not captured in the PAI model, such as for hawthorn (tree C, Figure 7-7), the source of SOP discrepancies particularly for the woodland are more complex in origin. In part these are expected to relate to saturation in the NDVI-PAI relationship not being able to infer PAI accurately for

the multi-layered canopy. Additionally, a bias may arise from underestimated PAI based on DHP. This could not be verified due to a lack of direct measurements but is an issue which has previously been highlighted for DHP (Toda and Richardson, 2018).

A number of simplifying assumptions were made during model parameterization (optical properties, leaf angular distribution). We showed that not simulating leaf reflectance and transmittance added up to 15% relative error to understory PAR simulations at maximum PAI (Figure A 12), a value consistent with previous findings (Hutchison and Matt, 1976). This error is considerably lower than the total SOP errors found in this study which means it is not a pivotal factor. The leaf angular distribution used on the other hand (planophile vs spherical) showed a large influence of up to 372% for the maximum solar elevation angle (Figure A 13) and could have contributed to discrepancies where the true angular distribution is closer to planophile (possible for the deciduous canopy) than the simulated spherical distribution. While assuming spherical distributions is common (Brunner, 1998; Chianucci et al., 2016; Gastellu-Etchegorry et al., 1999), our findings indicate that this may not be adequate for the purpose of understory PAR simulation. Options for constraining this parameter are limited. Inferring angular distribution from drone measurements has been trialled (McNeil et al., 2016) but is difficult to implement across dense stands with many species. Point-based angular distribution can be retrieved from DHP, though conventional methods are uncertain (Zhao et al., 2019). Canopy layering has also been shown to have considerable impacts on radiation propagation (Schneider et al., 2014) but is more relevant for vertical PAR distributions within canopies which was not investigated here.

7.4.3 Capability of drone-data parameterised models to improve simulations of small-scale understory PAR variations

In contrast to DLI variations in transition zones between isolated crowns and open sky, the simulations did not appear to represent the small spatial variations in understory light availability under the woodland canopy (Table 7-3, Figure A 14). No significant correlations with spatial validation measurements were found when using multiple alternative methods of crown representations and PAD variations

(Table 7-3). Spatial differences in simulated DLI between Sim_main and the simulations using ellipsoid crown representations (Figure 7-9) were likely associated with spatial mismatches in crown shapes between ellipsoid approximations and the CHM while some overestimations were due to missing representations of shorter vegetation in the ellipsoid models.

Studies using geometric primitives generally focus mainly on spatially aggregated statistics on variability (Ligot et al., 2016; Martens et al., 2000) as simulating variations for precise locations is challenging. Successful simulations at microsite level (1 m^2) have however been performed in predominantly coniferous forest systems (Stadt et al., 2005). Variations at these scales are influenced by specific locations of canopy gaps and tree stems which could not be described appropriately following the drone-data informed model parameterisation as presented here. To better exploit the fine spatial grain of SfM point-cloud information for understory PAR estimation, the point cloud can be used to generate virtual DHPs as demonstrated by Brüllhardt et al. (2020) which allows estimates of spatial variations and vertical profiles of light availability. Such models are however likely to be very sensitive to point cloud density and size of point representations, considerably underestimate PAI under dense vegetation due to the lack of canopy penetration of photogrammetric methods and can't easily be extended to include e.g. light transmission through leaves.

Representing these structural variations in 3D requires highly accurate models of woody structure and PAI/PAD which is likely only possible using LiDAR methods. A simple model of PAR extinction through forest canopies based on drone LiDAR has recently illustrated the potential of these datasets (Zeng et al., 2019) and the TLS-based representations of forest structure in combination with species-specific optical properties show promise for accurate RT simulations (Calders et al., 2018). Building upon LiDAR based forest structure models as a baseline, drone multispectral data could provide auxiliary data with the flexibility and ease of acquisition required to characterise and simulate spatiotemporal changes.

7.4.4 Opportunities for 3D RT models informed by drone acquired data

3D RTMs are a powerful tool which can benefit from the simplified acquisition of finely resolved structural information on vegetation which is now possible using drones. In addition to enabling PAR simulations as shown here, the presented methodology of characterising vegetated scenes is a widely applicable low-cost option which can enable a range of further studies. The forward simulation of remote observations or the inversion thereof for retrieval of vegetation properties at the individual and leaf level was previously explored using purely in-situ measurements or airborne LiDAR data for model inputs (Kötz et al., 2004b; Schneider et al., 2014). Accurate parameterisation of forest stands in terms of structure and optical properties allows insights into ecosystem functioning, where for example DART has been used to simulate absorbed photosynthetically active radiation (APAR) in 3D (Damm et al., 2020). Applications in microclimate modelling are also being explored as the simulation of shortwave radiation propagation through 3D scenes could be coupled with other models making use of drone based structural data for simulating accurate local microclimatic conditions (Zellweger et al., 2019). The adjustment of the presented drone-based scene parameterisation for these applications requires additional information on optical and thermal properties of vegetation elements which may in turn be constrained by drawing on the additional spectral information provided by drone mounted sensors.

7.5 Conclusions

Our study highlights that there is potential for making use of fine grained drone SfM and multispectral data within 3D RTMs as it is an efficient and cost-effective data acquisition method which allows the representation of true vegetation canopy extents, heights and PAI variations. The DART model and drone acquired vegetation information was used to generate spatially explicit maps of understory PAR. The implementation needs to be improved to accurately simulate PAR propagation as evidenced by validation efforts. The main sources of uncertainties in this approach are related to known limitations of SfM and VI datasets, as well as structural parameters which are difficult to measure (small gaps and leaf angle

distribution). Additional measurements of these key parameters could greatly benefit model parameterisation. There exist options to improve upon this, such as developing season specific relationships of VIs with PAI, retrieving PAI through RTM inversions or making use of additional metrics extracted from the finely resolved image datasets. While drone LiDAR could address many of the limitations identified in this study, the added value of spectral information should not be neglected and its potential has yet to be demonstrated in a modelling context. Given additional inputs of optical properties and surface emissivity, the presented parameterisation of the DART model could be extended to generate valuable products for a range of applications including microclimate modelling, ecosystem functioning, and for simulating scene surface reflectance for scaling from leaf to canopy and landscape scale for vegetation monitoring purposes.

8 Synthesis

In the following, key findings from the previous chapters and further preliminary studies are discussed in the context of the main research aims and how they contribute to the wider fields of vegetation remote sensing and modelling.

The questions associated with the research aims introduced in chapter 2 were as follows and are addressed in sections 8.1, 8.2 and 8.3 respectively:

- 1) To what extent can SfM photogrammetry-derived products deliver accurate information about vegetation height parameters?
- 2) How accurate and consistent are surface reflectance and VI products acquired from drone-based sensors over vegetation canopies?
- 3) Can drone-based data be used to constrain and drive models of radiative transfer for understanding photon-plant interactions in complex heterogeneous canopies?

Section 8.4 provides an overview of the potential of the presented methodologies for studying the global carbon cycle.

8.1 Retrieving vegetation height metrics using drone-based SfM photogrammetry

SfM using drone-acquired image data for vegetation height and volume estimations have been studied extensively in recent years with a primary focus on forest inventories (Alonzo et al., 2018; Fraser and Congalton, 2018; Frey et al., 2018; Guerra-Hernández et al., 2018; Jayathunga et al., 2018; Karpina et al., 2016; Krause et al., 2019; Mlambo et al., 2017; Nuijten et al., 2019; Panagiotidis et al., 2017; Puliti et al., 2015) and applications in precision agriculture and crop phenotyping contexts (Holman et al., 2016; Michez et al., 2018; Schirrmann et al., 2016; Wilke et al., 2019; Yang et al., 2017). The findings presented in chapters 4 and 7 expanded upon this work by applying a drone SfM based and LiDAR DTM independent height retrieval to a new study system (oil palm plantations), trialling DSM based SfM point-cloud segmentation methods (oil palm plantations and mixed woodland), assessing two different acquisition strategies and

demonstrating good practice methods of uncertainty estimation (MC for point cloud precision, *in situ* validation and replicates for height metrics). Height metrics including individual tree height percentiles, heights of top palm fronds (TFH) and continuous vegetation heights were derived from SfM photogrammetry point clouds while palm stem heights and crown base height required empirical models based on the relationship of primary height metrics to *in situ* measurements.

Results showing that SfM point clouds could represent vegetation heights with errors of 11.7 to 18.9% for oil palms of different ages (2-10 years) heights and 11.8% for deciduous trees were comparable or better compared to similar previous studies (Dandois et al., 2015; Mlambo et al., 2017; Wallace et al., 2016). Height errors for the deciduous tree crowns on the Trelusback study site were comparable to the errors in oil palm heights despite the use of a LiDAR DTM for CHM generation and the differences of vegetation structure (height dominated by single palm fronds versus branch structure). While the lack of a LiDAR DTM was previously identified as greatly limiting for the application of SfM methods (Puliti et al., 2015), this did not prove detrimental for the plantation based analysis undertaken here, despite very few visible ground areas, mainly due to gently varying topography. In areas of more complex topography, the interpolation of few ground observations would introduce greater uncertainty. LiDAR DTM independent workflows are of great interest as they ensure the wide applicability and low cost of drone SfM methodology. Recently, a study on forest growing stock volume even demonstrated a LiDAR DTM independent workflow which was able to provide good estimates for deciduous forests on sloped terrain which represents the most challenging combination of ground occlusion and terrain variation (Giannetti et al., 2018).

Finally, an experiment showed that higher flying altitude (150 m vs 100 m) and lower overlap (60% vs >75%) leading to coarser resolution and sparser point clouds but greater spatial coverage, did not negatively impact the derived height metrics which is a promising result regarding the application of the drone SfM methodology over larger extents. The combined findings of the presented experiments in this thesis, therefore demonstrates that where top-of-crown heights and volumetric representations of vegetation suffice, drone SfM methods are an efficient low-cost option for the survey of plantations and natural systems for areas covering up to 20 ha, also corroborating findings of Ni et al. (2019) and

Guerra-Hernández et al., (2018). While these studies focused on multi-rotor drones as more flexible experimental platforms, greater coverage is possible when using fixed wing systems (Puliti et al., 2017b).

The MC method of point-cloud precision estimation (James et al., 2017b) which was here pioneered for vegetation applications in the first study of its kind, proved a valuable addition to replicate surveys for quality assurance purposes, as assessments of height errors using laser rangefinder or similar validation methods are limited by decimetre scale uncertainties comparable to the CHM errors themselves (Krause et al., 2019). Combined with replicated surveys as the previously advocated method of point cloud uncertainty estimation (Dandois and Ellis, 2013), this can greatly benefit the robustness of SfM-based studies.

The identified need to infer stem height and crown base height from empirical relationships highlights a key drawback of SfM-based analysis of vegetation structure. Due to the demonstrated uncertainties involved in this approach (relative errors of 12.2 and 30.9% for palm stem heights (7 and 10 year palm age), 42.1% for tree crown base height), the trade-offs between SfM and drone LiDAR acquisitions which is capable of directly resolving these metrics need to be carefully assessed. For dedicated small study sites where precise crown shapes and within-crown branch structure and foliage distribution is of interest, a drone-based LiDAR system is preferable, but may not be suitable for financial, logistical or legal reasons due to the weight of sensor and platform and prices of \$6'000-100'000. The use of modified flight plans and varied camera angles to improve SfM based 3D representations of trees including crown shape and stem diameter were briefly explored during a preliminary analysis for this thesis (Appendix A5) and shown to deliver point clouds representing the outer tree crown boundary with a mean distance of 6.5 cm to a TLS scan reference, but are limited in their applicability to natural systems due to the many acquisition angles required.

The limitations of conventional drone based SfM point clouds for resolving vertical vegetation structure and stems result in difficulties when it comes to crown identification and delineation in complex systems. Plant crown segmentation based on the SfM point clouds and CHM as was performed in this work for oil palms and a variety of deciduous and coniferous trees were highly dependent on clearly identifiable local maxima and the distance constraints for the algorithm (segmentation methods of the lidR package V. 2.2 (Roussel and Auty, 2018; Silva

et al., 2016)). Segmentation worked well (94.9% and 98.2% for palm ages 7 and 10 respectively), which was expected, in a plantation context with prescribed planting distances and little topographic variation. For deciduous crowns in the closed woodland canopy of the Trelusback study site, little height variation led to the number of identified crowns relying exclusively on the distance constraint but the selection of a value representative of the whole study site was not possible. This work highlights the need for additional information to be used for crown segmentation, e.g. as inputs for machine learning based approaches, and supports the recent findings of Nuijten et al. (2019) and Xu et al. (2020).

In conclusion, and in response to the original question posed, this work has shown that drone-captured SfM photogrammetry-derived products can deliver information about vegetation height parameters with relatively high precision and accuracy, though the assessment of accuracy is somewhat limited by the uncertainty in validation methods. Users should also be aware of the method's constraints highlighted by this and related work. These relate primarily to the lack of vegetation canopy penetration for robust DTM generation and the segmentation of individual plant crowns which however could be addressed with dedicated workflows.

8.2 Accuracy and consistency of surface reflectance and vegetation indices derived from drone acquired measurements

8.2.1 Drone acquired surface reflectance and vegetation indices

Multi- and hyperspectral imaging from drones can combine fine spatial resolution with spectral information for retrieving object specific optical properties, from plants to individual leaves, with unique potential applications for smaller scale study sites such as flux-tower footprints (Gamon, 2015). As highlighted previously, there are however many potential sources of uncertainty affecting such measurements from drone platforms, which should be assessed and motivated the investigation of such data from relatively low-cost sensors which are now being widely applied in both scientific and industrial vegetation monitoring. In chapter 5, surface reflectance (HCRF) results from a commonly used consumer grade MCA system (Parrot Sequoia) were presented for both natural and

reference panel surfaces. Results showed that the reflectance for low reflective targets was generally overestimated, likely related to unaccounted adjacency effects and dark current. Surface reflectance errors were in the range of 2-4% (4-15% relative error) for the four spectral bands. Similar errors over reference panels were identified in other studies using MCA systems (Deng et al., 2018; Stow et al., 2019). The assessment of different calibration methods (single panel versus ELM) for the study in chapter 5 showed greater bias either at visible or NIR wavelengths with no method clearly performing better overall. This is in contrast to a similar experiment which showed much smaller errors for ELM over reference panels (Fawcett and Anderson, 2019) (Appendix A6), however this experiment did not use a zero intercept for the ELM and panels were imaged at a lower flying altitude, mitigating adjacency effects. The need for a zero intercept or modified zero intercept as was also trialled in chapter 5 was identified due to the ELM based on a bright and dark target leading to negative surface reflectance values in shaded regions, an issue previously identified within studies using the same sensor (Tu et al., 2018). The presented work confirmed that this issue, which most likely relates to non-linearity or poor characterisation of the sensor response for very low radiance values, coupled with saturation over higher reflective surfaces, is a clear limitation for the calibration to surface reflectance of these low-cost sensor data. Performing an absolute radiometric calibration of the sensor in an optical laboratory instead of relying on manufacturer provided coefficients is an option to minimize encountered uncertainties, however such facilities are not readily available and considerable financial costs are involved (Hakala et al., 2018; Minařík et al., 2019). Recent efforts towards developing a drone based robust spectral sampling platform seek to forgo the need for vicarious calibration and focus on direct calibration using incoming radiance, but instead face difficulties related to stabilisation and varying sun-irradiance sensor geometry (Suomalainen et al., 2018).

Besides the reference panel based analysis, our study presented the first assessment of drone-acquired surface reflectance spatially by comparing it to a 1 m spatial resolution simultaneous acquisition with the HyPlant imaging spectrometer. Consistency in reflectance across scales is an important requirement if drones are to be applied for high resolution spectral sampling e.g. to link ecophysiological mechanisms at individual level to patterns observed at

coarser scales, the need for which was outlined by Gamon (2015). The spatial assessment performed here revealed that BRDF effects in the drone surface reflectance mosaics were most prominent at the NIR wavelengths but overall did not appear to result in a confounding spatial bias. Reflectance at visible wavelengths was slightly overestimated for vegetated surfaces and underestimated for bright bare soil which was attributed to issues in the simplified radiometric calibration procedures described previously.

Ratio based indices (incl. NDVI, CHL, NDRE) are commonly used in place of spectral reflectance values of individual bands which mitigate many of these issues (Deng et al., 2018) and are sufficient for most applications of drone acquired information such as detecting spatial variability of vegetation cover and status including changes over time. Results from chapter 5 confirmed this as it showed that NDVI values derived from calibrated reflectance values acquired with the Parrot Sequoia camera corresponded to airborne and satellite acquisitions using comparable bands, thus showing that drone measurements can supplement such acquisitions by providing higher spatial or temporal resolution for spatial subsets. This comparison did however rely on data captured very proximal in time and recent studies using the same sensor model showed that illumination geometry which changes over time had a considerable impact with implications for the temporal consistency of such indices (Jiang et al., 2020; Stow et al., 2019). Nevertheless, the work in chapter 6 clearly showed that such impacts are secondary for applications such as monitoring the gradual NDVI increase during Spring green-up.

8.2.2 Deriving LAI and PAI from drone NDVI measurements

The VI based retrieval of LAI is well explored on the basis of airborne and satellite image data using empirical and physically based methods (Fensholt et al., 2004; Haboudane et al., 2004; Houborg et al., 2007; Kang et al., 2016; Zheng and Moskal, 2009). Such studies have identified key limitations of VIs such as background effects and saturation at high LAI values (Heiskanen, 2006; Spanner et al., 1990; Wang et al., 2005). LAI retrieval from drone acquired VI data has focused mostly on agricultural crops (Yao et al., 2017; Zhu et al., 2019) with few studies covering forest ecosystems. Here insights from the tree focused studies

of chapters 6 and 7 provide important contributions to the field. While drone data provides information at fine spatial scales and thus has the potential to identify very localised LAI variations, one of the main difficulties encountered is the provision of *in situ* reference measurements at appropriate scales for calibration and validation. For field crops, this is possible through destructive sampling (Yao et al., 2017; Zhu et al., 2019) but for many natural ecosystems this is not an option. Indirect assessments of LAI are possible but due to common methods (LAI-2000, DHP) integrating data over the hemisphere, developed sampling protocols focus on acquiring data representative of larger elementary sampling units (Baret et al., 2005), see also the ESUs and sampling method presented in chapter 5. For smaller extents such as individual crowns, a modified approach is needed.

For the work presented in chapters 6 and 7 a similar issue in the sampling of PAI was addressed by implementing a novel sampling methodology which focused on single crowns and incorporated drone CHM information in place of extensive field measurements of crown geometry. This allowed a first PAI estimation from drone NDVI data at the individual tree level. It is accepted that such approaches have high uncertainties and encounter the limitations of what can be inferred from hemispherical observations (Bréda, 2003; Cutini and Varallo, 2006), and further dedicated assessments of this methodology are therefore needed. Further results from the presented work revealed NDVI saturation at higher LAI and PAI values for a maize field and for tree crowns of a woodland canopy. This corroborates findings from field-spectrometer and satellite based observations concerning NDVI saturation (Gamon et al., 1995; Huete et al., 1997; Wang et al., 2005) but identifying this influence also at the fine spatial scale of drone measurements represents an important insight. Notably, the strong saturation effect was observed in absence of any notable atmospheric influence, which was previously identified as an important factor regarding VI fidelity (Huete et al., 2002). Instead, in chapter 5 it was found that drone NDVI sensitivity to LAI was reduced in comparison to an airborne NDVI dataset which were attributed to calibration related uncertainties. Combined with the variability of woody vegetation structure this contributed to the relatively high observed errors for the empirical NDVI-PAI relationship in chapter 7 (RMSE= 0.885, mean PAI = 3.05). These findings back up the fact that LAI and PAI retrieval based solely on VIs has limitations and therefore to make the most use of the fine spatial resolution information which

can be provided by drone acquired VI data, it is worth exploring the added value of textural metrics and plot or crown-scale statistics of VI variability which has been the focus of recent studies (Duan et al., 2019; Li et al., 2019; Yue et al., 2019).

Besides the fine spatial resolution, one of the main advantages of drone-based LAI or PAI retrievals is the ability to acquire the data in both, overcast and clear sky conditions. Results from chapter 6 highlighted the potential for stable PAI time-series based on VIs. Although a comparison of derived PAI at crown scale on subsequent days of differing illumination during leaf-on conditions (chapter 7, Appendix A4) showed relatively high deviations ($\text{RMSE} = 0.48$), this difference was exacerbated by the saturation related uncertainty in the empirical relationship at high PAI values and should prove less of a problem for a sparser vegetation canopy.

Regarding the original question about the accuracy and consistency of surface reflectance and VI products acquired from drones, this work has highlighted that drone data can suffer from the same uncertainties found in other remote sensing datasets (NDVI saturation at high LAI/PAI) and additional uncertainties due to the use of low-cost sensors and simplified calibration workflows, influencing surface reflectance estimates. They can however provide remarkably spatially and temporally consistent, highly resolved VI information which allows the monitoring of individual tree crowns and variability within agricultural fields. With regards to wider deployment, users should be aware of the limitations observed and consider whether additional sensor calibration efforts are required, as well as seek to reduce uncertainties introduced by illumination variations.

8.3 Use of drone-acquired data to constrain and drive 3D radiative transfer models

The level of detail with which vegetated scenes are represented in RTMs represents a trade-off between processing time or capacity, the spatial resolution at which processes should be represented and the available data. Highly detailed simulations are needed as benchmarks to test the impact of simplified assumptions (Guillevic and Gastellu-Etchegorry, 1999) or to generate spatially

specific maps and allow deriving parameters of interest at the level of individual plants (Berni et al., 2009; Guillen-Climent et al., 2012; Schneider et al., 2017). For such simulations, some simplifications, e.g. the use of geometric primitives to represent crown geometry, are used in absence of scale-appropriate structural data to represent vegetation (Ligot et al., 2016). This is where drones can be leveraged by acquiring information on vegetation structure as described in section 8.1.

The workflow presented in chapter 7 provides the first detailed demonstration of how drone acquired data on essential vegetation structure parameters (horizontal and vertical extents, PAI) may be used for descriptions of vegetation in a 3D RTM. By using DART with drone-data informed scene representations to model the availability of understory PAR, the potentials and limitations of such an approach were highlighted for the first time. Advantages include the rapid acquisition of vegetation height for study sites that are multiple hectares in size and resolving small height differences. Repeat multi-spectral acquisitions allowed representing PAI changes at individual crown level by exploiting a NDVI time-series and an empirical NDVI-PAI relationship, thus demonstrating how drone data may be used to update model parameters and simulate temporal variations of the modelled quantity. Drone-data based representations of vegetation in physical models is not yet widespread to the author's knowledge, with just a few publications detailing irradiance and energy balance modelling (Abdollahnejad et al., 2018; Aboutalebi et al., 2020; Zeng et al., 2019), so this work represents an important demonstration. While it is anticipated that these studies and the presented work herein will spark further interest in such applications, the lack of substantial work may also relate to current limitations of data and methodologies. SfM-based representations of vegetation from standard acquisition methods result in predominantly 2.5 D photogrammetric point clouds, but understory vegetation and within-crown structures are important for modelling many physical processes of interest, such as interception and scattering of radiation and beyond radiative transfer e.g. the interception of precipitation (Chen et al., 1994; Disney et al., 2006; Muzylo et al., 2009; Schneider et al., 2014; Van der Zande et al., 2011). Multi-spectral data can supplement structural information by deriving PAI through empirical relationships with VIs as presented here, but such relationships are uncertain particularly when including a wide range of vegetation structural

types and suffer from saturation at high PAI values. Furthermore, leaf angle distribution and clumping remain unknowns, though work which further develops levelled drone image-based approaches such as presented by McNeil et al. (2016) may yield solutions.

Recent advances in drone LiDAR show promise for enhanced 3D representations of vegetation canopies in RTMs and address some of the shortcomings of SfM datasets. ALS and TLS data have previously proved effective for these purposes, e.g. by deriving foliage density per voxel based on 3D point densities (Calders et al., 2018; Kükenbrink et al., 2019; Schneider et al., 2014), and first related applications of drone LiDAR for modelling PAR transmission in forest stands have been demonstrated (Zeng et al., 2019). Recently developed TLS-based methods for retrieving leaf angle distribution (Vicari et al., 2019) could also be adapted for use with drone acquired data. Further developing from the work in this thesis, it is anticipated that drone-based SfM derived vegetation information will find application for modelling purposes as low cost alternative to drone LiDAR and where lightweight equipment is required, e.g. in remote areas or where drone LiDAR systems fall into a higher weight category and require advanced permissions. Additionally the optical information accompanying photogrammetric point clouds is often a by-product but has added value for classification purposes (Alonzo et al., 2018), particularly if they are based on acquisitions from calibrated off-the-shelf cameras (Holman et al., 2019).

The capability of drones to acquire optical properties of surfaces was discussed in the previous section 8.2, which is also of interest for radiative transfer modelling. Efficient acquisition of optical properties of many scene elements would enable the realistic forward modelling of scene reflectance (Schneider et al., 2014) and aid in understanding spectral measurements acquired at coarser resolutions (satellite and airborne data), such as the impact of sun-ground-sensor geometry (Verhoef and Bach, 2003). Low-cost MCA sensors and simplified calibration procedures result in uncertainties and coupled with wavelength bands which do not perfectly match those of satellite sensors (chapter 5) make them unsuited for this purpose. Instead, advances in this field are expected from drone-based hyperspectral sensing and MCAs with purpose designed transmission filters (e.g. MAIA camera with Sentinel-2 equivalent band-pass filters, (Revill et al., 2019)).

The work delivered in this thesis includes one of the first demonstrations of how the value of drone-captured data goes beyond the quantification of structural parameters at fine resolutions by integrating derived values for 3D RTM scene descriptions, which can provide important insights into light availability, and further, ecosystem functioning. To answer the posed question on whether drone acquired data can be used to constrain and drive models of radiation interaction with vegetation, a widely applicable method of representing vegetation in the free DART model with easily acquired drone SfM derived CHMs was presented, along with an NDVI based approach to prescribe PAI per crown. This allowed the representation of spatial heterogeneity in discontinuous tree stands but showed limitations for modelling radiation interactions post canopy closure in denser stands. It is anticipated that advances in the areas of drone LiDAR and spectroscopy can provide missing metrics to extend upon this framework in the coming years.

8.4 Drone based observations for global studies of the carbon cycle

Recent work has demonstrated methods to effectively incorporate datasets with limited coverage from drone acquisitions for the calibration and validation of landscape scale models based on coarser resolution satellite data (Kattenborn et al., 2019; Puliti et al., 2017b; Wang et al., 2020). Based on such modelling frameworks it is anticipated that drone data will play an increasingly important role in the study of carbon stocks and fluxes (Réjou-Méchain et al., 2019; Xiao et al., 2019). This section outlines how the work presented in this thesis can contribute towards understanding the global carbon cycle.

The use of drone-based SfM to derive plot-scale AGC for a variety of vegetation types has been demonstrated previously (Cunliffe et al., 2020, 2016; Navarro et al., 2020; Roth and Streit, 2017). The analysis in chapter 4 presented the first estimation of AGC-related height metrics for oil palms. Precise estimates of oil palm AGC at different growing stages are central to better quantifying the carbon budget of land-cover conversions from tropical rainforest to plantations (Kho and Jepsen, 2015). Furthermore, when seeking to assimilate AGC or growing-stock volume estimates from drone-based height metrics at inventory plot scales (multiple hectares) into satellite data based models (see Puliti et al. (2017b)),

point cloud precision estimates as were generated in the presented study will prove important for the propagation of measurement uncertainty and their reporting in carbon budgets.

The study of drone-acquired surface reflectance products and derived indices (chapter 5) demonstrated that vegetation index maps from low-cost multispectral cameras were consistent and highly correlated to spatial reference datasets. Combined with field measurements such index maps can be used to generate maps of structural properties such as LAI and, potentially, pigment contents with appropriate contiguous spatial coverage for comparisons with coarser resolution satellite datasets (Zhu et al., 2019). Satellite-based LAI estimates are key inputs for the spatial modelling of GPP (Xiao et al., 2004; Xie et al., 2019; Y. Zhang et al., 2019). Their calibration and validation using drone acquired data could further constrain uncertainties about the role of different vegetation types in the global carbon cycle.

Investigating the impact of climatic change on the timing of vegetation phenological events such as green-up and senescence is important for assessing the future vulnerability of ecosystems and their ability to sequester carbon (Polgar and Primack, 2011). The need for drone observations to scale species to landscape level phenology has been highlighted (Piao et al., 2019) and in chapter 6 we demonstrate that drone NDVI observations can indeed be used to distinguish the timing of vegetation green-up at the species level, further paving the way for such scaling studies.

Finally, fine scale modelling of radiative transfer in vegetation canopies, presented using drone data for the first time in chapter 7, holds the key to better relate remote observations to the functioning of complex vegetation stands such as forests. Models informed by estimates of vegetation structure and light availability will eventually enable a scaling of gas exchange processes from leaf to forest stands and landscape scales, leading to a better understanding of their functioning under climatic change (Damm et al., 2020).

9 Conclusions

- The application of SfM photogrammetry to drone acquired overlapping images yielded point clouds from which reliable vegetation height could be derived with relative errors of approximately 10% for deciduous and palm trees > 7 years of age. LiDAR DTMs were not required for point cloud normalisation in an oil palm plantation due to small topographic variations, backing up the usefulness of SfM approaches for vegetation structure in absence of such auxiliary data. Deriving advanced structural metrics such as palm stem height and tree crown base height required empirical models which introduced greater uncertainty and where drone LiDAR would provide clear advantages. Acquisition designs favouring coverage over image overlap didn't increase errors in the derived heights of individual palms. The findings in this thesis indicate that the drone-based SfM method represents a flexible option for the rapid acquisition of vegetation heights and crown shape for non-overlapping crowns.
- When deriving surface reflectance values from low-cost MCA cameras, issues due to saturation over highly reflective surfaces and over-estimations at low reflectance values were identified regardless of calibration methodology (single panel imaged pre-flight versus ELM using panels imaged in-flight). This highlighted the limitations of using such systems for accurate surface reflectance retrievals, though lab-based characterisations of these sensors without relying on manufacturer provided values for calibration may yield improvements. VI values proved to be highly correlated to lower resolution reference datasets and in the case of NDVI the absolute values were also very similar to airborne and satellite derived values. Drone acquired VI orthomosaics have great potential for providing finely resolved insights for vegetation monitoring studies which can be directly related to satellite acquired values to upscale such analyses.

- Multi-temporal NDVI orthomosaics acquired using a low-cost drone-mounted MCA system under either overcast or cloud-free sky conditions were sufficiently consistent geometrically and in their value ranges to be able to track spring phenology related changes of individual tree crowns. Uncertainties arising from the combination of acquisition geometry, calibration and illumination related differences were an order of magnitude smaller than mean NDVI increase across the Spring for deciduous crowns. This dataset allowed differentiating green-up timing between multiple deciduous species. The methodology shows promise for monitoring inter-annual changes in deciduous species phenology and could fill cloud-related gaps in satellite records for small study sites.
- Reliable drone acquired vegetation height metrics and consistent VIs allow the creation of fully drone-based characterisations of vegetated study sites for radiative transfer modelling purposes. By relating NDVI to PAI and using SfM point clouds to populate a scene with turbid voxels representing vegetation a 1 m spatial resolution simulation of understory PAR was achieved. Biased results for peak-greenness indicated limitations in the empirical relationship to determine PAI but there are avenues to improve PAI estimates by making better use of the finely resolved data provided by drone-mounted MCAs. Overall, this application demonstrated how drone acquired structural and spectral data could be used to create a spatially detailed representation of vegetation functioning, given additional input parameters such as leaf optical properties.

10 References

- 3D Robotics, 2015. SOLO operation manual.
- Aasen, H., Bolten, A., 2018. Multi-temporal high-resolution imaging spectroscopy with hyperspectral 2D imagers – From theory to application. *Remote Sens. Environ.* 205, 374–389. doi:10.1016/j.rse.2017.10.043
- Aasen, H., Burkart, A., Bolten, A., Bareth, G., 2015. Generating 3D hyperspectral information with lightweight UAV snapshot cameras for vegetation monitoring: From camera calibration to quality assurance. *ISPRS J. Photogramm. Remote Sens.* 108, 245–259. doi:10.1016/j.isprsjprs.2015.08.002
- Aasen, H., Honkavaara, E., Lucieer, A., Zarco-Tejada, P.J., 2018. Quantitative remote sensing at ultra-high resolution with UAV spectroscopy: A review of sensor technology, measurement procedures, and data correction workflows. *Remote Sens.* 10, 1–42. doi:10.3390/rs10071091
- Abdollahnejad, A., Panagiotidis, D., Surový, P., Ulbrichová, I., 2018. UAV Capability to Detect and Interpret Solar Radiation as a Potential Replacement Method to Hemispherical Photography. *Remote Sens.* 3, 1–17. doi:10.3390/rs10030423
- Abdulridha, J., Ampatzidis, Y., Kakarla, S.C., Roberts, P., 2020. Detection of target spot and bacterial spot diseases in tomato using UAV-based and benchtop-based hyperspectral imaging techniques. *Precis. Agric.* 21, 955–978. doi:10.1007/s11119-019-09703-4
- Aboutalebi, M., Torres-Rua, A.F., Kustas, W.P., Nieto, H., Coopmans, C., McKee, M., 2019. Assessment of different methods for shadow detection in high-resolution optical imagery and evaluation of shadow impact on calculation of NDVI, and evapotranspiration. *Irrig. Sci.* 37, 407–429. doi:10.1007/s00271-018-0613-9
- Aboutalebi, M., Torres-Rua, A.F., McKee, M., Kustas, W.P., Nieto, H., Alsina, M.M., White, A., Prueger, J.H., McKee, L., Alfieri, J., Hipps, L., Coopmans, C., Dokoozlian, N., 2020. Incorporation of Unmanned Aerial Vehicle (UAV) point cloud products into remote sensing evapotranspiration models.

Remote Sens. 12. doi:10.3390/RS12010050

Adams, H.D., Collins, A.D., Briggs, S.P., Vennetier, M., Dickman, L.T., Sevanto, S.A., Garcia-Forner, N., Powers, H.H., McDowell, N.G., 2015. Experimental drought and heat can delay phenological development and reduce foliar and shoot growth in semiarid trees. *Glob. Chang. Biol.* 21, 4210–4220. doi:10.1111/gcb.13030

Adão, T., Hruška, J., Pádua, L., Bessa, J., Peres, E., Morais, R., Sousa, J.J., 2017. Hyperspectral Imaging: A Review on UAV-Based Sensors, Data Processing and Applications for Agriculture and Forestry. *Remote Sens.* 9. doi:10.3390/rs9111110

Adler, K., 2018. Radiometric correction of multispectral images collected by a UAV for phenology studies. Lund University.

Ahl, D.E., Gower, S.T., Burrows, S.N., Shabanov, N. V., Myneni, R.B., Knyazikhin, Y., 2006. Monitoring spring canopy phenology of a deciduous broadleaf forest using MODIS. *Remote Sens. Environ.* 104, 88–95. doi:<https://doi.org/10.1016/j.rse.2006.05.003>

Ahmed, O.S., Shemrock, A., Chabot, D., Dillon, C., Williams, G., Wasson, R., Franklin, S.E., 2017. Hierarchical land cover and vegetation classification using multispectral data acquired from an unmanned aerial vehicle. *Int. J. Remote Sens.* 38, 1–16. doi:10.1080/01431161.2017.1294781

Alados, I., Foyo-Moreno, I., Alados Arboledas, L., 1996. Photosynthetically active radiation: Measurements and modelling. *Agric. For. Meteorol.* 78, 27–38. doi:10.1016/S0168-1923(98)00107-5

Alonso, M., Andersen, H.-E., Morton, D.C., Cook, B.D., 2018. Quantifying Boreal Forest Structure and Composition Using UAV Structure from Motion. *Forests* 9. doi:10.3390/f9030119

Alonso, M., Dial, R.J., Schulz, B.K., Andersen, H.-E., Lewis-Clark, E., Cook, B.D., Morton, D.C., 2020. Mapping tall shrub biomass in Alaska at landscape scale using structure-from-motion photogrammetry and lidar. *Remote Sens. Environ.* 245, 111841. doi:<https://doi.org/10.1016/j.rse.2020.111841>

- Anderson, K., Gaston, K.J., 2013. Lightweight unmanned aerial vehicles will revolutionize spatial ecology. *Front. Ecol. Environ.* 11, 138–146.
doi:10.1890/120150
- Anderson, M.C., 1964. Studies of the Woodland Light Climate : I . The Photographic Computation of Light Conditions. *J. Ecol.* 52, 27–41.
- Aragones, D., Rodriguez-Galiano, V.F., Caparros-Santiago, J.A., Navarro-Cerrillo, R.M., 2019. Could land surface phenology be used to discriminate Mediterranean pine species? *Int. J. Appl. Earth Obs. Geoinf.* 78, 281–294.
doi:10.1016/j.jag.2018.11.003
- Arroyo-Mora, J.P., Kalacska, M., Inamdar, D., Soffer, R., Lucanus, O., Gorman, J., Naprstek, T., Schaaf, E.S., Ifimov, G., Elmer, K., Leblanc, G., 2019. Implementation of a UAV–Hyperspectral Pushbroom Imager for Ecological Monitoring. *Drones* 3. doi:10.3390/drones3010012
- Asner, G.P., 2009. Tropical forest carbon assessment: integrating satellite and airborne mapping approaches. *Environ. Res. Lett.* 4, 034009.
doi:10.1088/1748-9326/4/3/034009
- Asner, G.P., Martin, R.E., Knapp, D.E., Tupayachi, R., Anderson, C.B., Sinca, F., Vaughn, N.R., Llactayo, W., 2017. Airborne laser-guided imaging spectroscopy to map forest trait diversity and guide conservation. *Science* (80-.). 355, 385–389. doi:10.1126/science.aaj1987
- Assmann, J.J., Kerby, J.T., Cunliffe, A.M., Myers-smith, I.H., 2019. Vegetation monitoring using multispectral sensors — best practices and lessons learned from high latitudes. *J. Unmanned Veh. Syst.* 7, 54–75.
doi:<https://doi.org/10.1139/juvs-2018-0018>
- Atzberger, C., Richter, K., 2012. Spatially constrained inversion of radiative transfer models for improved LAI mapping from future Sentinel-2 imagery. *Remote Sens. Environ.* 120, 208–218. doi:10.1016/j.rse.2011.10.035
- Avitabile, V., Herold, M., Heuvelink, G.B.M., Lewis, S.L., Phillips, O.L., Asner, G.P., Armston, J., Ashton, P.S., Banin, L., Bayol, N., Berry, N.J., Boeckx, P., de Jong, B.H.J., DeVries, B., Girardin, C.A.J., Kearsley, E., Lindsell, J.A., Lopez-Gonzalez, G., Lucas, R., Malhi, Y., Morel, A., Mitchard, E.T.A., Nagy, L., Qie, L., Quinones, M.J., Ryan, C.M., Ferry, S.J.W., Sunderland,

T., Laurin, G.V., Gatti, R.C., Valentini, R., Verbeeck, H., Wijaya, A., Willcock, S., 2016. An integrated pan-tropical biomass map using multiple reference datasets. *Glob. Chang. Biol.* 22, 1406–1420.
doi:10.1111/gcb.13139

Baccini, A., Goetz, S.J., Walker, W.S., Laporte, N.T., Sun, M., Sulla-Menashe, D., Hackler, J., Beck, P.S.A., Dubayah, R., Friedl, M.A., Samanta, S., Houghton, R.A., 2012. Estimated carbon dioxide emissions from tropical deforestation improved by carbon-density maps. *Nat. Clim. Chang.* 2, 182–185. doi:10.1038/nclimate1354

Baldocchi, D., Hutchison, B., Matt, D., McMillen, R., 1984. Seasonal variations in the radiation regime within an oak-hickory forest. *Agric. For. Meteorol.* 33, 177–191.

Baldocchi, D., Valentini, R., Running, S., Oechel, W., Dahlman, R., 1996. Strategies for measuring and modelling carbon dioxide and water vapour fluxes over terrestrial ecosystems. *Glob. Chang. Biol.* 2, 159–168.
doi:10.1111/j.1365-2486.1996.tb00069.x

Banerjee, B.P., Raval, S., Cullen, P.J., 2020. UAV-hyperspectral imaging of spectrally complex environments. *Int. J. Remote Sens.* 41, 4136–4159.
doi:10.1080/01431161.2020.1714771

Baret, F., Weiss, M., Allard, D., Garrigues, S., Leroy, M., Jeanjean, H., Fernandes, R., Myneni, R., Privette, J., Morisette, J., 2005. VALERI: a network of sites and a methodology for the validation of medium spatial resolution land satellite products. *Remote Sens. Environ.* 76, 36–39.

Basler, D., Körner, C., 2012. Photoperiod sensitivity of bud burst in 14 temperate forest tree species. *Agric. For. Meteorol.* 165, 73–81.
doi:10.1016/j.agrformet.2012.06.001

Bayer, B.E., 1976. Color Imaging Array. U. S. Pat. 3971 065.

Bazzaz, F.A., 1996. Plants in changing environments : linking physiological, population, and community ecology. Cambridge ; New York : Cambridge University Press.

Beck, H.E., Zimmermann, N.E., McVicar, T.R., Vergopolan, N., Berg, A., Wood,

- E.F., 2018. Present and future köppen-geiger climate classification maps at 1-km resolution. *Sci. Data* 5, 1–12. doi:10.1038/sdata.2018.214
- Bendig, J., Bolten, A., Bennertz, S., Broscheit, J., Eichfuss, S., Bareth, G., 2014. Estimating biomass of barley using crop surface models (CSMs) derived from UAV-based RGB imaging. *Remote Sens.* 6, 10395–10412. doi:10.3390/rs61110395
- Bendig, J., Yu, K., Aasen, H., Bolten, A., Bennertz, S., Broscheit, J., Gnyp, M.L., Bareth, G., 2015. Combining UAV-based plant height from crop surface models, visible, and near infrared vegetation indices for biomass monitoring in barley. *Int. J. Appl. Earth Obs. Geoinf.* 39, 79–87. doi:10.1016/j.jag.2015.02.012
- Berni, J.A.J., Zarco-Tejada, P.J., Suárez, L., Fereres, E., 2009. Thermal and narrowband multispectral remote sensing for vegetation monitoring from an unmanned aerial vehicle. *IEEE Trans. Geosci. Remote Sens.* 47, 722–738. doi:10.1109/TGRS.2008.2010457
- Berra, E.F., Gaulton, R., Barr, S., 2019. Assessing spring phenology of a temperate woodland: A multiscale comparison of ground, unmanned aerial vehicle and Landsat satellite observations. *Remote Sens. Environ.* 223, 229–242. doi:10.1016/j.rse.2019.01.010
- Berra, E.F., Gaulton, R., Barr, S., 2017. Commercial Off-the-Shelf Digital Cameras on Unmanned Aerial Vehicles for Multitemporal Monitoring of Vegetation Reflectance and NDVI. *IEEE Trans. Geosci. Remote Sens.* 55, 4878–4886. doi:10.1109/TGRS.2017.2655365
- Birky, A.K., 2001. NDVI and a simple model of deciduous forest seasonal dynamics. *Ecol. Modell.* 143, 43–58. doi:10.1016/S0304-3800(01)00354-4
- Bolton, D.K., Gray, J.M., Melaas, E.K., Moon, M., Eklundh, L., Friedl, M.A., 2020. Continental-scale land surface phenology from harmonized Landsat 8 and Sentinel-2 imagery. *Remote Sens. Environ.* 240, 111685. doi:10.1016/j.rse.2020.111685
- Bowman, G., Tarayre, M., Atlan, A., 2008. How is the invasive gorse *Ulex europaeus* pollinated during winter? A lesson from its native range. *Plant Ecol.* 197, 197–206. doi:10.1007/s11258-007-9370-1

- Boyd, D.S., Almond, S., Dash, J., Curran, P.J., Hill, R.A., 2011. Phenology of vegetation in southern england from envisat meris terrestrial chlorophyll index (MTCI) data. *Int. J. Remote Sens.* 32, 8421–8447. doi:10.1080/01431161.2010.542194
- Braswell, B.H., Sacks, W.J., Linder, E., Schimel, D.S., 2005. Estimating diurnal to annual ecosystem parameters by synthesis of a carbon flux model with eddy covariance net ecosystem exchange observations. *Glob. Chang. Biol.* 11, 335–355. doi:10.1111/j.1365-2486.2005.00897.x
- Bréda, N.J.J., 2003. Ground-based measurements of leaf area index: A review of methods, instruments and current controversies. *J. Exp. Bot.* 54, 2403–2417. doi:10.1093/jxb/erg263
- Brede, B., Calders, K., Lau, A., Raumonen, P., Bartholomeus, H.M., Herold, M., Kooistra, L., 2019. Non-destructive tree volume estimation through quantitative structure modelling: Comparing UAV laser scanning with terrestrial LiDAR. *Remote Sens. Environ.* 233, 111355. doi:10.1016/j.rse.2019.111355
- Brede, B., Lau, A., Bartholomeus, H.M., Kooistra, L., 2017. Comparing RIEGL RiCOPTER UAV LiDAR Derived Canopy Height and DBH with Terrestrial LiDAR. *Sensors* 17. doi:10.3390/s17102371
- Brown, L.A., Dash, J., Ongutu, B.O., Richardson, A.D., 2017. On the relationship between continuous measures of canopy greenness derived using near-surface remote sensing and satellite-derived vegetation products. *Agric. For. Meteorol.* 247, 280–292. doi:10.1016/j.agrformet.2017.08.012
- Brown, T.B., Hultine, K.R., Steltzer, H., Denny, E.G., Denslow, M.W., Granados, J., Henderson, S., Moore, D., Nagai, S., Sanclementes, M., Sánchez-Azofeifa, A., Sonnentag, O., Tazik, D., Richardson, A.D., 2016. Using phenocams to monitor our changing earth: Toward a global phenocam network. *Front. Ecol. Environ.* 14, 84–93. doi:10.1002/fee.1222
- Browning, D.M., Peters, D.C., Steele, C., Rango, A., 2010. Field Validation of Biomass Retrieved From Landsat for Rangeland, in: International Geoscience and Remote Sensing Symposium Proceedings. pp. 3–6.
- Bruggisser, M., Hollaus, M., Otepka, J., Pfeifer, N., 2020. Influence of ULS

acquisition characteristics on tree stem parameter estimation. ISPRS J. Photogramm. Remote Sens. 168, 28–40.
doi:<https://doi.org/10.1016/j.isprsjprs.2020.08.002>

Brüllhardt, M., Rotach, P., Schleppi, P., Bugmann, H., 2020. Vertical light transmission profiles in structured mixed deciduous forest canopies assessed by UAV-based hemispherical photography and photogrammetric vegetation height models. Agric. For. Meteorol. 281, 107843.
doi:[10.1016/j.agrformet.2019.107843](https://doi.org/10.1016/j.agrformet.2019.107843)

Brunner, A., 1998. A light model for spatially explicit forest stand models. For. Ecol. Manage. 107, 19–46. doi:[10.1016/S0378-1127\(97\)00325-3](https://doi.org/10.1016/S0378-1127(97)00325-3)

Burkart, A., Aasen, H., Alonso, L., Menz, G., Bareth, G., Rascher, U., 2015. Angular dependency of hyperspectral measurements over wheat characterized by a novel UAV based goniometer. Remote Sens. 7, 725–746. doi:[10.3390/rs70100725](https://doi.org/10.3390/rs70100725)

Burkart, A., Cogliati, S., Schickling, A., Rascher, U., 2014. A Novel UAV-Based Ultra-Light Weight Spectrometer for Field Spectroscopy. IEEE Sens. J. 14, 62–67. doi:[10.1109/JSEN.2013.2279720](https://doi.org/10.1109/JSEN.2013.2279720)

Burt, A., Disney, M., Calders, K., 2019. Extracting individual trees from lidar point clouds using treeseg. Methods Ecol. Evol. 10, 438–445.
doi:[10.1111/2041-210X.13121](https://doi.org/10.1111/2041-210X.13121)

Butler, R. a, Laurance, W.F., 2009. Is oil palm the next emerging threat to the Amazon? Trop. Conserv. Sci. 2, 1–10.
doi:papers2://publication/uuid/5F4271A6-E2C2-4771-9248-7C5BC701B38B

Byun, Y., Song, J., Song, W., Kang, B., 2016. Conceptual Study of a Smart Docking System for VTOL-UAV. J. Aerosp. Eng. 29, 1–9.
doi:[10.1061/\(ASCE\)AS.1943-5525.0000508](https://doi.org/10.1061/(ASCE)AS.1943-5525.0000508)

Calders, K., Newnham, G., Burt, A., Murphy, S., Raumonen, P., Herold, M., Culvenor, D., Avitabile, V., Disney, M., Armston, J., Kaasalainen, M., 2015. Nondestructive estimates of above-ground biomass using terrestrial laser scanning. Methods Ecol. Evol. 6, 198–208. doi:[10.1111/2041-210X.12301](https://doi.org/10.1111/2041-210X.12301)

- Calders, K., Origo, N., Burt, A., Disney, M., Nightingale, J., Raumonen, P., Åkerblom, M., Malhi, Y., Lewis, P., 2018. Realistic forest stand reconstruction from terrestrial LiDAR for radiative transfer modelling. *Remote Sens.* 10, 1–15. doi:10.3390/rs10060933
- Candiago, S., Remondino, F., Giglio, M. De, Dubbini, M., Gattelli, M., 2015. Evaluating Multispectral Images and Vegetation Indices for Precision Farming Applications from UAV Images. *Remote Sens.* 7, 4026–4047. doi:10.3390/rs70404026
- Cannon, J.B., Tinkham, W.T., DeAngelis, R.K., Hill, E.M., Battaglia, M.A., 2019. Variability in mixed conifer spatial structure changes understory light environments. *Forests* 10. doi:10.3390/f10111015
- Cao, L., Liu, H., Fu, X., Zhang, Z., Shen, X., Ruan, H., 2019. Comparison of UAV LiDAR and Digital Aerial Photogrammetry Point Clouds for Estimating Forest Structural Attributes in Subtropical Planted Forests. *Forests* 10. doi:10.3390/f10020145
- Carlson, K.M., Curran, L.M., Asner, G.P., Pittman, A.M., Trigg, S.N., Marion Adeney, J., 2012. Carbon emissions from forest conversion by Kalimantan oil palm plantations. *Nat. Clim. Chang.* 3, 283–287. doi:10.1038/nclimate1702
- Casalegno, S., Anderson, K., Hancock, S., Gaston, K.J., 2017. Improving models of urban greenspace: from vegetation surface cover to volumetric survey using waveform laser scanning. *Methods Ecol. Evol.* 8, 1443–1452. doi:10.1111/2041-210X.12794
- Cendrero-Mateo, M.P., Wienke, S., Damm, A., Alonso, L., Pinto, F., Moreno, J., Guanter, L., Celesti, M., Rossini, M., Sabater, N., Cogliati, S., Julitta, T., Rascher, U., Goulas, Y., Aasen, H., Pacheco-Labrador, J., Mac Arthur, A., 2019. Sun-Induced Chlorophyll Fluorescence III: Benchmarking Retrieval Methods and Sensor Characteristics for Proximal Sensing. *Remote Sens.* 11. doi:10.3390/rs11080962
- Chang, C.Y., Zhou, R., Kira, O., Marri, S., Skovira, J., Gu, L., Sun, Y., 2020. An Unmanned Aerial System (UAS) for concurrent measurements of solar-induced chlorophyll fluorescence and hyperspectral reflectance toward

improving crop monitoring. *Agric. For. Meteorol.* 294, 108145.

doi:<https://doi.org/10.1016/j.agrformet.2020.108145>

Chen, B., Coops, N.C., Fu, D., Margolis, H.A., Amiro, B.D., Black, T.A., Arain, M.A., Barr, A.G., Bourque, C.P.A., Flanagan, L.B., Lafleur, P.M., McCaughey, J.H., Wofsy, S.C., 2012. Characterizing spatial representativeness of flux tower eddy-covariance measurements across the Canadian Carbon Program Network using remote sensing and footprint analysis. *Remote Sens. Environ.* 124, 742–755.

doi:[10.1016/j.rse.2012.06.007](https://doi.org/10.1016/j.rse.2012.06.007)

Chen, J., Saunders, S.C., Crow, T.R., Naiman, R.J., Brosofske, K.D., Mroz, G.D., Brookshire, B.L., Franklin, J.F., 1999. Microclimate in Forest Ecosystem the effects of different management regimes. *Bioscience* 49, 288–297.

Chen, S.G., Ceulemans, R., Impens, I., 1994. A fractal-based *Populus* canopy structure model for the calculation of light interception. *For. Ecol. Manage.* 69, 97–110. doi:[https://doi.org/10.1016/0378-1127\(94\)90222-4](https://doi.org/10.1016/0378-1127(94)90222-4)

Chen, X., Wang, D., Chen, J., Wang, C., Shen, M., 2018. The mixed pixel effect in land surface phenology: A simulation study. *Remote Sens. Environ.* 211, 338–344. doi:[10.1016/j.rse.2018.04.030](https://doi.org/10.1016/j.rse.2018.04.030)

Cheng, Y., Gamon, J.A., Fuentes, D.A., Mao, Z., Sims, D.A., Qiu, H. lie, Claudio, H., Huete, A., Rahman, A.F., 2006. A multi-scale analysis of dynamic optical signals in a Southern California chaparral ecosystem: A comparison of field, AVIRIS and MODIS data. *Remote Sens. Environ.* 103, 369–378. doi:[10.1016/j.rse.2005.06.013](https://doi.org/10.1016/j.rse.2005.06.013)

Cheng, Y., Yu, L., Xu, Y., Lu, H., Cracknell, A.P., Kanniah, K., Gong, P., 2018. Mapping oil palm extent in Malaysia using ALOS-2 PALSAR-2 data. *Int. J. Remote Sens.* 39, 432–452. doi:[10.1080/01431161.2017.1387309](https://doi.org/10.1080/01431161.2017.1387309)

Chianucci, F., Disperati, L., Guzzi, D., Bianchini, D., Nardino, V., Lastri, C., Rindinella, A., Corona, P., 2016. Estimation of canopy attributes in beech forests using true colour digital images from a small fixed-wing UAV. *Int. J. Appl. Earth Obs. Geoinf.* 47, 60–68. doi:[10.1016/j.jag.2015.12.005](https://doi.org/10.1016/j.jag.2015.12.005)

Chong, K.L., Kanniah, K.D., Pohl, C., Tan, K.P., 2017. A review of remote

sensing applications for oil palm studies. *Geo-Spatial Inf. Sci.* 20, 184–200. doi:10.1080/10095020.2017.1337317

Ciais, P., Dolman, A.J., Bombelli, A., Duren, R., Peregon, A., Rayner, P.J., Miller, C., Gobron, N., Kinderman, G., Marland, G., Gruber, N., Chevallier, F., Andres, R.J., Balsamo, G., Bopp, L., Bréon, F.M., Broquet, G., Dargaville, R., Battin, T.J., Borges, A., Bovensmann, H., Buchwitz, M., Butler, J., Canadell, J.G., Cook, R.B., Defries, R., Engelen, R., Gurney, K.R., Heinze, C., Heimann, M., Held, A., Henry, M., Law, B., Luyssaert, S., Miller, J., Moriyama, T., Moulin, C., Myneni, R.B., Nussli, C., Obersteiner, M., Ojima, D., Pan, Y., Paris, J.D., Piao, S.L., Poulter, B., Plummer, S., Quegan, S., Raymond, P., Reichstein, M., Rivier, L., Sabine, C., Schimel, D., Tarasova, O., Valentini, R., Wang, R., Van Der Werf, G., Wickland, D., Williams, M., Zehner, C., 2014. Current systematic carbon-cycle observations and the need for implementing a policy-relevant carbon observing system. *Biogeosciences* 11, 3547–3602. doi:10.5194/bg-11-3547-2014

Clark, D.A., Asao, S., Fisher, R., Reed, S., Reich, P.B., Ryan, M.G., Wood, T.E., Yang, X., 2017. Reviews and syntheses: Field data to benchmark the carbon cycle models for tropical forests. *Biogeosciences* 14, 4663–4690. doi:10.5194/bg-14-4663-2017

Cleland, E.E., Chuine, I., Menzel, A., Mooney, H.A., Schwartz, M.D., 2007. Shifting plant phenology in response to global change. *Trends Ecol. Evol.* 22, 357–365. doi:10.1016/j.tree.2007.04.003

Cogliati, S., Verhoef, W., Kraft, S., Sabater, N., Alonso, L., Vicent, J., Moreno, J., Drusch, M., Colombo, R., 2015. Retrieval of sun-induced fluorescence using advanced spectral fitting methods. *Remote Sens. Environ.* 169, 344–357. doi:10.1016/j.rse.2015.08.022

Colomina, I., Molina, P., 2014. Unmanned aerial systems for photogrammetry and remote sensing: A review. *ISPRS J. Photogramm. Remote Sens.* 92, 79–97. doi:10.1016/j.isprsjprs.2014.02.013

Comeau, P.G., Gendron, F., Letchford, T., 1998. A comparison of several methods for estimating light under a paper birch mixedwood stand. *Can. J. For. Res.* 28, 1843–1850. doi:10.1139/x98-159

Constantin, D., Rehak, M., Akhtman, Y., Liebisch, F., 2015. Detection of crop properties by means of hyperspectral remote sensing from a micro UAV. 20. und 21. Work. Comput. der Landwirtschaft - 3. Work. Unbemannte Auton. fliegende Syst. der Landwirtschaft.

Corley, R.H. V., Tinker, P.B., 2016. The Oil Palm, 5th ed. Wiley Blackwell, Chichester, UK.

Cunliffe, A.M., Assmann, J.J., Daskalova, G., Kerby, J.T., Myers-Smith, I.H., 2020. Aboveground biomass corresponds strongly with drone-derived canopy height but weakly with greenness (NDVI) in a shrub tundra landscape. *Environ. Res. Lett.*

Cunliffe, A.M., Brazier, R.E., Anderson, K., 2016. Ultra-fine grain landscape-scale quantification of dryland vegetation structure with drone-acquired structure-from-motion photogrammetry. *Remote Sens. Environ.* 183, 129–143. doi:10.1016/j.rse.2016.05.019

Cutini, A., Varallo, A., 2006. Estimation of foliage characteristics of isolated trees with the Plant Canopy Analyzer LAI-2000. *Curr. Trends Ecol.* 1, 49–56.

D'Odorico, P., Besik, A., Wong, C.Y.S., Isabel, N., Ensminger, I., 2020. High-throughput drone-based remote sensing reliably tracks phenology in thousands of conifer seedlings. *New Phytol.* 226, 1667–1681. doi:10.1111/nph.16488

D'Odorico, P., Gonsamo, A., Damm, A., Schaepman, M.E., 2013. Experimental evaluation of sentinel-2 spectral response functions for NDVI time-series continuity. *IEEE Trans. Geosci. Remote Sens.* 51, 1336–1348. doi:10.1109/TGRS.2012.2235447

Dalponte, M., Coomes, D.A., 2016. Tree-centric mapping of forest carbon density from airborne laser scanning and hyperspectral data. *Methods Ecol. Evol.* 7, 1236–1245. doi:10.1111/2041-210X.12575

Damm, A., Elber, J., Erler, A., Gioli, B., Hamdi, K., Hutjes, R., Kosvancova, M., Meroni, M., Miglietta, F., Moersch, A., Moreno, J., Schickling, A., Sonnenschein, R., Udelhoven, T., Van der Linden, S., Hostert, P., Rascher, U., 2010. Remote sensing of sun-induced fluorescence to improve

modeling of diurnal courses of gross primary production (GPP). *Glob. Chang. Biol.* 16, 171–186. doi:10.1111/j.1365-2486.2009.01908.x

Damm, A., Guanter, L., Paul-Limoges, E., Van der Tol, C., Hueni, A., Buchmann, N., Eugster, W., Ammann, C., Schaepman, M.E., 2015a. Far-red sun-induced chlorophyll fluorescence shows ecosystem-specific relationships to gross primary production: An assessment based on observational and modeling approaches. *Remote Sens. Environ.* 166, 91–105. doi:10.1016/j.rse.2015.06.004

Damm, A., Guanter, L., Verhoef, W., Schläpfer, D., Garbari, S., Schaepman, M.E., 2015b. Impact of varying irradiance on vegetation indices and chlorophyll fluorescence derived from spectroscopy data. *Remote Sens. Environ.* 156, 202–215. doi:10.1016/j.rse.2014.09.031

Damm, A., Paul-Limoges, E., Kükenbrink, D., Bachofen, C., Morsdorf, F., 2020. Remote sensing of forest gas exchange: Considerations derived from a tomographic perspective. *Glob. Chang. Biol.* 26, 2717–2727. doi:10.1111/gcb.15007

Dandois, J.P., Baker, M., Olano, M., Parker, G.G., Ellis, E.C., 2017. What is the point? Evaluating the structure, color, and semantic traits of computer vision point clouds of vegetation. *Remote Sens.* 9, 1–20. doi:10.3390/rs9040355

Dandois, J.P., Ellis, E.C., 2013. High spatial resolution three-dimensional mapping of vegetation spectral dynamics using computer vision. *Remote Sens. Environ.* 136, 259–276. doi:10.1016/j.rse.2013.04.005

Dandois, J.P., Ellis, E.C., 2010. Remote sensing of vegetation structure using computer vision. *Remote Sens.* 2, 1157–1176. doi:10.3390/rs2041157

Dandois, J.P., Olano, M., Ellis, E.C., 2015. Optimal altitude, overlap, and weather conditions for computer vision uav estimates of forest structure. *Remote Sens.* 7, 13895–13920. doi:10.3390/rs71013895

Dannenberg, M., Wang, X., Yan, D., Smith, W., 2020. Phenological Characteristics of Global Ecosystems Based on Optical, Fluorescence, and Microwave Remote Sensing. *Remote Sens.* 12. doi:10.3390/rs12040671

- Darvishzadeh, R., Skidmore, A., Schlerf, M., Atzberger, C., 2008. Inversion of a radiative transfer model for estimating vegetation LAI and chlorophyll in a heterogeneous grassland. *Remote Sens. Environ.* 112, 2592–2604. doi:10.1016/j.rse.2007.12.003
- DeBell, L., Anderson, K., Brazier, R.E., King, N., Jones, L., 2016. Water resource management at catchment scales using lightweight UAVs: current capabilities and future perspectives. *J. Unmanned Veh. Syst.* 4, 7–30. doi:10.1139/juvs-2015-0026
- Delbart, N., Kergoat, L., Le Toan, T., Lhermitte, J., Picard, G., 2005. Determination of phenological dates in boreal regions using normalized difference water index. *Remote Sens. Environ.* 97, 26–38. doi:10.1016/j.rse.2005.03.011
- Delegido, J., Verrelst, J., Alonso, L., Moreno, J., 2011. Evaluation of sentinel-2 red-edge bands for empirical estimation of green LAI and chlorophyll content. *Sensors* 11, 7063–7081. doi:10.3390/s110707063
- Delegido, J., Verrelst, J., Meza, C.M., Rivera, J.P., Alonso, L., Moreno, J., 2013. A red-edge spectral index for remote sensing estimation of green LAI over agroecosystems. *Eur. J. Agron.* 46, 42–52. doi:10.1016/j.eja.2012.12.001
- Deng, L., Mao, Z., Li, X., Hu, Z., Duan, F., Yan, Y., 2018. UAV-based multispectral remote sensing for precision agriculture: A comparison between different cameras. *ISPRS J. Photogramm. Remote Sens.* 146, 124–136. doi:10.1016/j.isprsjprs.2018.09.008
- Diebel, J., 2006. Representing attitude: Euler angles, unit quaternions, and rotation vectors. *Matrix* 58, 1–35. doi:10.1093/jxb/erm298
- Disney, M., 2019. Terrestrial LiDAR: a three-dimensional revolution in how we look at trees. *New Phytol.* 222, 1736–1741. doi:10.1111/nph.15517
- Disney, M., Lewis, P., Saich, P., 2006. 3D modelling of forest canopy structure for remote sensing simulations in the optical and microwave domains. *Remote Sens. Environ.* 100, 114–132. doi:<https://doi.org/10.1016/j.rse.2005.10.003>
- Drusch, M., Moreno, J., Bello, U. Del, Franco, R., Goulas, Y., Huth, A., Kraft, S.,

- Middleton, E.M., Miglietta, F., Mohammed, G., Nedbal, L., Rascher, U., Schüttemeyer, D., Verhoef, W., 2017. The FLuorescence EXplorer Mission Concept—ESA's Earth Explorer 8. *IEEE Trans. Geosci. Remote Sens.* 55, 1273–1284. doi:10.1109/TGRS.2016.2621820
- Duan, B., Liu, Y., Gong, Y., Peng, Y., Wu, X., Zhu, R., Fang, S., 2019. Remote estimation of rice LAI based on Fourier spectrum texture from UAV image. *Plant Methods* 15, 124. doi:10.1186/s13007-019-0507-8
- Duan, T., Chapman, S.C., Guo, Y., Zheng, B., 2017. Dynamic monitoring of NDVI in wheat agronomy and breeding trials using an unmanned aerial vehicle. *F. Crop. Res.* 210, 71–80. doi:10.1016/j.fcr.2017.05.025
- Dubayah, R., Blair, J.B., Goetz, S., Fatoyinbo, L., Hansen, M., Healey, S., Hofton, M., Hurt, G., Kellner, J., Luthcke, S., Armston, J., Tang, H., Duncanson, L., Hancock, S., Jantz, P., Marselis, S., Patterson, P.L., Qi, W., Silva, C., 2020. The Global Ecosystem Dynamics Investigation: High-resolution laser ranging of the Earth's forests and topography. *Sci. Remote Sens.* 1. doi:<https://doi.org/10.1016/j.srs.2020.100002>
- Duffy, J.P., Cunliffe, A.M., DeBell, L., Sandbrook, C., Wich, S.A., Shutler, J.D., Myers-Smith, I.H., Varela, M.R., Anderson, K., 2017. Location, location, location: considerations when using lightweight drones in challenging environments. *Remote Sens. Ecol. Conserv.* 7–19. doi:10.1002/rse2.58
- Duffy, J.P., Pratt, L., Anderson, K., Land, P.E., Shutler, J.D., 2018a. Spatial assessment of intertidal seagrass meadows using optical imaging systems and a lightweight drone. *Estuar. Coast. Shelf Sci.* 200, 169–180. doi:10.1016/j.ecss.2017.11.001
- Duffy, J.P., Shutler, J.D., Witt, M.J., DeBell, L., Anderson, K., 2018b. Tracking fine-scale structural changes in coastal dune morphology using kite aerial photography and uncertainty-assessed structure-from-motion photogrammetry. *Remote Sens.* 10. doi:10.3390/rs10091494
- Duncanson, L.I., Cook, B.D., Hurt, G.C., Dubayah, R.O., 2014. An efficient, multi-layered crown delineation algorithm for mapping individual tree structure across multiple ecosystems. *Remote Sens. Environ.* 154, 378–386. doi:10.1016/j.rse.2013.07.044

- Duthoit, S., Demarez, V., Gastellu-Etchegorry, J.-P., Martin, E., Roujean, J., 2008. Assessing the effects of the clumping phenomenon on BRDF of a maize crop based on 3D numerical scenes using DART model 148, 1341–1352. doi:10.1016/j.agrformet.2008.03.011
- Dworak, V., Selbeck, J., Dammer, K.H., Hoffmann, M., Zarezadeh, A.A., Bobda, C., 2013. Strategy for the development of a smart NDVI camera system for outdoor plant detection and agricultural embedded systems. Sensors 13, 1523–1538. doi:10.3390/s130201523
- Easterday, K., Kislik, C., Dawson, T., Hogan, S., Kelly, M., 2019. Remotely Sensed Water Limitation in Vegetation: Insights from an Experiment with Unmanned Aerial Vehicles (UAVs). Remote Sens. 11, 1853. doi:10.3390/rs11161853
- Eltner, A., Schneider, D., 2015. Analysis of Different Methods for 3D Reconstruction of Natural Surfaces from Parallel-Axes UAV Images. Photogramm. Rec. doi:10.1111/phor.12115
- Facchi, A., Baroni, G., Boschetti, M., Gandolfi, C., 2010. Comparing Optical and Direct Methods for Leafarea Index Determination in a Maize Crop. J. Agric. Eng. 41, 33. doi:10.4081/jae.2010.1.33
- Fallet, C., Domenzain, L.M., 2018. Necessary steps for the systematic calibration of a multispectral imaging system to achieve a targetless workflow in reflectance estimation: a study of Parrot SEQUOIA for precision agriculture, in: Algorithms and Technologies for Multispectral, Hyperspectral, and Ultraspectral Imagery XXIV. SPIE, Orlando, Florida, US, p. 42. doi:10.1117/12.2304334
- Fawcett, D., Anderson, K., 2019. Investigating impacts of calibration methodology and irradiance variations on lightweight drone-based sensor derived surface reflectance products, in: Remote Sensing for Agriculture, Ecosystems, and Hydrology XXI. SPIE, Strasbourg. doi:10.1117/12.2533106
- Fawcett, D., Azlan, B., Hill, T.C., Kho, L.K., Bennie, J., Anderson, K., 2019a. Unmanned aerial vehicle (UAV) derived structure- from-motion photogrammetry point clouds for oil palm (Elaeis guineensis) canopy

segmentation and height estimation. *Int. J. Remote Sens.* 40.

doi:10.1080/01431161.2019.1591651

Fawcett, D., Blanco-Sacristán, J., Benaud, P., 2019b. Two decades of digital photogrammetry : Revisiting Chandler ' s 1999 paper on “ Effective application of automated digital photogrammetry for geomorphological research ” – a synthesis. *Prog. Phys. Geogr.* 43.

doi:10.1177/0309133319832863

Fensholt, R., Sandholt, I., Rasmussen, M.S., 2004. Evaluation of MODIS LAI, fAPAR and the relation between fAPAR and NDVI in a semi-arid environment using in situ measurements. *Remote Sens. Environ.* 91, 490–507. doi:10.1016/j.rse.2004.04.009

Féret, J.B., Gitelson, A.A., Noble, S.D., Jacquemoud, S., 2017. PROSPECT-D: Towards modeling leaf optical properties through a complete lifecycle. *Remote Sens. Environ.* 193, 204–215. doi:10.1016/j.rse.2017.03.004

Ferraccioli, F., Gerard, F., Robinson, C., Jordan, T., Biszczuk, M., Ireland, L., Beasley, M., Vidamour, A., Barker, A., Arnold, R., Dinn, M., Fox, A., Howard, A., 2014. LiDAR based Digital Terrain Model (DTM) data for South West England.

Field, C.B., Randerson, J.T., Malmström, C.M., 1995. Global net primary production: Combining ecology and remote sensing. *Remote Sens. Environ.* 51, 74–88. doi:10.1016/0034-4257(94)00066-V

Fitzherbert, E.B., Struebig, M.J., Morel, A., Danielsen, F., Brühl, C.A., Donald, P.F., Phalan, B., 2008. How will oil palm expansion affect biodiversity? *Trends Ecol. Evol.* 23, 538–545. doi:10.1016/j.tree.2008.06.012

Fladeland, M.M., Ashton, M.S., Lee, X., 2003. Landscape variations in understory PAR for a mixed deciduous forest in New England, USA. *Agric. For. Meteorol.* 118, 137–141. doi:10.1016/S0168-1923(03)00105-9

Forlani, G., Dall'Asta, E., Diotri, F., di Cellà, U.M., Roncella, R., Santise, M., 2018. Quality assessment of DSMs produced from UAV flights georeferenced with on-board RTK positioning. *Remote Sens.* 10. doi:10.3390/rs10020311

- Forsmoo, J., Anderson, K., Macleod, C.J.A., Wilkinson, M.E., Brazier, R., 2018. Drone-based structure-from-motion photogrammetry captures grassland sward height variability. *J. Appl. Ecol.* 55, 2587–2599. doi:10.1111/1365-2664.13148
- Forsmoo, J., Anderson, K., Macleod, C.J.A., Wilkinson, M.E., DeBell, L., Brazier, R.E., 2019. Structure from motion photogrammetry in ecology: Does the choice of software matter? *Ecol. Evol.* 9, 12964–12979. doi:10.1002/ece3.5443
- Fournier, R.A., Landry, R., August, N.M., Fedosejevs, G., Gauthier, R.P., 1996. Modelling light obstruction in three conifer forests using hemispherical photography and fine tree architecture. *Agric. For. Meteorol.* 82, 47–72. doi:10.1016/0168-1923(96)02345-3
- Franklin, S.E., Ahmed, O.S., Williams, G., 2017. Northern Conifer Forest Species Classification Using Multispectral Data Acquired from an Unmanned Aerial Vehicle. *Photogramm. Eng. Remote Sens.* 83, 501–507. doi:10.14358/PERS.83.7.501
- Fraser, B.T., Congalton, R.G., 2018. Issues in Unmanned Aerial Systems (UAS) data collection of complex forest environments. *Remote Sens.* 10. doi:10.3390/rs10060908
- Fraser, R., van der Sluijs, J., Hall, R., 2017. Calibrating Satellite-Based Indices of Burn Severity from UAV-Derived Metrics of a Burned Boreal Forest in NWT, Canada. *Remote Sens.* 9, 279. doi:10.3390/rs9030279
- Frey, J., Kovach, K., Stemmler, S., Koch, B., 2018. UAV Photogrammetry of Forests as a Vulnerable Process. A Sensitivity Analysis for a Structure from Motion RGB-Image Pipeline. *Remote Sens.* 10. doi:10.3390/rs10060912
- Friedlingstein, P., Jones, M.W., O’Sullivan, M., Andrew, R.M., Hauck, J., Peters, G.P., Peters, W., Pongratz, J., Sitch, S., Le Quéré, C., Bakker, D.C.E., Canadell, J.G., Ciais, P., Jackson, R.B., Anthoni, P., Barbero, L., Bastos, A., Bastrikov, V., Becker, M., Bopp, L., Buitenhuis, E., Chandra, N., Chevallier, F., Chini, L.P., Currie, K.I., Feely, R.A., Gehlen, M., Gilfillan, D., Gkritzalis, T., Goll, D.S., Gruber, N., Gutekunst, S., Harris, I., Haverd, V., Houghton, R.A., Hurt, G., Ilyina, T., Jain, A.K., Joetzjer, E., Kaplan, J.O.,

Kato, E., Klein Goldewijk, K., Korsbakken, J.I., Landschützer, P., Lauvset, S.K., Lefèvre, N., Lenton, A., Lienert, S., Lombardozzi, D., Marland, G., McGuire, P.C., Melton, J.R., Metzl, N., Munro, D.R., Nabel, J.E.M.S., Nakaoka, S.-I., Neill, C., Omar, A.M., Ono, T., Peregon, A., Pierrot, D., Poulter, B., Rehder, G., Resplandy, L., Robertson, E., Rödenbeck, C., Séférian, R., Schwinger, J., Smith, N., Tans, P.P., Tian, H., Tilbrook, B., Tubiello, F.N., van der Werf, G.R., Wiltshire, A.J., Zaehle, S., 2019. Global Carbon Budget 2019. *Earth Syst. Sci. Data* 11, 1783–1838.
doi:10.5194/essd-11-1783-2019

Galkin, B., Kibilda, J., DaSilva, L.A., 2019. UAVs as Mobile Infrastructure: Addressing Battery Lifetime. *IEEE Commun. Mag.* 57, 132–137.
doi:10.1109/MCOM.2019.1800545

Gamon, J.A., 2015. Reviews and Syntheses: Optical sampling of the flux tower footprint. *Biogeosciences* 12, 4509–4523. doi:10.5194/bg-12-4509-2015

Gamon, J.A., Cheng, Y., Claudio, H., MacKinney, L., Sims, D.A., 2006. A mobile tram system for systematic sampling of ecosystem optical properties. *Remote Sens. Environ.* 103, 246–254.
doi:10.1016/j.rse.2006.04.006

Gamon, J.A., Field, C.B., Goulden, M.L., Griffin, K.L., Hartley, A.E., Joel, G., Peñuelas, J., Valentini, R., 1995. Relationships Between NDVI, Canopy Structure, and Photosynthesis in Three Californian Vegetation Types. *Ecol. Appl.* 5, 28–41. doi:10.2307/1942049

Gamon, J.A., Serrano, L., Surfus, J.S., 1997. The photochemical reflectance index: An optical indicator of photosynthetic radiation use efficiency across species, functional types, and nutrient levels. *Oecologia* 112, 492–501.
doi:10.1007/s004420050337

Gamon, J.A., Somers, B., Malenovský, Z., Middleton, E.M., Rascher, U., Schaepman, M.E., 2019. Assessing Vegetation Function with Imaging Spectroscopy. *Surv. Geophys.* 40, 489–513. doi:10.1007/s10712-019-09511-5

Garzonio, R., di Mauro, B., Colombo, R., Cogliati, S., 2017. Surface reflectance and sun-induced fluorescence spectroscopy measurements using a small

hyperspectral UAS. *Remote Sens.* 9, 1–24. doi:10.3390/rs9050472

Gastellu-Etchegorry, J.-P., Demarez, V., Pinel, V., Zagolski, F., 1996. Modeling radiative transfer in heterogeneous 3-D vegetation canopies. *Remote Sens. Environ.* 58, 131–156. doi:10.1016/0034-4257(95)00253-7

Gastellu-Etchegorry, J.-P., Grau, E., Lauret, N., 2012. DART: A 3D Model for Remote Sensing Images and Radiative Budget of Earth Surfaces, in: Modeling and Simulation in Engineering. InTech. doi:10.5772/31315

Gastellu-Etchegorry, J.-P., Guillevic, P., Zagolski, F., Demarez, V., Trichon, V., Deering, D., Leroy, M., 1999. Modeling BRF and radiation regime of boreal and tropical forests. *Remote Sens. Environ.* 68, 281–316. doi:10.1016/S0034-4257(98)00119-9

Gastellu-Etchegorry, J.-P., Yin, T., Lauret, N., Cajgfinger, T., Gregoire, T., Grau, E., Feret, J., Guilleux, J., Cook, B.D., Morton, D., Rubio, J., Durrieu, S., Cazanave, G., Martin, E., Ristorcelli, T., Thenkabail, P.S., 2015. Discrete anisotropic radiative transfer (DART 5) for modelling airborne and satellite spectroradiometer and LIDAR acquisitions of natural and urban landscapes. *Remote Sens.* 7, 1667–1701. doi:doi:10.3390/rs70201667

Gehlhausen, S.M., Schwartz, M.W., Augspurger, C.K., 2000. Vegetation and microclimatic edge effects in two mixed-mesophytic forest fragments. *Plant Ecol.* 147, 21–35. doi:10.1023/A:1009846507652

Gendron, F., Messier, C., Comeau, P.G., 1998. Comparison of various methods for estimating the mean growing season percent photosynthetic photon flux density in forests. *Agric. For. Meteorol.* 92, 55–70. doi:10.1016/S0168-1923(98)00082-3

Germer, J., Sauerborn, J., 2008. Estimation of the impact of oil palm plantation establishment on greenhouse gas balance. *Environ. Dev. Sustain.* 10, 697–716. doi:10.1007/s10668-006-9080-1

Gevaert, C.M., Suomalainen, J., Tang, J., Kooistra, L., 2015. Generation of Spectral-Temporal Response Surfaces by Combining Multispectral Satellite and Hyperspectral UAV Imagery for Precision Agriculture Applications. *IEEE J. Sel. Top. Appl. Earth Obs. Remote Sens.* 8, 3140–3146. doi:10.1109/JSTARS.2015.2406339

- Giannetti, F., Chirici, G., Gobakken, T., Næsset, E., Travaglini, D., Puliti, S., 2018. A new approach with DTM-independent metrics for forest growing stock prediction using UAV photogrammetric data. *Remote Sens. Environ.* 213, 195–205. doi:<https://doi.org/10.1016/j.rse.2018.05.016>
- Gilliot, J.-M., Michelin, J., Faroux, R., Domenzain, L.M., Fallet, C., 2018. Correction of in-flight luminosity variations in multispectral UAS images, using a luminosity sensor and camera pair for improved biomass estimation in precision agriculture. *Proc. SPIE - Int. Soc. Opt. Eng.* 10664. doi:[10.1117/12.2303804](https://doi.org/10.1117/12.2303804)
- Gitelson, A., Merzlyak, M.N., 1994. Spectral Reflectance Changes Associated with Autumn Senescence of *Aesculus hippocastanum* L. and *Acer platanoides* L. Leaves. Spectral Features and Relation to Chlorophyll Estimation. *J. Plant Physiol.* 143, 286–292. doi:[https://doi.org/10.1016/S0176-1617\(11\)81633-0](https://doi.org/10.1016/S0176-1617(11)81633-0)
- Gitelson, A.A., Keydan, G.P., Merzlyak, M.N., 2006a. Three-band model for noninvasive estimation of chlorophyll, carotenoids, and anthocyanin contents in higher plant leaves. *Geophys. Res. Lett.* 33, L11402. doi:[10.1029/2006GL026457](https://doi.org/10.1029/2006GL026457)
- Gitelson, A.A., Viña, A., Ciganda, V., Rundquist, D.C., Arkebauer, T.J., 2005. Remote estimation of canopy chlorophyll content in crops. *Geophys. Res. Lett.* 32, 1–4. doi:[10.1029/2005GL022688](https://doi.org/10.1029/2005GL022688)
- Gitelson, A.A., Viña, A., Verma, S.B., Rundquist, D.C., Arkebauer, T.J., Keydan, G., Leavitt, B., Ciganda, V., Burba, G.G., Suyker, A.E., 2006b. Relationship between gross primary production and chlorophyll content in crops: Implications for the synoptic monitoring of vegetation productivity. *J. Geophys. Res. Atmos.* 111, 1–13. doi:[10.1029/2005JD006017](https://doi.org/10.1029/2005JD006017)
- Gitelson, A.A., Wardlow, B.D., Keydan, G.P., Leavitt, B., 2007. An evaluation of MODIS 250-m data for green LAI estimation in crops. *Geophys. Res. Lett.* 34, 2–5. doi:[10.1029/2007GL031620](https://doi.org/10.1029/2007GL031620)
- Gong, P., Pu, R., Biging, G.S., Larrieu, M.R., 2003. Estimation of forest leaf area index using vegetation indices derived from Hyperion hyperspectral data. *IEEE Trans. Geosci. Remote Sens.* 41, 1355–1362.

doi:10.1109/TGRS.2003.812910

Gonzalez-Dugo, V., Zarco-Tejada, P., Nicolás, E., Nortes, P.A., Alarcón, J.J., Intrigliolo, D.S., Fereres, E., 2013. Using high resolution UAV thermal imagery to assess the variability in the water status of five fruit tree species within a commercial orchard. *Precis. Agric.* 14, 660–678.
doi:10.1007/s11119-013-9322-9

Guay, K.C., Beck, P.S.A., Berner, L.T., Goetz, S.J., Baccini, A., Buermann, W., 2014. Vegetation productivity patterns at high northern latitudes: A multi-sensor satellite data assessment. *Glob. Chang. Biol.* 20, 3147–3158.
doi:10.1111/gcb.12647

Guerra-Hernández, J., Cosenza, D.N., Rodriguez, L.C.E., Silva, M., Tomé, M., Díaz-Varela, R.A., González-Ferreiro, E., 2018. Comparison of ALS- and UAV(SfM)-derived high-density point clouds for individual tree detection in Eucalyptus plantations. *Int. J. Remote Sens.* 39, 5211–5235.
doi:10.1080/01431161.2018.1486519

Guillen-Climent, M.L., Zarco-Tejada, P.J., Berni, J.A.J., North, P.R.J., Villalobos, F.J., 2012. Mapping radiation interception in row-structured orchards using 3D simulation and high-resolution airborne imagery acquired from a UAV. *Precis. Agric.* 13, 473–500. doi:10.1007/s11119-012-9263-8

Guillevic, P., Gastellu-Etchegorry, J.P., 1999. Modeling BRF and radiation regime of boreal and tropical forest: II. PAR regime. *Remote Sens. Environ.* 68, 317–340. doi:10.1016/S0034-4257(98)00120-5

Guirado, E., Blanco-Sacristán, J., Rigol-Sánchez, J.P., Alcaraz-Segura, D., Cabello, J., 2019. A multi-temporal object-based image analysis to detect long-lived shrub cover changes in drylands. *Remote Sens.* 11, 1–17.
doi:10.3390/rs11222649

Haboudane, D., Miller, J.R., Pattey, E., Zarco-Tejada, P.J., Strachan, I.B., 2004. Hyperspectral vegetation indices and novel algorithms for predicting green LAI of crop canopies: Modeling and validation in the context of precision agriculture. *Remote Sens. Environ.* 90, 337–352.
doi:10.1016/j.rse.2003.12.013

- Hakala, T., Honkavaara, E., Saari, H., Mäkinen, J., Kaivosoja, J., Pesonen, L., Pöölönen, I., 2013. Spectral Imaging From Uavs Under Varying Illumination Conditions. *ISPRS - Int. Arch. Photogramm. Remote Sens. Spat. Inf. Sci.* XL-1/W2, 189–194. doi:10.5194/isprsarchives-XL-1-W2-189-2013
- Hakala, T., Markelin, L., Honkavaara, E., Scott, B., Theocharous, T., Nevalainen, O., Näsi, R., Suomalainen, J., Viljanen, N., Greenwell, C., Fox, N., 2018. Direct reflectance measurements from drones: Sensor absolute radiometric calibration and system tests for forest reflectance characterization. *Sensors* 18. doi:10.3390/s18051417
- Hakala, T., Suomalainen, J., Peltoniemi, J.I., 2010. Acquisition of bidirectional reflectance factor dataset using a micro unmanned aerial vehicle and a consumer camera. *Remote Sens.* 2, 819–832. doi:10.3390/rs2030819
- Han, Q., Luo, G., Li, C., 2013. Remote sensing-based quantification of spatial variation in canopy phenology of four dominant tree species in Europe. *J. Appl. Remote Sens.* 7, 073485. doi:10.1117/1.jrs.7.073485
- Hassika, P., Berbigier, P., 1998. Annual cycle of photosynthetically active radiation in maritime pine forest. *Agric. For. Meteorol.* 90, 157–171.
- Hay, J.E., McKay, D.C., 1985. Estimating solar irradiance on inclined surfaces: A review and assessment of methodologies. *Int. J. Sol. Energy* 3, 203–240. doi:10.1080/01425918508914395
- Heiskanen, J., 2006. Estimating aboveground tree biomass and leaf area index in a mountain birch forest using ASTER satellite data. *Int. J. Remote Sens.* 27, 1135–1158. doi:10.1080/01431160500353858
- Hernández-Clemente, R., North, P.R.J., Hornero, A., Zarco-Tejada, P.J., 2017. Assessing the effects of forest health on sun-induced chlorophyll fluorescence using the FluorFLIGHT 3-D radiative transfer model to account for forest structure. *Remote Sens. Environ.* 193, 165–179. doi:10.1016/j.rse.2017.02.012
- Hilker, T., Coops, N.C., Nesic, Z., Wulder, M.A., Black, A.T., 2007. Instrumentation and approach for unattended year round tower based measurements of spectral reflectance. *Comput. Electron. Agric.* 56, 72–84. doi:10.1016/j.compag.2007.01.003

Holman, F.H., Riche, A.B., Castle, M., Wooster, M.J., Hawkesford, M.J., 2019.

Radiometric calibration of “commercial off the shelf” cameras for UAV-based high-resolution temporal crop phenotyping of reflectance and NDVI. *Remote Sens.* 11. doi:10.3390/rs11141657

Holman, F.H., Riche, A.B., Michalski, A., Castle, M., Wooster, M.J., Hawkesford, M.J., 2016. High Throughput Field Phenotyping of Wheat Plant Height and Growth Rate in Field Plot Trials Using UAV Based Remote Sensing. *Remote Sens.* 8. doi:10.3390/rs8121031

Houborg, R., Anderson, M.C., Daughtry, C.S.T., Kustas, W.P., Rodell, M., 2011. Using leaf chlorophyll to parameterize light-use-efficiency within a thermal-based carbon, water and energy exchange model. *Remote Sens. Environ.* 115, 1694–1705. doi:10.1016/j.rse.2011.02.027

Houborg, R., Cescatti, A., Migliavacca, M., Kustas, W.P., 2013. Satellite retrievals of leaf chlorophyll and photosynthetic capacity for improved modeling of GPP. *Agric. For. Meteorol.* 117, 10–23. doi:10.1016/j.agrformet.2013.04.006

Houborg, R., Fisher, J.B., Skidmore, A.K., 2015. Advances in remote sensing of vegetation function and traits. *Int. J. Appl. Earth Obs. Geoinf.* 43, 1–6. doi:10.1016/j.jag.2015.06.001

Houborg, R., Soegaard, H., Boegh, E., 2007. Combining vegetation index and model inversion methods for the extraction of key vegetation biophysical parameters using Terra and Aqua MODIS reflectance data. *Remote Sens. Environ.* 106, 39–58. doi:10.1016/j.rse.2006.07.016

Hueni, A., Damm, A., Kneubuehler, M., Schl, D., Schaepman, M.E., Member, S., 2017. Field and Airborne Spectroscopy Cross Validation — Some Considerations. *IEEE J. Sel. Top. Appl. Earth Obs. Remote Sens.* 10, 1117–1135. doi:10.1109/JSTARS.2016.2593984

Huete, A., Didan, K., Miura, T., Rodriguez, E.P., Gao, X., Ferreira, L.G., 2002. Overview of the radiometric and biophysical performance of the MODIS vegetation indices. *Remote Sens. Environ.* 83, 195–213. doi:10.1016/S0034-4257(02)00096-2

Huete, A.R., Liu, H.Q., van Leeuwen, W.J.D., 1997. Use of vegetation indices in

forested regions: Issues of linearity and saturation. *Int. Geosci. Remote Sens. Symp.* 4, 1966–1968. doi:10.1109/igarss.1997.609169

Hufkens, K., Friedl, M., Sonnentag, O., Braswell, B.H., Milliman, T., Richardson, A.D., 2012. Linking near-surface and satellite remote sensing measurements of deciduous broadleaf forest phenology. *Remote Sens. Environ.* 117, 307–321. doi:10.1016/j.rse.2011.10.006

Hutchison, B.A., Matt, D.R., 1976. Beam enrichment of diffuse radiation in a deciduous forest. *Agric. Meteorol.* 17, 93–110. doi:10.1016/0002-1571(76)90025-X

Immitzer, M., Neuwirth, M., Böck, S., Brenner, H., Vuolo, F., Atzberger, C., 2019. Optimal input features for tree species classification in Central Europe based on multi-temporal Sentinel-2 data. *Remote Sens.* 11. doi:10.3390/rs11222599

IPCC, 2014. Climate Change 2014: Synthesis Report. Contribution of Working Groups I, II and III to the Fifth Assessment Report of the Intergovernmental Panel on Climate Change. Geneva.

Itten, K.I., Dell'Endice, F., Hueni, A., Kneubühler, M., Schläpfer, D., Odermatt, D., Seidel, F., Huber, S., Schopfer, J., Kellenberger, T., Bühler, Y., D'Odorico, P., Nieke, J., Alberti, E., Meuleman, K., 2008. APEX - The hyperspectral ESA airborne prism experiment. *Sensors* 8, 6235–6259. doi:10.3390/s8106235

Jacquemoud, S., Bacour, C., Poilv  , H., Frangi, J.P., 2000. Comparison of four radiative transfer models to simulate plant canopies reflectance: Direct and inverse mode. *Remote Sens. Environ.* 74, 471–481. doi:10.1016/S0034-4257(00)00139-5

Jacquemoud, S., Baret, F., 1990. PROSPECT: A model of leaf optical properties spectra. *Remote Sens. Environ.* 34, 75–91. doi:10.1016/0034-4257(90)90100-Z

Jacquemoud, S., Verhoef, W., Baret, F., Bacour, C., Zarco-Tejada, P.J., Asner, G.P., Fran  ois, C., Ustin, S.L., 2009. PROSPECT + SAIL models: A review of use for vegetation characterization. *Remote Sens. Environ.* 113, S56–S66. doi:10.1016/j.rse.2008.01.026

- Jakob, S., Zimmermann, R., Gloaguen, R., 2017. The Need for Accurate Geometric and Radiometric Corrections of Drone-Borne Hyperspectral Data for Mineral Exploration : MEPhySTo — A Toolbox for Pre-Processing Drone-Borne Hyperspectral Data. *Remote Sens.* 9. doi:10.3390/rs9010088
- James, M.R., Antoniazza, G., Robson, S., Lane, S.N., 2020. Mitigating systematic error in topographic models for geomorphic change detection: accuracy, precision and considerations beyond off-nadir imagery. *Earth Surf. Process. Landforms* 45, 2251–2271. doi:10.1002/esp.4878
- James, M.R., Robson, S., 2014. Mitigating systematic error in topographic models derived from UAV and ground-based image networks. *Earth Surf. Process. Landforms* 39, 1413–1420. doi:10.1002/esp.3609
- James, M.R., Robson, S., 2012. Straightforward reconstruction of 3D surfaces and topography with a camera: Accuracy and geoscience application. *J. Geophys. Res. Earth Surf.* 117, 1–17. doi:10.1029/2011JF002289
- James, M.R., Robson, S., D’Oleire-Oltmanns, S., Niethammer, U., 2017a. Optimising UAV topographic surveys processed with structure-from-motion: Ground control quality, quantity and bundle adjustment. *Geomorphology* 280, 51–66. doi:10.1016/j.geomorph.2016.11.021
- James, M.R., Robson, S., Smith, M.W., 2017b. 3-D uncertainty-based topographic change detection with structure-from-motion photogrammetry: precision maps for ground control and directly georeferenced surveys. *Earth Surf. Process. Landforms* 42, 1769–1788. doi:10.1002/esp.4125
- Jayathunga, S., Owari, T., Tsuyuki, S., 2018. The use of fixed-wing UAV photogrammetry with LiDAR DTM to estimate merchantable volume and carbon stock in living biomass over a mixed conifer–broadleaf forest. *Int. J. Appl. Earth Obs. Geoinf.* 73, 767–777.
doi:<https://doi.org/10.1016/j.jag.2018.08.017>
- Jenkins, J.P., Richardson, A.D., Braswell, B.H., Ollinger, S. V., Hollinger, D.Y., Smith, M.L., 2007. Refining light-use efficiency calculations for a deciduous forest canopy using simultaneous tower-based carbon flux and radiometric measurements. *Agric. For. Meteorol.* 143, 64–79.
doi:10.1016/j.agrformet.2006.11.008

Jensen, A.M., Hardy, T., McKee, M., Chen, Y.Q., 2011. Using a multispectral autonomous unmanned aerial remote sensing platform (AggieAir) for riparian and wetlands applications, in: International Geoscience and Remote Sensing Symposium (IGARSS). Vancouver BC, Canada, pp. 3413–3416. doi:10.1109/IGARSS.2011.6049953

Ji, H., Wang, K., 2012. Robust image deblurring with an inaccurate blur kernel. *IEEE Trans. Image Process.* 21, 1624–1634. doi:10.1109/TIP.2011.2171699

Jiang, R., Wang, P., Xu, Y., Zhou, Z., Luo, X., Lan, Y., Zhao, G., Sanchez-Azofeifa, A., Laakso, K., 2020. Assessing the Operation Parameters of a Low-altitude UAV for the Collection of NDVI Values Over a Paddy Rice Field. *Remote Sens.* 12. doi:10.3390/rs12111850

Johansen, K., Raharjo, T., McCabe, M.F., 2018. Using multi-spectral UAV imagery to extract tree crop structural properties and assess pruning effects. *Remote Sens.* 10. doi:10.3390/rs10060854

Kachamba, D., Ørka, H., Gobakken, T., Eid, T., Mwase, W., 2016. Biomass Estimation Using 3D Data from Unmanned Aerial Vehicle Imagery in a Tropical Woodland. *Remote Sens.* 2016, Vol. 8, Page 968 8, 968. doi:10.3390/RS8110968

Kang, Y., Özdoğan, M., Zipper, S.C., Román, M.O., Walker, J., Hong, S.Y., Marshall, M., Magliulo, V., Moreno, J., Alonso, L., Miyata, A., Kimball, B., Loheide, S.P., 2016. How universal is the relationship between remotely sensed vegetation indices and crop leaf area index? A global assessment. *Remote Sens.* 8. doi:10.3390/rs8070597

Kanning, M., Kühling, I., Trautz, D., Jarmer, T., 2018. High-Resolution UAV-Based Hyperspectral Imagery for LAI and Chlorophyll Estimations from Wheat for Yield Prediction. *Remote Sens.* 10. doi:10.3390/rs10122000

Karpina, M., Jarzabek-Rychard, M., Tymków, P., Borkowski, A., 2016. Uav-based automatic tree growth measurement for biomass estimation. *Int. Arch. Photogramm. Remote Sens. Spat. Inf. Sci. - ISPRS Arch.* 41, 685–688. doi:10.5194/isprsarchives-XLI-B8-685-2016

Kattenborn, T., Lopatin, J., Förster, M., Braun, A.C., Fassnacht, F.E., 2019.

UAV data as alternative to field sampling to map woody invasive species based on combined Sentinel-1 and Sentinel-2 data. *Remote Sens. Environ.* 227, 61–73. doi:10.1016/j.rse.2019.03.025

Kattenborn, T., Schmidlein, S., 2019. Radiative transfer modelling reveals why canopy reflectance follows function. *Sci. Rep.* 9, 6541. doi:10.1038/s41598-019-43011-1

Kattenborn, T., Sperlich, M., Bataua, K., Koch, B., 2014. Automatic single palm tree detection in plantations using UAV-based photogrammetric point clouds. *Int. Arch. Photogramm. Remote Sens. Spat. Inf. Sci. - ISPRS Arch.* 40, 139–144. doi:10.5194/isprsarchives-XL-3-139-2014

Keenan, T.F., Darby, B., Felts, E., Sonnentag, O., Friedl, M.A., Hufkens, K., O'Keefe, J., Klosterman, S., Munger, J.W., Toomey, M., Richardson, A.D., 2014. Tracking forest phenology and seasonal physiology using digital repeat photography: A critical assessment. *Ecol. Appl.* 24, 1478–1489. doi:10.1890/13-0652.1

Kelcey, J., Lucieer, A., 2012. Sensor correction of a 6-band multispectral imaging sensor for UAV remote sensing. *Remote Sens.* 4, 1462–1493. doi:10.3390/rs4051462

Kho, L.K., Jepsen, M.R., 2015. Carbon stock of oil palm plantations and tropical forests in Malaysia: A review. *Singap. J. Trop. Geogr.* 36, 249–266. doi:10.1111/sjtg.12100

Klosterman, S., Melaas, E., Wang, J., Martinez, A., Frederick, S., O'Keefe, J., Orwig, D.A., Wang, Z., Sun, Q., Schaaf, C., Friedl, M., Richardson, A.D., 2018. Fine-scale perspectives on landscape phenology from unmanned aerial vehicle (UAV) photography. *Agric. For. Meteorol.* 248, 397–407. doi:10.1016/j.agrformet.2017.10.015

Klosterman, S.T., Hufkens, K., Gray, J.M., Melaas, E., Sonnentag, O., Lavine, I., Mitchell, L., Norman, R., Friedl, M.A., Richardson, A.D., 2014. Evaluating remote sensing of deciduous forest phenology at multiple spatial scales using PhenoCam imagery. *Biogeosciences* 11, 4305–4320. doi:10.5194/bg-11-4305-2014

Knyazikhin, Y., Mießen, G., Panfyorov, O., Gravenhorst, G., 1997. Small-scale

study of three-dimensional distribution of photosynthetically active radiation in a forest. *Agric. For. Meteorol.* 88, 215–239. doi:10.1016/S0168-1923(97)00036-1

Knyazikhin, Y., Schull, M.A., Stenberg, P., Mottus, M., Rautiainen, M., Yang, Y., Marshak, A., Latorre Carmona, P., Kaufmann, R.K., Lewis, P., Disney, M.I., Vanderbilt, V., Davis, A.B., Baret, F., Jacquemoud, S., Lyapustin, A., Myneni, R.B., 2013. Hyperspectral remote sensing of foliar nitrogen content. *Proc. Natl. Acad. Sci.* 110, E185–E192. doi:10.1073/pnas.1210196109

Koetz, B., Baret, F., Poilv  , H., Hill, J., 2005. Use of coupled canopy structure dynamic and radiative transfer models to estimate biophysical canopy characteristics. *Remote Sens. Environ.* 95, 115–124. doi:10.1016/j.rse.2004.11.017

Koh, L.P., Miettinen, J., Liew, S.C., Ghazoul, J., 2011. Remotely sensed evidence of tropical peatland conversion to oil palm. *Proc. Natl. Acad. Sci.* 108, 5127–5132. doi:10.1073/pnas.1018776108

Koh, L.P., Wilcove, D.S., 2008. Is oil palm agriculture really destroying tropical biodiversity? *Conserv. Lett.* 1, 60–64. doi:10.1111/j.1755-263X.2008.00011.x

K  rner, C., Basler, D., 2010. Phenology Under Global Warming. *Science* (80-.). 327, 1461 LP – 1462. doi:10.1126/science.1186473

K  tz, B., Schaepman, M., Morsdorf, F., Bowyer, P., Itten, K., Allg  wer, B., 2004a. Radiative transfer modeling within a heterogeneous canopy for estimation of forest fire fuel properties. *Remote Sens. Environ.* 92, 332–344. doi:10.1016/j.rse.2004.05.015

K  tz, B., Schaepman, M., Morsdorf, F., Bowyer, P., Itten, K., Allg  wer, B., 2004b. Radiative transfer modeling within a heterogeneous canopy for estimation of forest fire fuel properties. *Remote Sens. Environ.* 92, 332–344. doi:10.1016/j.rse.2004.05.015

Kowalski, K., Senf, C., Hostert, P., Pflugmacher, D., 2020. Characterizing spring phenology of temperate broadleaf forests using Landsat and Sentinel-2 time series. *Int. J. Appl. Earth Obs. Geoinf.* 92, 102172.

doi:10.1016/j.jag.2020.102172

Krause, A., Pugh, T.A.M., Bayer, A.D., Li, W., Leung, F., Bondeau, A., Doelman, J.C., Humpenöder, F., Anthoni, P., Bodirsky, B.L., Ciais, P., Müller, C., Murray-Tortarolo, G., Olin, S., Popp, A., Sitch, S., Stehfest, E., Arneth, A., 2018. Large uncertainty in carbon uptake potential of land-based climate-change mitigation efforts. *Glob. Chang. Biol.* 24, 3025–3038. doi:10.1111/gcb.14144

Krause, S., Sanders, T.G.M., Mund, J.-P., Greve, K., 2019. UAV-Based Photogrammetric Tree Height Measurement for Intensive Forest Monitoring. *Remote Sens.* 11. doi:10.3390/rs11070758

Kükenbrink, D., Hueni, A., Schneider, F.D., Damm, A., Gastellu-Etchegorry, J., Schaepman, M.E., Morsdorf, F., 2019. Mapping the Irradiance Field of a Single Tree: Quantifying Vegetation-Induced Adjacency Effects. *IEEE Trans. Geosci. Remote Sens.* 57, 4994–5011. doi:10.1109/TGRS.2019.2895211

Kushida, K., Yoshino, K., 2010. Estimation of LAI and FAPAR by constraining the leaf and soil spectral characteristics in a radiative transfer model. *Int. J. Remote Sens.* 31, 2351–2375. doi:10.1080/01431160902998367

Kuster, T.M., Dobbertin, M., Günthardt-Goerg, M.S., Schaub, M., Arend, M., 2014. A phenological timetable of oak growth under experimental drought and air warming. *PLoS One* 9. doi:10.1371/journal.pone.0089724

Kuželka, K., Slavík, M., Surový, P., 2020. Very high density point clouds from UAV laser scanning for automatic tree stem detection and direct diameter measurement. *Remote Sens.* 12. doi:10.3390/RS12081236

Lafleur, P.M., Farnsworth, A.G., 2008. Light interception and canopy radiation balance of staghorn sumac (*Rhus typhina*). *Can. J. For. Res.* 38, 1695–1700. doi:10.1139/X08-016

Laurent, V.C.E., Schaepman, M.E., Verhoef, W., Weyermann, J., Chávez, R.O., 2014. Bayesian object-based estimation of LAI and chlorophyll from a simulated Sentinel-2 top-of-atmosphere radiance image. *Remote Sens. Environ.* 140, 318–329. doi:10.1016/j.rse.2013.09.005

Lawrence, D.M., Fisher, R.A., Koven, C.D., Oleson, K.W., Swenson, S.C., Bonan, G., Collier, N., Ghimire, B., van Kampenhout, L., Kennedy, D., Kluzek, E., Lawrence, P.J., Li, F., Li, H., Lombardozzi, D., Riley, W.J., Sacks, W.J., Shi, M., Vertenstein, M., Wieder, W.R., Xu, C., Ali, A.A., Badger, A.M., Bisht, G., van den Broeke, M., Brunke, M.A., Burns, S.P., Buzan, J., Clark, M., Craig, A., Dahlin, K., Drewniak, B., Fisher, J.B., Flanner, M., Fox, A.M., Gentine, P., Hoffman, F., Keppel-Aleks, G., Knox, R., Kumar, S., Lenaerts, J., Leung, L.R., Lipscomb, W.H., Lu, Y., Pandey, A., Pelletier, J.D., Perket, J., Randerson, J.T., Ricciuto, D.M., Sanderson, B.M., Slater, A., Subin, Z.M., Tang, J., Thomas, R.Q., Val Martin, M., Zeng, X., 2019. The Community Land Model Version 5: Description of New Features, Benchmarking, and Impact of Forcing Uncertainty. *J. Adv. Model. Earth Syst.* 11, 4245–4287. doi:10.1029/2018MS001583

Lebourgeois, V., Bégué, A., Labbé, S., Mallavan, B., Prévot, L., Roux, B., 2008. Can commercial digital cameras be used as multispectral sensors? A crop monitoring test. *Sensors* 8, 7300–7322. doi:10.3390/s8117300

Lee, H., Slatton, K.C., Roth, B.E., Cropper, W.P., 2008. Prediction of forest canopy light interception using three-dimensional airborne LiDAR data. *Int. J. Remote Sens.* 30, 189–207. doi:10.1080/01431160802261171

Lee, T.Y., Kaufman, Y.J., 1986. Non-Lambertian Effects on Surface Reflectance and Vegetation Index. *IEEE Trans. Geosci. Remote Sens.* 24, 699–708. doi:10.1109/TGRS.1986.289617

Lefsky, M.A., Cohen, W.B., Parker, G.G., Harding, D.J., 2002. Lidar Remote Sensing for ecosystem studies. *Bioscience* 52, 19–30.

Leslie, A.D., Mencuccini, M., Perks, M.P., 2017. A resource capture efficiency index to compare differences in early growth of four tree species in northern England. *IForest* 10, 397–405. doi:10.3832/ifor2248-010

Li-Cor, 1992. LAI-2000 plant canopy analyser. Operating manual.

Li, H., Zhang, H., Zhang, B., Member, S., Chen, Z., Yang, M., Zhang, Y., 2015. A Method Suitable for Vicarious Calibration of a UAV Hyperspectral Remote Sensor. *IEEE J. Sel. Top. Appl. Earth Obs. Remote Sens.* 8, 3209–3223. doi:10.1109/JSTARS.2015.2416213

- Li, L., Dong, J., Tenku, S.N., Xiao, X., 2015. Mapping oil palm plantations in cameroon using PALSAR 50-m orthorectified mosaic images. *Remote Sens.* 7, 1206–1224. doi:10.3390/rs70201206
- Li, S., Yuan, F., Ata-Ul-Karim, S.T., Zheng, H., Cheng, T., Liu, X., Tian, Y., Zhu, Y., Cao, W., Cao, Q., 2019. Combining Color Indices and Textures of UAV-Based Digital Imagery for Rice LAI Estimation. *Remote Sens.* 11. doi:10.3390/rs11151763
- Li, W., Fu, H., Yu, L., Cracknell, A., 2016. Deep Learning Based Oil Palm Tree Detection and Counting for High-Resolution Remote Sensing Images. *Remote Sens.* 9, 22. doi:10.3390/rs9010022
- Li, W., Niu, Z., Chen, H., Li, D., 2016. Characterizing canopy structural complexity for the estimation of maize LAI based on ALS data and UAV stereo images. *Int. J. Remote Sens.* 38, 2106–2116. doi:10.1080/01431161.2016.1235300
- Li, W., Niu, Z., Chen, H., Li, D., Wu, M., Zhao, W., 2016. Remote estimation of canopy height and aboveground biomass of maize using high-resolution stereo images from a low-cost unmanned aerial vehicle system. *Ecol. Indic.* 67, 637–648. doi:10.1016/j.ecolind.2016.03.036
- Lieth, H., 1974. *Phenology and Seasonality Modeling*. Springer Berlin Heidelberg, Berlin, Heidelberg. doi:10.1007/978-3-642-51863-8_1
- Ligot, G., Ameztegui, A., Courbaud, B., Coll, L., Kneeshaw, D., 2016. Tree light capture and spatial variability of understory light increase with species mixing and tree size heterogeneity. *Can. J. For. Res.* 46, 968–977. doi:10.1139/cjfr-2016-0061
- Ligot, G., Balandier, P., Courbaud, B., Claessens, H., 2014a. Forest radiative transfer models : which approach for which application ? *Can. J. For. Res.* 44, 391–403.
- Ligot, G., Balandier, P., Courbaud, B., Jonard, M., Kneeshaw, D., Claessens, H., 2014b. Managing understory light to maintain a mixture of species with different shade tolerance. *For. Ecol. Manage.* 327, 189–200. doi:10.1016/j.foreco.2014.05.010

- Lisein, J., Pierrot-Deseilligny, M., Bonnet, S., Lejeune, P., 2013. A photogrammetric workflow for the creation of a forest canopy height model from small unmanned aerial system imagery. *Forests* 4, 922–944. doi:10.3390/f4040922
- Liu, F., Wang, X., Wang, C., 2019. Measuring vegetation phenology with near-surface remote sensing in a temperate deciduous forest: Effects of sensor type and deployment. *Remote Sens.* 11. doi:10.3390/rs11091063
- Liu, Y., Hill, M.J., Zhang, X., Wang, Z., Richardson, A.D., Hufkens, K., Filippa, G., Baldocchi, D.D., Ma, S., Verfaillie, J., Schaaf, C.B., 2017. Using data from Landsat, MODIS, VIIRS and PhenoCams to monitor the phenology of California oak/grass savanna and open grassland across spatial scales. *Agric. For. Meteorol.* 237–238, 311–325. doi:10.1016/j.agrformet.2017.02.026
- Livens, S., Pauly, K., Baeck, P., Blommaert, J., Nuyts, D., Zender, J., Delauré, B., 2017. A spatio-spectral camera for high resolution hyperspectral imaging. *Int. Arch. Photogramm. Remote Sens. Spat. Inf. Sci. - ISPRS Arch.* 42, 223–228. doi:10.5194/isprs-archives-XLII-2-W6-223-2017
- Lowe, D.G., 2004. Distinctive Image Features from Scale-Invariant Keypoints. *Int. J. Comput. Vis.* 60, 91–110. doi:10.1023/B:VISI.0000029664.99615.94
- Lu, B., He, Y., 2017. Species classification using Unmanned Aerial Vehicle (UAV)-acquired high spatial resolution imagery in a heterogeneous grassland. *ISPRS J. Photogramm. Remote Sens.* 128, 73–85. doi:10.1016/j.isprsjprs.2017.03.011
- Luscombe, D.J., Anderson, K., Gatis, N., Wetherelt, A., Grand-Clement, E., Brazier, R.E., 2015. What does airborne LiDAR really measure in upland ecosystems? *Ecohydrology* 8, 584–594. doi:10.1002/eco.1527
- MacArthur, A., Anderson, K., 2007. Field Guide for the ASD FieldSpec Pro - White Reference Mode.
- MacArthur, A., Robinson, I., Rossini, M., Davis, N., MacDonald, K., 2014. A dual-field-of-view spectrometer system for reflectance and fluorescence measurements (Piccolo Doppio) and correction of etaloning, in: 5th International Workshop on Remote Sensing of Vegetation Fluorescence.

Paris, France.

- Maes, W.H., Steppe, K., 2019. Perspectives for Remote Sensing with Unmanned Aerial Vehicles in Precision Agriculture. *Trends Plant Sci.* 24, 152–164. doi:<https://doi.org/10.1016/j.tplants.2018.11.007>
- Mäkinen, J., Saari, H., Holmlund, C., Mannila, R., Antila, T., 2012. Multi- and hyperspectral UAV imaging system for forest and agriculture applications. *Proc. SPIE* 8374, Next-Generation Spectrosc. Technol. V 8374, 837409. doi:[10.1117/12.918571](https://doi.org/10.1117/12.918571)
- Malek, S., Bazi, Y., Alajlan, N., AlHichri, H., Melgani, F., 2014. Efficient framework for palm tree detection in UAV images. *IEEE J. Sel. Top. Appl. Earth Obs. Remote Sens.* 7, 4692–4703. doi:[10.1109/JSTARS.2014.2331425](https://doi.org/10.1109/JSTARS.2014.2331425)
- Manandhar, A., Hoegner, L., Stilla, U., 2016. Palm Tree Detection Using Circular Autocorrelation of Polar Shape Matrix. *ISPRS Ann. Photogramm. Remote Sens. Spat. Inf. Sci.* 3, 465–472. doi:[10.5194/isprs-annals-III-3-465-2016](https://doi.org/10.5194/isprs-annals-III-3-465-2016)
- Manuel Fernández-Guisuraga, J., Sanz-Ablanedo, E., Suárez-Seoane, S., Calvo, L., 2018. Using Unmanned Aerial Vehicles in Postfire Vegetation Survey Campaigns through Large and Heterogeneous Areas: Opportunities and Challenges. *Sensors* 18. doi:[10.3390/s18020586](https://doi.org/10.3390/s18020586)
- Marconi, S., Graves, S.J., Weinstein, B.G., Bohlman, S., White, E.P., 2019. Rethinking the fundamental unit of ecological remote sensing: Estimating individual level plant traits at scale. *bioRxiv* 556472. doi:[10.1101/556472](https://doi.org/10.1101/556472)
- Marques, P., Pádua, L., Adão, T., Hruška, J., Peres, E., Sousa, A., Sousa, J.J., 2019. UAV-based automatic detection and monitoring of chestnut trees. *Remote Sens.* 11, 1–32. doi:[10.3390/RS11070855](https://doi.org/10.3390/RS11070855)
- Martens, S.N., Breshears, D.D., Meyer, C.W., 2000. Spatial distributions of understory light along the grassland/forest continuum: Effects of cover, height, and spatial pattern of tree canopies. *Ecol. Modell.* 126, 79–93. doi:[10.1016/S0304-3800\(99\)00188-X](https://doi.org/10.1016/S0304-3800(99)00188-X)
- Matese, A., Toscano, P., Di Gennaro, S.F., Genesio, L., Vaccari, F.P.,

- Primicerio, J., Belli, C., Zaldei, A., Bianconi, R., Gioli, B., 2015. Intercomparison of UAV, aircraft and satellite remote sensing platforms for precision viticulture. *Remote Sens.* 7, 2971–2990. doi:10.3390/rs70302971
- Mathews, A.J., Jensen, J.L.R., 2013. Visualizing and quantifying vineyard canopy LAI using an unmanned aerial vehicle (UAV) collected high density structure from motion point cloud. *Remote Sens.* 5, 2164–2183. doi:10.3390/rs5052164
- McCree, K.J., 1972. Test of current definitions of photosynthetically active radiation against leaf photosynthesis data. *Agric. Meteorol.* 10, 443–453. doi:[https://doi.org/10.1016/0002-1571\(72\)90045-3](https://doi.org/10.1016/0002-1571(72)90045-3)
- McNeil, B.E., Pisek, J., Lepisk, H., Flamenco, E.A., 2016. Measuring leaf angle distribution in broadleaf canopies using UAVs. *Agric. For. Meteorol.* 218–219, 204–208. doi:10.1016/j.agrformet.2015.12.058
- Melaas, E.K., Friedl, M.A., Zhu, Z., 2013. Detecting interannual variation in deciduous broadleaf forest phenology using Landsat TM/ETM+ data. *Remote Sens. Environ.* 132, 176–185. doi:10.1016/j.rse.2013.01.011
- Menouar, H., Guvenc, I., Akkaya, K., Uluagac, A.S., Kadri, A., Tuncer, A., 2017. UAV-enabled intelligent transportation systems for the smart city: Applications and challenges. *IEEE Commun. Mag.* 55, 22–28. doi:10.1109/MCOM.2017.1600238CM
- Messina, G., Modica, G., 2020. Applications of UAV Thermal Imagery in Precision Agriculture: State of the Art and Future Research Outlook. *Remote Sens.* 12. doi:10.3390/rs12091491
- Messinger, M., Asner, G.P., Silman, M., 2016. Rapid assessments of amazon forest structure and biomass using small unmanned aerial systems. *Remote Sens.* 8, 1–15. doi:10.3390/rs8080615
- Mialon, A., Rodríguez-Fernández, N.J., Santoro, M., Saatchi, S., Mermoz, S., Bousquet, E., Kerr, Y.H., 2020. Evaluation of the sensitivity of SMOS L-VOD to forest above-ground biomass at global scale. *Remote Sens.* 12, 1–10. doi:10.3390/RS12091450
- Michez, A., Bauwens, S., Brostaux, Y., Hiel, M.-P., Garré, S., Lejeune, P.,

- Dumont, B., 2018. How Far Can Consumer-Grade UAV RGB Imagery Describe Crop Production? A 3D and Multitemporal Modeling Approach Applied to *Zea mays*. *Remote Sens.* 10. doi:10.3390/rs10111798
- Mijnsbrugge, K. Vander, Janssens, A., 2019. Differentiation and non-linear responses in temporal phenotypic plasticity of seasonal phenophases in a common garden of *Crataegus monogyna* Jacq. *Forests* 10. doi:10.3390/f10040293
- Miller, J.B., 1967. A formula for average foliage density. *Aust. J. Bot.* 15, 141–144.
- Minařík, R., Langhammer, J., Hanuš, J., 2019. Radiometric and atmospheric corrections of multispectral μMCA Camera for UAV spectroscopy. *Remote Sens.* 11. doi:10.3390/rs11202428
- Mitchard, E.T.A., Saatchi, S.S., Woodhouse, I.H., Nangendo, G., Ribeiro, N.S., Williams, M., Ryan, C.M., Lewis, S.L., Feldpausch, T.R., Meir, P., 2009. Using satellite radar backscatter to predict above-ground woody biomass: A consistent relationship across four different African landscapes. *Geophys. Res. Lett.* 36, 1–6. doi:10.1029/2009GL040692
- Miura, T., Huete, A.R., Yoshioka, H., 2000. Evaluation of sensor calibration uncertainties on vegetation indices for MODIS. *IEEE Trans. Geosci. Remote Sens.* 38, 1399–1409. doi:10.1109/36.843034
- Mlambo, R., Woodhouse, I.H., Gerard, F., Anderson, K., 2017. Structure from motion (SfM) photogrammetry with drone data: A low cost method for monitoring greenhouse gas emissions from forests in developing countries. *Forests* 8. doi:10.3390/f8030068
- Mohammed, G.H., Colombo, R., Middleton, E.M., Rascher, U., van der Tol, C., Nedbal, L., Goulas, Y., Pérez-Priego, O., Damm, A., Meroni, M., Joiner, J., Cogliati, S., Verhoef, W., Malenovský, Z., Gastellu-Etchegorry, J.-P., Miller, J.R., Guanter, L., Moreno, J., Moya, I., Berry, J.A., Frankenberg, C., Zarco-Tejada, P.J., 2019. Remote sensing of solar-induced chlorophyll fluorescence (SIF) in vegetation: 50 years of progress. *Remote Sens. Environ.* 231, 111177. doi:<https://doi.org/10.1016/j.rse.2019.04.030>
- Möller, W., Nikolaus, K.-P., Höpe, A., 2003. Degradation of the diffuse

reflectance of Spectralon under low-level irradiation. *Metrologia* 40, S212–S215.

Monteith, J.L., 1972. Solar Radiation and Productivity in Tropical Ecosystems. *J. Appl. Ecol.* 9, 747–766. doi:10.2307/2401901

Morel, A.C., Saatchi, S.S., Malhi, Y., Berry, N.J., Banin, L., Burslem, D., Nilus, R., Ong, R.C., 2011. Estimating aboveground biomass in forest and oil palm plantation in Sabah, Malaysian Borneo using ALOS PALSAR data. *For. Ecol. Manage.* 262, 1786–1798. doi:10.1016/j.foreco.2011.07.008

Mõttus, M., Sulev, M., Baret, F., Lopez-Lozano, R., Reinart, A., 2011. Photosynthetically Active Radiation: Measurement and Modeling, in: Meyers, R. (Ed.), *Encyclopedia of Sustainability Science and Technology*. Springer. doi:10.1007/springerreference_310766

Mõttus, M., Takala, T.L.H., Stenberg, P., Knyazikhin, Y., Yang, B., Nilson, T., 2015. Diffuse sky radiation influences the relationship between canopy PRI and shadow fraction. *ISPRS J. Photogramm. Remote Sens.* 105, 54–60. doi:10.1016/j.isprsjprs.2015.03.012

Mutanga, O., Skidmore, A.K., 2004. Narrow band vegetation indices overcome the saturation problem in biomass estimation. *Int. J. Remote Sens.* 25, 3999–4014. doi:10.1080/01431160310001654923

Muzylo, A., Llorens, P., Valente, F., Keizer, J.J., Domingo, F., Gash, J.H.C., 2009. A review of rainfall interception modelling. *J. Hydrol.* 370, 191–206. doi:<https://doi.org/10.1016/j.jhydrol.2009.02.058>

Myneni, R.B., Nemani, R.R., Running, S., 1997. Estimation of global leaf area index and absorbed par using radiative transfer models. *IEEE Trans. Geosci. Remote Sens.* 35, 1380–1393. doi:10.1109/36.649788

Navarro, A., Young, M., Allan, B., Carnell, P., Macreadie, P., Ierodiaconou, D., 2020. The application of Unmanned Aerial Vehicles (UAVs) to estimate above-ground biomass of mangrove ecosystems. *Remote Sens. Environ.* 242, 111747. doi:<https://doi.org/10.1016/j.rse.2020.111747>

Nebiker, S., Lack, N., Abächerli, M., Läderach, S., 2016. Light-weight multispectral uav sensors and their capabilities for predicting grain yield

and detecting plant diseases. Int. Arch. Photogramm. Remote Sens. Spat. Inf. Sci. - ISPRS Arch. 2016-Janua, 963–970. doi:10.5194/isprsarchives-XLI-B1-963-2016

Nemani, R.R., Keeling, C.D., Hashimoto, H., Jolly, W.M., Piper, S.C., Tucker, C.J., Myneni, R.B., Running, S.W., 2003. Climate-driven increases in global terrestrial net primary production from 1982 to 1999. *Science* (80-.). 300, 1560–1563. doi:10.1126/science.1082750

Nemani, R.R., Pierce, L., Running, S., Band, L., 1993. Forest ecosystem processes at the watershed scale: Sensitivity to remotely-sensed leaf area index estimates. *Int. J. Remote Sens.* 14, 2519–2534. doi:10.1080/01431169308904290

Neumann, C., Behling, R., Schindhelm, A., Itzerott, S., Weiss, G., Wichmann, M., Müller, J., 2020. The colors of heath flowering – quantifying spatial patterns of phenology in Calluna life-cycle phases using high-resolution drone imagery. *Remote Sens. Ecol. Conserv.* 6, 35–51. doi:10.1002/rse2.121

Nevalainen, O., Honkavaara, E., Tuominen, S., Viljanen, N., Hakala, T., Yu, X., Hyppä, J., Saari, H., Pölönen, I., Imai, N.N., Tommaselli, A.M.G., 2017. Individual tree detection and classification with UAV-Based photogrammetric point clouds and hyperspectral imaging. *Remote Sens.* 9. doi:10.3390/rs9030185

Nezami, S., Khoramshahi, E., Nevalainen, O., Pölönen, I., Honkavaara, E., 2020. Tree Species Classification of Drone Hyperspectral and RGB Imagery with Deep Learning Convolutional Neural Networks. *Remote Sens.* 12. doi:10.3390/rs12071070

Ni, W., Dong, J., Sun, G., Zhang, Z., Pang, Y., Tian, X., Li, Z., Chen, E., 2019. Synthesis of Leaf-on and Leaf-off Unmanned Aerial Vehicle (UAV) Stereo Imagery for the Inventory of Aboveground Biomass of Deciduous Forests. *Remote Sens.* 11. doi:10.3390/rs11070889

North, P.R.J., 1996. Three-dimensional forest light interaction model using a monte carlo method. *IEEE Trans. Geosci. Remote Sens.* 34, 946–956. doi:10.1109/36.508411

Nuijten, R.J.G., Coops, N.C., Goodbody, T.R.H., Pelletier, G., 2019. Examining the multi-seasonal consistency of individual tree segmentation on deciduous stands using Digital Aerial Photogrammetry (DAP) and unmanned aerial systems (UAS). *Remote Sens.* 11.

doi:10.3390/rs11070739

O'Connor, J., Smith, M.J., James, M.R., 2017. Cameras and settings for aerial surveys in the geosciences: Optimising image data. *Prog. Phys. Geogr.* 41, 325–344. doi:10.1177/0309133317703092

Onset, 2018. HOBO® Pendant® Temperature/Light Data Logger (UA-002-xx) Manual.

Pacheco-Labrador, J., El-Madany, T., Martín, M., Migliavacca, M., Rossini, M., Carrara, A., Zarco-Tejada, P.J., 2017. Spatio-Temporal Relationships between Optical Information and Carbon Fluxes in a Mediterranean Tree-Grass Ecosystem. *Remote Sens.* 9, 608. doi:10.3390/rs9060608

Padró, J.C., Muñoz, F.J., Ávila, L.Á., Pesquer, L., Pons, X., 2018. Radiometric correction of Landsat-8 and Sentinel-2A scenes using drone imagery in synergy with field spectroradiometry. *Remote Sens.* 10.

doi:10.3390/rs10111687

Pan, Y., Birdsey, R.A., Fang, J., Houghton, R., Kauppi, P.E., Kurz, W.A., Phillips, O.L., Shvidenko, A., Lewis, S.L., Canadell, J.G., Ciais, P., Jackson, R.B., Pacala, S.W., McGuire, A.D., Piao, S., Rautiainen, A., Sitch, S., Hayes, D., 2011. A Large and Persistent Carbon Sink in the World's Forests. *Science* (80-.). 333, 988–993. doi:10.1126/science.1201609

Panagiotidis, D., Abdollahnejad, A., Surový, P., Chiteculo, V., 2017. Determining tree height and crown diameter from high-resolution UAV imagery. *Int. J. Remote Sens.* 38, 2392–2410.

doi:10.1080/01431161.2016.1264028

Papale, D., Reichstein, M., Aubinet, M., Canfora, E., Bernhofer, C., Kutsch, W., Longdoz, B., Rambal, S., Valentini, R., Vesala, T., Yakir, D., 2006. Towards a standardized processing of Net Ecosystem Exchange measured with eddy covariance technique: Algorithms and uncertainty estimation. *Biogeosciences* 3, 571–583. doi:10.5194/bg-3-571-2006

- Park, J.Y., Muller-Landau, H.C., Lichstein, J.W., Rifai, S.W., Dandois, J.P., Bohlman, S.A., 2019. Quantifying leaf phenology of individual trees and species in a tropical forest using unmanned aerial vehicle (UAV) images. *Remote Sens.* 11. doi:10.3390/rs11131534
- Parrot, 2019. Spectral response functions [WWW Document]. Parrot Dev. Forum. URL <https://forum.developer.parrot.com/t/spectral-response-functions/7096/4> (accessed 8.15.20).
- Parrot, 2017a. Parrot announcement - Release of application notes (discussion) [WWW Document]. Parrot Dev. Forum. URL <https://forum.developer.parrot.com/t/archive-parrot-announcement-release-of-application-notes-discussion/5613> (accessed 8.15.20).
- Parrot, 2017b. Parrot Sequoia application notes [WWW Document]. URL <https://forum.developer.parrot.com/t/parrot-announcement-release-of-application-notes/5455> (accessed 11.29.19).
- Pastor-Guzman, J., Dash, J., Atkinson, P.M., 2018. Remote sensing of mangrove forest phenology and its environmental drivers. *Remote Sens. Environ.* 205, 71–84. doi:10.1016/j.rse.2017.11.009
- Pennec, A., Gond, V.R., Sabatier, D., 2011. Tropical forest phenology in French Guiana from MODIS time series. *Remote Sens. Lett.* 2, 337–345. doi:10.1080/01431161.2010.507610
- Persson, M., Lindberg, E., Reese, H., 2018. Tree species classification with multi-temporal Sentinel-2 data. *Remote Sens.* 10, 1–17. doi:10.3390/rs10111794
- Pettorelli, N., Wegmann, M., Skidmore, A., Mücher, S., Dawson, T.P., Fernandez, M., Lucas, R., Schaepman, M.E., Wang, T., O'Connor, B., Jongman, R.H.G., Kempeneers, P., Sonnenschein, R., Leidner, A.K., Böhm, M., He, K.S., Nagendra, H., Dubois, G., Fatoynbo, T., Hansen, M.C., Paganini, M., de Klerk, H.M., Asner, G.P., Kerr, J.T., Estes, A.B., Schmeller, D.S., Heiden, U., Rocchini, D., Pereira, H.M., Turak, E., Fernandez, N., Lausch, A., Cho, M.A., Alcaraz-Segura, D., McGeoch, M.A., Turner, W., Mueller, A., St-Louis, V., Penner, J., Vihervaara, P., Belward, A., Reyers, B., Geller, G.N., 2016. Framing the concept of satellite remote

sensing essential biodiversity variables: challenges and future directions.

Remote Sens. Ecol. Conserv. 2, 122–131. doi:10.1002/rse2.15

Piao, S., Liu, Q., Chen, A., Janssens, I.A., Fu, Y., Dai, J., Liu, L., Lian, X., Shen, M., Zhu, X., 2019. Plant phenology and global climate change: Current progresses and challenges. Glob. Chang. Biol. 25, 1922–1940. doi:10.1111/gcb.14619

Piao, S., Sitch, S., Ciais, P., Friedlingstein, P., Peylin, P., Wang, X., Ahlström, A., Anav, A., Canadell, J.G., Cong, N., Huntingford, C., Jung, M., Levis, S., Levy, P.E., Li, J., Lin, X., Lomas, M.R., Lu, M., Luo, Y., Ma, Y., Myneni, R.B., Poulter, B., Sun, Z., Wang, T., Viovy, N., Zaehle, S., Zeng, N., 2013. Evaluation of terrestrial carbon cycle models for their response to climate variability and to CO₂ trends. Glob. Chang. Biol. 19, 2117–2132. doi:10.1111/gcb.12187

Pincebourde, S., Sinoquet, H., Combes, D., Casas, J., 2007. Regional climate modulates the canopy mosaic of favourable and risky microclimates for insects. J. Anim. Ecol. 76, 424–438. doi:10.1111/j.1365-2656.2007.01231.x

Pix4D, 2019. Pix4D vignetting correction [WWW Document]. URL <https://support.pix4d.com/hc/en-us/articles/115001846106-Camera-radiometric-correction-specifications> (accessed 8.7.19).

Poblete, T., Ortega-Farías, S., Ryu, D., 2018. Automatic coregistration algorithm to remove canopy shaded pixels in UAV-borne thermal images to improve the estimation of crop water stress index of a drip-irrigated cabernet sauvignon vineyard. Sensors 18, 1–17. doi:10.3390/s18020397

Polgar, C.A., Primack, R.B., 2011. Leaf-out phenology of woody plants: From trees to ecosystems. New Phytol. 926–941. doi:10.1111/j.1365-2486.2005.01097.x

Porcar-Castell, A., Tyystjärvi, E., Atherton, J., Van der Tol, C., Flexas, J., Pfundel, E.E., Moreno, J., Frankenberg, C., Berry, J.A., 2014. Linking chlorophyll a fluorescence to photosynthesis for remote sensing applications: Mechanisms and challenges. J. Exp. Bot. 65, 4065–4095. doi:10.1093/jxb/eru191

Potithep, S., Nagai, S., Nasahara, K.N., Muraoka, H., Suzuki, R., 2013. Two

separate periods of the LAI-VIs relationships using in situ measurements in a deciduous broadleaf forest. *Agric. For. Meteorol.* 169, 148–155.
doi:10.1016/j.agrformet.2012.09.003

Potter, C.S., Randerson, J.T., Field, C.B., Matson, P.A., Vitousek, P.M., Mooney, H.A., Klooster, S.A., 1993. Terrestrial ecosystem production: A process model based on global satellite and surface data. *Global Biogeochem. Cycles* 7, 811–841. doi:<https://doi.org/10.1029/93GB02725>

Poulter, B., Frank, D., Ciais, P., Myneni, R.B., Andela, N., Bi, J., Broquet, G., Canadell, J.G., Chevallier, F., Liu, Y.Y., Running, S.W., Sitch, S., van der Werf, G.R., 2014. Contribution of semi-arid ecosystems to interannual variability of the global carbon cycle. *Nature* 509, 600–603.
doi:10.1038/nature13376

Prabakaran, C., Singh, C.P., Panigrahy, S., Parihar, J.S., 2013. Retrieval of forest phenological parameters from remote sensing-based NDVI time-series data. *Curr. Sci.* 105, 795–802.

Puliti, S., Ene, L.T., Gobakken, T., Næsset, E., 2017a. Use of partial-coverage UAV data in sampling for large scale forest inventories. *Remote Sens. Environ.* 194, 115–126. doi:10.1016/j.rse.2017.03.019

Puliti, S., Olerka, H., Gobakken, T., Næsset, E., 2015. Inventory of Small Forest Areas Using an Unmanned Aerial System. *Remote Sens.* 7, 9632–9654.
doi:10.3390/rs70809632

Puliti, S., Saarela, S., Gobakken, T., Ståhl, G., Næsset, E., 2017b. Combining UAV and Sentinel-2 auxiliary data for forest growing stock volume estimation through hierarchical model-based inference. *Remote Sens. Environ.* 204, 485–497. doi:10.1016/j.rse.2017.10.007

Qi, J., Chehbouni, A., Huete, A.R., Kerr, Y.H., Sorooshian, S., 1994. A modified soil adjusted vegetation index. *Remote Sens. Environ.* 48, 119–126.
doi:10.1016/0034-4257(94)90134-1

Qiu, L., Jing, L., Hu, B., Li, H., Tang, Y., 2020. A new individual tree crown delineation method for high resolution multispectral imagery. *Remote Sens.* 12, 1–20. doi:10.3390/rs12030585

Quegan, S., Le Toan, T., Chave, J., Dall, J., Exbrayat, J.-F., Minh, D.H.T., Lomas, M., D'Alessandro, M.M., Paillou, P., Papathanassiou, K., Rocca, F., Saatchi, S., Scipal, K., Shugart, H., Smallman, T.L., Soja, M.J., Tebaldini, S., Ulander, L., Villard, L., Williams, M., 2019. The European Space Agency BIOMASS mission: Measuring forest above-ground biomass from space. *Remote Sens. Environ.* 227, 44–60.
doi:<https://doi.org/10.1016/j.rse.2019.03.032>

Rascher, U., Alonso, L., Burkart, A., Cilia, C., Cogliati, S., Colombo, R., Damm, A., Drusch, M., Guanter, L., Hanus, J., Hyvärinen, T., Julitta, T., Jussila, J., Kataja, K., Kokkalis, P., Kraft, S., Kraska, T., Matveeva, M., Moreno, J., Muller, O., Panigada, C., Piki, M., Pinto, F., Prey, L., Pude, R., Rossini, M., Schickling, A., Schurr, U., Schüttemeyer, D., Verrelst, J., Zemek, F., 2015. Sun-induced fluorescence - a new probe of photosynthesis: First maps from the imaging spectrometer HyPlant. *Glob. Chang. Biol.* 21, 4673–4684.
doi:10.1111/gcb.13017

Réjou-Méchain, M., Barbier, N., Couteron, P., Ploton, P., Vincent, G., Herold, M., Mermoz, S., Saatchi, S., Chave, J., de Boissieu, F., Féret, J.B., Takoudjou, S.M., Pélissier, R., 2019. Upscaling Forest Biomass from Field to Satellite Measurements: Sources of Errors and Ways to Reduce Them, *Surveys in Geophysics*. Springer Netherlands. doi:10.1007/s10712-019-09532-0

Remondino, F., Barazzetti, L., Nex, F., Scaioni, M., Sarazzi, D., 2011. UAV Photogrammetry for mapping and 3D modeling - current status and future perspectives. *ISPRS - Int. Arch. Photogramm. Remote Sens. Spat. Inf. Sci.* XXXVIII-1/, 25–31. doi:10.5194/isprsarchives-XXXVIII-1-C22-25-2011

Revill, A., Florence, A., MacArthur, A., Hoad, S., Rees, R., Williams, M., 2019. The Value of Sentinel-2 Spectral Bands for the Assessment of Winter Wheat Growth and Development. *Remote Sens.* 11, 2050.
doi:10.3390/rs11172050

Rokhmana, C.A., 2015. The Potential of UAV-based Remote Sensing for Supporting Precision Agriculture in Indonesia. *Procedia Environ. Sci.* 24, 245–253. doi:10.1016/j.proenv.2015.03.032

Rollin, E.M., Milton, E.J., Emery, D.R., 2000. Reference panel anisotropy and
269

diffuse radiation - some implications for field spectroscopy. *Int. J. Remote Sens.* 21, 2799–2810. doi:10.1080/01431160050121258

Román, M.O., Gatebe, C.K., Schaaf, C.B., Poudyal, R., Wang, Z., King, M.D., 2011. Variability in surface BRDF at different spatial scales (30m-500m) over a mixed agricultural landscape as retrieved from airborne and satellite spectral measurements. *Remote Sens. Environ.* 115, 2184–2203. doi:10.1016/j.rse.2011.04.012

Roosjen, P.P.J., Brede, B., Suomalainen, J.M., Bartholomeus, H.M., Kooistra, L., Clevers, J.G.P.W., 2018. Improved estimation of leaf area index and leaf chlorophyll content of a potato crop using multi-angle spectral data – potential of unmanned aerial vehicle imagery. *Int. J. Appl. Earth Obs. Geoinf.* 66, 14–26. doi:<https://doi.org/10.1016/j.jag.2017.10.012>

Rosati, A., Wolz, K.J., Murphy, L., Ponti, L., Jose, S., 2020. Modeling light below tree canopies overestimates net photosynthesis and radiation use efficiency in understory crops by averaging light in space and time. *Agric. For. Meteorol.* 284, 107892. doi:10.1016/j.agrformet.2019.107892

Roth, L., Streit, B., 2017. Predicting cover crop biomass by lightweight UAS-based RGB and NIR photography : an applied photogrammetric approach. *Precis. Agric.* doi:10.1007/s11119-017-9501-1

Roussel, J.-R., Auty, D., 2018. lidR: Airborne LiDAR Data Manipulation and Visualization for Forestry Applications.

Running, S.W., Nemani, R.R., Heinsch, F.A., Zhao, M., Reeves, M., Hashimoto, H., 2004. A Continuous Satellite-Derived Measure of Global Terrestrial Primary Production. *Bioscience* 54, 547. doi:10.1641/0006-3568(2004)054[0547:ACSMOG]2.0.CO;2

Ryu, Y., Lee, G., Jeon, S., Song, Y., Kimm, H., 2014. Monitoring multi-layer canopy spring phenology of temperate deciduous and evergreen forests using low-cost spectral sensors. *Remote Sens. Environ.* 149, 227–238. doi:<https://doi.org/10.1016/j.rse.2014.04.015>

Salamí, E., Barrado, C., Pastor, E., 2014. UAV flight experiments applied to the remote sensing of vegetated areas. *Remote Sens.* 6, 11051–11081. doi:10.3390/rs61111051

- Sandmeier, S.R., Itten, K.I., 1999. A field goniometer system (FIGOS) for acquisition of hyperspectral BRDF data. *IEEE Trans. Geosci. Remote Sens.* 37, 978–986. doi:10.1109/36.752216
- Sankey, T.T., McVay, J., Swetnam, T.L., McClaran, M.P., Heilman, P., Nichols, M., 2018. UAV hyperspectral and lidar data and their fusion for arid and semi-arid land vegetation monitoring. *Remote Sens. Ecol. Conserv.* 4, 20–33. doi:10.1002/rse2.44
- Santesteban, L.G., Di Gennaro, S.F., Herrero-Langreo, A., Miranda, C., Royo, J.B., Matese, A., 2016. High-resolution UAV-based thermal imaging to estimate the instantaneous and seasonal variability of plant water status within a vineyard. *Agric. Water Manag.* 183, 49–59. doi:10.1016/j.agwat.2016.08.026
- Savitzky, A., Golay, M.J.E., 1964. Smoothing and Differentiation of Data by Simplified Least Squares Procedures. *Anal. Chem.* 36, 1627–1639. doi:10.1021/ac60214a047
- Schaepman-Strub, G., Schaepman, M.E., Painter, T.H., Dangel, S., Martonchik, J. V., 2006. Reflectance quantities in optical remote sensing-definitions and case studies. *Remote Sens. Environ.* 103, 27–42. doi:10.1016/j.rse.2006.03.002
- Scheffler, D., Hollstein, A., Diedrich, H., Segl, K., Hostert, P., 2017. AROSICS: An automated and robust open-source image co-registration software for multi-sensor satellite data. *Remote Sens.* 9. doi:10.3390/rs9070676
- Schimel, D.S., Pavlick, R., Fisher, J.B., Asner, G.P., Saatchi, S., Townsend, P., Miller, C., Frankenberg, C., Hibbard, K., Cox, P., 2015. Observing terrestrial ecosystems and the carbon cycle from space. *Glob. Chang. Biol.* 21, 1762–1776. doi:10.1111/gcb.12822
- Schirrmann, M., Giebel, A., Gleiniger, F., Pflanz, M., Lentschke, J., Dammer, K.-H., 2016. Monitoring Agronomic Parameters of Winter Wheat Crops with Low-Cost UAV Imagery. *Remote Sens.* 8. doi:10.3390/rs8090706
- Schläpfer, D., Richter, R., Damm, A., 2013. Correction of shadowing in imaging spectroscopy data by quantification of the proportion of diffuse illumination, in: 8th EARSeL Workshop on Imaging Spectroscopy. Nantes, France.

- Schlemmera, M., Gitelson, A., Schepersa, J., Fergusona, R., Peng, Y., Shanahana, J., Rundquist, D., 2013. Remote estimation of nitrogen and chlorophyll contents in maize at leaf and canopy levels. *Int. J. Appl. Earth Obs. Geoinf.* 25, 47–54. doi:10.1016/j.jag.2013.04.003
- Schneider, F.D., Leiterer, R., Morsdorf, F., Gastellu-Etchegorry, J.P., Lauret, N., Pfeifer, N., Schaepman, M.E., 2014. Simulating imaging spectrometer data: 3D forest modeling based on LiDAR and in situ data. *Remote Sens. Environ.* 152, 235–250. doi:10.1016/j.rse.2014.06.015
- Schneider, F.D., Morsdorf, F., Schmid, B., Petchey, O.L., Hueni, A., Schimel, D.S., Schaepman, M.E., 2017. Mapping functional diversity from remotely sensed morphological and physiological forest traits. *Nat. Commun.* 8, 1441. doi:10.1038/s41467-017-01530-3
- Scholze, M., Buchwitz, M., Dorigo, W., Guanter, L., Quegan, S., 2017. Reviews and syntheses: Systematic Earth observations for use in terrestrial carbon cycle data assimilation systems. *Biogeosciences* 14, 3401–3429. doi:10.5194/bg-14-3401-2017
- Sellers, P.J., 1987. Canopy reflectance, photosynthesis, and transpiration, II. The role of biophysics in the linearity of their interdependence. *Remote Sens. Environ.* 21, 143–183. doi:10.1016/0034-4257(87)90051-4
- Shafri, H.Z.M., Hamdan, N., 2009. Hyperspectral imagery for mapping disease infection in oil palm plantation using vegetation indices and red edge techniques. *Am. J. Appl. Sci.* 6, 1031–1035. doi:10.3844/ajassp.2009.1031.1035
- Sheeren, D., Fauvel, M., Josipović, V., Lopes, M., Planque, C., Willm, J., Dejoux, J.F., 2016. Tree species classification in temperate forests using Formosat-2 satellite image time series. *Remote Sens.* 8, 1–29. doi:10.3390/rs8090734
- Siegmann, B., Alonso, L., Celesti, M., Cogliati, S., Colombo, R., Damm, A., Douglas, S., Guanter, L., Hanuš, J., Kataja, K., Kraska, T., Matveeva, M., Moreno, J., Muller, O., Píkl, M., Pinto, F., Quirós Vargas, J., Rademske, P., Rodriguez-Moreno, F., Sabater, N., Schickling, A., Schüttemeyer, D., Zemek, F., Rascher, U., 2019. The high-performance airborne imaging

spectrometer HyPlant – From raw images to top-of-canopy reflectance and fluorescence products: Introduction of an automatized processing chain.

Remote Sens. 11. doi:10.3390/rs11232760

Silva, B., Lehnert, L., Roos, K., Fries, A., Rollenbeck, R., Beck, E., Bendix, J., 2014. Mapping two competing grassland species from a low-altitude helium balloon. IEEE J. Sel. Top. Appl. Earth Obs. Remote Sens. 7, 3038–3049. doi:10.1109/JSTARS.2014.2321896

Silva, C.A., Hudak, A.T., Vierling, L.A., Loudermilk, E.L., O'Brien, J.J., Hiers, J.K., Jack, S.B., Gonzalez-Benecke, C., Lee, H., Falkowski, M.J., Khosravipour, A., 2016. Imputation of Individual Longleaf Pine (*Pinus palustris* Mill.) Tree Attributes from Field and LiDAR Data. Can. J. Remote Sens. 42, 554–573. doi:10.1080/07038992.2016.1196582

Smith, G.M., Milton, E.J., 1999. The use of the empirical line method to calibrate remotely sensed data to reflectance. Int. J. Remote Sens. 20, 2653–2662. doi:10.1080/014311699211994

Soenen, S.A., Peddle, D.R., Hall, R.J., Coburn, C.A., Hall, F.G., 2010. Estimating aboveground forest biomass from canopy reflectance model inversion in mountainous terrain. Remote Sens. Environ. 114, 1325–1337. doi:10.1016/j.rse.2009.12.012

Soudani, K., François, C., le Maire, G., Le Dantec, V., Dufrêne, E., 2006. Comparative analysis of IKONOS, SPOT, and ETM+ data for leaf area index estimation in temperate coniferous and deciduous forest stands. Remote Sens. Environ. 102, 161–175. doi:10.1016/j.rse.2006.02.004

Soudani, K., Hmimina, G., Delpierre, N., Pontailler, J.-Y., Aubinet, M., Bonal, D., Caquet, B., de Grandcourt, A., Burban, B., Flechard, C., Guyon, D., Granier, A., Gross, P., Heinesh, B., Longdoz, B., Loustau, D., Moureaux, C., Ourcival, J.-M., Rambal, S., Saint André, L., Dufrêne, E., 2012. Ground-based Network of NDVI measurements for tracking temporal dynamics of canopy structure and vegetation phenology in different biomes. Remote Sens. Environ. 123, 234–245. doi:<https://doi.org/10.1016/j.rse.2012.03.012>

Spanner, M.A., Piercej, L.L., Peterson, D.L., Running, S.W., 1990. Remote sensing of temperate coniferous forest leaf area index the influence of

canopy closure, understory vegetation and background reflectance. *Int. J. Remote Sens.* 11, 95–111. doi:10.1080/01431169008955002

Spectrum Technologies, 2011. Lightscout PAR Light Sensor Manual.

Spitters, C.J.T., Toussaint, H.A.J.M., Goudriaan, J., 1986. Separating the diffuse and direct component of global radiation and its implications for modeling canopy photosynthesis part i. components of incoming radiation. *Agric. For. Meteorol.* 38, 217–229.

Srestasathiern, P., Rakwatin, P., 2014. Oil palm tree detection with high resolution multi-spectral satellite imagery. *Remote Sens.* 6, 9749–9774. doi:10.3390/rs6109749

St-Onge, B., Audet, F.A., Bégin, J., 2015. Characterizing the height structure and composition of a boreal forest using an individual tree crown approach applied to photogrammetric point clouds. *Forests* 6, 3899–3922. doi:10.3390/f6113899

Stadt, K.J., Lieffers, V.J., Hall, R.J., Messier, C., 2005. Spatially explicit modeling of PAR transmission and growth of *Picea glauca* and *Abies balsamea* in the boreal forests of Alberta and Quebec. *Can. J. For. Res.* 35, 1–12. doi:10.1139/x04-141

Stempfhuber, W., Buchholz, M., 2011. A Precise , Low-Cost Rtk Gnss System for Uav Applications. *UAV-g* 2011 XXXVIII, 289–293. doi:10.5194/isprsarchives-XXXVIII-1-C22-289-2011

Stow, D., Nichol, C.J., Wade, T., Assmann, J.J., Simpson, G., Helfter, C., 2019. Illumination Geometry and Flying Height Influence Surface Reflectance and NDVI Derived from Multispectral UAS Imagery. *Drones* 3, 55. doi:10.3390/drones3030055

Suomalainen, J., Hakala, T., de Oliveira, R.A., Markelin, L., Viljanen, N., Näsi, R., Honkavaara, E., 2018. A novel tilt correction technique for irradiance sensors and spectrometers on-board unmanned aerial vehicles. *Remote Sens.* 10, 1–18. doi:10.3390/rs10122068

Tagesson, T., Schurgers, G., Horion, S., Ciais, P., Tian, F., Brandt, M., Ahlström, A., Wigneron, J.P., Ardö, J., Olin, S., Fan, L., Wu, Z., Fensholt,

R., 2020. Recent divergence in the contributions of tropical and boreal forests to the terrestrial carbon sink. *Nat. Ecol. Evol.* 4, 202–209.
doi:10.1038/s41559-019-1090-0

Takala, T.L.H., Mõttus, M., 2016. Spatial variation of canopy PRI with shadow fraction caused by leaf-level irradiation conditions. *Remote Sens. Environ.* 182, 99–112. doi:10.1016/j.rse.2016.04.028

Thenkabail, P.S., Stucky, N., Griscom, B.W., Ashton, M.S., Diels, J., Van der Meer, B., Enclona, E., 2004. Biomass estimations and carbon stock calculations in the oil palm plantations of African derived savannas using IKONOS data. *Int. J. Remote Sens.* 25, 5447–5472.
doi:10.1080/01431160412331291279

Thiel, C., Schmullius, C., 2017. Comparison of UAV photograph-based and airborne lidar-based point clouds over forest from a forestry application perspective. *Int. J. Remote Sens.* 38, 2411–2426.
doi:10.1080/01431161.2016.1225181

Thimonier, A., Sedivy, I., Schleppi, P., 2010. Estimating leaf area index in different types of mature forest stands in Switzerland: A comparison of methods. *Eur. J. For. Res.* 129, 543–562. doi:10.1007/s10342-009-0353-8

Thome, K., Smith, N., Scott, K., 2001. Vicarious calibration of MODIS using Railroad Valley Playa, in: International Geoscience and Remote Sensing Symposium (IGARSS). IEEE, pp. 1209–1211.
doi:10.1109/igarss.2001.976794

Tian, J., Wang, L., Li, X., Gong, H., Shi, C., Zhong, R., Liu, X., 2017. Comparison of UAV and WorldView-2 imagery for mapping leaf area index of mangrove forest. *Int. J. Appl. Earth Obs. Geoinf.* 61, 22–31.
doi:10.1016/j.jag.2017.05.002

Tillack, A., Clasen, A., Kleinschmit, B., Förster, M., 2014. Estimation of the seasonal leaf area index in an alluvial forest using high-resolution satellite-based vegetation indices. *Remote Sens. Environ.* 141, 52–63.
doi:10.1016/j.rse.2013.10.018

Toda, M., Richardson, A.D., 2018. Estimation of plant area index and phenological transition dates from digital repeat photography and

radiometric approaches in a hardwood forest in the Northeastern United States. *Agric. For. Meteorol.* 249, 457–466.
doi:10.1016/j.agrformet.2017.09.004

Tomaštík, J., Mokroš, M., Surový, P., Grznárová, A., Merganič, J., 2019. UAV RTK/PPK Method—An Optimal Solution for Mapping Inaccessible Forested Areas? *Remote Sens.* 11. doi:10.3390/rs11060721

Tommaselli, A.M.G., Torres, F.M., 2016. A light-weight laser scanner for UAV applications. *Int. Arch. Photogramm. Remote Sens. Spat. Inf. Sci. - ISPRS Arch.* 2016-Janua, 711–715. doi:10.5194/isprsarchives-XLI-B1-711-2016

Tonkin, T.N., Midgley, N.G., 2016. Ground-control networks for image based surface reconstruction: An investigation of optimum survey designs using UAV derived imagery and structure-from-motion photogrammetry. *Remote Sens.* 8, 16–19. doi:10.3390/rs8090786

Torres-Sánchez, J., de Castro, A.I., Peña, J.M., Jiménez-Brenes, F.M., Arquero, O., Lovera, M., López-Granados, F., 2018. Mapping the 3D structure of almond trees using UAV acquired photogrammetric point clouds and object-based image analysis. *Biosyst. Eng.* 176, 172–184.
doi:10.1016/j.biosystemseng.2018.10.018

Torres-Sánchez, J., Peña, J.M., de Castro, A.I., López-Granados, F., 2014. Multi-temporal mapping of the vegetation fraction in early-season wheat fields using images from UAV. *Comput. Electron. Agric.* 103, 104–113.
doi:10.1016/j.compag.2014.02.009

Toulios, L., Dercas, N., Psomiadis, E., Kavvadias, A., Chanioti, M., Tsitouras, A., 2017. Unmanned Aerial Vehicle (UAV) data analysis for fertilization dose assessment, in: *Remote Sensing for Agriculture, Ecosystems, and Hydrology XIX*. SPIE, Warsaw, p. 78. doi:10.1117/12.2278152

Trimble, 2018. Geo 7 Series Datasheet.

Tu, Y.-H., Johansen, K., Phinn, S., Robson, A., 2019. Measuring Canopy Structure and Condition Using Multi-Spectral UAS Imagery in a Horticultural Environment. *Remote Sens.* 11, 1–19.
doi:10.3390/rs11030269

- Tu, Y.-H., Phinn, S., Johansen, K., Robson, A., 2018. Assessing Radiometric Correction Approaches for Multi-Spectral UAS Imagery for Horticultural Applications. *Remote Sens.* 10, 1684. doi:10.3390/rs10111684
- Tucker, C.J., 1979. Red and photographic infrared linear combinations for monitoring vegetation. *Remote Sens. Environ.* 8, 127–150. doi:10.1016/0034-4257(79)90013-0
- Tucker, C.J., Vanpraet, C.L., Sharman, M.J., Van Ittersum, G., 1985. Satellite remote sensing of total herbaceous biomass production in the senegalese sahel: 1980-1984. *Remote Sens. Environ.* 17, 233–249. doi:10.1016/0034-4257(85)90097-5
- Tulldahl, H.M., Larsson, H., 2014. Lidar on small UAV for 3D mapping 9250, 925009. doi:10.1111/12.2068448
- Turner, D., Lucieer, A., Malenovský, Z., King, D.H., Robinson, S.A., 2014a. Spatial co-registration of ultra-high resolution visible, multispectral and thermal images acquired with a micro-UAV over antarctic moss beds. *Remote Sens.* 6, 4003–4024. doi:10.3390/rs6054003
- Turner, D., Lucieer, A., Wallace, L., 2014b. Direct georeferencing of ultrahigh-resolution UAV imagery. *IEEE Trans. Geosci. Remote Sens.* 52, 2738–2745. doi:10.1109/TGRS.2013.2265295
- Turner, W., Spector, S., Gardiner, N., Fladeland, M., Sterling, E., Steininger, M., 2003. Remote sensing for biodiversity science and conservation. *Trends Ecol. Evol.* 18, 306–314. doi:10.1016/S0169-5347(03)00070-3
- Ustin, S.L., Roberts, D.A.R.A., Gamon, J.A., Green, R.O., 2004. Using Imaging Spectroscopy to Study Ecosystem Processes and Properties. *Bioscience* 54, 523–534. doi:10.1641/0006-3568(2004)054[0523:UITSTSE]2.0.CO;2
- Van der Zande, D., Stuckens, J., Verstraeten, W.W., Mereu, S., Muys, B., Coppin, P., 2011. 3D modeling of light interception in heterogeneous forest canopies using ground-based LiDAR data. *Int. J. Appl. Earth Obs. Geoinf.* 13, 792–800. doi:<https://doi.org/10.1016/j.jag.2011.05.005>
- Van Iersel, W., Straatsma, M., Addink, E., Middelkoop, H., 2018. Monitoring height and greenness of non-woody floodplain vegetation with UAV time

series. ISPRS J. Photogramm. Remote Sens. 141, 112–123.

doi:10.1016/j.isprsjprs.2018.04.011

Van Leeuwen, W.J.D., Orr, B.J., Marsh, S.E., Herrmann, S.M., 2006. Multi-sensor NDVI data continuity: Uncertainties and implications for vegetation monitoring applications. *Remote Sens. Environ.* 100, 67–81.
doi:10.1016/j.rse.2005.10.002

Vane, G., Green, R.O., Chrien, T.G., Enmark, H.T., Hansen, E.G., Porter, W.M., 1993. The airborne visible/infrared imaging spectrometer (AVIRIS). *Remote Sens. Environ.* 44, 127–143. doi:10.1016/0034-4257(93)90012-M

Vargas, J.Q., Bendig, J., Mac Arthur, A., Burkart, A., Julitta, T., Maseyk, K., Thomas, R., Siegmann, B., Rossini, M., Celesti, M., Schüttemeyer, D., Kraska, T., Muller, O., Rascher, U., 2020. Unmanned Aerial Systems (UAS)-Based Methods for Solar Induced Chlorophyll Fluorescence (SIF) Retrieval with Non-Imaging Spectrometers: State of the Art. *Remote Sens.* 12. doi:10.3390/rs12101624

Verhoef, W., 1984. Light Scattering by Leaf layers with Application to Canopy Reflectance Modeling: the SAIL Model. *Remote Sens. Environ.* 141, 125–141.

Verhoef, W., Bach, H., 2003. Simulation of hyperspectral and directional radiance images using coupled biophysical and atmospheric radiative transfer models. *Remote Sens. Environ.* 87, 23–41. doi:10.1016/S0034-4257(03)00143-3

Vicari, M.B., Pisek, J., Disney, M., 2019. New estimates of leaf angle distribution from terrestrial LiDAR: Comparison with measured and modelled estimates from nine broadleaf tree species. *Agric. For. Meteorol.* 264, 322–333. doi:<https://doi.org/10.1016/j.agrformet.2018.10.021>

Vilhar, U., Beuker, E., Mizunuma, T., Skudnik, M., Lebourgeois, F., Soudani, K., Wilkinson, M., 2013. Tree Phenology, in: Ferretti, M., Fischer, R. (Eds.), *Developments in Environmental Science*. Elsevier, pp. 169–182.
doi:10.1016/B978-0-08-098222-9.00009-1

Vitasse, Y., Bresson, C.C., Kremer, A., Michalet, R., Delzon, S., 2010. Quantifying phenological plasticity to temperature in two temperate tree

species. *Funct. Ecol.* 24, 1211–1218. doi:10.1111/j.1365-2435.2010.01748.x

Von Bueren, S.K., Burkart, A., Hueni, A., Rascher, U., Tuohy, M.P., Yule, I.J., 2015. Deploying four optical UAV-based sensors over grassland: Challenges and limitations. *Biogeosciences* 12, 163–175. doi:10.5194/bg-12-163-2015

Wagner, F.H., Ferreira, M.P., Sanchez, A., Hirye, M.C.M., Zortea, M., Gloor, E., Phillips, O.L., de Souza Filho, C.R., Shimabukuro, Y.E., Aragão, L.E.O.C., 2018. Individual tree crown delineation in a highly diverse tropical forest using very high resolution satellite images. *ISPRS J. Photogramm. Remote Sens.* 145, 362–377. doi:10.1016/j.isprsjprs.2018.09.013

Wagner, W., Ullrich, A., Ducic, V., Melzer, T., Studnicka, N., 2006. Gaussian decomposition and calibration of a novel small-footprint full-waveform digitising airborne laser scanner. *ISPRS J. Photogramm. Remote Sens.* 60, 100–112. doi:10.1016/j.isprsjprs.2005.12.001

Walker, A.P., Zaehle, S., Medlyn, B.E., De Kauwe, M.G., Asao, S., Hickler, T., Parton, W., Ricciuto, D.M., Wang, Y.-P., Wårlid, D., Norby, R.J., 2015. Predicting long-term carbon sequestration in response to CO₂ enrichment: How and why do current ecosystem models differ? *Global Biogeochem. Cycles* 29, 476–495. doi:10.1002/2014GB004995

Walker, J.J., De Beurs, K.M., Wynne, R.H., Gao, F., 2012. Evaluation of Landsat and MODIS data fusion products for analysis of dryland forest phenology. *Remote Sens. Environ.* 117, 381–393. doi:10.1016/j.rse.2011.10.014

Wallace, L., Lucieer, A., Malenovský, Z., Turner, D., Vopěnka, P., 2016. Assessment of forest structure using two UAV techniques: A comparison of airborne laser scanning and structure from motion (SfM) point clouds. *Forests* 7, 1–16. doi:10.3390/f7030062

Wallace, L., Lucieer, A., Watson, C., Turner, D., 2012. Development of a UAV-LiDAR system with application to forest inventory. *Remote Sens.* 4, 1519–1543. doi:10.3390/rs4061519

Wallace, L., Lucieer, A., Watson, C.S., 2014. Evaluating tree detection and

- segmentation routines on very high resolution UAV LiDAR data. *IEEE Trans. Geosci. Remote Sens.* 52, 7619–7628. doi:10.1109/TGRS.2014.2315649
- Wang, C., Myint, S.W., 2015. A Simplified Empirical Line Method of Radiometric Calibration for Small Unmanned Aircraft Systems-Based Remote Sensing. *IEEE J. Sel. Top. Appl. Earth Obs. Remote Sens.* 8, 1876–1885. doi:10.1109/JSTARS.2015.2422716
- Wang, D., Wan, B., Liu, J., Su, Y., Guo, Q., Qiu, P., Wu, X., 2020. Estimating aboveground biomass of the mangrove forests on northeast Hainan Island in China using an upscaling method from field plots, UAV-LiDAR data and Sentinel-2 imagery. *Int. J. Appl. Earth Obs. Geoinf.* 85, 101986. doi:10.1016/j.jag.2019.101986
- Wang, Q., Adiku, S., Tenhunen, J., Granier, A., 2005. On the relationship of NDVI with leaf area index in a deciduous forest site. *Remote Sens. Environ.* 94, 244–255. doi:10.1016/j.rse.2004.10.006
- Wang, S., Garcia, M., Ibrom, A., Bauer-gottwein, P., 2019. Temporal interpolation of land surface fluxes derived from remote sensing - results with an Unmanned Aerial System. *Hydrol. Earth Syst. Sci.*
- Wang, Z., Skidmore, A.K., Darvishzadeh, R., Wang, T., 2018. Mapping forest canopy nitrogen content by inversion of coupled leaf-canopy radiative transfer models from airborne hyperspectral imagery. *Agric. For. Meteorol.* 253–254, 247–260. doi:<https://doi.org/10.1016/j.agrformet.2018.02.010>
- Welles, J.M., Cohen, S., 1996. Canopy structure measurement by gap fraction analysis using commercial instrumentation. *J. Exp. Bot.* 47, 1335–1342. doi:10.1093/jxb/47.9.1335
- Westoby, M.J., Brasington, J., Glasser, N.F., Hambrey, M.J., Reynolds, J.M., 2012. “Structure-from-Motion” photogrammetry: A low-cost, effective tool for geoscience applications. *Geomorphology* 179, 300–314. doi:10.1016/j.geomorph.2012.08.021
- White, K., Pontius, J., Schaberg, P., 2014. Remote sensing of spring phenology in northeastern forests: A comparison of methods, field metrics and sources of uncertainty. *Remote Sens. Environ.* 148, 97–107. doi:<https://doi.org/10.1016/j.rse.2014.03.017>

- Wilke, N., Siegmann, B., Klingbeil, L., Burkart, A., Kraska, T., Muller, O., van Doorn, A., Heinemann, S., Rascher, U., 2019. Quantifying Lodging Percentage and Lodging Severity Using a UAV-Based Canopy Height Model Combined with an Objective Threshold Approach. *Remote Sens.* 11. doi:10.3390/rs11050515
- Wong, C.Y.S., D'Odorico, P., Bhathena, Y., Arain, M.A., Ensminger, I., 2019. Carotenoid based vegetation indices for accurate monitoring of the phenology of photosynthesis at the leaf-scale in deciduous and evergreen trees. *Remote Sens. Environ.* 233, 111407. doi:10.1016/j.rse.2019.111407
- Xiao, J., Chevallier, F., Gomez, C., Guanter, L., Hicke, J.A., Huete, A.R., Ichii, K., Ni, W., Pang, Y., Rahman, A.F., Sun, G., Yuan, W., Zhang, L., Zhang, X., 2019. Remote sensing of the terrestrial carbon cycle: A review of advances over 50 years. *Remote Sens. Environ.* 233, 111383. doi:10.1016/j.rse.2019.111383
- Xiao, X., Zhang, Q., Braswell, B., Urbanski, S., Boles, S., Wofsy, S., Moore, B., Ojima, D., 2004. Modeling gross primary production of temperate deciduous broadleaf forest using satellite images and climate data. *Remote Sens. Environ.* 91, 256–270. doi:10.1016/j.rse.2004.03.010
- Xie, X., Li, A., Jin, H., Tan, J., Wang, C., Lei, G., Zhang, Z., Bian, J., Nan, X., 2019. Assessment of five satellite-derived LAI datasets for GPP estimations through ecosystem models. *Sci. Total Environ.* 690, 1120–1130. doi:<https://doi.org/10.1016/j.scitotenv.2019.06.516>
- Xu, Z., Shen, X., Cao, L., Coops, N.C., Goodbody, T.R.H., Zhong, T., Zhao, W., Sun, Q., Ba, S., Zhang, Z., Wu, X., 2020. Tree species classification using UAS-based digital aerial photogrammetry point clouds and multispectral imageries in subtropical natural forests. *Int. J. Appl. Earth Obs. Geoinf.* 92, 102173. doi:10.1016/J.JAG.2020.102173
- Yan, G., Hu, R., Luo, J., Weiss, M., Jiang, H., Mu, X., Xie, D., Zhang, W., 2019. Review of indirect optical measurements of leaf area index: Recent advances, challenges, and perspectives. *Agric. For. Meteorol.* 265, 390–411. doi:10.1016/j.agrformet.2018.11.033
- Yang, G., Liu, J., Zhao, C., Li, Zhenhong, Huang, Y., Yu, H., Xu, B., Yang, X.,

Zhu, D., Zhang, X., Zhang, R., Feng, H., Zhao, X., Li, Zhenhai, Li, H., Yang, H., 2017. Unmanned Aerial Vehicle Remote Sensing for Field-Based Crop Phenotyping: Current Status and Perspectives. *Front. Plant Sci.* 8, 1111. doi:10.3389/fpls.2017.01111

Yang, H., Ciais, P., Santoro, M., Huang, Y., Li, W., Wang, Y., Bastos, A., Goll, D., Arneth, A., Anthoni, P., Arora, V.K., Friedlingstein, P., Harverd, V., Joetzjer, E., Kautz, M., Lienert, S., Nabel, J.E.M.S., Sullivan, M.O., Sitch, S., Vuichard, N., Wiltshire, A., Zhu, D., 2020. Comparison of forest above-ground biomass from dynamic global vegetation models with spatially explicit remotely sensed observation-based estimates. *Glob. Chang. Biol.* 26, 3997–4012. doi:10.1111/gcb.15117

Yao, H., Qin, R., Chen, X., 2019. Unmanned Aerial Vehicle for Remote Sensing Applications—A Review. *Remote Sens.* . doi:10.3390/rs11121443

Yao, X., Wang, N., Liu, Y., Cheng, T., Tian, Y., Chen, Q., Zhu, Y., 2017. Estimation of wheat LAI at middle to high levels using unmanned aerial vehicle narrowband multispectral imagery. *Remote Sens.* 9. doi:10.3390/rs9121304

Yue, J., Yang, G., Tian, Q., Feng, H., Xu, K., Zhou, C., 2019. Estimate of winter-wheat above-ground biomass based on UAV ultrahigh-ground-resolution image textures and vegetation indices. *ISPRS J. Photogramm. Remote Sens.* 150, 226–244. doi:<https://doi.org/10.1016/j.isprsjprs.2019.02.022>

Zandler, H., Brenning, A., Samimi, C., 2015. Quantifying dwarf shrub biomass in an arid environment: Comparing empirical methods in a high dimensional setting. *Remote Sens. Environ.* 158, 140–155. doi:10.1016/j.rse.2014.11.007

Zarco-Tejada, P.J., Diaz-Varela, R., Angileri, V., Loudjani, P., 2014. Tree height quantification using very high resolution imagery acquired from an unmanned aerial vehicle (UAV) and automatic 3D photo-reconstruction methods. *Eur. J. Agron.* 55, 89–99. doi:10.1016/j.eja.2014.01.004

Zarco-Tejada, P.J., Morales, A., Testi, L., Villalobos, F.J., 2013. Spatio-temporal patterns of chlorophyll fluorescence and physiological and structural indices acquired from hyperspectral imagery as compared with carbon fluxes

measured with eddy covariance. *Remote Sens. Environ.* 133, 102–115.
doi:10.1016/j.rse.2013.02.003

Zellweger, F., De Frenne, P., Lenoir, J., Rocchini, D., Coomes, D., 2019.
Advances in Microclimate Ecology Arising from Remote Sensing. Trends Ecol. Evol. 34, 327–341. doi:10.1016/j.tree.2018.12.012

Zeng, K., Zheng, G., Ma, L., Ju, W., Pang, Y., 2019. Modelling three-dimensional spatiotemporal distributions of forest photosynthetically active radiation using UAV-Based lidar data. *Remote Sens.* 11.
doi:10.3390/rs11232806

Zhang, C., Kovacs, J.M., 2012. The application of small unmanned aerial systems for precision agriculture: A review. *Precis. Agric.* 13, 693–712.
doi:10.1007/s11119-012-9274-5

Zhang, H., Aldana-Jague, E., Clapuyt, F., Wilken, F., Vanacker, V., Van Oost, K., 2019. Evaluating the potential of post-processing kinematic (PPK) georeferencing for UAV-based structure-from-motion (SfM) photogrammetry and surface change detection. *Earth Surf. Dyn.* 7, 807–827. doi:10.5194/esurf-7-807-2019

Zhang, K., Chen, S.C., Whitman, D., Shyu, M.L., Yan, J., Zhang, C., 2003. A progressive morphological filter for removing nonground measurements from airborne LIDAR data. *IEEE Trans. Geosci. Remote Sens.* 41, 872–882. doi:10.1109/TGRS.2003.810682

Zhang, X., Friedl, M.A., Schaaf, C.B., Strahler, A.H., Hodges, J.C.F., Gao, F., Reed, B.C., Huete, A., 2003. Monitoring vegetation phenology using MODIS. *Remote Sens. Environ.* 84, 471–475. doi:10.1016/S0034-4257(02)00135-9

Zhang, Y., Kong, D., Gan, R., Chiew, F.H.S., McVicar, T.R., Zhang, Q., Yang, Y., 2019. Coupled estimation of 500 m and 8-day resolution global evapotranspiration and gross primary production in 2002–2017. *Remote Sens. Environ.* 222, 165–182. doi:10.1016/j.rse.2018.12.031

Zhang, Y., Liang, S., 2020. Fusion of Multiple Gridded Biomass Datasets for Generating a Global Forest Aboveground Biomass Map. *Remote Sens.* 12.
doi:10.3390/rs12162559

- Zhao, K., Popescu, S., Nelson, R., 2009. Lidar remote sensing of forest biomass: A scale-invariant estimation approach using airborne lasers. *Remote Sens. Environ.* 113, 182–196. doi:10.1016/j.rse.2008.09.009
- Zhao, K., Ryu, Y., Hu, T., Garcia, M., Li, Y., Liu, Z., Londo, A., Wang, C., 2019. How to better estimate leaf area index and leaf angle distribution from digital hemispherical photography? Switching to a binary nonlinear regression paradigm. *Methods Ecol. Evol.* 10, 1864–1874. doi:10.1111/2041-210X.13273
- Zheng, G., Moskal, L.M., 2009. Retrieving Leaf Area Index (LAI) Using Remote Sensing: Theories, Methods and Sensors. *Sensors* 9. doi:10.3390/s90402719
- Zhong, Y., Wang, X., Xu, Y., Wang, S., Jia, T., Hu, X., Zhao, J., Wei, L., Zhang, L., 2018. Mini-UAV-Borne Hyperspectral Remote Sensing: From Observation and Processing to Applications. *IEEE Geosci. Remote Sens. Mag.* 6, 46–62. doi:10.1109/MGRS.2018.2867592
- Zhu, W., Sun, Z., Huang, Y., Lai, J., Li, J., Zhang, J., Yang, B., Li, B., Li, S., Zhu, K., Li, Y., Liao, X., 2019. Improving Field-Scale Wheat LAI Retrieval Based on UAV Remote-Sensing Observations and Optimized VI-LUTs. *Remote Sens.* 11. doi:10.3390/rs11202456
- Zhu, X., Liu, D., 2015. Improving forest aboveground biomass estimation using seasonal Landsat NDVI time-series. *ISPRS J. Photogramm. Remote Sens.* 102, 222–231. doi:10.1016/j.isprsjprs.2014.08.014

11 Appendices

A1 Supplementary information for chapter 4

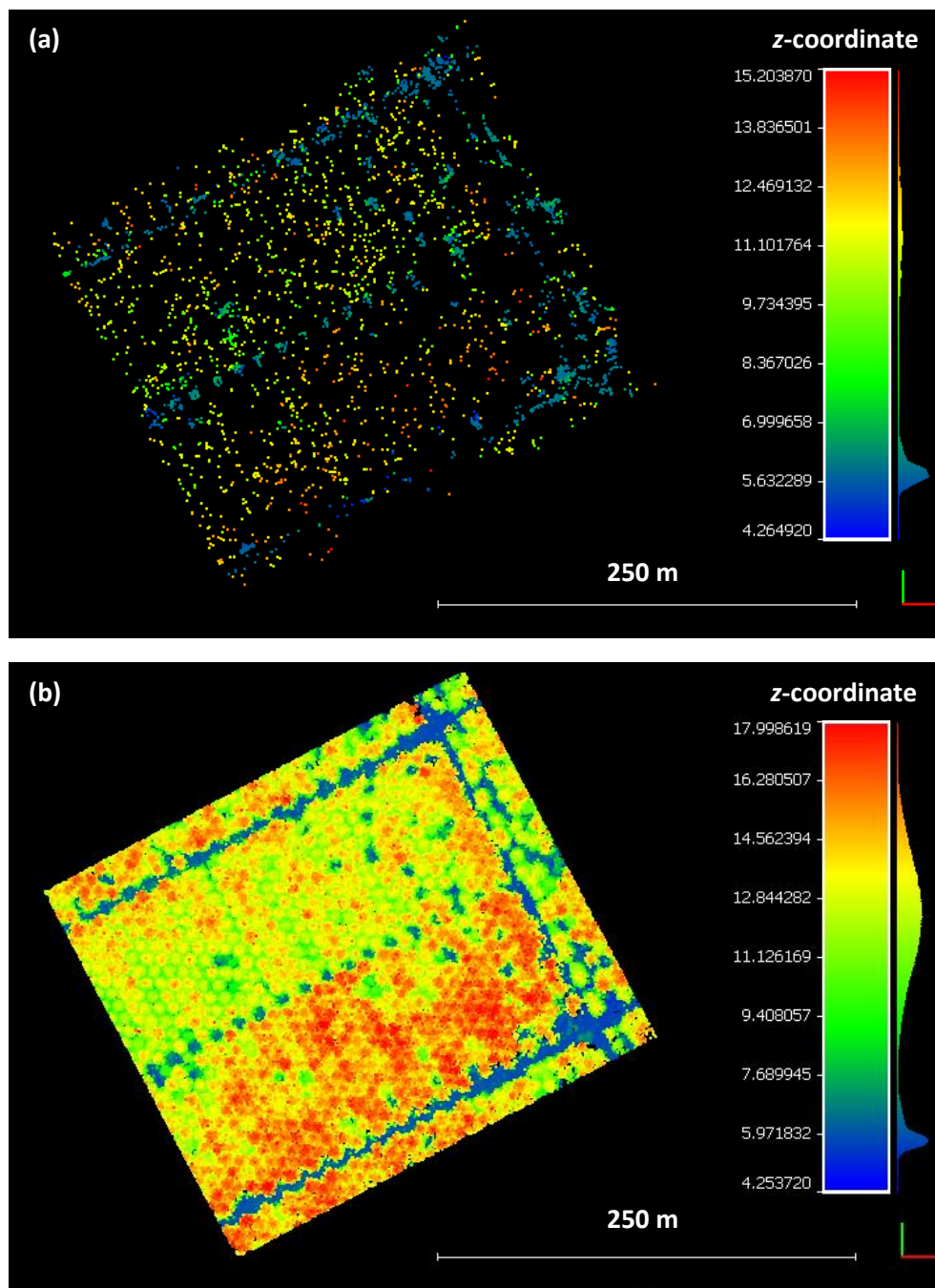


Figure A 1: Sparse point cloud tie points resulting from Photoscan processing for LO_10yr (a) and HO1_10yr (b).

Agisoft Metashape settings and processing information

The following software information and processing settings were identical for all reconstructions presented in chapter 4.

Software

Version: 1.4.2 build 6205
Platform: Windows 64

Alignment parameters

Accuracy: High
Generic preselection: Yes
Reference preselection: Yes
Key point limit: 80,000
Tie point limit: 8,000
Adaptive camera model fitting: Yes

Reconstruction parameters

Quality: High
Depth filtering: Disabled

A2 Supplementary information for chapter 5

In order to investigate the sensitivity of the Sequoia derivable indices NDVI and CHL to the variables of interest as well as the effect of band position differences and its implications for the comparability of Sequoia and S2 derived products in isolation of other influencing factors (e.g., differences due to atmospheric correction, Sequoia data calibration and viewing geometry), a range of vegetation reflectance spectra were simulated using the PROSAIL model which couples the leaf reflectance model PROSPECT with the canopy geometry model SAIL (Jacquemoud et al., 2009). All parameters besides the LAI and Chlorophyll a+b content were fixed following (Atzberger and Richter, 2012) to values typical for maize, though they do acknowledge that the model is not ideally suited for simulating the geometric properties of a row crop.

The simulations were also used to evaluate the uncertainty due to the HyPlant band spacing when resampled to Sequoia spectral bands.

For the first series, LAI was varied between values of 1 and 10 m²/ m² (10 steps) while Chlorophyll a+b content was set to 50 µg/cm². For the second series, LAI was kept constant at a value of 3 while Chlorophyll a+b content was varied between 0 and 100 µg/cm² (10 steps).

Results revealed that for varying LAI, NDVI values derived from Sequoia bands should match those from the equivalent S2 bands despite SRF differences. CHL values on the other hand were found, via PROSAIL, to be not directly comparable due to slight band position differences (Figure A1).

Mean estimated errors due to the HyPlant spectral sampling interval for all bands were very small across a variation of LAI and chlorophyll content values (Table A1).

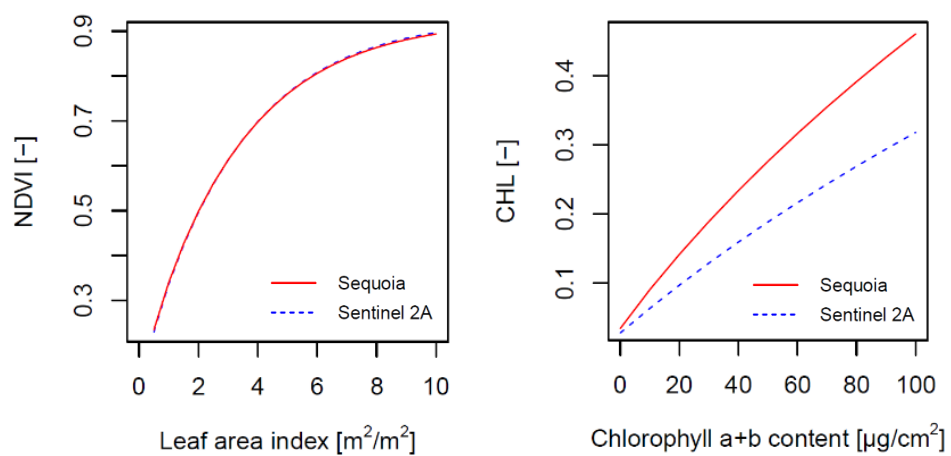


Figure A 2: Simulated Sequoia and Sentinel 2A derived NDVI and CHL values for simulations of varying LAI and Chlorophyll a + b content respectively.

Table A 1: Simulated Sequoia and Sentinel 2A derived NDVI and CHL values for simulations of varying LAI and Chlorophyll a + b content respectively.

MAD between Sequoia Band Resampled Values and HyPlant to Sequoia Band Resampled Values.	LAI Series (0.5–10)	Chlorophyll Content Series (0–100 $\mu\text{g}/\text{cm}^2$)
Green	0.0002	0.0001
Red	5.2631×10^{-6}	1.6583×10^{-6}
Red edge	0.0001	6.4832×10^{-5}
NIR	5.7975×10^{-5}	2.0239×10^{-5}

A3 Supplementary information for chapter 6

Table A 2: Sampling date and illumination conditions for each drone acquisition of the study site, along with the panel reflected pseudo-radiance (homogenous to actual radiance, (Parrot, 2017) measured by the Parrot Sequoia in the red and NIR band as well as their ratio which indicates wavelength-specific differences in reflected radiance.

Sampling Date	Illumination condition	Panel red pseudo-radiance	Panel NIR pseudo-radiance	Red/NIR ratio
22.03.2019	Diffuse	6.840354	5.346008	1.279526
24.03.2019	Direct	28.17773	16.57323	1.700195
31.03.2019	Direct	25.20113	15.25855	1.651608
01.04.2019	Diffuse	7.310436	5.307056	1.377494
07.04.2019	Diffuse	7.862407	5.398735	1.456342
10.04.2019	Direct	26.40424	16.00822	1.649418
19.04.2019	Direct	26.14368	15.25292	1.714011
23.04.2019	Direct	28.62107	17.38891	1.645938
28.04.2019	Diffuse	9.597564	7.238315	1.325939
19.05.2019	Diffuse	9.400095	7.217701	1.302367
21.05.2019	Direct	33.41043	19.90472	1.678518
01.06.2019	Diffuse	13.70269	9.399796	1.457765
06.06.2019	Direct	43.58222	27.21291	1.601528
12.06.2019	Diffuse	3.467557	3.224286	1.07545
04.07.2019	Direct	33.52088	19.8	1.692974
21.06.2019	Direct	34.5928	19.73772	1.752624
11.07.2019	Diffuse	14.87469	9.631458	1.544386
16.07.2019	Direct	30.56373	17.10692	1.786629
22.07.2019	Diffuse	11.49727	7.409198	1.551757
23.07.2019	Direct	32.64224	18.07462	1.805971

Table A 3: Per-class mean of the RSE of the logistic model fits to the NDVI time series for each individual deciduous crown.

Species	Mean RSE (20% brightest pixels method)	Mean RSE (mean of all crown pixels method)
Hawthorn (<i>Crataegus monogyna</i>)	0.0191	0.0126
Oak (<i>Quercus</i> spp.)	0.0178	0.0154
Goat Willow (<i>Salix caprea</i>)	0.0174	0.0146
Grey Willow (<i>Salix cinerea</i>)	0.0154	0.0128
Elm (<i>Ulmus</i> spp.)	0.0304	0.0147
Sycamore (<i>Acer pseudoplatanus</i>)	0.0185	0.0138
Sweet Chestnut (<i>Castanea sativa</i>)	0.0179	0.0138
Lime (<i>Tilia</i> spp.)	0.0140	0.011
Alder (<i>Alnus glutinosa</i>)	0.0152	0.0141
Beech (<i>Fagus sylvatica</i>)	0.0195	0.016
Ash (<i>Fraxinus excelsior</i>)	0.0257	0.0198
Apple (<i>Malus domestica</i>)	0.0237	0.0181
Elder (<i>Sambucus nigra</i>)	0.0331	0.0157

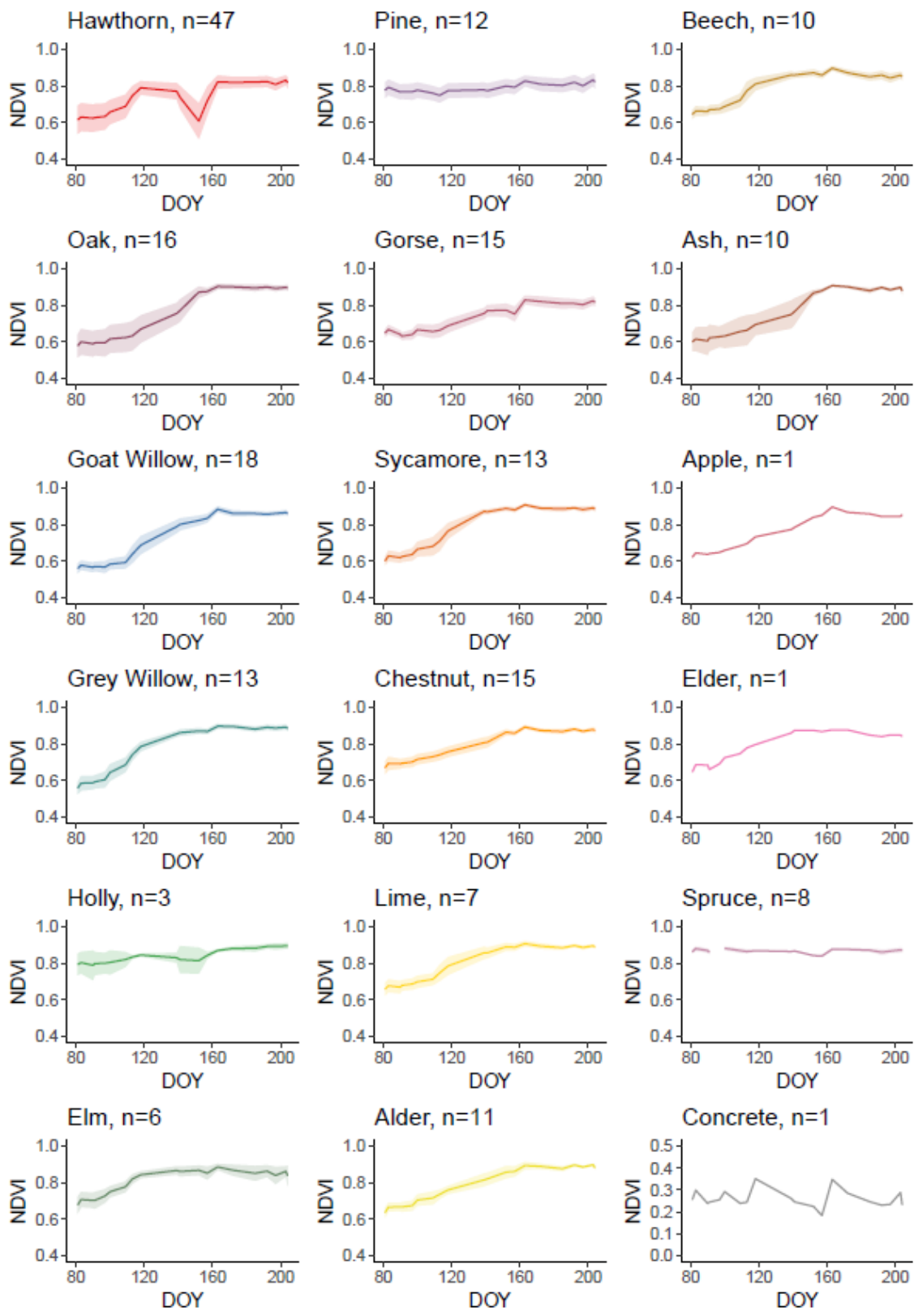


Figure A 3: Spring time-series of NDVI per species from 20 drone acquisitions, using the mean of all crown pixels (no brightest pixel extraction step as opposed to Figure 6-6 of the study). Lines represent the means, ribbons the standard deviation of all individual canopy NDVI means. Species names and number of individuals (n) are also reported.

PAI retrieval for single crowns

This information has been incorporated into the thesis methods section 3.4.1.2: Leaf and plant area index.

PAI/NDVI progression at individual and small stand level

The progression of NDVI and PAI at individual and small stand level is shown in Figure A 4. The four oak crowns (A-D) exhibit later increase in NDVI as well as PAI when compared to hawthorn (E-F), which show an earlier green-up for both metrics. The large dip in hawthorn NDVI post green-up (4 observations) was omitted here to enable the logistic fit. For grey willow (G-H) there were some discrepancies of NDVI increase with very slow PAI increase. This may be related to slow leaf extension up to canopy closure which was observed in the field, while the NDVI shows a rapid increase related to flowering with green catkins and/or initial leaf emergence. Due to a lack of multiple PAI observations prior to green-up, the fitted function for E and I was poorly constrained and omitted. For all cases where the logistic function could be fitted, the SOS derived from PAI observations was later than the corresponding SOS from NDVI observations.

While images were only captured under diffuse irradiance conditions, variability in PAI post green-up as is visible particularly for E, F, G and J is likely due to remaining uncertainties in adjusting image exposure to varying diffuse illumination and some gaps in cloud-cover.

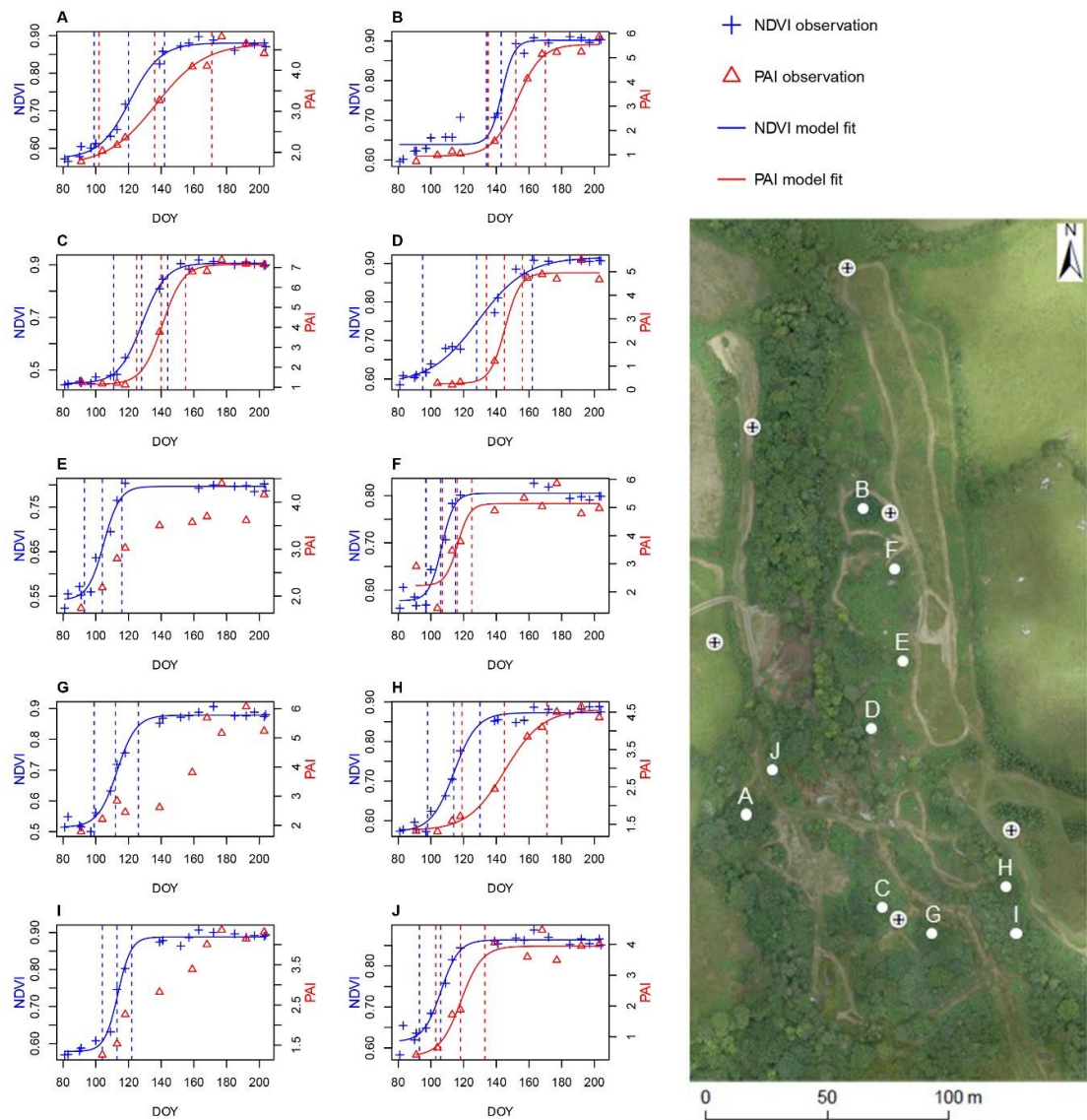


Figure A 4: Temporal progression (DOY) of drone measured NDVI values (20 dates) and PAI values derived from hemispherical photography (9-10 dates) including fitted logistic functions and identified SOS, MOG and SOP (vertical dashed lines from left to right), across the 2019 period of spring green-up for 10 locations across the study site. A-D: oak (*Quercus spp.*), E-F: hawthorn (*Crataegus monogyna*), G-H: grey willow (*Salix cinerea*), I: goat willow (*Salix caprea*), J: elm (*Ulmus spp.*). All measurements represent individual crowns except I which represents a closed stand of multiple individuals. The logistic fit to PAI values was not possible for G and omitted for E and I due to non-distinct SOS. The inset map shows the measurement locations across the study site.

SOS correspondence with budburst and first leaf observations

Citizen science (UKPN) based phenological observations of individual trees in the UK are made available on the Woodland Trust's "Nature's Calendar" platform (<https://naturescalendar.woodlandtrust.org.uk/>). The timing of budburst and emergence of the first leaf are reported for 7 of the species analysed in this study in 2019 (oak includes sessile and pedunculate oaks). "First leaf" is defined as the first unfurled leaf that is recognisable in shape. Reported dates for counties Cornwall and Devon (South West England) were extracted and compared to the medians of the drone NDVI derived SOS dates (Table A 4).

Most species showed a later median SOS date than the budburst mean with the exception of ash, where SOS corresponded very closely to budburst. The median SOS date identified for alder, ash, beech, oak and sycamore was within ± 1 standard deviation of the database mean first leaf date. Alder and ash were the only species where median SOS date was closer to the budburst than to the first leaf date. The median SOS dates of the other species were later than the first leaf mean dates. Hawthorn and elder budburst and first leaf dates had the largest standard deviation of the analysed species but the median SOS dates exceeded this range. Note that elder only had one drone based SOS observation.

Table A 4: Reported timing (DOY) for budburst and first leaf of individual trees in the South West UK from the Nature's Calendar database for Spring 2019. The number of individuals (n), mean, median and standard deviation (sd) are reported for 7 species. The median of drone NDVI derived SOS per species is compared to the Nature's Calendar budburst and first leaf mean and the difference reported (SOS minus budburst or first leaf). Where the difference is greater than ± 1 sd, the cell is shaded.

species	beech	alder	ash	oak	sycamore	hawthorn	elder
drone SOS							
median	106	89	106.5	112.5	104	100.5	88
n	9	7	10	16	12	44	1
budburst							
n	21	10	18	22	13	16	13
mean	93.38	80.6	107.61	94.36	77.08	63.81	51.69
median	92	80.5	108	92.5	76	62.5	55
sd	8.69	20.27	17.16	11.36	8.02	21.99	30.34
difference	12.62	8.4	-1.11	18.14	26.92	36.69	36.31
first leaf							
n	26	9	20	27	18	27	22
mean	104.5	103.33	115.25	101.3	95.44	71.52	61.45
median	104	108	120.5	100	92.5	76	60
sd	6.98	14.34	13.33	13.15	13.36	21.69	24.43
difference	1.5	-14.33	-8.75	11.2	8.56	28.98	26.55

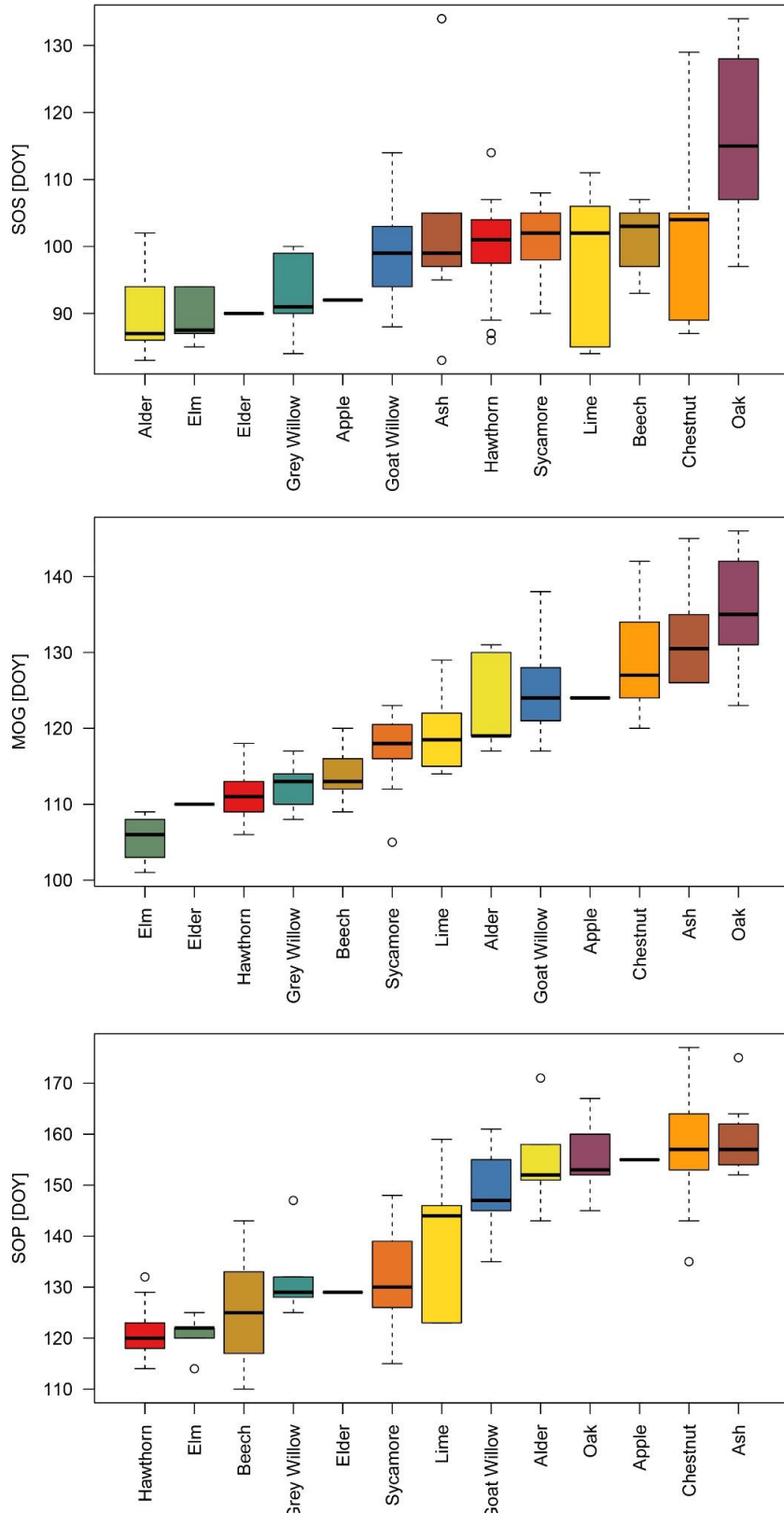


Figure A 5: Boxplots of SOS, MOG and SOP of all individual deciduous crowns grouped by species and ordered by median values. The bold line represents the median value, the lower and upper bounds of the boxes represent the 25th and 75th percentiles, the whiskers extend to the furthest values from the mean within 1.5 times the interquartile range and the circles are identified as outliers beyond this range.

Table A 5: Difference between the means of phenological metrics over all deciduous classes extracted from crown time-series using the 20% brightest pixel method and the mean of all crown pixels.

Species	SOS difference over all crowns	MOG difference over all crowns	SOP difference over all crowns
Hawthorn (<i>Crataegus monogyna</i>)	0.2	-0.1	-0.3
Oak (<i>Quercus</i> spp.)	-3.2	-2.6	-1.7
Goat Willow (<i>Salix caprea</i>)	0.1	-1.9	-4.0
Grey Willow (<i>Salix cinerea</i>)	-0.2	-0.9	-1.3
Elm (<i>Ulmus</i> spp.)	6.8	0.0	-6.7
Sycamore (<i>Acer pseudoplatanus</i>)	0.8	-0.6	-1.3
Sweet Chestnut (<i>Castanea sativa</i>)	0.6	-2.5	-5.4
Lime (<i>Tilia</i> spp.)	3.0	-1.2	-5.1
Alder (<i>Alnus glutinosa</i>)	0	-1.9	-3.7
Beech (<i>Fagus sylvatica</i>)	1.9	-1.7	-5.0
Ash (<i>Fraxinus excelsior</i>)	7	1.6	-4.0
Apple (<i>Malus domestica</i>)	2.0	4.0	6.0
Elder (<i>Sambucus nigra</i>)	-2.0	-5.0	-7.0

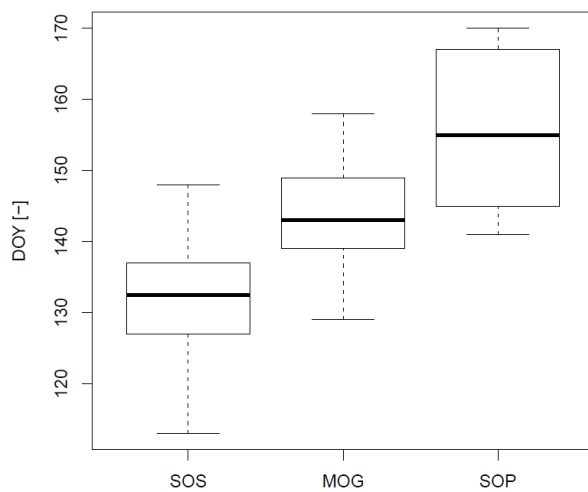


Figure A 6: Boxplots of SOS, MOG and SOP of pine crowns. The bold line represents the mean value, the lower and upper bounds of the boxes represent the 25th and 75th percentiles, the whiskers extend to the furthest values from the mean within 1.5 times the interquartile range and the circles are identified as outliers beyond this range.

A4 Supplementary information for chapter 7

SI1 Daily simulation details

Table A 6. Days for which half-hourly understory PAR and DLI were simulated, divided into SOS, MOG and SOP time periods. Includes the corresponding date of the closest drone observation, the location of the PAR loggers and summary of illumination conditions for the simulated day. ‘Mixed’ indicates variable conditions throughout the day with the predominant illumination condition specified in brackets.

Simulation date	Closest drone observation date	Tree logger location	Woodland logger location	Illumination (simulation date)
SOS				
3 April 2019	1 April 2019	Oak tree A	South	mixed (diffuse)
6 April 2019	7 April 2019	Oak tree A	South	mixed (direct)
10 April 2019	10 April 2019	Oak tree B	North	direct
12 April 2019	10 April 2019	Oak tree B	North	diffuse
16 April 2019	19 April 2019	Hawthorn tree C	Mid	mixed (diffuse)
18 April 2019	19 April 2019	Hawthorn tree C	Mid	mixed (direct)
20 April 2019	19 April 2019	Oak tree D	South	direct
24 April 2019	23 April 2019	Oak tree D	South	diffuse
MOG				
19 May 2019	19 May 2019	Oak tree B	Mid	diffuse
21 May 2019	21 May 2019	Oak tree B	Mid	direct
23 May 2019	21 May 2019	Oak tree A	South	mixed (direct)
29 May 2019	1 June 2019	Oak tree A	South	diffuse
1 June 2019	1 June 2019	Oak tree D	North	mixed (direct)
2 June 2019	1 June 2019	Oak tree D	North	diffuse

SOP				
08 July 2019	11 July 2019	Oak tree B	South	diffuse
09 July 2019	11 July 2019	Oak tree B	South	direct
12 July 2019	11 July 2019	Hawthorn tree C	North	diffuse
15 July 2019	16 July 2019	Hawthorn tree C	North	direct
21 July 2019	22 July 2019	Oak tree A	Mid	mixed (direct)
22 July 2019	22 July 2019	Oak tree A	Mid	diffuse
23 July 2019	23 July 2019	Oak tree D	South	direct
24 July 2019	23 July 2019	Oak tree D	South	diffuse

SI2 Crown ration model

The following tree height (h) based model was used instead of a constant crown ratio (CR: Crown height / tree height) as a significant relationship between CR and tree height was identified ($R^2= 0.3$, RMSE=0.12 (results in mean base height error of 0.78 m, 42.1% relative error), p-value < 0.05):

$$CR = 0.9638 - h * 0.0332 \quad (\text{Eq. A4-1})$$

SI3 Diffuse fraction model

When comparing the weather-station measured diffuse PAR fractions with $R_s(0)/R_0$ it was observed that $R_s(0)/R_0 < 0.25$ converged on a diffuse fraction of 1, a threshold identified by Hassika and Berbigier (1998). Omitting these values, as well as all readings where R_0 is below a threshold of 30 PPFD (resulting from very low solar angles at the start of the day and introducing outliers), yields a strong empirical relationship ($R^2 = 0.84$, see Figure A 7) and we can therefore utilise the modified function (Eq. 7-2) for diffuse fraction ($R_d(0)/R_s(0)$) based on local conditions.

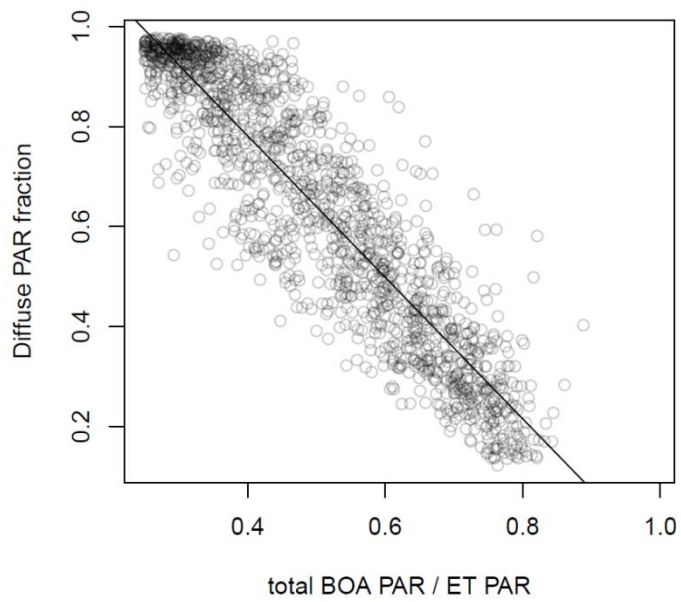


Figure A 7: Relationship between average hourly diffuse PAR fraction and the ratio of total PAR at BOA and modelled ET PAR.

SI4 Manual crown identification

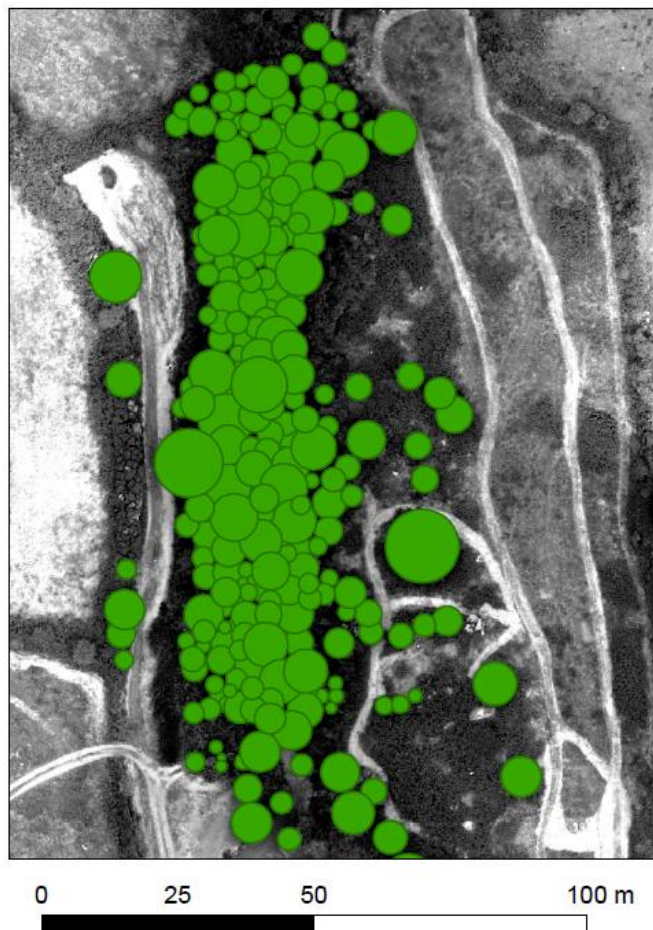


Figure A 8: Crown locations and diameters manually identified from drone RGB orthomosaics. Low vegetation without clearly distinguishable crowns was omitted. The circular representation is consistent with the implementation in DART.

SI5 Vegetation indices and PAI relationships

Table A 7: Formulas for the calculation of the five assessed VIs from Parrot Sequoia surface reflectance bands as well as references to studies using or developing these indices.

VI formula	Reference
$NDVI = \frac{\rho_{NIR} - \rho_{red}}{\rho_{NIR} + \rho_{red}}$ (eq. A4-2)	(Tucker, 1979).
$NDRE = \frac{\rho_{NIR} - \rho_{r.edge}}{\rho_{NIR} + \rho_{r.edge}}$ (eq. A4-3)	(Gitelson and Merzlyak, 1994)
$NDRI = \frac{\rho_{r.edge} - \rho_{red}}{\rho_{r.edge} + \rho_{red}}$ (eq. A4-4)	(Delegido et al., 2013)
$MSAVI2 = \rho_{NIR} + 0.5 - \sqrt{(\rho_{NIR} + 0.5)^2 - 2 \times (\rho_{NIR} - \rho_{red})}$ (eq. A4-5)	(Heiskanen, 2006; Qi et al., 1994)
$MTVI2 = 1.5 \times \frac{(1.2 \times (\rho_{NIR} - \rho_{green})) - 2.5 \times (\rho_{red} - \rho_{green})}{(2 \times (\rho_{NIR} + 1)^2 - (6 \times \rho_{NIR} - 5 \times \rho_{red})^{0.5} - 0.5)^{0.5}}$ (eq. A4-6)	(Haboudane et al., 2004; Yao et al., 2017)

Table A 8: Coefficient of determination R2 and RMSE from LOOCV for the OLS and nonlinear (exponential) regression models of PAI against five vegetation indices for sampled trees/plots. For nonlinear models only RMSE is reported due to a potentially misleading R2 metric.

OLS	NDVI	NDRE	RREGind	MSAVI	MTVI
Class means (R2)	0.689249	0.42088	0.688644	0.736716	0.668164
Class means (LOOCV RMSE)	0.796545	1.077188	0.793579	0.728403	0.816771
All (R2)	0.571567	0.413854	0.576949	0.659858	0.601506
All (LOOCV RMSE)	1.124901	1.309754	1.116839	0.99918	1.080534
NLS	NDVI	NDRE	RREGind	MSAVI	MTVI
Class means (LOOCV RMSE)	0.668045	NA	0.709454	0.718015	0.826937
All (LOOCV RMSE)	0.885335	NA	0.96672	0.948822	1.056707

SI6 PAI retrieval for single crowns

This information has been incorporated into the thesis methods section 3.4.1.2: Leaf and plant area index.

SI7 Impact of illumination conditions on PAI estimation

a)

b)

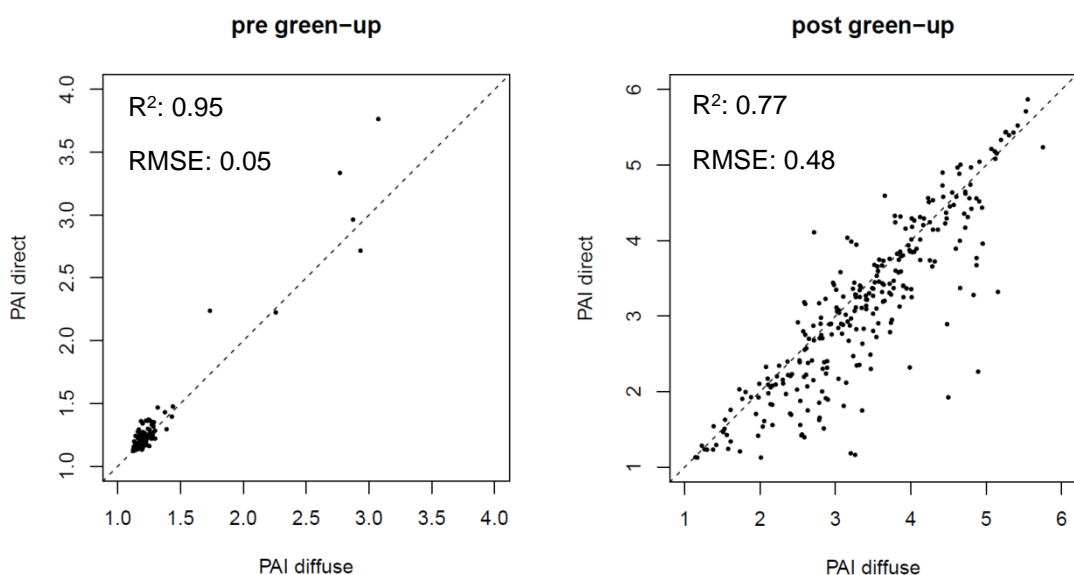
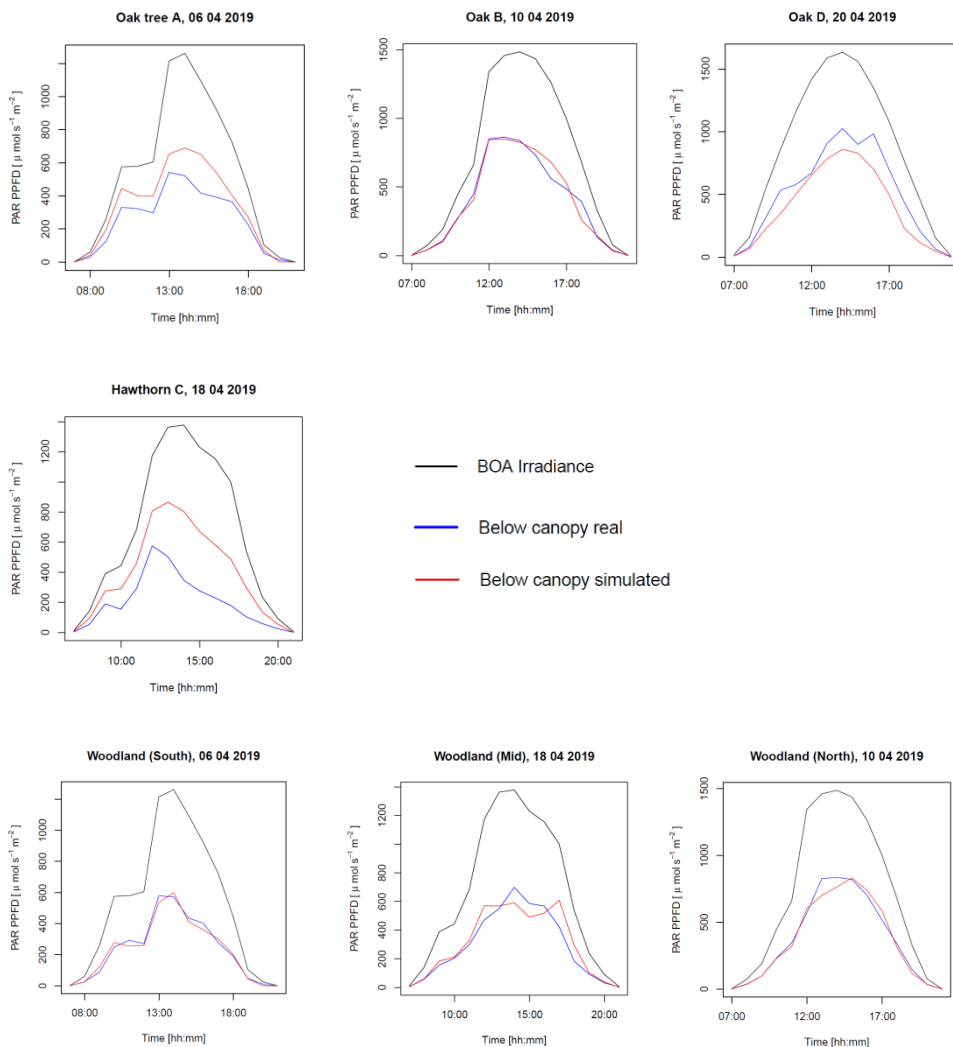


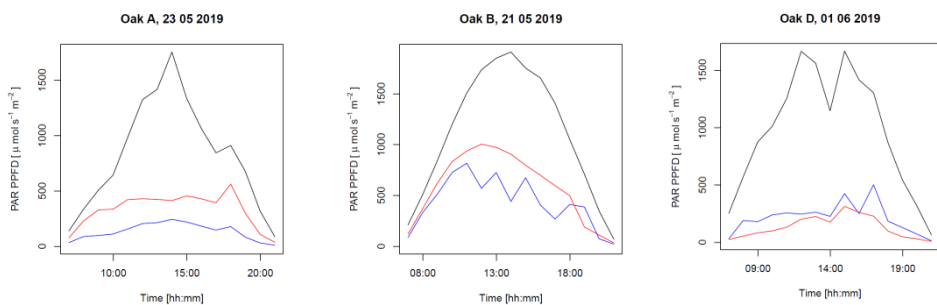
Figure A 9: Comparison of replicated PAI estimates from drone NDVI orthomosaics acquired during direct and diffuse irradiance conditions a) pre overstory green-up (31 March and 1 April) and b) post overstory green-up (22 July and 23 July).

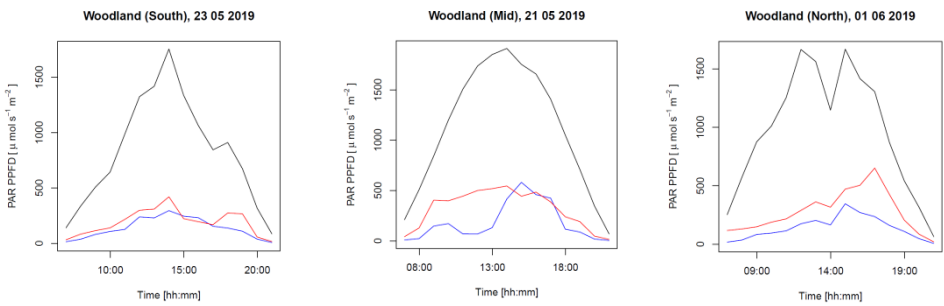
SI8 Hourly PAR simulations

Pre green-up



Mid green-up





Post green-up

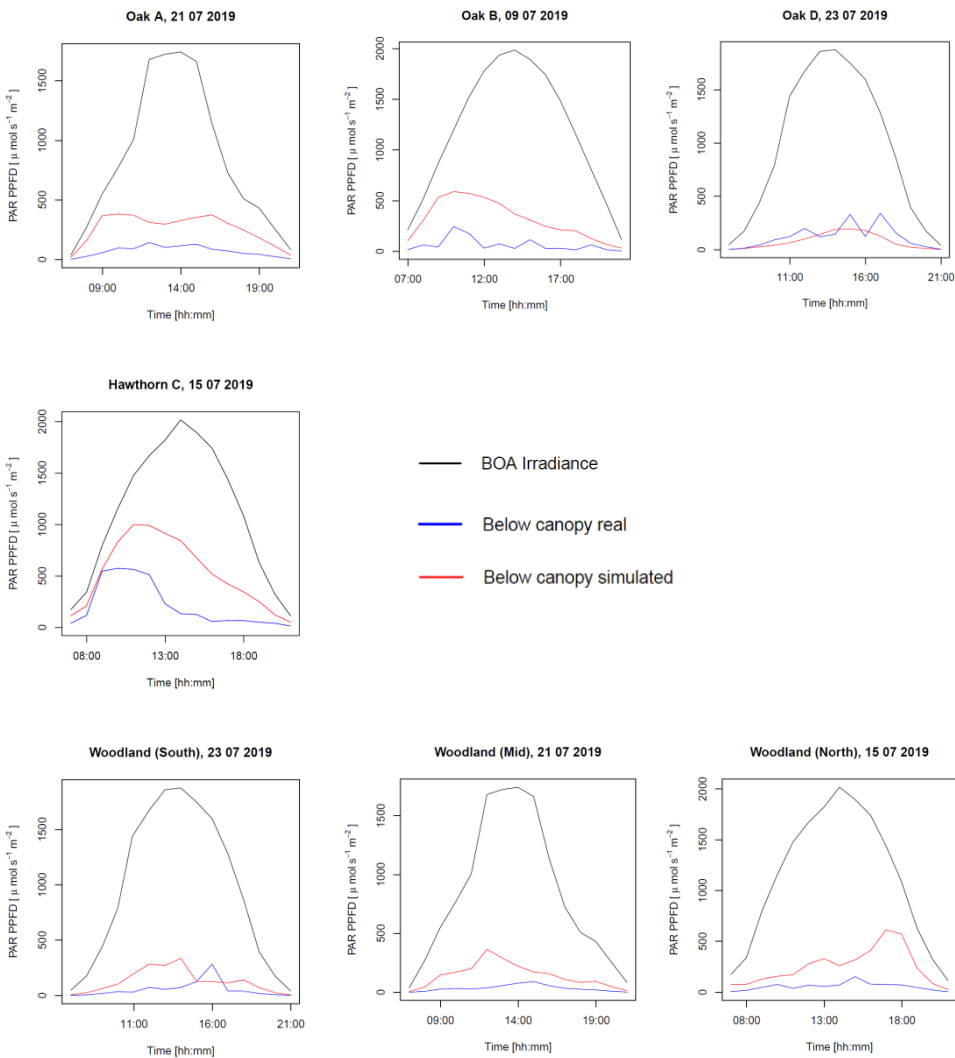


Figure A 10: Graphs of hourly BOA PAR (black), simulated understory PAR (red) and true understory PAR (blue) for individual days pre- mid and post overstory green-up (leaf emergence to full expansion) and all measured locations below single trees and within the woodland. No results are presented for Hawthorn mid green-up due to flowering induced noise.

SI9 PAR transmittance as function of PAI

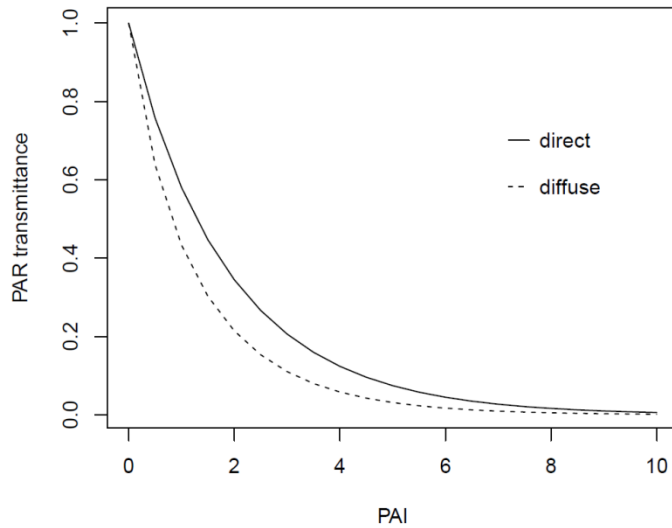


Figure A 11: Sensitivity analysis for DART simulations of direct and diffuse irradiance (sun at nadir) showing the relationship of the PAR fraction reaching the ground underneath a vegetated layer of given PAI.

SI10 Impact of leaf optical properties

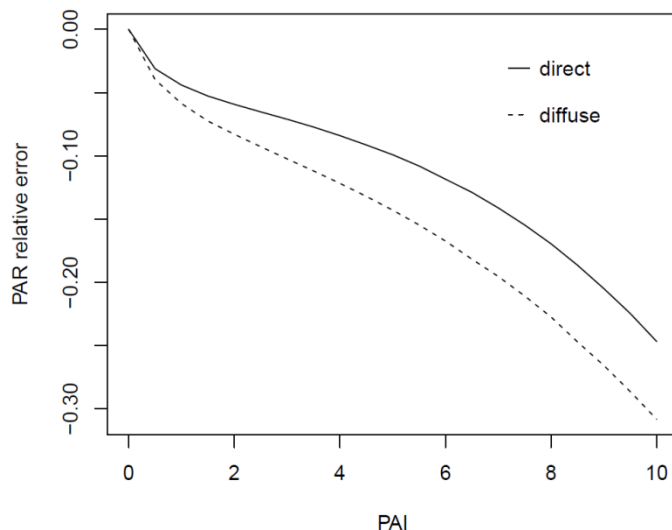


Figure A 12: Sensitivity analysis for DART simulations of direct and diffuse irradiance (sun at nadir) showing the relative error in simulated PAR fraction reaching the ground underneath a vegetated layer of given PAI if leaf reflectance and transmittance is not modelled. For this comparison, the simulation was run with deciduous leaf optical properties available in the DART database.

SI10 Impact of leaf angular distribution

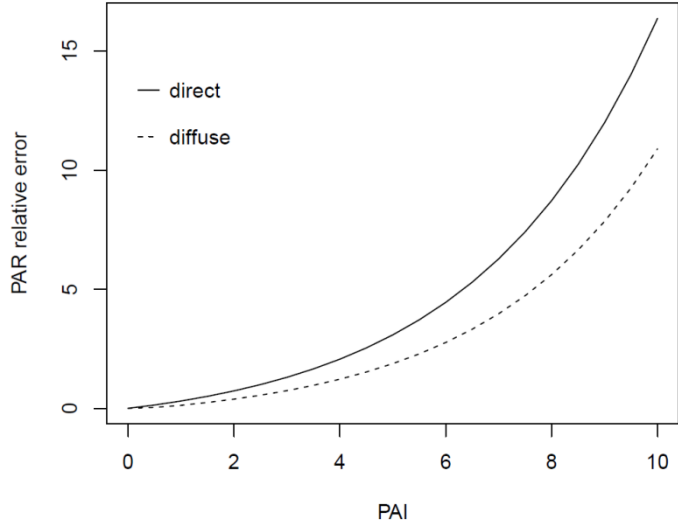


Figure A 13: Sensitivity analysis for DART simulations of direct and diffuse irradiance at maximum solar elevation (63.24°), showing the relative error in simulated PAR fraction reaching the ground underneath a vegetated layer of given PAI if true leaf angle distribution is planophile but assumed spherical.

SI11 HOBO light logger locations and comparison to DLI simulations

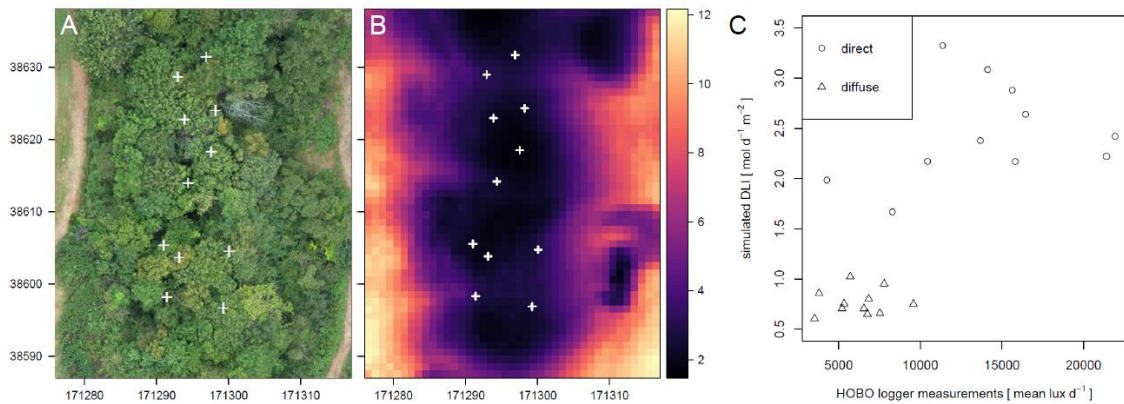


Figure A 14: HOBO logger locations (white crosses) in A) an RGB orthomosaic and B) the simulated DLI at ground level in mol d⁻¹ m⁻². C) Relationship between DART simulated DLI in PAR mol d⁻¹ m⁻² and HOBO logger recorded light in mean lux d⁻¹ for two days at SOP with predominantly direct (15 July 2019) and diffuse (22 July 2019) irradiance respectively.

A5 Hemispherical flight experiment for tree crown reconstruction

The potential of utilising unconventional drone flight-plans for the imaging and reconstruction of single crowns was explored. This involved adapting existing software for hemispherical flight planning (Burkart et al., 2015) and the use of a DJI Inspire drone (DJI, China) with a gimbaled camera (DJI Zenmuse X3) for fully automatic multi-angular acquisitions of a lone standing oak tree (*Quercus robur*) at 30 metres, in September 2017 (Figure A 15). The tree was also scanned using a Leica ScanStation P16 terrestrial laser scanner from four positions in 10 metres distance of the tree. SfM processing of the drone acquired images demonstrated that the angle between individual images had to be sufficiently small (approximately <10 degrees) in order to allow sufficient image alignment. 672 images were used in the final processing. Alignment was improved by geotagging images based on on-board GPS, despite GPS accuracy being low in respect to the distances between images. For these applications, using a drone RTK GNSS system would be advisable (Stempfhuber and Buchholz, 2011). It would also allow more proximal acquisitions which are too hazardous otherwise. The TLS and drone point clouds were co-registered using deployed reference targets.

Results showed that hemispherical drone SfM approaches can reconstruct the oak tree crown surface geometry with the potential for providing crown volume estimates, as well as stem location and diameter. Compared to TLS scans, volume and area appears only slightly underestimated (6.5 cm cloud-to-cloud distance calculated in CloudCompare, V. 2.9.1), while the point density at the top of the tree canopy is higher due to occlusion in the laser scans (Figure A 16). Unlike the TLS scans, SfM does not capture interior canopy structure. This is to be expected due to the photogrammetric methodology, however the use of a higher resolution camera system than the integrated DJI Zenmuse X3 and in-flight adjustment of camera parameters may yield a higher resolved structure for gaps in the canopy.

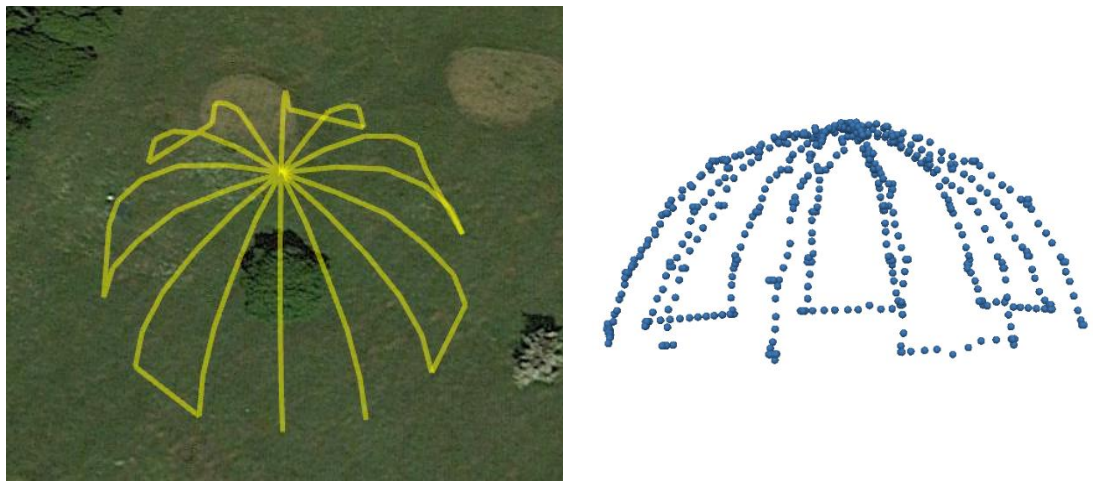


Figure A 15: Left: Hemispherical flight plan displayed in Google Earth. Right: UAV image geotagged locations from the flight.

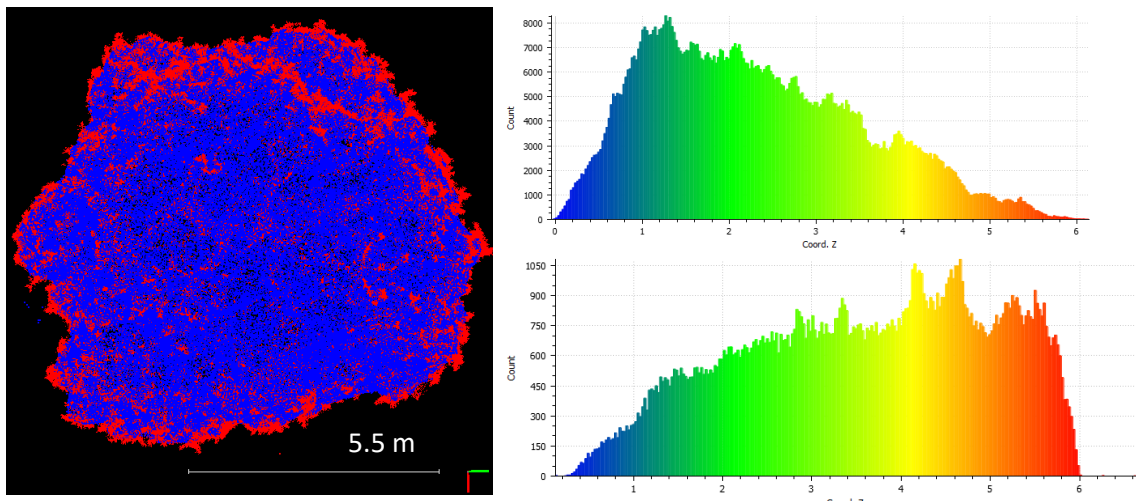


Figure A 16: Left: Nadir view of oak tree canopy with SfM points in blue and TLS points in red. Right: Histograms of point counts per height (m) of the TLS (top) and SfM point cloud (bottom).

A6 Investigating impacts of calibration methodology and irradiance variations on lightweight drone-based sensor derived surface reflectance products

Abstract

The miniaturisation of multispectral sensors in recent years have resulted in a proliferation of applications particularly in vegetation-focused studies using lightweight drones. MCAs, capable of capturing information over different wavelength intervals using separate cameras with specific band-pass filters, are now commonplace in this field. However, data from MCAs require a considerable amount of geometric and radiometric corrections if high quality reflectance products are to be delivered. Some aspects of this workflow can be handled by commercial software packages (e.g. Pix4D and Agisoft Metashape), using black box algorithms, however radiometric uncertainties within products are not reported to the end-user by the software. We present the results of two experiments using a low-cost MCA complete with irradiance sensor (Parrot Sequoia), which set out to assess the accuracy and consistency of hemispherical-conical surface reflectance factors from MCA data. Using reference panels in the field, we found that the empirical line method (ELM) generated the smallest RMSEs (0.0037) when compared to simplified single-panel based workflows; while for the latter there was little difference between using a calibrated Spectralon® panel or grey card imaged prior to the flight (0.0215 vs 0.0154 average over the four bands). Errors for a vegetated target within the survey flight were larger and comparable for all cases. Furthermore, a study on median VI values for single vegetation canopies showed that illumination correction using irradiance data still yields significant differences in resulting values between two acquisitions during changing direct and diffuse irradiance conditions. We therefore highlight the importance of critical assessment prior to integrating drone derived MCA-measured reflectance factors into further geospatial workflows.

INTRODUCTION

The MCA solution to multi-spectral imaging is attractive due to the relatively low-cost and light weight of the required hardware, meaning the cameras can be deployed on small multi-rotor drones which offer unique flexibility. Furthermore, the fully integrated systems usually weigh in at < 3 kg making them exempt from regulations that control the deployments of heavier drone aircraft; and are therefore deployable by scientists at a large range of study sites. In particular the Parrot Sequoia camera has been applied in a number of recent vegetation related studies (Ahmed et al., 2017; Franklin et al., 2017; Johansen et al., 2018). However, in part due to fully integrated processing in commercial software (i.e. Pix4D), reports regarding the uncertainties within surface reflectance and derived indices are often lacking. In particular, the quality of the reference panel and its calibrated reflectance used to convert the generated pseudo-radiance orthomosaics to surface reflectance factors has been shown to be a potential large source of error due to degradation, an issue which is commonly encountered for spectroradiometric studies in the field (Assmann et al., 2019; Hueni et al., 2017; Möller et al., 2003).

Furthermore, important metadata such as temporal/spatial irradiance variations during acquisitions are not commonly reported, and instead there is often a reliance on the integrated irradiance compensation to provide homogenous products, although it has been previously observed that this does not always lead to consistent improvements (Tu et al., 2018).

Within this study, we assess two key constraints regarding the reliability of drone-mounted MCA derived surface reflectance factors:

- the influence of the type of reflectance calibration method used
- the compensation of irradiance variations.

Experiment 1 tested the hypothesis that the two most commonly employed approaches for the retrieval of surface reflectance from MCA image data would deliver the same information. First, a standard ELM (Smith and Milton, 1999) was used, using reference points of multiple panels of known reflectance imaged in-flight. Second, a simplified ELM (e.g. (Aasen et al., 2018; Wang and Myint, 2015)) implemented in software packages which relies on a single ground-based calibration image of a reference panel was used as a comparison. Panels for the

in-flight ELM correction were self-manufactured while for the simplified ELM a Kodak grey card middle grey reference as well as a Spectralon®¹ calibrated reflectance panel was used. Derived surface reflectance factors were compared to those of validation targets measured *in-situ* using an OceanOptics FLAME spectrometer measuring over the same spectral range as the MCA instrument.

The second experiment tested the hypothesis that in-flight irradiance information could eliminate variations stemming from changing illumination within the generated surface reflectance product. The impact of correcting for illumination variations based on irradiance sensor data was assessed by comparing surface reflectance factors and derived VI values (NDVI and CHL) from acquisitions with changing irradiance conditions due to patchy cloud cover.

MATERIALS AND METHODS

Both experiments were conducted using a low-cost MCA complete with irradiance sensor (Parrot Sequoia, Parrot, France) mounted on a 3DR Solo quadcopter using custom 3D printed mounts. The Sequoia is mounted at 3° off-nadir in forward direction to compensate the average forward tilt of the drone when flying at 5 m/s.

The Sequoia multispectral sensor consists of four cameras with different band-pass filters located in the green, red, red-edge and NIR regions of the spectrum with centre wavelengths at 550, 640, 735 and 790 nm and varying bandwidths. The approximated sensor response per band is visualised in Figure A 17 along with a simulated reflectance spectrum representing healthy vegetation.

¹ Spectralon is a registered trademark of Labsphere, Inc.

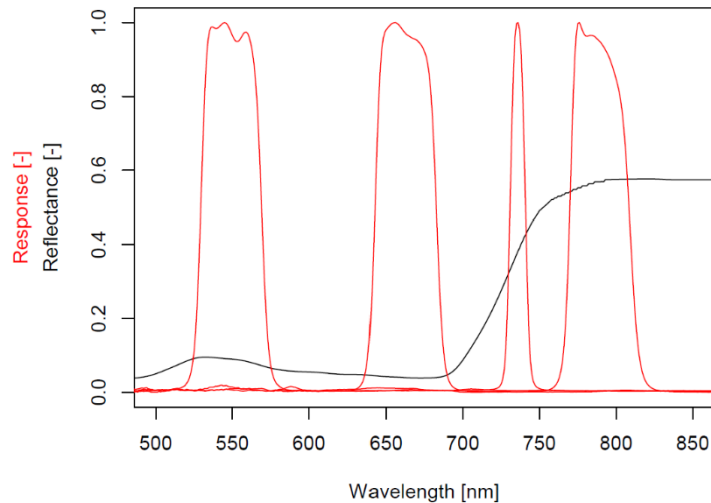


Figure A 17: Red: Sequoia normalised spectral response, Black: Simulated vegetation spectrum for illustration.

Experiment 1

Study site and drone flights

Data were acquired over a pasture and mixed woodland study area in South West UK during cloud-free conditions at 11:30 AM BST (UTC+1) on 4th July 2019. The drone was flown in a pre-programmed north-south oriented lawnmower pattern at 70 m elevation above ground at a speed of 5 m/s. This resulted in ~80% lateral and ~90% frontal overlap between images and a nominal ground resolution of 6.6 cm. Calibration panels deployed in the field were imaged at a lower elevation of 25 m resulting in a nominal ground resolution of 2.36 cm.

Calibration panels

A calibrated Spectralon panel of 42.5% average reflectance over the Sequoia wavelength range (SRT-40-050) as well as a calibrated grey card of ~20% average reflectance were imaged prior to the flight at three different exposures with the Sequoia Radiometric Calibration setting. For each band, the non-saturated image with the longest exposure was selected as reference.

Five reference panels of varying reflectances ranging from 2% to 42% (Figure A 18) were levelled and imaged at a lower flying altitude of 25 m in order to resolve sufficient pure pixels per panel and reduce adjacency effects. Panels (c), (d) and (e) are plywood painted with Rust-Oleum® matte furniture paint while (f) and (g)

are fabric panels manufactured by MosaicMill (Finland). All panels are designed to minimise bi-directional effects, though the actual BRDF was not assessed here.

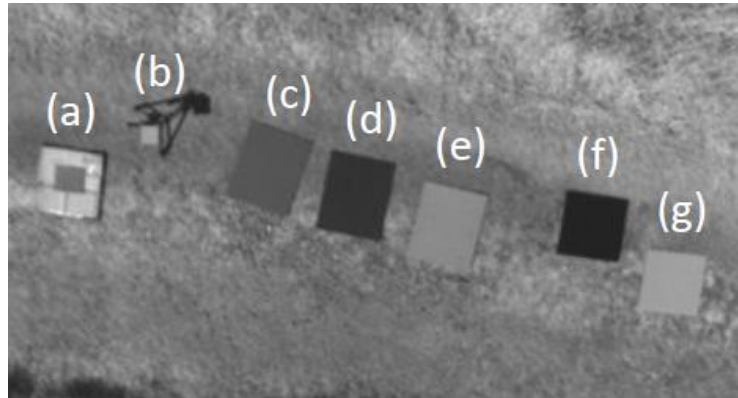


Figure A 18: The grey card (a) and Spectralon panel on tripod (b) imaged pre-flight, and the five larger reference panels (c-g, with averaged reflectances of 0.2, 0.07, 0.39, 0.02 and 0.42 respectively) imaged at 25 m altitude, displayed in the NIR band.

Field spectral measurements

The reflectance of the five reference panels as well as one grass and one pseudo-invariant concrete surface were measured immediately prior to the drone acquisition (11:20-11:25 UTC+1), using an OceanOptics FLAME spectrometer and a calibrated Spectralon white reference panel (SRS-99-020, 99% reflectance across the Sequoia wavelength range). Measured reflectance spectra were post-processed by interpolating artefacts stemming from absorption features, the most prominent in the O₂A band (760 nm), and smoothing the spectra using Savitzky-Golay filtering (Savitzky and Golay, 1964).

In order to compare the reference values to the measured Sequoia band values, the spectra were convolved with each band's SRF. Due to the true SRFs being unavailable, they were derived from filter transmission values per wavelength and the approximated camera CMOS sensor response (see Figure A 17).

Drone derived HCRF

The following formulas for the calibration of Sequoia images using information recorded in image EXIF tags are based on information provided by the manufacturer (Parrot, 2017b) and are fully integrated within the Pix4D software (with the exception of the standard ELM based on multiple panels). However, the implementation of the full processing pipeline remains black-box and cannot be

detailed here. Lens distortion and vignetting corrections are also applied within the software (see Pix4D, 2019).

The DNs P as recorded per pixel by the Sequoia sensor are converted to radiance-equivalent values, here termed pseudo-radiance R , following eq. A6-1 in Table A 9. Here f is the focal ratio, γ the ISO and ε the exposure time in seconds whereas A , B and C are camera specific calibration factors provided by the manufacturer.

For the single-panel simplified ELM calibration, R is converted to surface reflectance ρ using calibration coefficient K (eq. A6-3,Table A 9). K is derived from the calibrated reflectance value ρ_{ref} of a reference panel imaged prior to the flight, as well as the average R over the surface of the imaged panel, termed \overline{R}_{ref} (eq. A6-2,Table A 9).

Alternatively, the irradiance counts in DNs (C) recorded by the irradiance sensor are converted to pseudo-irradiance (R_{irr}) using eq. (A6-4), where g is the gain and ε_{irr} is the exposure time of the irradiance sensor. R_{irr} can then be used to account for the variation in irradiance in respect to the single panel reference image and derive a ρ which is less susceptible to irradiance differences, using eq. (A6-6) in Table A 9. K' is derived similarly to K but includes the irradiance measured during the capture of the single panel calibration image R_{refirr} (eq. A6-5, Table A 9). This factor also accounts for the differences in sensitivities and solid angles between the irradiance sensor and camera pixel measurements.

Table A 9: Formulas used to convert DNs as measured by the Sequoia camera and irradiance sensor to surface reflectance. Left column: reflectance calibration not considering irradiance, Right column: Reflectance calibration with irradiance compensation.

Pseudo-Radiance (R) from DNs (P):	Pseudo-Irradiance (R_{irr}) from DNs (C):
$R = f^2 \frac{P-B}{A\varepsilon\gamma+C} \quad (\text{eq. A6-1})$	$R_{irr} = \frac{C}{g\varepsilon_{irr}} \quad (\text{eq. A6-4})$
Calibration coefficient using reference panel (simplified ELM):	Calibration coefficient using reference panel and measured irradiance (simplified ELM):
$K = \frac{\rho_{ref}}{R_{ref}} \quad (\text{eq. A6-2})$	$K' = \rho_{ref} \frac{R_{ref,irr}}{R_{ref}} \quad (\text{eq. A6-5})$
$\rho = KR \quad (\text{eq. A6-3})$	$\rho = K' \frac{R}{R_{irr}} \quad (\text{eq. A6-6})$

For the ELM calibration method, surface reflectance ρ was predicted from pseudo radiance R using a linear model based on a dark and bright reference target. The bright targets used were different for the visible bands due to saturation (here 2% and 25% reflective panels for the Green and Red bands, 2% and 42% reflective panels for the red edge and NIR bands).

Experiment 2

Study site and drone flights

These data were acquired over a 10 year old oil-palm plantation in Sarawak, Malaysian Borneo between 10:30 and 11:20 AM UTC+8 on 3rd February 2018. Two identical flights were conducted following a lawnmower pattern flight plan at 100 m elevation above ground and 5 m/s speed with image acquisitions triggered by intervalometer which ensured 80% lateral and >90% frontal image overlap and yielded 9.42 cm ground resolution. For the first flight, here referred to as F1, illumination conditions were more uniform throughout the flight than compared to

the second flight (F2). However, while for F1 irradiance was mostly diffuse, both flights showed variations in irradiance

Calibration panels

The flights were calibrated using a Spectralon white reference panel (SRT-99-050, 99% reflectance over the Sequoia wavelength regions) imaged during overcast conditions at three different exposures with the Sequoia Radiometric Calibration setting. For each band, the non-saturated image with the longest exposure was selected as reference.

Drone derived HCRF

The simplified ELM radiometric calibration is the same as described for Experiment 1.

The pseudo radiance R from both flights was calibrated to surface reflectance by alternatively using equations (A6-3) and (A6-6), resulting in two surface reflectance products each, one which considers measured irradiance and one which uses only the Spectralon (SRT-99-050, 99% reflective) panel as reference.

Per-palm NDVI and CHL values

The NDVI and CHL indices were calculated for both acquisitions as follows:

$$NDVI = \frac{NIR - Red}{NIR + Red} \quad (\text{eq. A6-7}) \quad CHL = \frac{NIR}{Red\ edge} - 1 \quad (\text{eq. A6-8})$$

Eq. (A6-7) is based on the work by Gitelson et al. (2006).

The locations of 496 palm tree tops were derived using SfM photogrammetry in a previous study conducted on this site (Fawcett et al., 2019a). Median NDVI and CHL values were extracted within a 2.5 m buffer around each point, the buffer size was chosen to minimise the impact of overlapping palm fronds or visible ground between palms.

RESULTS

Experiment 1

The measured surface reflectance averaged over the area of each target is plotted against the field-measured reference reflectance (HCRF) in Figure A 19, while corresponding RMSE and standard deviations over the reference panel areas are recorded in Table A 10.

The two brightest targets with >30% average reflectance saturated in the green and red band and were therefore omitted from this analysis. This represents a limitation of the minimum automatic exposure time of the Parrot Sequoia sensor, which is designed to capture small variations within vegetation reflectance which is very low in the green and red bands due to absorption. The dark and bright targets used to construct the empirical line for the ELM were also omitted from the further analysis.

As is apparent from Table A 10, for the reference panels the mean RMSEs over all bands is considerably lower for the ELM calibration compared to the single-panel approaches. Between the two panels used for the simplified ELM, the Kodak grey card performs better than the Spectralon (SRT-40-050) panel with 0.0154 mean RMSE over all bands compared to 0.0215 for the Spectralon panel. In the red edge and NIR bands, larger deviations for the single panel calibrations can be observed at lower reflectance. As these panels were imaged at lower altitude to prevent adjacency effects and the influence of water vapour and aerosols is assumed to be negligible at these altitudes (Jakob et al., 2017), one possible source of error is dark-current which may not be adequately accounted for within the calibration workflow. This does not appear to influence the visible bands.

Errors are highest for the grass meadow target in the red edge and NIR bands, with mean absolute errors up to 6.7% in the red edge when using the grey card. These errors can have a substantial impact, particularly for the derivation of chlorophyll content from indices. The source of this anomaly is unclear and may be related to non-representative measurements in the field or uncertainties within the sensor response used to convolve the measured spectra to representative Sequoia measurements. The latter should be investigated as it has far reaching

consequences when seeking to use Sequoia reflectances for the retrieval of biochemical parameters.

It should also be noted that the ELM does not perform better than the single panel calibration for the grass and concrete reference targets within the survey flight. As the ELM was derived from panels imaged at a lower altitude and slightly different sun-sensor geometry, the difference is likely BRDF related.

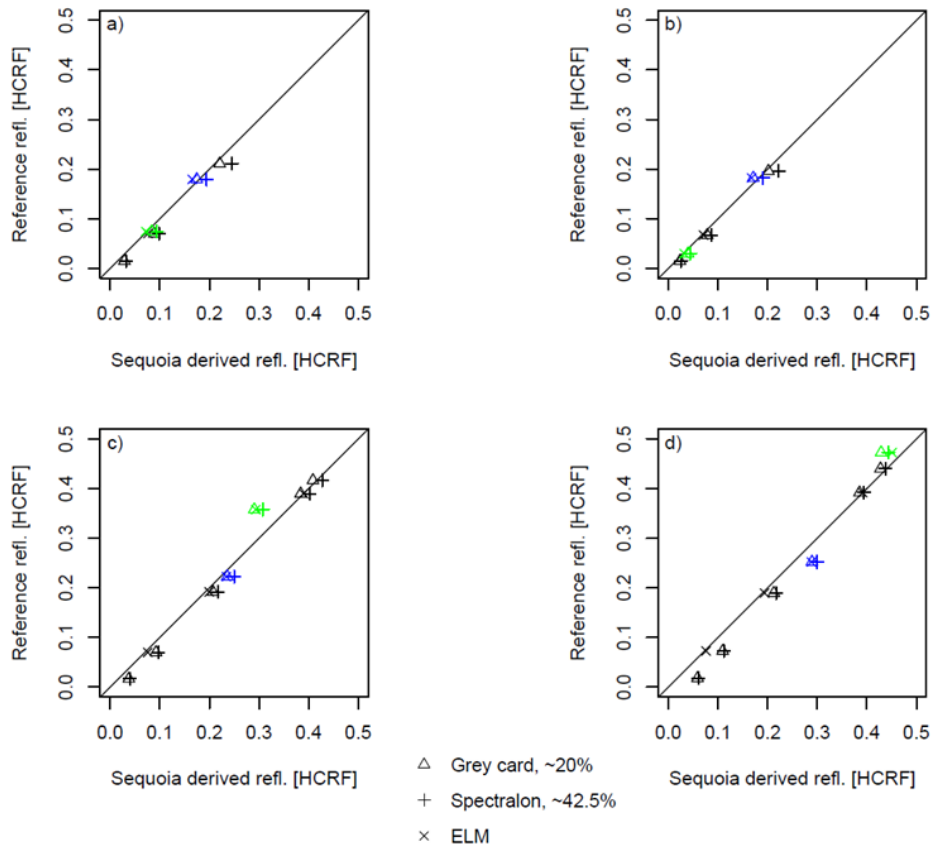


Figure A 19: Reflectance values as derived from multispectral imagery using different calibration methods for five reference panels of different reflectance as well as a pseudo-invariant concrete surface (blue) and grass meadow (green). Results are plotted by band: a) Green, b) Red, c) Red edge and d) NIR bands.

Table A 10: RMSE per band and calibration method between the measured reflectance and the reference reflectance for the reference panels. In brackets: Standard deviations over the pixels of each panel.

RMSE and SD	GRE	RED	REG	NIR	RMSE all bands
GreyCard	0.0113 (0.0014)	0.0067 (0.0017)	0.0159 (0.0022)	0.0274 (0.0031)	0.0154
Spectralon (SRT-40-050)	0.0213 (0.0016)	0.0153 (0.0019)	0.0206 (0.0023)	0.0288 (0.0031)	0.0215
ELM	0.0036 (0.0016)	0.0022 (0.0019)	0.0056 (0.0024)	0.0032 (0.0034)	0.0037

A visual comparison of the green band surface reflectance (HCRF) results for a subset of the actual surveyed scene is displayed in Figure A 20. It is evident that there are slight offsets depending on the calibration method used, with the highest values for the Spectralon (SRT-40-050) calibrated product and the ELM resulting in generally lower values, even slightly negative for the dark cast-shadow region.

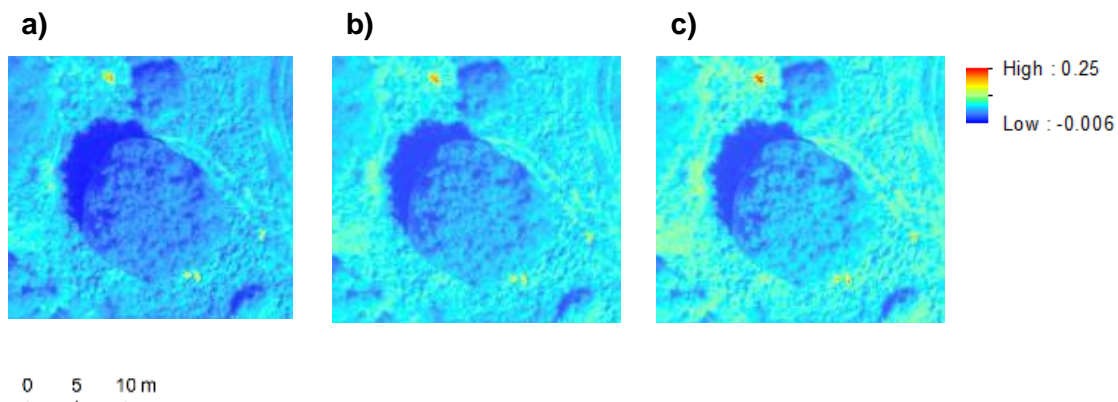


Figure A 20: HCRF values in the green wavelength band for a subset of the scene showing an oak tree canopy and cast shadow for a) the standard ELM, b) simplified ELM with grey card and c) simplified ELM with Spectralon panel.

Experiment 2

The derived pseudo-irradiance values for each flight are visualised in Figure A 21. The recorded camera positions for F2 appear more unequally spaced as opposed to F1. As the wind speeds and directions were similar for both flights, this is likely a camera related issue appearing due to continuous operation. As frontal image overlap was very high, this issue is not expected to significantly impact the results.

The surface reflectance for F1 and F2 and the two different calibration approaches are displayed for the NIR wavelength band in the area of interest in Figure A 22. As the single panel calibration image was acquired during overcast conditions, HCRF is greater than 1 for areas imaged during direct irradiance conditions if irradiance is not considered. If measured irradiance is considered, illumination-based anomalies are reduced in magnitude. Visual inspection of F1 shows that there are no large differences apparent due to more stable irradiance conditions. Comparing the F2 reflectance maps to F1, it is clear that considerable variations due to irradiance are still present, even when irradiance information is included in the calibration. The spatial distribution of brighter and darker areas is however different.

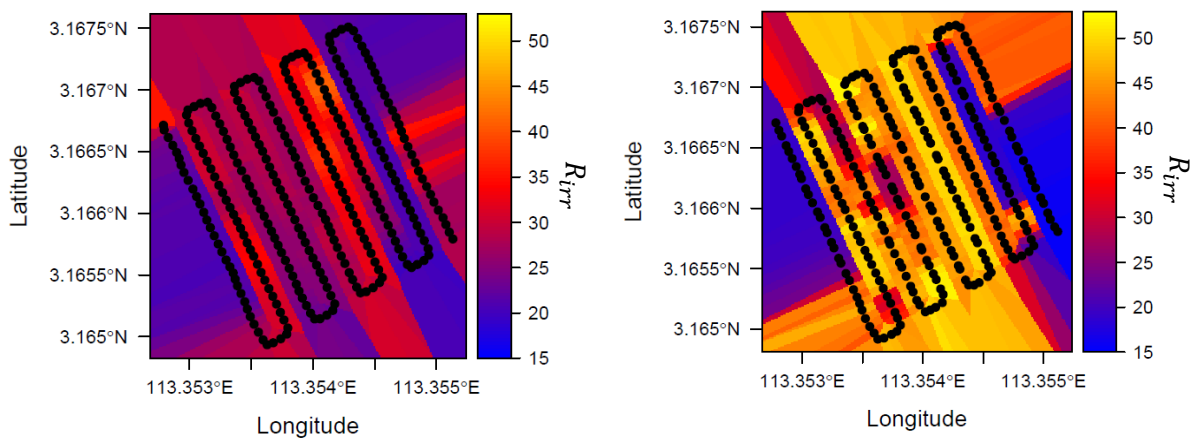


Figure A 21: Spatial representations of the pseudo-irradiance values captured per image in the green band for the two drone acquisitions. Left: Flight 1 (F1), Right: Flight 2 (F2). The black dots represent the GPS position recorded for each captured image.

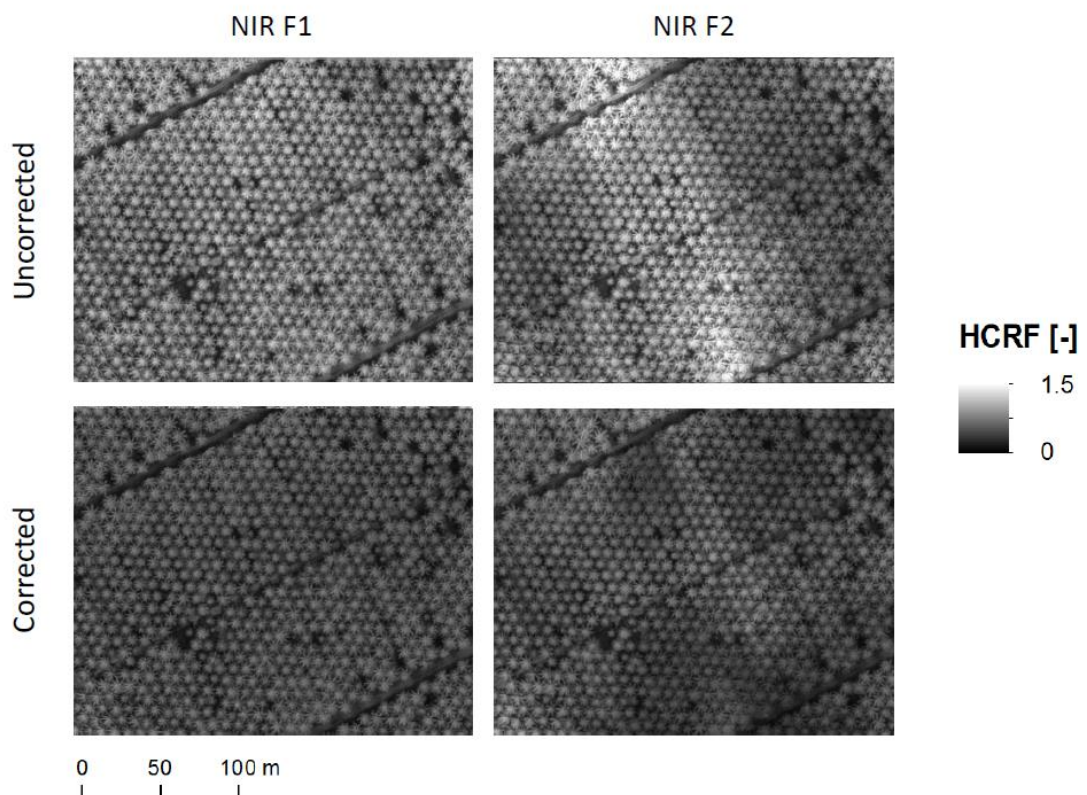


Figure A 22: Surface reflectance in the NIR band for the consecutive acquisitions F1 and F2, with and without accounting for measured irradiance information.

The values of indices derived using band-ratios are impacted due to wavelength-dependent differences in apparent reflectance depending on direct or diffuse illumination conditions (Damm et al., 2015b). As is evident in Figure A 23 and Table A 11, the mean index values differ considerably between F1 and F2 due to illumination dependent differences. The difference between mean values is greatly reduced by compensating for irradiance and the value spreads are reduced, also clearly visualised in Figure A 24. However, a paired t-test showed that the differences between means was still significant for both NDVI and CHL values ($p < 0.05$). The standard deviation of CHL values within the more variable acquisition F2 are still almost double those of F1. This means it is likely that index variations even within irradiance-compensated products may mask actual physiologically based differences between palm canopy reflectances.

Table A 11: Means and standard deviations of per-palm index values for the two acquisitions F1 and F2, with and without irradiance compensation.

	F1	F2	F1 corr.	F2 corr.
NDVI mean	0.892	0.846	0.903	0.898
NDVI SD	0.013	0.025	0.011	0.017
CHL mean	0.870	0.308	0.986	0.928
CHL SD	0.164	0.214	0.125	0.241

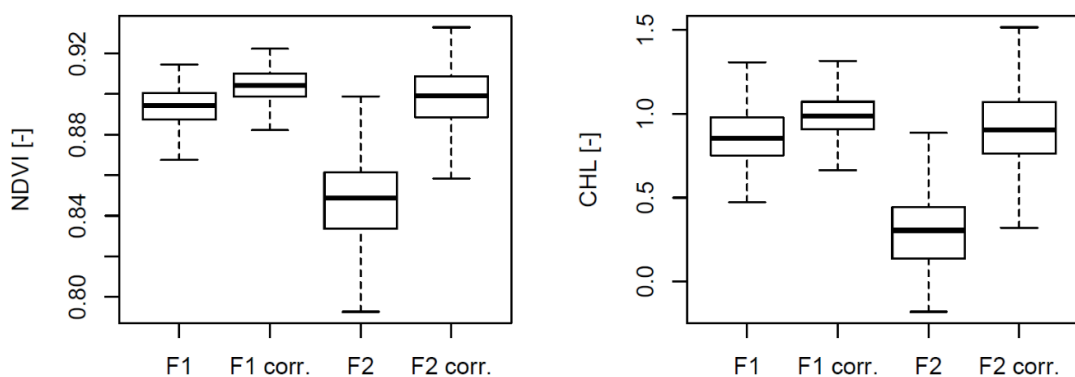


Figure A 23: Boxplots of palm median NDVI (left) and CHL (right) values for acquisitions F1 and F2, with and without irradiance compensation (corr.). The bold central line represents the median, the lower and upper boundaries of the boxes are the 25th and 75th percentile respectively and the whiskers extend to the furthest data points within 1.5 times the interquartile range, outliers beyond are omitted.

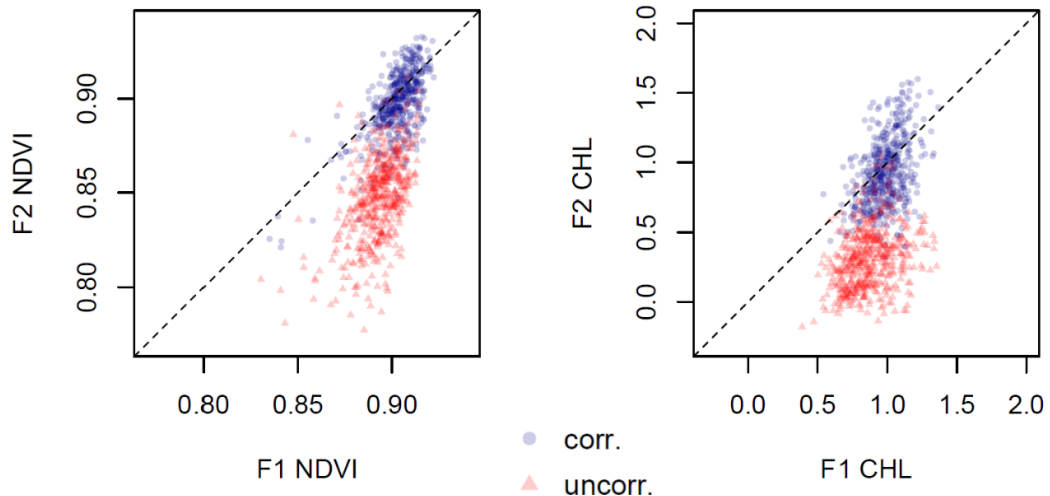


Figure A 24: Per palm CHL and NDVI values for two replicate flights of varying illumination. Red: Irradiance considered during reflectance calibration, Blue: Irradiance not considered during reflectance calibration.

DISCUSSION AND CONCLUSIONS

In this study, we firstly assessed the accuracy of drone-based MCA data derived surface HCRF for two different calibration approaches and reference panels (experiment 1) as well as the impact of illumination variations on HCRF derived VIs and the performance of corrections using irradiance data (experiment 2).

Experiment 1

We found that the standard ELM based method can provide surface reflectance factor estimates which are more consistent with *in-situ* measured values, if acquired at the same altitude and viewing geometry. The ELM can compensate for the influence of aerosols and water vapour between the ground and sensor given a uniform distribution of these throughout the imaged scene, whereas a calibration based on a single reference panel imaged on the ground would be susceptible to this bias. The ELM also has the advantage that the panels are imaged with the same viewing geometry as ~50% of the scene (flight lines of same orientation). However, as in this study the panels were imaged at a significantly lower altitude than the rest of the scene (45 m difference), atmospheric effects and viewing geometry will be slightly different and indeed for

the two targets measured within the survey flight, the performance of the same standard ELM and single-panel calibration was comparable.

To enable the ELM at flight altitude, significantly larger panels would be required. For practical reasons, this is commonly solved by using tarpaulins (H. Li et al., 2015), though these cannot be levelled and may introduce variations in reflectance due to BRDF effects.

When using the standard ELM a divergence in areas of low reflectance (cast shadows) was observed when the ELM intercept is not constrained to zero. Assuming adjacency effects are indeed negligible for the panels imaged at lower altitude and dark current offset is constant, the cause of this phenomenon is unclear but may be due to non-linearity in sensor response for very low incoming radiance.

There did not appear to be a large difference when considering the use of the 42.5% Spectralon panel for single-panel calibration as compared to a much more affordable Kodak grey card. Although the Spectralon panel can be expected to exhibit more Lambertian reflectance properties than the grey card, it should be noted that carbon-dosed Spectralon has been found to be slightly less Lambertian than purely white panels (Rollin et al., 2000). It should however be stressed that our study did not investigate degradation of actual reflectance versus the calibrated reflectance values over time which has been shown to be larger for lower quality panels such as the Kodak grey card used here (Assmann et al., 2019).

Experiment 2

Experiment two showed that corrections for irradiance variations based solely on irradiance sensor information can improve the consistency of results acquired during overcast conditions with varying diffuse illumination but cannot fully compensate for the impact of direct/diffuse irradiance variations. This is due to the point-based irradiance measurement representative for the image not being representative for the actual top-of-canopy irradiance of the imaged scene due to a large spatial extent being imaged, often not perfectly nadir due to non-gimbaled acquisition. Cloud shadows and gaps can therefore lead to significant variations in derived indices which is superimposed on natural variation within the scene.

This is true even for the NDVI which is considered more robust to wavelength dependent variations (Damm et al., 2015b).

From the two experiments presented here, we conclude that standard ELM calibrations of pseudo-radiance orthomosaics generated using black-box processing software remain the most reliable way of deriving true HCRF from MCA drone imagery, however the deployment of panels of sufficient size and Lambertian reflectance is limiting in practice. Reference panels imaged in-flight are still highly recommended either for calibration or accuracy assessment of any study seeking to make use of individual band HCRF information. Furthermore, in order to generate spatially consistent HCRF products, irradiance conditions should be as homogenous as possible and any greater variations will introduce errors which cannot be adequately compensated using drone-based irradiance measurements. There is therefore a need for scientists working with multispectral drone data to be aware of these limitations and transparently report illumination conditions during acquisitions, ideally through concurrent measurements.

A7 TRUSTEE deliverable 1.6: Procedure for the in-flight definition of the flight plan for multi-rotor drones

Changes to the initial definition of the deliverable

The initial definition of this deliverable was modified due to a different focus of the overall PhD topic of the primary contributor (ESR3 at UNEXE) and the only other collaborator (QUEST-UAV with ESR12) leaving the network. Keeping in line with the intent of this deliverable, an in-field optimisation of drone flight plans for acquisition of data over vegetation, UNEXE proposed the development of a sensor system to deliver auxiliary information on illumination and surface brightness variations throughout the flight. This information is crucial to understanding data quality from multi-spectral sensors which are commonly deployed on drone systems. By enabling the display of georeferenced illumination data corresponding to image acquisitions immediately after drone flights in the form of illumination maps, areas affected by illumination changes can be identified and further flight plans can be adjusted in the field to ensure the repeat capture of homogenous data over these areas. A low-cost and operational implementation of such a system can greatly aid the acquisition of scientific data from drone systems.

Summary

Drone acquisitions which are performed under changeable conditions may be influenced by illumination effects. Due to larger areas covered, these impacts are not always apparent in the field. To aid with the identification of regions affected by cloud shadow and the following adjustment of further flight planning, we present the design and tests of a drone mountable system able to record such variations and compile a visual report to inform the pilot on completion of the flight. The system is designed to be low-cost and easy to implement for the gathering of illumination related metadata for a variety of applications and users. It is primarily of interest when acquiring radiometric data and multispectral mapping, e.g. in agriculture.

The system was implemented and first tests of components and operational acquisitions were performed. The tests were successful and data acquired is considered promising. Illumination variations as measured by the sensor, if stationary, show a good relationship to calibrated measurements. In-flight tests under changing illumination conditions demonstrated the system's capability to report spatially resolved relative changes to the user as an indicator of acquired data quality. However, tests under constant direct illumination demonstrated angular effects which could not be characterized well.

Aspects which needed further study were identified, such as the angular dependence of the measured illumination values, as well as elements in the acquisition and processing pipeline which require further refinement, such as efficiently deriving image metrics.

Background and Aims

Irradiance during drone spectral acquisitions is commonly assumed constant or its variability addressed by using a stationary spectrometer or PAR sensor on the ground (Burkart et al., 2014; Hakala et al., 2010). Such sensors can be added to drones, though they are expensive and will only guarantee reliable data if they are highly stabilised using gimbals. Instead, the use of simple photoreceptors is affordable while allowing the monitoring of relative irradiance variations during a flight (Hakala et al., 2013). The defined aim for this deliverable, which was discussed further and slightly modified at the start of this project, was to produce a method of informing on the quality of drone data acquisitions and allowing optimised definitions of further flight plans by developing and testing a low-cost and lightweight illumination sensor that can be easily mounted on drones to enable the collection of irradiance related metadata.

The aim was to integrate the sensor and develop accompanying software which would allow the download of data immediately following each flight on a field laptop and to display the spatially interpolated values of individual georeferenced measurement points along the drone flight-line as a map of scene illumination. The low-cost illumination sensor to be used was characterised in terms of noise and further tests were carried out to assess the necessity of correcting for vehicle orientation during the flight, depending on the magnitude of sun-sensor geometry

related effects. The resulting maps should provide a useful way of reporting metadata for scientific studies but also allow for rapid decisions in the field regarding further flight planning. Resulting from this project is a fully open source solution to collect illumination related metadata consisting of this report including the sensor design and code to be shared for the implementation by third parties.

Sensor implementation

The system is comprised of a Raspberry-Pi (RPi) Zero powered by a Micro Lithium-Potassium (LiPo) battery and communicating with other devices through WiFi, circumventing the need of full integration with the drone system itself (Figure A 25). The RPi Zero model has a low power consumption while providing all the required functionality. It allows for more advanced applications and flexibility as opposed to an Arduino based system. The design includes an illumination sensor (SI1145, Adafruit Industries) with two photodiodes for visible and infrared light, to be fastened to the top of the drone, as well as a Raspberry-Pi ZeroCam NoIR camera which is sensitive to light in the infrared region and will image the ground below. Simple image statistics such as mean and standard-deviation per band will be derived from the RPi-Cam imagery to generate measures of the overall scene brightness and brightness variations. The combined cost of all the essential sensor components at time of writing was 35.50 € (SI1145, Raspberry-Pi Zero W, ZeroCam NoIR).

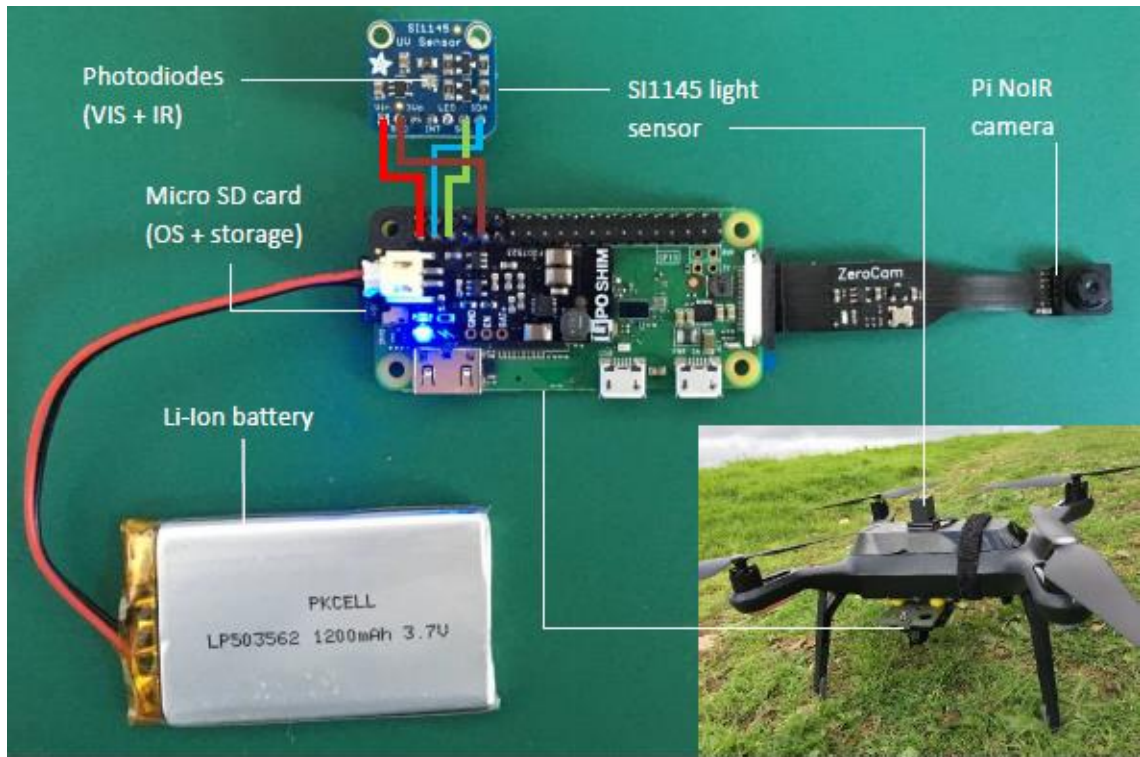


Figure A 25: Main components of the illumination sensor system prototype and its drone mounting solution (inset) using 3D printed parts.

Illumination sensor characteristics

The SI1145 digital illumination sensor is a low-cost sensor board (Silicon Labs, US) designed to be integrated within an Arduino based system, though Python libraries also exist for the use with RPi (https://github.com/THP-JOE/Python_SI1145, 06.09.2018). The SI1145 contains two photodiodes sensitive to visible and IR light. The manufacturer provides an indicative response graph (Figure A 26), from which it is apparent that there is significant overlap between the photodiode responses. The sensor also provides the functionality to calculate an UV index based on the response from the two photodiodes. For the application in this project, the expected difference in sensitivity between the sensors for direct and diffuse light can be of interest, with diffuse light showing a higher relative contribution in the visible spectrum (400-700 nm).

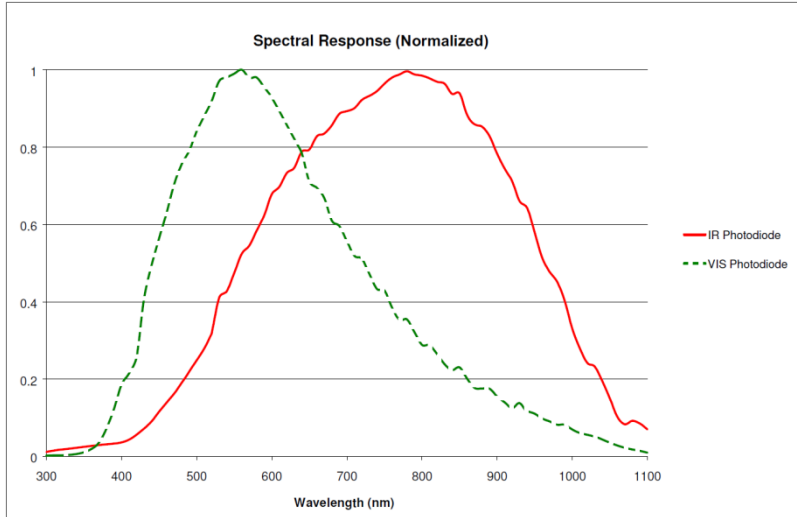


Figure A 26: Indicative response of the SI1145 photodiodes as reported by the manufacturer (Silicon Labs, US).

A number of tests were performed to assess the sensor's suitability for the desired application of identifying changes in illumination during acquisition. In a first step, the dark current was characterised by operating the sensor in completely dark conditions in a laboratory. Results showed that even in the absence of light, the measured counts (DN) equated to means of 260.3 for the visible and 253.3 for the IR diode with no apparent drift over 5 minutes of measuring time (Figure A 27). The standard deviation (noise) equated to 0.8 counts for the visible and 0.7 counts for the IR.

Further, initial tests were carried out using a constant light source (solar simulator for testing photovoltaics), which showed a saturation of the readings for both diodes at the lowest energy of 400 W/m^2 . Therefore, it is likely for the diodes to saturate in full sunlight, depending on atmospheric conditions and sun angles. This limits some applications of the sensor, for example to detect slight variations in direct irradiance due to changes in atmospheric composition.

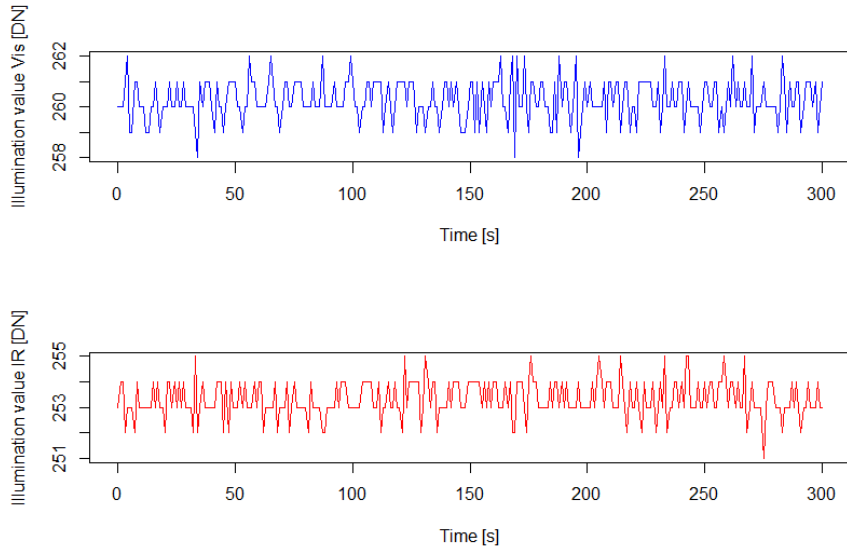


Figure A 27: Values recorded by the photodiodes in the absence of light (dark current).

To test the SI1145's response to real illumination conditions and its relationship to calibrated illumination measurements, multiple short measurements were carried out on a roof during different conditions. Transitions from direct solar illumination to diffuse conditions due to movements of clouds in front of the sun are evident as large changes in DNs measured by the light sensor. Comparing DNs over time with pyranometer reference measurements showed good agreement ($R^2 = 0.995$ after applying a spline interpolation to the pyranometer reference) of relative variations even under highly diffuse and low-light conditions (see Figure A 28, steps in the pyranometer measurements are due to sensor realignments every 30 seconds). Going forward, thresholds could be applied to the measured illumination changes to quantify the severity of the change effects on the acquired data. Parallel measurements with the pyranometer could also be used to attempt a calibration of the illumination sensor DNs to irradiance values, though this may not be necessary for our purpose of reporting relative changes.

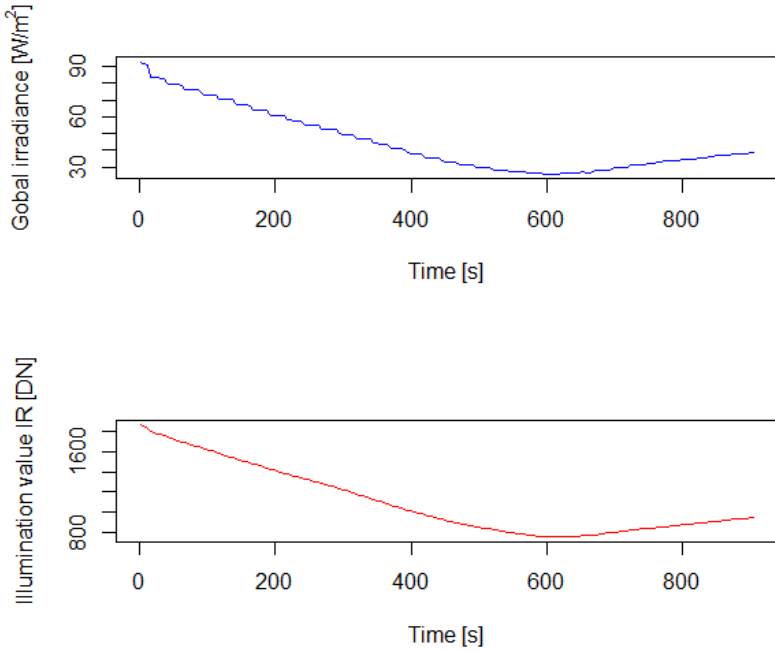


Figure A 28: Top: Pyranometer measurements of global irradiance during overcast conditions (12:04 to 12:19 UTC, 04.12.2017, Penryn, UK). *Bottom:* Concurrent measurements from the IR photodiode on the SI1145.

Imagery and derived metrics

The images captured by the NoIR Pi-cam are used to derive metrics which may represent useful information for further flight planning decisions. Due to the need for these metrics to be available immediately with minimal processing time, they are kept very simple and display interpolated point-based information identical to the illumination maps, without any orthorectification and mosaicking requiring computationally costly computer vision algorithms.

The Pi-Zero NoIR cam uses the same sensor as the V1 Pi-cam (OmniVision OV5647) with the IR filter removed. There is no published spectral response for the sensor in the IR region. Use of modified RGB cameras for low-cost applications is common practice, though the removed IR filter is usually replaced with another band pass filter to capture energy in specific regions of the spectrum (Dworak et al., 2013; Lebourgeois et al., 2008). For illustration, an example of an unfiltered RGB CMOS sensor response and the region cut by an IR filter is displayed in Figure A 29, taken from Dworak et al., (2013). Without further filtering, each band is sensitive over parts of the IR region, though the red band can

typically be expected to receive the most energy in IR. For further mentions of band colours, this must be considered.

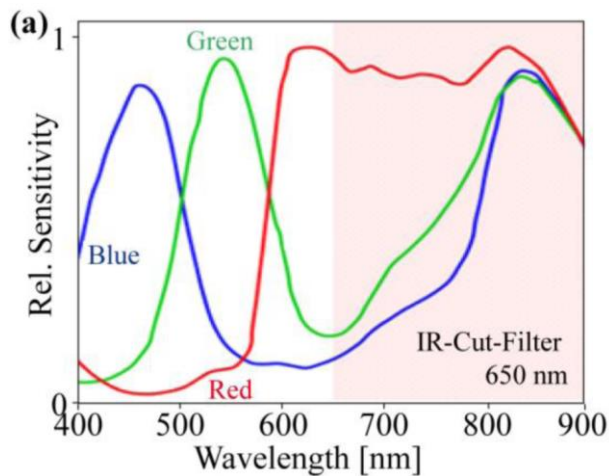


Figure A 29: Typical CMOS RGB sensor relative sensitivity per wavelength, including region cut by IR-filter (Dworak et al., 2013)

An RGB composite acquired by the NoIR camera is displayed in Figure A 30, along with histogram stretched greyscale images of the individual bands. Due to the reddish hue of vegetation, it is apparent that the red band receives the most energy over vegetated surfaces. The green band displays a brighter soil background as opposed to the other bands. Cast shadows are most apparent in the red band and brighter in the blue.

Although the camera possesses 5 megapixels, images are captured at a reduced 1280x720 pixel resolution as a trade-off between information, storage space and subsequent processing time. Depending on the metrics to be derived, for operational considerations the resolution could be further reduced.

In the first trial of this application, only two common and basic image metrics, the overall mean and entropy in the red band, are derived from the imagery. It is envisioned that depending on the application, further metrics related to scene complexity and local illumination differences as well as further bands and indices may be selected. Assuming uniform surface cover, the mean is sensitive to overall scene illumination given constant exposure time and shutter speed, while the entropy is expected to increase under direct illumination resulting in an abundance of brighter surfaces and cast shadows. Under constant illumination conditions, the variation of these metrics is linked to imaged surface cover change and viewing geometry.

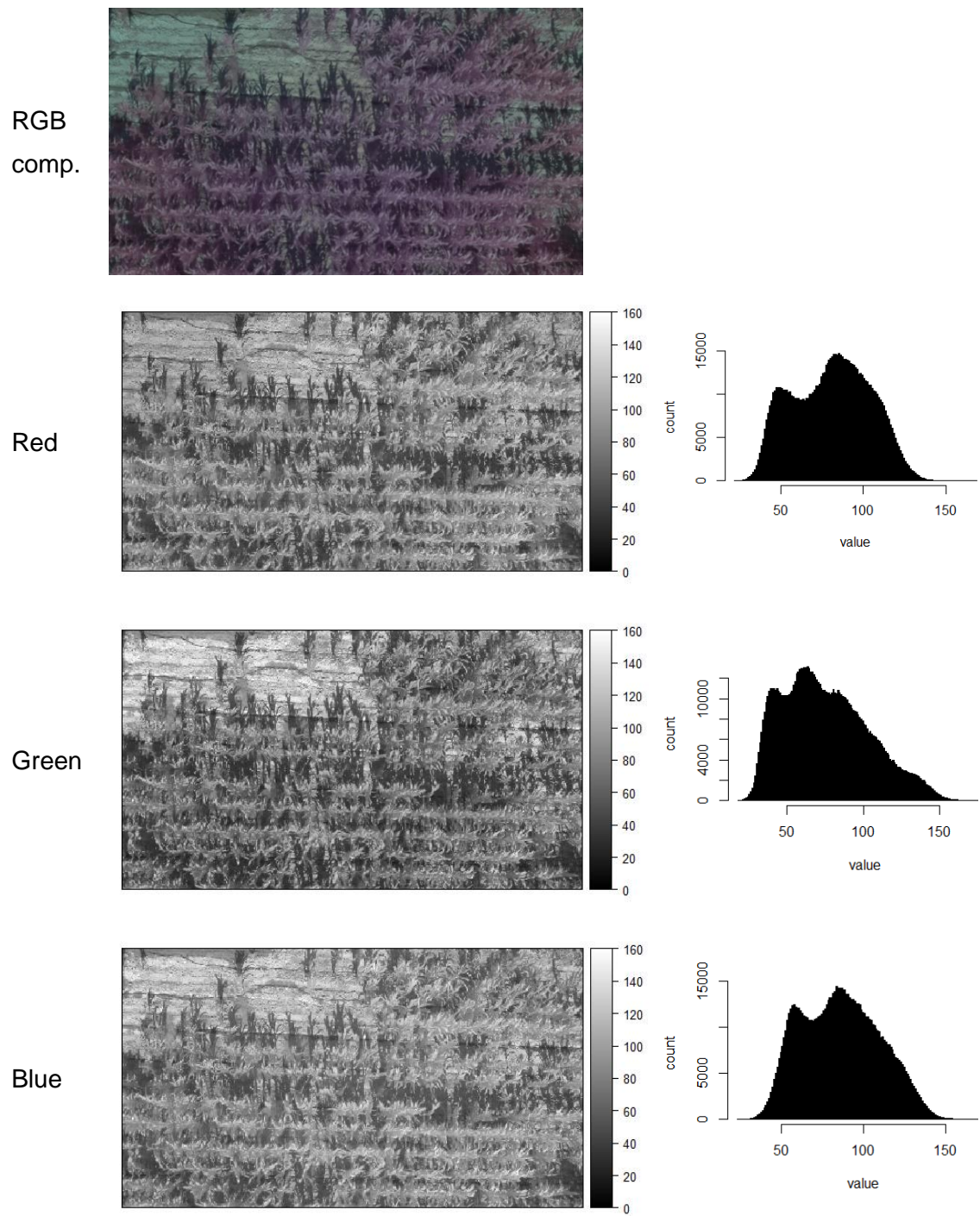


Figure A 30: Top: An RGB image as acquired by the Pi-NoIR camera over a maize field with purple vegetation, green bare soil and dark cast-shadows. Below: Stretched representations of the red, green and blue bands along with their original histograms.

Software implementation

The program running locally on the Raspberry Pi is written in Python 2.7 and is to be executed automatically on boot. It handles the setup of the camera and triggers both the camera and the irradiance sensor measurements. On initialising, the RPi connects to the drone WiFi and a UDP connection to the drone is established through Dronekit (<http://python.dronekit.io/>, 06.09.2018). Following this, a sequence of timestamps generated by the RPi and the drone on-board companion computer are written to a text file to allow later synchronisation of the data by the software. Drone parameters cannot be read continuously by the RPi throughout the acquisition as after a certain distance to the source (controller), the WiFi connection is lost. Therefore, after writing the synchronisation file, the connection to the drone is terminated for the remainder of the acquisition. The camera is triggered and illumination measurements are written to a file at a previously set time interval. The minimum interval is constrained by the exposure time set for the camera.

The base-station program is written in Python 2.7 while data is processed and displayed using an R script. Upon execution, the main R-script calls the Python implementation of the base-logger, a program which connects to the drone as described for the RPi above. This connection is sustained throughout the data acquisition and relevant drone telemetry information is written to a file for further use. This includes the timestamp, position in latitude and longitude (WGS84) and drone attitude information (roll, pitch and yaw). Once the drone has landed and is disarmed, this program establishes an SFTP connection with the RPi, terminates the acquisition and downloads the images and text files. In R, the downloaded data is coupled with the logged GPS information, the desired metrics derived from the Pi-cam images and the spatially referenced illumination information are interpolated using nearest-neighbour values and finally displayed and stored as maps.

An alternative to using the base-station to log relevant data would be to download the dataflash logs from the drone immediately following the flight. However, the overhead of downloading, converting the files from the pixhawk BIN format into an easily readable format and extracting the relevant parameters is anticipated to be higher than writing the parameters consecutively.

Field deployment

The sensor configuration is very lightweight and could be attached in addition to a primary sensor on most lightweight drone models. The mounting solution must be adjusted on a case-by-case basis. Mounting locations must be identified for the body, ideally below the airframe, and for the illumination sensor, ideally at the top of the airframe, extending above the propellers for multi-rotor drones.

The mounting solution used for testing on a 3DR Solo quadcopter platform was designed to attach the body to a vibration damped base for modular mounting of various sensors. The housing of the body and illumination sensor were custom designed in CAD software and are made available online (<https://www.thingiverse.com/thing:3081513> and <https://www.thingiverse.com/thing:3081549>, 06.09.2018). The illumination sensor housing is attached to the top of the drone using dual-lock Velcro.

This implementation of the sensor system is powered by a LiPo battery which is stored in the body housing. There is also the option of powering the RPi from the drone itself, either through Molex Picoblade 2-pin connector or micro-USB. The drone and controller should be powered on prior to supplying power to the RPi to ensure a seamless WiFi connection.

After start-up, an automatic adjustment of the Pi-camera settings is performed. After this adjustment they remain constant throughout the flight. During adjustment, the camera should be pointed at a surface representing the mean scene brightness. For this step, a calibration panel, bare or vegetated surface may be used, while a distance of >1m and the absence of cast shadows in the FOV of the camera is advised.

A field laptop is currently required as base station to run the accompanying programs which handle data processing and display. The script is run manually after data capture from the Pi-camera has started, indicated by a red LED visible on the Pi-camera.

Data capture should cease and the data downloaded automatically once the drone has landed and is disarmed. After processing has completed, the interpolated maps presented in the following section are made available to the user and the sensor and image data is stored.

Operational flight tests

Three operational flight tests were carried out with the goals of 1) demonstrating the functionality of the sensor system and its utility to identify changes in scene illumination and brightness, and 2) seeking to identify its susceptibility to angular effects.

Two autonomous flights following an identical lawnmower-pattern flight plan, as is commonly used for data acquisition, were conducted on the 6th of September 2018 at 10:20 and 10:36 local time over a pasture. Flight speed was set to 5 m/s and the altitude was 30 m throughout. During the first acquisition, the illumination was exclusively diffuse (overcast conditions) while for the second acquisition the illumination changed from direct to diffuse over the course of the flight (change from sunny to overcast conditions).

One manual flight with the aim of varying the sun-sensor geometry throughout was conducted on the 7th of July 2018 at 16:40 local time under direct illumination conditions. The yaw of the aircraft can be altered in small increments by the controller while the roll and pitch result from the forward or lateral speed of the aircraft and resistance e.g. by wind. The targeted speed was close to typical speeds chosen for photogrammetric acquisitions, roughly between 4 and 6 m/s.

The interpolated maps which are generated by the script upon completion of the flight are displayed in Figure A 31, Figure A 33 and Figure A 34. For the autonomous flights the colour scale was fixed to highlight strong changes in illumination (current implementation in associated code) while for analysing the influence of the sun-sensor geometries the colour scale is adjusted to the value ranges. The illumination values plotted against time are presented in Figure A 32 and Figure A 35. The standard deviations of the measured illumination values for the different conditions are reported in Table A 12.

The unequal spacing between measurement locations apparent in Figure A 31 may be attributed to synchronisation issues with image capture and storage due to the longer exposure times used and the defined capture frequency of 1 image per second. The cause should be investigated further to confirm the reliability of the geographic location.

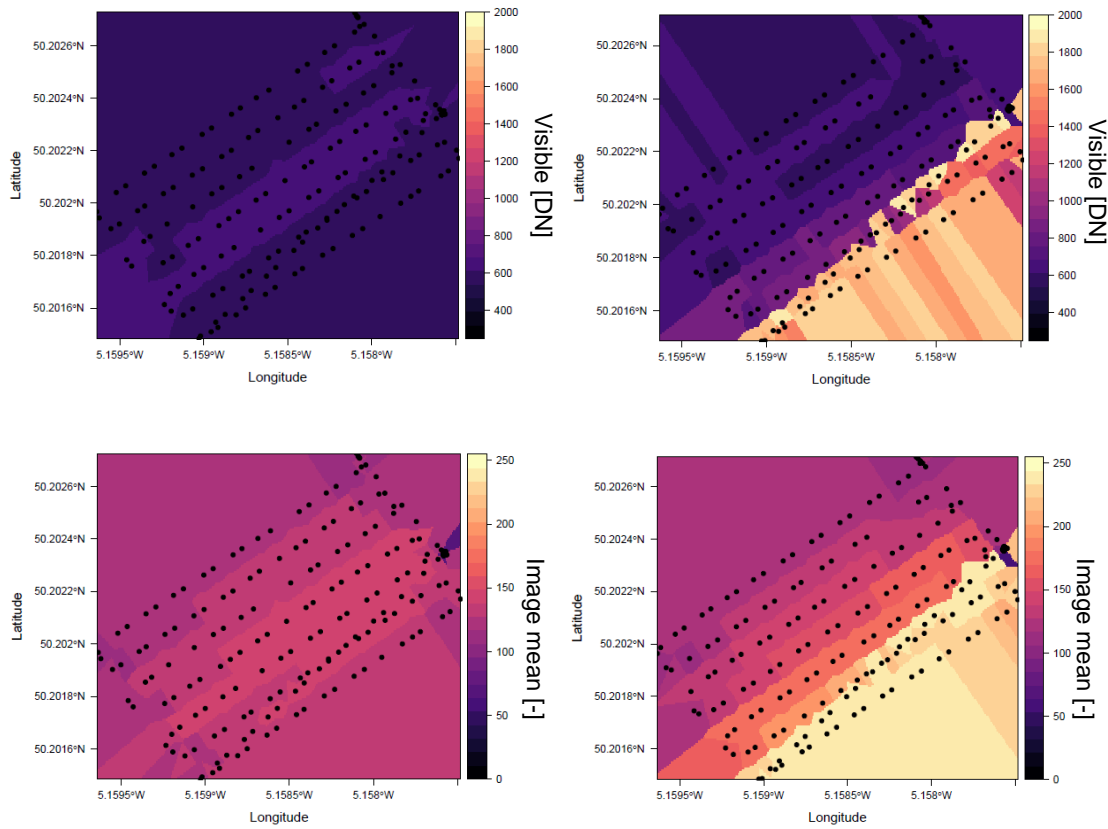


Figure A 31: Nearest neighbour interpolated maps automatically generated upon flight completion. Top: DN values reported by the visible diode of the illumination sensor for overcast (left) and changing conditions (right). Bottom: Mean RPi-cam image pixel values in the red band for overcast (left) and changing conditions (right).

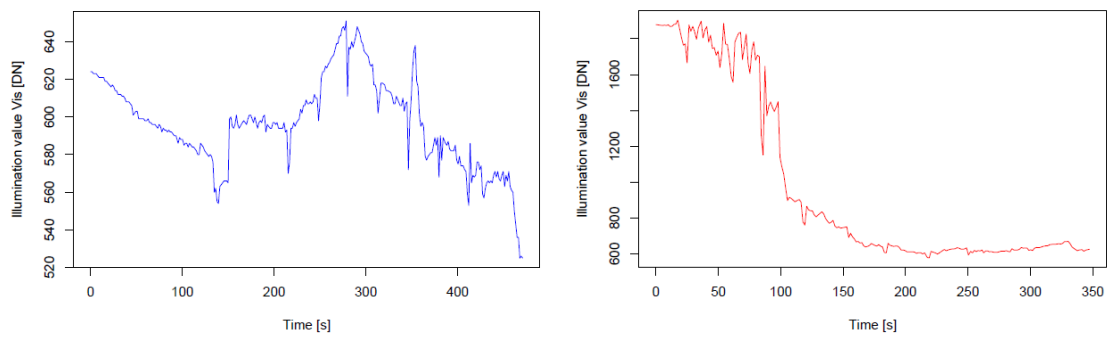


Figure A 32: DN values reported by the visible photodiode of the illumination sensor for overcast (left) and changing conditions (right) displayed over time.

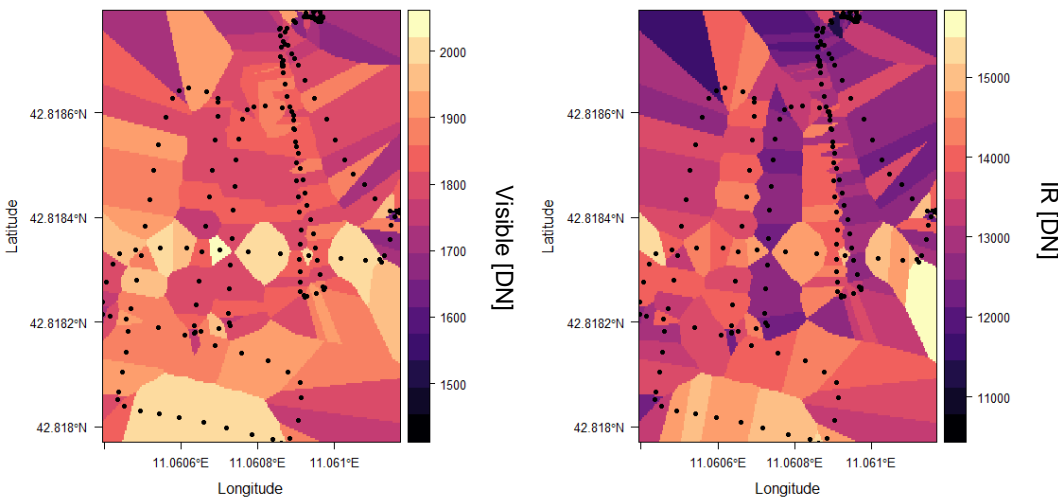


Figure A 33: Nearest neighbour interpolated maps of point-based illumination measurements (in DNs) acquired from the drone. Left: Vis-photodiode, Right: IR-photodiode

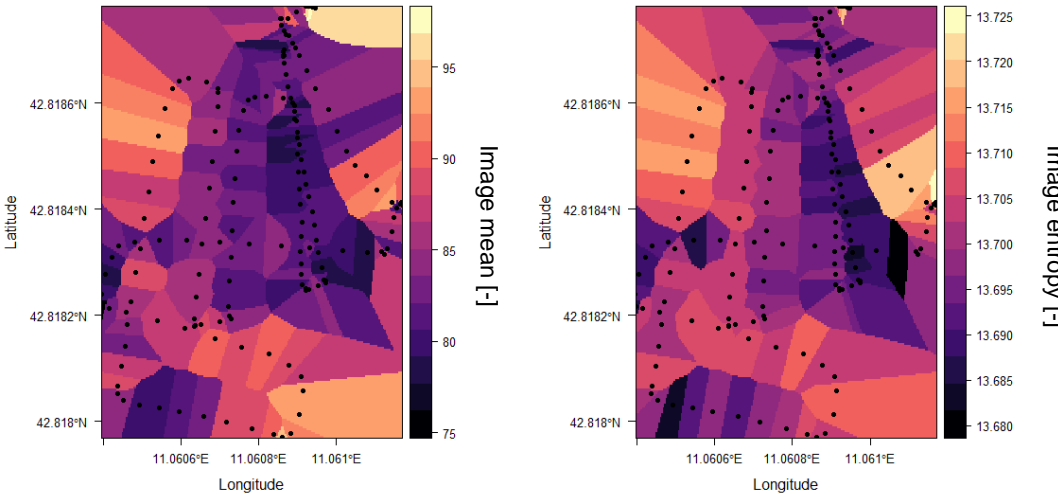


Figure A 34: Nearest neighbour interpolated maps of image based metrics acquired from the drone. Left: Mean RPi-cam image pixel values in the red band, Right: RPi-cam image image entropy values in the red band.

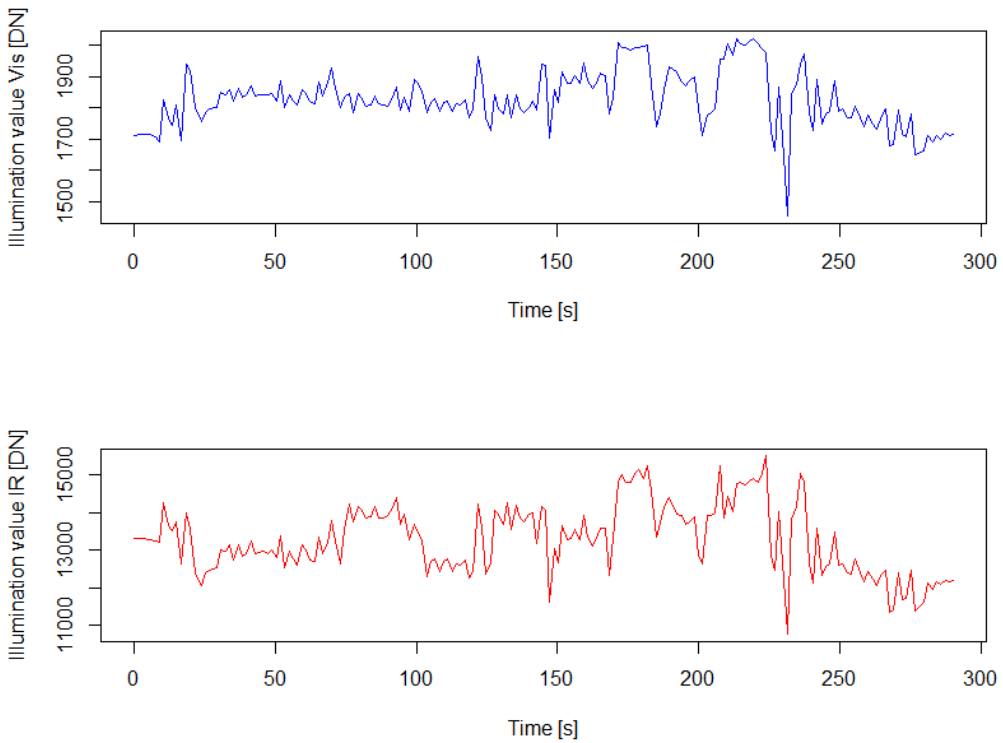


Figure A 35: DN values reported by the visible (top) and IR (bottom) photodiode for constant direct illumination conditions but varied sun-sensor geometry displayed over time.

Table A 12: Standard deviations of measured illumination values of the Vis and IR photodiodes for the three performed acquisitions.

Illumination conditions	Standard deviation Vis	Standard deviation IR
Diffuse (overcast)	23.78	217.93
Changing	489.88	4432.78
Direct (low solar angle)	90.13	907.32

Analysis of sun-sensor geometry influence

From an initial visual analysis of Figure A 33 and Figure A 34, the changing sun-sensor geometry appears to introduce variations in the measured DNs, due to straight flight lines of different geometries exhibiting different values. This is less evident in Figure A 35 due to the lack of geographical context but allows to better appreciate the magnitude of variations and noise generated by smaller vibrations.

The solar irradiance on a surface can be divided into a direct and diffuse component. In clear sky conditions, the direct component dominates and the direct irradiance on an inclined surface is related to the cosine of the illumination angle ($\cos i$) (Hay and McKay, 1985). Therefore, to quantify the relationship between the sun-sensor geometry and measured DN values, it is necessary to derive the solar illumination angle between the inclined sensor plane and the direction of solar rays (assumed parallel).

As the sensor is fixed on top of the drone and aligned to the aircraft's principal axes, the rotation around these (yaw, pitch and roll) which are logged for each measurement can be used to translate the drone normal vector into the world (or reference) coordinate system. The angle-derived rotation matrix used to achieve this is described in Diebel, (2006) as "Euler Angle Sequence (1, 2, 3)".

Applying the rotation matrix to the drone normal vector ([0,0,-1], z component is negative due to a downward pointing z axis) yields the unit vector in the world coordinate system ($uavV$). The unit vector in direction of the Sun is derived from azimuth (α) and elevation angle (β) as follows:

$$solV = \begin{bmatrix} \sin \alpha \cos \beta \\ \cos \alpha \cos \beta \\ \sin \beta \end{bmatrix} \quad (1)$$

Finally, the smallest angle between the normalised solar and the drone normal vectors is found as follows:

$$i = \cos^{-1}(solV \cdot uavV) \quad (2)$$

The plot of $\cos i$ against measured DN values by the IR diode (Figure A 36) reveals a weak negative relationship ($R^2 = 0.23$) which is contrary to what is expected according to Hay & McKay, (1985).

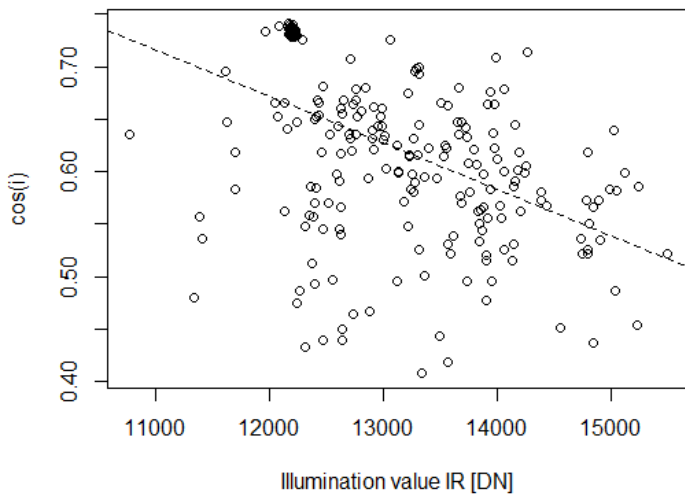


Figure A 36: Relationship between the measured illumination values measured by the IR diode and the cosine of the illumination angle derived from vehicle attitude information (yaw, pitch, roll) and sun angles.

Discussion of results and outlook

The system was successfully implemented based on its initial design and data was gathered under different illumination conditions. The produced maps of measured illumination values and scene brightness allow a clear visual interpretation of changes in illumination conditions throughout the acquisition and which areas were affected. An additional dataset informs on angular dependencies between measured DN values and scene illumination under direct illumination conditions.

The current nearest neighbour implementation of the map visualisation has the benefit of enabling rapid map generation and displaying values which are representative of the expected variations and approximate coverage after stitching for data acquired with the same frequency from a nadir-looking imaging sensor. The interpolation method and parameters such as the value ranges for the colour bar and number of levels displayed may be adjusted to suit individual applications.

For constant direct illumination, there proved to be considerable influences of varying sun-sensor geometry on the measured values, especially in the IR,

though measured DNs should be treated with caution due to the observed saturation at 400 W/m^2 when measuring in the laboratory. The measured values did not appear to be positively correlated with the solar illumination angle as was expected. This presents difficulties for the correction of the observed effect. It is also possible that oversaturation occurred for parts of the flight, despite low sun-angles, which would influence the result and warrants further investigation. Furthermore, it appears likely that the angular relationship with the measured illumination value is influenced by the protective transparent cover of the photodiode and its refractive index. To avoid this effect and create a more predictable relationship between illumination angle and measured DNs, the installation of a diffuser above the photodiode would be required, as was implemented by T. Hakala et al., (2013) who used an opal glass diffuser. To better understand the relationship, a more controlled experiment where the angles are varied in predefined intervals with a constant light source is desirable. Finally, the angular dependency of the contribution of diffuse (sky) irradiance is not considered (see Hay & McKay, (1985)). To avoid the influence of varying sun-sensor geometry altogether, a gimballed solution would be preferred. However, this requires a very specific setup and goes against the intended purpose of an easily implementable and affordable solution for metadata collection. Of importance for using the reported relative information in the field, the magnitude of change between direct and diffuse conditions must be larger than the angular influence, which going by the standard deviations of the acquisitions presented here appears to be the case.

Variations within the image-derived metrics don't appear to follow a strong angular relationship which is to be expected. Instead, for constant illumination the mean pixel value and image entropy will vary with changes to the surface cover imaged beneath. For a homogenous surface, brightness variations are clearly linked to illumination changes. Currently, the calculation of the image based metrics is the most time-consuming step of the post-acquisition processing pipeline, which is otherwise very rapid. A more efficient solution should therefore be found. An evaluation of which band combinations and metrics are more sensitive to different scene brightness changes should also be performed.

The use of low-cost sensors like the SI1145 and RPi-cam brings with it some limitations to their application, such as noise and saturation of the sensor, rolling

shutter effects in RPi-cam imagery as well as the absence of additional band-stop filters for the camera which would allow the reliable calculation of VIs. This also limits the use of the data in terms of scientific application. For the desired purpose of giving first indications of relative changes they are still considered suitable.

In previously performed tests, there is one stage in the acquisition and processing pipeline which was identified as most prone to failure. Due to the necessity of communication of the RPi with the drone and base station over WiFi, it is essential that the RPi automatically connects to the drone WiFi network on startup and reconnects once it is within range again, prior to landing. In case of failure, the RPi must be accessed manually.

There are still some remaining steps to make this system and accompanying software package a viable auxiliary tool for drone data acquisition. Firstly, a different base station implementation is desirable with the trend of flight planning and control of autonomous acquisitions moving to handheld devices such as smartphones and tablets. Dronekit is available for Android as well as Python which provides the base functionality required. The programs running on the RPi itself could be left unchanged. A further limitation is the requirement of Dronekit which limits the application of the current system to ArduPilot-based drones. With the rising popularity of drones from different manufacturers, there is a need for a more flexible system which is independent of the platform it is deployed on. This can be achieved by developing software to be run on the base station which is able to download and interpret flight logs from different systems. Alternatively, through the integration of an IMU and GPS receiver, the RPi can become fully independent of the drone. The drawbacks are an increase in weight and cost of the system, as well as possible interference with the drone's own GPS receiver, depending on proximity.

A8 TRUSTEE training certificates

See the following pages for attached certificates of the TRUSTEE training courses.



This certificate has been granted to

Dominic Fawcett

In recognition of his lecture on:

Cloud computing in remote sensing: An introduction to Google Earth Engine (4 hours)



held in University of Milano Bicocca

Milano, Italy on 27 June 2017

Michael Renn





Certificate of course completion

Presented by University of Exeter to:

DOMINIC FAWCETT

For attendance and participation in the course:

Drone field operations for environmental monitoring

Held at the University of Exeter from 30 October to 1 November 2017

(Course convenor: Dr Karen Anderson)





MAX-PLANCK-INSTITUT

Max Planck Institute
for Biogeochemistry



CONSEJO SUPERIOR DE INVESTIGACIONES CIENTÍFICAS



Certificate of Participation

Awarded to

Dominic Fawcett

For his attendance and participation at the Marie Curie ITN:

"Summer School on Field Experimental Design and Data Acquisition"
held in Navalmaral de la Mata- Cáceres, Spain from 11 to 18 March 2018





This certificate has been granted to

Dominic Fawcett

In recognition of his attendance to the Summer School /

Remote sensing for traits mapping in agriculture

Held in Forschungszentrum Jülich

Jülich, Germany 2 – 3 May 2019

Mico Rossini

Dr. Mico Rossini,
Project coordinator





This certificate has been granted to

Dominic Fawcett

In recognition of his attendance to Thematic Workshop 3

(32 hours)

Held in KU Leuven and VITO

Leuven, Belgium 6 – 9 May 2019

Micol Rossini

Dr. Micol Rossini,
Project coordinator





This certificate has been granted to

Dominic Fawcett

In recognition of his attendance to

Thematic Course 4 on Soft Skills (8 hours)

Course on Transferable Skills (8 hours)

Held in Fondazione Edmund Mach

San Michele all'Adige (Trento), Italy on 23 – 24 January 2020

Dr. Miccol Rossini, project coordinator

